

Anomalous Transport and Non-Gaussian Dynamics in Mobile-Immobile Models



Timo Julian Dörries

Publikationsbasierte Dissertation

zur Erlangung des akademischen Grades doctor rerum
naturalium (Dr. rer. nat.) in der Wissenschaftsdisziplin:
Theoretische Physik

Vorgelegt am Institut für Physik und Astronomie an der Mathematisch-
Naturwissenschaftliche Fakultät der Universität Potsdam.

This work is protected by copyright and/or related rights. You are free to use this work in any way that is permitted by the copyright and related rights legislation that applies to your use. For other uses you need to obtain permission from the rights-holder(s).

<https://rightsstatements.org/page/InC/1.0/?language=en>

Erstbetreuer:

Prof. Dr. Ralf Metzler

Mathematisch-Naturwissenschaftliche Fakultät

Institut für Physik und Astronomie

Universität Potsdam

Zweitbetreuer und erster Gutachter:

Prof. Dr. Arkady Pikovsky

Mathematisch-Naturwissenschaftliche Fakultät

Institut für Physik und Astronomie

Universität Potsdam

Zweiter Gutachter:

Dr. Andrey Cherstvy

Mathematisch-Naturwissenschaftliche Fakultät

Institut für Physik und Astronomie

Universität Potsdam

Dritter Gutachter:

Prof. Dr. Benjamin Lindner

Mathematisch-Naturwissenschaftliche Fakultät

Institut für Physik

Humboldt-Universität zu Berlin

Published online on the

Publication Server of the University of Potsdam:

<https://doi.org/10.25932/publishup-63495>

<https://nbn-resolving.org/urn:nbn:de:kobv:517-opus4-634959>

*I dedicate this dissertation
to my wonderful wife.*

Declaration

I hereby declare that this dissertation contains my own work and the work that I carried out in collaboration with others, as specified in the text and acknowledgements. Except where specific reference is made to the work of others, the contents of this dissertation are original and have not been submitted in whole or in part for consideration for any other degree or qualification in this, or any other university.

Timo Dörries
Potsdam, 21st October 2023

Acknowledgements

First of all, I would like to thank Ralf Metzler for giving me the opportunity to pursue my PhD in this vivid group, allowing me to work very independently and autonomously. I could always rely on your support through advice and guidance, especially in the first part of my PhD, which took place during a global pandemic. During the numerous scientific discussions we have had, you always created a receptive environment where I could confidently put forward my own thoughts and ideas. Special thanks go to Aleksei Chechkin for discussing our joint projects in great detail and sharing his scientific expertise with me. Without these countless hours of meditating about our equations and the physics behind it this thesis would not have been possible. Furthermore, I would like to thank Erik Kalz for fruitful discussions and a very nice atmosphere in our shared office. I also want to thank Trifce Sandev and Irina Petreska, who were always ready for a coffee and a discussion about science and everything around it. I would like to thank Andrés Fernando for the fruitful collaboration. This list would not be complete without thanking Christopher Jones for all the wonderful lunch breaks and joint explorations of the surroundings in Potsdam full of inspiring conversations. Finally, I would like to thank all regular participants of our seminar including Andrey Cherstvy, Yingjie Liang and Wei Wang for the lively discussions.

List of publications

This is the complete list of publications of the candidate, the ones contributing to the cumulative dissertation are [D1], [D2] and [D3]. The publications are ordered following the discussion in the main text.

- [D1] T. J. Doerries, A.V. Chechkin, and R. Metzler, Apparent anomalous diffusion and non-Gaussian distributions in a simple mobile-immobile transport model with Poissonian switching, *J. R. Soc. Interface* **19**, 20220233 (2022).
- [D2] T. J. Doerries, R. Metzler, and A.V. Chechkin, Emergent anomalous transport and non-Gaussianity in a simple mobile-immobile model: the role of advection, *NJP* **25**, 063009 (2023).
- [D3] T. J. Doerries, A. V. Chechkin, R. Schumer, and R. Metzler, Rate equations, spatial moments, and concentration profiles for mobile-immobile models with power-law and mixed waiting time distributions, *Phys. Rev. E* **105**, 014105 (2022).

Additionally, the following work has been published

- T. J. Doerries, S. A. M. Loos, and S. H. L. Klapp, Correlation functions of non-Markovian systems out of equilibrium: analytical expressions beyond single-exponential memory, *J. Stat. Mech.* **2021**, 033202 (2021).

Abstract

The mobile-immobile model (MIM) has been established in geoscience in the context of contaminant transport in groundwater. Here the tracer particles effectively immobilise, e.g., due to diffusion into dead-end pores or sorption. The main idea of the MIM is to split the total particle density into a mobile and an immobile density. Individual tracers switch between the mobile and immobile state following a two-state telegraph process, i.e., the residence times in each state are distributed exponentially. In geoscience the focus lies on the breakthrough curve (BTC), which is the concentration at a fixed location over time. We apply the MIM to biological experiments with a special focus on anomalous scaling regimes of the mean squared displacement (MSD) and non-Gaussian displacement distributions. As an exemplary system, we have analysed the motion of tau proteins, that diffuse freely inside axons of neurons. Their free diffusion thereby corresponds to the mobile state of the MIM. Tau proteins stochastically bind to microtubules, which effectively immobilises the tau proteins until they unbind and continue diffusing. Long immobilisation durations compared to the mobile durations give rise to distinct non-Gaussian Laplace shaped distributions. It is accompanied by a plateau in the MSD for initially mobile tracer particles at relevant intermediate timescales. An equilibrium fraction of initially mobile tracers gives rise to non-Gaussian displacements at intermediate timescales, while the MSD remains linear at all times. In another setting bio molecules diffuse in a biosensor and transiently bind to specific receptors, where advection becomes relevant in the mobile state. The plateau in the MSD observed for the advection-free setting and long immobilisation durations persists also for the case with advection. We find a new clear regime of anomalous diffusion with non-Gaussian distributions and a cubic scaling of the MSD. This regime emerges for initially mobile and for initially immobile tracers. For an equilibrium fraction of initially mobile tracers we observe an intermittent ballistic scaling of the MSD. The long-time effective diffusion coefficient is enhanced by advection, which we physically explain with the variance of mobile durations. Finally, we generalize the MIM to incorporate arbitrary immobilisation time distributions and focus on a Mittag-Leffler immobilisation time

distribution with power-law tail $\simeq t^{-1-\mu}$ with $0 < \mu < 1$ and diverging mean immobilisation durations. A fit of our model to the BTC of experimental data from tracer particles in aquifers matches the BTC including the power-law tail. We use the fit parameters for plotting the displacement distributions and the MSD. We find Gaussian normal diffusion at short times and long-time power-law decay of mobile mass accompanied by anomalous diffusion at long times. The long-time diffusion is subdiffusive in the advection-free setting, while it is either subdiffusive for $0 < \mu < 1/2$ or superdiffusive for $1/2 < \mu < 1$ when advection is present. In the long-time limit we show equivalence of our model to a bi-fractional diffusion equation.

Abstrakt

In den Geowissenschaften wurde das „mobile-immobile model“ (MIM) entwickelt, um den Transport von Verunreinigungen in Grundwässern zu beschreiben. Diese Verunreinigungen können in Sackgassenporen diffundieren oder an Oberflächen adsorbieren. Dabei bewegen sich die Verunreinigungen effektiv nicht. Der Grundgedanke des MIMs besteht darin, die Dichte der Verunreinigungen in eine Dichte aus mobilen Partikeln und eine Dichte aus immobilen Partikeln aufzuteilen. Jedes einzelne Teilchen der Verunreinigung wechselt dabei zwischen dem mobilen Zustand, wo es diffundiert und sich durch Advektion bewegt und dem immobilen Zustand, wo es sich nicht bewegt. Je nach Zustand wird die Verunreinigung der mobilen oder der immobilen Dichte zugerechnet. Die Aufenthaltsdauern im mobilen und immobilen Zustand folgen jeweils einer Exponentialverteilung. Dies bedeutet, dass der Wechsel zwischen mobilen und immobilen Zustand durch einen Telegrafprozess beschrieben werden kann. In den Geowissenschaften liegt der Fokus auf der „breakthrough curve“ (BTC), was die Konzentrationskurve an einem festen Ort definiert. Der Grundgedanke dieser Arbeit besteht nun darin, das MIM auf biologische Systeme zu übertragen, wo beispielsweise Proteine zwischen einem diffusiven und einem immobilen Zustand wechseln. Dabei fokussieren wir uns auf Messgrößen, die üblicherweise in Experimenten mit einzelnen Molekülen oder Proteinen gemessen werden. Typische Messgrößen stellen die mittlere quadratische Verschiebung (MSD) und die Verschiebungsdichte dar, wobei wir besonderen Fokus auf nicht-lineare MSDs und nicht-Gaußsche Verteilungen legen. Als tragendes Beispiel für MIM in biologischen Systemen identifizieren wir Tau Proteine, welche in Nervenzellen diffundieren und für eine zufällige Dauer an Mikrotubuli binden, wobei sie effektiv unbeweglich werden. In der eindimensionalen Beschreibung des Systems sind die mittleren Bindungsdauern wesentlich länger als die durchschnittlichen Diffusionsdauern. Dadurch entsteht eine exponentielle Ortswahrscheinlichkeitsverteilung begleitet von einem Plateau im MSD auf mittleren Zeitskalen, wenn die Proteine zu Beginn alle mobil sind. Für eine Gleichgewichtsverteilung an mobilen Proteinen zu Beginn ist das MSD linear, wobei die Verteilung einer skalierten Laplaceverteilung entspricht. In anderen Systemen, wie beispielsweise

biologischen Molekülen in Biosensoren, spielt Advektion eine wichtige Rolle. Das Plateau, welches wir im MSD für lange mittlere Immobilisierungsdauern finden, besteht auch mit Advektion. Zusätzlich finden wir ein neues Regime mit einem anomalen Skalierungsverhalten des MSDs. Dabei wächst das MSD kubisch unabhängig von der mittleren Immobilisierungsdauer, sofern die Advektionsgeschwindigkeit hinreichend groß ist. Für eine Gleichgewichtsverteilung an mobilen Molekülen finden wir ein ballistisches Regime im MSD. Das Langzeitverhalten vom MSD ist linear, wobei der effektive Diffusionskoeffizient durch Advektion verstärkt wird. Dieser Effekt ist in der Literatur bekannt. Wir bieten hier aber eine physikalische Erklärung über eine Kopplung der Advektion mit der Varianz der gesamten Aufenthaltsdauer im mobilen Zustand. Abschließend erweitern wir das MIM, indem wir über exponentiell verteilte Immobilisierungsdauern hinausgehen und beliebige Verteilungen zulassen. Das entsprechende Modell nennen wir extended MIM (EMIM). Besonderen Fokus legen wir dabei auf eine Mittag-Leffler Verteilung, die sich durch ein Potenzgesetz $\simeq t^{-1-\mu}$ mit $0 < \mu < 1$ für lange Immobilisierungsdauern auszeichnet. Solche Verteilungen werden in Experimenten gemessen. Das Potenzgesetz hat zur Folge, dass der Mittelwert divergiert. Wir fitten EMIM zu einer BTC aus einem Experiment, in dem die Konzentration von fluoreszenter Farbe nach Durchlauf eines Aquäduktes gemessen wird. Das gemessene Potenzgesetz der BTC kann durch MIM erklärt werden. Wir verwenden die erhaltenen Fitparameter, um das MSD und die Dichten darzustellen. Dabei finden wir ein lineares MSD mit Gaußscher Verteilung zu Beginn und eine nicht-Gaußsche Verteilung im Langzeitverhalten. Im Allgemeinen ist das MSD von EMIM mit der Mittag-Leffler Verteilung subdiffusiv im advektionsfreien Fall. Mit vorhandener Advektion finden wir Subdiffusion für $0 < \mu < 1/2$ und Superdiffusion für $1/2 < \mu < 1$. Im Langzeitlimit konvergiert EMIM zu einer bifraktionellen Diffusionsgleichung.

Contents

List of abbreviations and symbols	1
1 Introduction	3
Synopsis	15
2 Single rate mobile/immobile model	19
2.1 Formulation of the model	19
2.1.1 Solution in Laplace space	22
2.1.2 Solution using subordination	25
2.2 Results for the advection-free model	28
2.2.1 Displacement distributions	29
2.2.2 Mean squared displacements	32
2.3 Results for the model including advection	35
2.3.1 Long-time asymptote	37
2.3.2 Displacement distributions	38
2.3.3 Mean squared displacements	40
2.4 Comparison to the continuous time random walk	42
3 The extended mobile/immobile model	51
3.1 Mobile/immobile models beyond single rates	52
3.2 Formulation of the model	55
3.3 Results for the extended mobile/immobile model	61
3.3.1 Concentration profiles	61
3.3.2 Mean squared displacements	62

3.4	Relation between our model and the continuous time random walk	66
4	Summary and outlook	71
A	Expressions in Fourier-Laplace space	77
B	Following the steps of Langevin to obtain the MSD	79
C	Time averaged mean squared displacement	81
D	Collection of papers	87
	Bibliography	163

List of abbreviations and symbols

ADE	advection dispersion equation
BTC	breakthrough curve (concentration over time at a fixed location)
CLT	central limit theorem
CTRW	continuous time random walk
EMIM	extended mobile/immobile model
FCS	fluorescence correlation spectroscopy
FnG	Fickian yet non-Gaussian diffusion
FRAP	fluorescence recovery after photoactivation
MADE-1	first macrodispersion experiment
MIM	mobile/immobile model
MRMT	multirate mass transfer model
nG	non-Gaussian
TAMSD	time averaged MSD
PDF	probability density function

m	mass
$\gamma_\eta = 6\pi\eta r$	friction coefficient
η	viscosity
k_B	Boltzmann constant
T	temperature
v	advection speed
D	diffusion / dispersion coefficient
Pe	Péclet number
$L(x) = -v\frac{\partial}{\partial x} + D\frac{\partial^2}{\partial x^2}$	Advection-dispersion operator
$p(x, t)$	displacement distribution function
α	anomalous diffusion exponent
τ_m/τ_{im}	mean mobile/immobile duration
$\gamma(\tau)$	immobilisation time distribution
$\psi(\tau)$	sojourn time distribution of CTRW
$n_m(x, t)/n_{im}(x, t)$	mobile/immobile density
$n_{tot}(x, t)$	total density
f_m^0/f_{im}^0	fraction of initially mobile/immobile tracer particles
θ_m/θ_{im}	mobile/immobile pore volume
$\beta = \frac{\theta_{im}}{\theta_m}$	capacity coefficient

Chapter 1

Introduction

Under a microscope the world can be seen at the length scale of a few micrometres. The observed motion of, e.g., pollen appears very different from the behaviour of, e.g., a chair, that we know from the world on the metre scale. Ingen-Housz observed that all matter, including non-living particles, is in continuous motion [1]. Later, Brown studied this erratic motion systematically, which is nowadays known as Brownian motion [2]. It arises from collisions of the tracer particle with molecules from the surrounding medium, the so-called bath. A microscopic description using classical mechanics such as a Hamiltonian description of the tracer particle to predict the exact trajectory is unfeasible due to the enormous number of interacting particles. To illustrate, one millilitre of water contains around 3×10^{22} water molecules. Another practical issue is the reproducibility of an experiment. Due to the unknown initial conditions of the surrounding bath, the observed trajectories of a tracer particle will differ from experiment to experiment. The description developed by Einstein, Sutherland, Langevin and others overcomes this issue by describing the bath probabilistically [3–11]. Moreover, Langevin starts with Newton's second law for a tracer with mass m and replaces all interactions of the tracer particle with the bath particles by the effective forces acting on the tracer particle [8],

$$m \frac{d^2}{dt^2} x(t) = -\gamma_\eta \frac{d}{dt} x(t) + \sqrt{2k_B T \gamma_\eta} \xi(t). \quad (1.1)$$

The first term on the right side is the deterministic Stokes friction force with friction coefficient $\gamma_\eta = 6\pi\eta r$ for a spherical particle, viscosity η and particle radius r . We note that a recent study showed that similar laws hold for single proteins on the length scale of a few nanometres [12]. Secondly, a random thermal force $\xi(t)$ is introduced to model random kicks of the bath particles. If times longer than the correlation time of collisions are considered, the force can be assumed to be delta correlated $\langle \xi(t)\xi(t+\Delta t) \rangle = \delta(\Delta t)$ Gaussian white noise. The angular brackets $\langle \cdot \rangle$ denote averaging over noise realizations, i.e. averaging over the unknown initial conditions of the bath. In the Langevin equation (1.1) the random force has the amplitude $2k_B T \gamma_\eta$, which is proportional to the Boltzmann constant k_B , the temperature T , and the friction coefficient γ_η , which is a characteristic of an equilibrium system. In equilibrium the energy obtained from random kicks of the surrounding medium is dissipated with the friction term. If we consider timescales, when the momentum has relaxed, i.e., for $t \gg m/\gamma_\eta$, the friction term becomes dominant over the acceleration term, and we obtain the overdamped Langevin equation $dx(t)/dt = \sqrt{2D}\xi(t)$ with $D = k_B T/\gamma_\eta$. For small spherical particles the timescale scales as $m/\gamma_\eta \simeq r^2$, rendering the overdamped Langevin equation relevant for single particle tracking experiments of small tracers [13].

Instead of deterministic trajectories in a microscopic description we now obtain a probability density function (PDF) $p(x, t)$, where $p(x, t)dx$ denotes the probability of finding the tracer in the interval $[x, x+dx]$ at time t . In the overdamped limit $p(x, t)$ follows the deterministic Smoluchowski equation

$$\frac{\partial}{\partial t} p(x, t) = \left[-\frac{1}{m\gamma_\eta} \frac{\partial}{\partial x} F(x) + D \frac{\partial^2}{\partial x^2} \right] p(x, t), \quad (1.2)$$

which can be derived from the Langevin equation (1.1) with an external force $F(x)$ [14, Eq. (1.23)]. In the force-free setting the resulting Brownian motion is characterised by a Gaussian displacement distribution function $p(x, t) = \exp(-x^2/4Dt)/\sqrt{4\pi Dt}$. The spread of particles is often characterised by the mean squared displacement (MSD), which is the second central moment of $p(x, t)$. For Brownian motion it is linear and given by $\langle x^2(t) \rangle = 2Dt$. Langevin obtains this MSD directly from (1.1) and finds the

same MSD for $t \gg m/\gamma_\eta$. The Gaussian PDF and the linear MSD are characteristic features of Brownian motion. They naturally arise from the central limit theorem (CLT), when the increments of the position due to collisions with the bath meet three conditions [15]. The increments must be independent, identically distributed, and they must have a finite mean. Physically this implies a homogenous stationary medium, i.e., a medium constant in space and time such that all tracers of an ensemble experience similar environments. Therefore, if non-Gaussian (nG) displacements or non-linear MSDs are observed, then at least one of the three conditions is not fulfilled. This further implies that a physical mechanism is present, that leads to the breaking of one of the CLT assumptions.

In this thesis we investigate how the displacement distributions and MSDs are affected when the tracer particles undergo intermittent immobilisations, i.e., switch between a mobile and an immobile state. The stochastic residence times in the mobile and immobile state lead to non-identically distributed displacements and as a result we find nG displacements and an anomalous scaling of the MSD at intermediate timescales. The latter refers to a scaling of the MSD with t^α . The case $0 < \alpha < 1$ is called subdiffusion, while $1 < \alpha \leq 2$ is called superdiffusion [13].

We adapt the mobile-immobile model (MIM) known from geoscience to biological experiments [16–18, D1, D2]. The main idea of the MIM is to split the total density of tracers $n_{\text{tot}}(x, t)$ into a mobile density $n_{\text{m}}(x, t)$, where tracers are subject to advection and diffusion and an immobile density $n_{\text{im}}(x, t)$, such that $n_{\text{tot}}(x, t) = n_{\text{m}}(x, t) + n_{\text{im}}(x, t)$. Tracers stochastically switch between a mobile and an immobile state and contribute either to $n_{\text{m}}(x, t)$ or $n_{\text{im}}(x, t)$, respectively. In the MIM the transitions between $n_{\text{m}}(x, t)$ and $n_{\text{im}}(x, t)$ are modelled with single rates, corresponding to exponential residence time distributions. In some experimental settings the splitting into the mobile and immobile density becomes relevant, when immobile tracers cannot be measured, for instance, because they need to enter the detector from a groundwater spring [17, 19–21]. Over the past five decades, the MIM has been extensively explored in the scientific literature, mostly with a focus on the breakthrough curves (BTC), which is the concentration $C(x, t)$ with

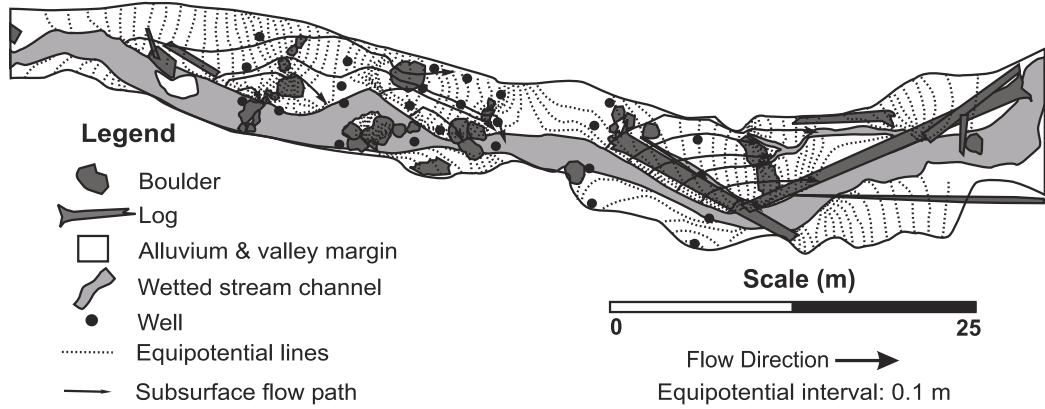


Figure 1.1: Sketch of a mountain stream, which is the experimental site of the groundwater transport experiment in [27]. Modified and reprinted with permission from [27]. Copyright 2002 by John Wiley & Sons, Inc.

units $[C(x, t)] = \mu\text{g/L}$ at a fixed location over time [16, 17, 22–26]. A sketch of a heterogeneous experimental site from [27] is shown in figure 1.1, where 11 g of rhodamine are injected at a single point and the BTC is measured 306, 4 m downstream. The sketch shows part of the H.J. Andrews Experimental Forest in Oregon, USA, where heterogeneities arise from various obstacles such as boulders, logs and subsurface flow paths. We note in passing a model similar to the MIM was proposed to describe charge carriers moving in photoreceptors with traps [28]. The model is identical to our formulation of the MIM for the special case of a single trap. The calculated observable in [28] is given by the electrical current. Similar models to the MIM have been analysed in biological contexts for experiments using fluorescence recovery after photobleaching and fluorescence correlation spectroscopy (FCS), while the MSD and PDF have not been analysed in this context [29, 30].

In other biological experiments the MSD is a common observable [31–34]. The MSD of the mobile, immobile and total density of the MIM have already been calculated, albeit without clearly identifying anomalous scaling regimes [23, 35, 36]. The goal of this thesis is to find anomalous diffusion, i.e. non-linear MSDs, and nG displacements in the MIM. We therefore systematically study the MSD in the light of anomalous diffusion and identify clear anomalous diffusion regimes at relevant intermediate timescales and provide physical explanations for them. In addition, we analyse the particle densi-

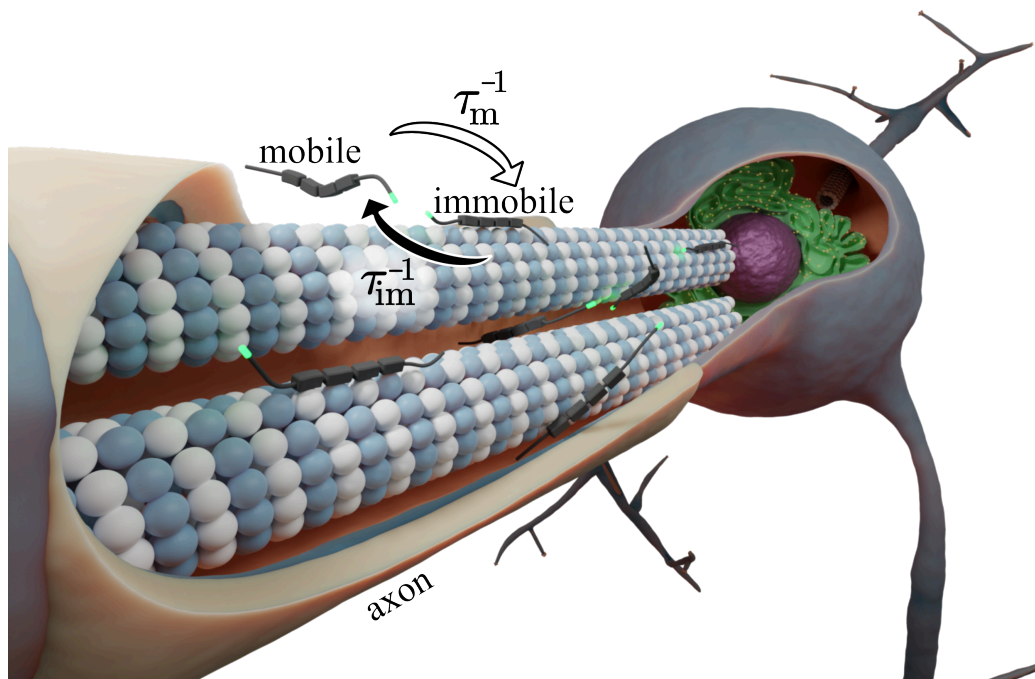


Figure 1.2: Schematic of tau proteins in the axon of a neuron not to scale. Microtubules are rod-like structures, that stabilize the axon and are depicted using blue and white spheres. Tau proteins tagged with a green fluorescent protein freely diffuse inside the axon until they bind to a microtubule. In the bound state the tau proteins are immobile. Switching between the two states occurs with constant rates $1/\tau_m$ and $1/\tau_{im}$.

ties and identify nG distributions at these timescales. The results strongly depend on the fraction of initially mobile tracers and are different for the advection-free case and the case with advection. Our results will be relevant for the interpretation of experiments in a range of systems, from biosensing to geophysics. As we will show, in particular, our results demonstrate that anomalous diffusion and nG densities emerge naturally from Poissonian switching and do not require the assumption of dedicated anomalous diffusion mechanisms.

We apply the advection-free MIM to tau proteins in neurons and re-

formulate it for the single-particle picture using normalized densities with $\int_{-\infty}^{\infty} n_{\text{tot}}(x, t) dx = 1$. As schematically depicted in figure 1.2, tau proteins diffuse freely inside the axons of neurons, where a large ratio of length to width allows a one-dimensional description. The axon is stabilized with microtubules, which are rod-like structures [37]. Tau proteins bind to microtubules with their four binding sites and immobilise. The function of tau proteins is to stabilize microtubules [37]. Moreover, tau proteins losing the ability to bind to microtubules is linked to diseases such as Alzheimer's disease [37]. In [38] it was shown that the motion of tau proteins can be modelled using a MIM with focus on fluorescence recovery after photoactivation (FRAP) experiments. The obtained mean immobile duration τ_{im} is long compared to the mean mobile duration τ_{m} .

To put our results into some context, we mention a selection of established models and experiments, that show nG displacements and anomalous scaling of the MSD similar to our findings. Anomalous diffusion and nG distributions are abundant in biological experiments. Single-molecule tracking experiments have shown that potassium channels in human embryonic kidney cells have nG displacements and are subject to subdiffusion due to transient binding to the actin cytoskeleton and the resulting immobilisations [39]. Other examples for nG distributions paired with (transient) subdiffusion due to immobilisations are given by the motion of insulin granules in biological cells, lipid granules in living fission yeast cells and acetylcholine receptors on live cell membranes [40–42]. Furthermore, simulations have shown nG displacements and subdiffusion of the drug doxorubicin in a silica nanoslit [43]. In other settings a plateau is observed in the MSD at intermediate timescales. For instance, this occurs in the case of two-dimensional fluids confined within a random matrix of obstacles or a porous cavity [45–47]. Additionally, plateaus in the MSD are observed in both two- and three-dimensional isotropic Lennard-Jones binary liquids [48]. A common feature of most of the mentioned systems with a plateau is the crossover from an exponential (Laplace) distribution to a Gaussian distribution. For long residence times in the immobile state compared to the mobile state we observe a plateau in the MSD paired with a transient Laplace distribution

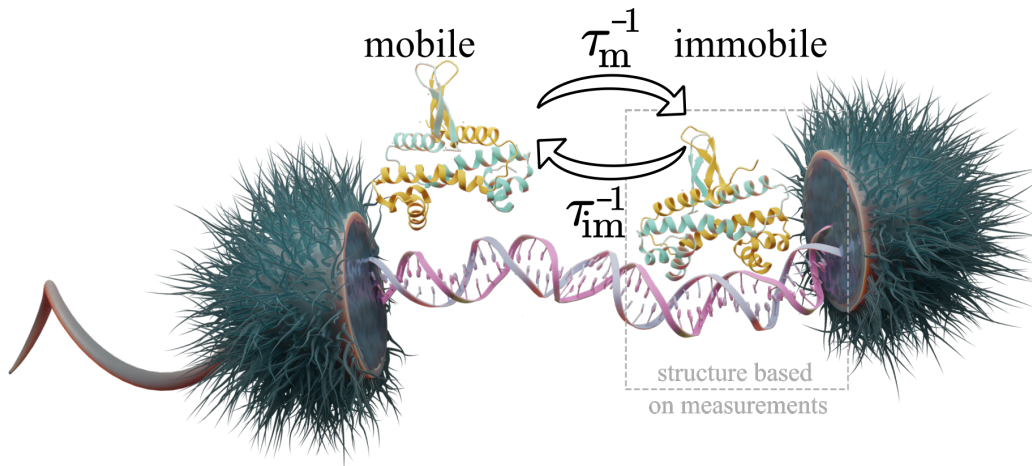


Figure 1.3: Schematic of the Fis DNA-binding protein inside an Escherichia Coli bacteria not to scale. On the left a flagellum is shown and the bacterium is covered in cilia. The cell wall is removed in the middle part of the figure. Fis slides along the DNA and transiently binds, resulting in nG displacements, that we model with the MIM using the transition rates $1/\tau_m$ and $1/\tau_{im}$ [49, D1]. The 3D model inside the dashed rectangle is based on the measured crystal structure of Fis bound to the DNA [50, 51].

for the MIM [D1].

Non-Gaussian displacement distributions do not necessarily imply an anomalous scaling of the MSD. We use the term Fickian yet non-Gaussian (FnG) diffusion in this thesis to describe this phenomenon, which refers to an MSD that is linear at all times paired with a nG displacement distribution. One of the first experiments to demonstrate FnG diffusion was carried out on colloidal beads diffusing along lipid tubes and beads diffusing through an entangled F-actin network [52]. Other systems with FnG diffusion pose acetylcholine receptors on live cell membranes and colloidal beads diffusing in a matrix of micropillars [42, 53]. Fis DNA binding proteins in Escherichia Coli bacteria are subject to FnG diffusion, as well [49]. We model the diffusion of Fis in this thesis, which is schematically shown in figure 1.3. The three-dimensional rendering inside the dashed rectangle of Fis bound to the DNA is based on the measured crystal structure [50, 51]. Fis slides along the DNA and transiently binds to the DNA, resulting in FnG diffusion, matching the predictions from the MIM [49, D1].

We briefly mention some models established in statistical physics to explain nG distributions. We start with models that display nG displacements with a crossover to Gaussian displacements at long times. For instance, diffusion in compartmentalized media yields PDFs with exponential tails [47]. The MSD is linear with an intermittent subdiffusive regime, similar to the plateau we find for the MIM [47, D1]. The second example for a theoretical model in which the PDF crosses over from a nG distribution to a Gaussian distribution is the diffusing diffusivity model [54]. Here, the diffusion coefficient $D(t)$ follows a stochastic process, modelling a heterogeneous medium [54]. In [54] the displacement distribution crosses over from a nG (Laplace) distribution at short times to a Gaussian distribution at long times. Depending on the initial distribution of $D(t = 0)$, the MSD scales linearly or ballistically $\simeq t^2$ at short times, similar to our findings for initially mobile or initially immobile tracer particles, respectively [54, 55, D1]. A special case of the diffusing diffusivity model is the jumping diffusivity model [56, 57]. There, $D(t)$ stochastically switches between the values D_- and D_+ . For residence times with finite mean this results in a tent-like shape of the PDF around the origin for short times, similar to our findings [57, D1]. In our study we additionally find a Laplace distribution at intermediate times. For power-law distributed residence times in both states long-time subdiffusion arises for $D_- \rightarrow 0$ [56]. The MIM can be understood in the light of diffusing diffusivity, with only two allowed values for the diffusivity and one of the values is zero.

In [D2] we analyse the effect of advection on the anomalous scaling regimes and nG distributions found in [D1]. This corresponds to the experimental setting of biomolecules flowing in a biosensor, when the biomolecules can specifically bind to receptors on the surface of the detector. We find that for initially mobile tracers and long immobilisations the plateau in the MSD persists at intermediate times also with advection present. At this point in time the displacement distribution is similar to the Laplace distribution found for the advection-free case. However, it falls off slower in the direction of advection compared to the opposite direction. For sufficiently high Péclet numbers we find a novel cubic scaling regime of the MSD, which appears for initially mobile and initially immobile tracers. The displacement densities

consist of a Gaussian and an additional spatially uniform tail or an exponential tail for initially mobile and initially immobile tracers, respectively. In the long-time limit the diffusion becomes Gaussian with an effective diffusion coefficient, that is enhanced by advection, as reported before [23, 35]. What we achieve here is an intuitive physical explanation for this effect due to a coupling of the advection and the variance of time spent in the mobile state.

So far, we have considered the case when the displacement densities converge to a Gaussian with linear MSD in the long-time limit. Now we introduce the continuous time random walk (CTRW), which can generate nG distributions and an anomalous scaling of the MSD also in the long-time limit. The CTRW was initially introduced to model the motion of charge carriers in amorphous semiconductors [58, 59]. In a CTRW the tracer particles wait for a random duration τ , called the sojourn time, followed by an instantaneous jump with a random length Δx . Both quantities are drawn from a transition probability density $\psi(\Delta x, \tau)$. Long-time anomalous diffusion emerges if the sojourn time distribution function $\psi(\tau) = \int_{-\infty}^{\infty} \psi(x, \tau) dx$ has a power-law scaling $\simeq \tau^{-1-\alpha}$ for large τ with $0 < \alpha < 1$. This power-law scaling results in a diverging mean sojourn time $\langle \tau \rangle = \lim_{T \rightarrow \infty} \int_0^T \tau \psi(\tau) d\tau = \infty$. Power-law sojourn times occur, e.g., in heterogeneous landscapes with exponentially distributed energy barriers [60].

In biological experiments the CTRW with power-law sojourn time distributions is applied to experiments mentioned above, e.g., lipid granules in living fission yeast cells with $\alpha \approx 0.8$ [41], potassium channels in the plasma membrane of kidney cells with $\alpha \approx 0.9$ [39] and the motion of a colloidal tracer in an entangled actin filament network with $\alpha \approx 0.33$ [61]. Long trapping has been observed for water molecules on the surface of cell membranes in simulations, where the position increments are additionally correlated due to membrane viscoelasticity [62]. The equations for CTRW are typically solved in Fourier-Laplace space with the so-called Montroll-Weiss equation or using a subordination approach [63]. The latter refers to using a probability distribution of jumps for a given time [63–65]. We adapt the subordination approach to our model, which gives insights, e.g., into enhanced diffusion at long times due to the coupling of advection and immobilisation at long

times [D2]. In the long-time limit CTRW dynamics with power-law sojourn times can be described with a fractional diffusion equation [63, 66, 67]

$$\frac{\partial^\alpha}{\partial t^\alpha} P(x, t) = -\frac{\partial}{\partial x} \frac{F(x)}{m\eta_\alpha} P(x, t) + K_\alpha \frac{\partial^2}{\partial x^2} P(x, t), \text{ for } 0 < \alpha < 1, \quad (1.3)$$

where $F(x)$ denotes an external force with the generalized friction constant η_α with units $[\eta_\alpha] = \text{sec}^{\alpha-2}$. The fractional advection-dispersion equation (1.3) is similar to the Smoluchowski equation (1.2), where the derivative with respect to time is replaced with a Caputo fractional derivative. The Caputo fractional derivative of order α is defined as

$$\frac{\partial^\alpha}{\partial t^\alpha} f(t) = \frac{1}{\Gamma(1-\alpha)} \int_0^t \frac{\partial}{\partial \tau} f(\tau) (t-\tau)^{-\alpha} d\tau, \text{ for } 0 < \alpha < 1, \quad (1.4)$$

and was initially introduced in the context of geoscience for a theory of viscoelasticity of the Earth's shell [68]. For a sojourn time distribution function $\simeq B_1 t^{-1-\alpha_1} + B_2 t^{-1-\alpha_2}$ with $B_1, B_2 > 0$ a bi-fractional diffusion equation emerges in the long-time limit of CTRW [69], meaning the single fractional derivative $\partial^\alpha/\partial t^\alpha$ in (1.3) is replaced by $B_1 \partial^{\alpha_1}/\partial t^{\alpha_1} + B_2 \partial^{\alpha_2}/\partial t^{\alpha_2}$. In the long-time limit our extended model with power-law immobile residence times follows a bi-fractional diffusion equation [D3]. We mention that in addition to power-law tailed sojourn time distributions, distributions with finite moments have recently received attention in CTRW [70, 71].

Moving on from biological systems on the micrometre scale we now go back to geological systems, where the transport of contaminants is investigated, that move through aquifers or streams on the kilometre scale. In a typical experiment the concentration of tracers $C(x, t)$ such as Bromide is measured over time at a fixed location, which is the BTC mentioned above [19, 72–74]. Contaminants diffusing in a homogenous medium can be described by the advection-dispersion equation (ADE), which is formally equivalent to the Smoluchowski equation (1.2) by replacing the forcing $F(x)/m\eta$ with the advection velocity v . It has the Gaussian solution $C(x, t) = C_0 \exp(-(x - vt)^2/4Dt)/\sqrt{4\pi Dt}$ for $C(x, 0) = C_0\delta(x)$, which results in a BTC with an exponential tail for $x > 0$. We point out a subtle difference between the

Smoluchowski equation (1.2) and the ADE regarding the parameter D . In the Smoluchowski equation D is the diffusion coefficient, while it is the dispersion coefficient in geological settings. The dispersion coefficient accounts for diffusion and turbulent mixing due to sheering profiles [75,76]. In contrast to the exponential tail predicted by the ADE, the long-time limit of experimental BTCs display power-law decay [19, 25, 27, 77] or power-law decay with a cut-off [74]. The CTRW with power-law sojourn time distributions is an established model to describe the power-law tailed BTCs of contaminants passing through streams or aquifers [19,23,26,78–83]. Tracers immobilise e.g., in the hyporheic zone, which is the region with non-flowing water adjacent to the flowing body of water in a stream [83–85]. Tracers may also effectively immobilise by adsorbing on streambed biofilms [74] or by diffusing in dead-end pores in porous media [86]. In the extended model that we propose in [D3] we fit our model to an experimental BTC with a power-law tail. In another experiment, called the first macrodispersion experiment (MADE-1), bromide was injected into a heterogeneous aquifer, where long immobilisations of tracers have been observed [87,88]. Multilevel sampling wells allowed measuring the plume profile over a distance of 300 m along the flow direction. A power-law decay of mobile mass was observed [21, 87, 88], that we model in [D3]. A model commonly used in geoscience is the multirate mass transfer model (MRMT), that includes multiple immobile zones with a distribution of exchange rates [23, 25, 79, 89]. For a power-law distribution of rates the model is called fractal MIM [21]. The total density follows a bi-fractional diffusion equation where one exponent is unity and the other between zero and one [21]. This fractal MIM can describe the long-time power-law decay of mobile mass. The fractal MIM cannot be written in terms of an immobilisation time distribution, due to a diverging memory function at zero. We introduce the extended MIM (EMIM) in [D3], where the model equations are given by an integro-differential equation, that explicitly takes immobilisation time distributions into account. We fit the mobile mass decay and BTC to experiments using a Mittag-Leffler (ML) trapping time density with a power-law tail. In contrast to the MIM, we obtain anomalous nG diffusion at long times for the EMIM. Recently, EMIM was applied to the diffusion of

excitons in layered perovskites and transition metal dichalcogenides [90].

In a nutshell, the MIM is a relatively simple model, where the dimensionless form of the MIM with advection only depends on two parameters: the ratio τ_m/τ_{im} for immobilisations and the Péclet number, which decides if the transport is advection or diffusion dominated. The research objective of this thesis is to identify anomalous scaling regimes in the MSD and nG displacement distribution in the MIM. Furthermore, we aim to apply it to biological applications such as tau proteins or Fis DNA-binding proteins as a first step [D1] and include advection as a second step [D2]. Finally, we include non-exponential immobile residence times and analyse the effect on the long-time behaviour [D3]. We find rich behaviour of nG diffusion and anomalous scaling of the MSD with a strong dependence on the fraction of initially mobile tracers, which can be chosen freely. For instance, in the advection-free model for an equilibrium fraction of initially mobile tracers we observe FnG diffusion, while the MSD for initially mobile tracers displays a plateau at intermediate time scales.

To put our results into some context, we make comparisons to the models and distributions introduced above throughout this thesis starting with a connection to the original derivation of the MSD by Langevin [8]. The plateau in the MSD of the MIM in the advection-free setting can be explained using the line of thought from Langevin [8], where we change one critical assumption. Langevin assumes equipartition $\langle [\frac{d}{dt}x(t)]^2 \rangle = k_B T$. This gives $d\langle x^2(t) \rangle / dt = 2k_B T / \gamma = 2D$ in the overdamped limit $t \gg m/\gamma$. In contrast, in the MIM only the fraction $f_m(t)$ of all tracers is mobile, therefore the kinetic energy is given by $k_B T f_m(t)$ this gives the relation $d\langle x^2(t) \rangle / dt = 2k_B T f_m(t) / \gamma$. This relation holds at all times for arbitrary fractions of initially mobile tracers. If we now define an effective temperature $T_{\text{eff}}(t) = T f_m(t)$, it becomes apparent that on the level of the MSD the MIM behaves the same as a cooling system for initially mobile tracers. The fraction $f_m(t)$ is a monotonically decreasing function in this case, rendering the MSD slower than linear. A detailed derivation is presented in Appendix B. Next, the structure of this thesis is outlined in the synopsis.

Synopsis

The general structure of this thesis is given by the discussion of the main results from [D1–D3] in chapters 2 and 3 followed by a summary and outlook in chapter 4. We start with the simplest formulation of the MIM and increase the complexity from section to section. In chapter 2 we analyse the MIM with linear transition rates. In the first part of chapter 2 we model the one-dimensional motion of tau proteins without advection inside the axons of neurons, as published in

T.J. Doerries, A.V. Chechkin, and R. Metzler, Apparent anomalous diffusion and non-Gaussian distributions in a simple mobile-immobile transport model with Poissonian switching, *J. R. Soc. Interface* **19**, 20220233 (2022),

which is reference [D1]. We discuss the mobile, immobile and total density of tracer particles and the corresponding MSDs. Moreover, we consider three fractions of initially mobile tracers, namely all tracers initially mobile, all tracers initially immobile and an equilibrium fraction of initially mobile tracers. The main features we find are FnG diffusion for an equilibrium fraction of initially mobile tracers and a plateau in the MSD of initially mobile tracers accompanied by a Laplace distribution of displacements at intermediate timescales. Initially immobile tracers spread ballistically for short times.

My contributions to [D1] are the formal analysis, investigation, methodology and validation. I wrote the original draft and edited the review. Moreover, I created all figures and performed all simulations presented in this manuscript. I performed the calculations.

In the second part of chapter 2 we include advection and explore how this

affects the plateau in the MSD and the Laplace distribution found for the advection-free setting. This is a discussion of the results published in

T.J. Doerries, R. Metzler, and A.V. Chechkin, Emergent anomalous transport and non-Gaussianity in a simple mobile-immobile model: the role of advection, *NJP* **25**, 063009 (2023),

which is reference [D2]. When including advection, we aim to model the motion of bio molecules in a biosensor, that specifically bind to receptors on the surface. Only the bound molecules can be detected, e.g., via plasmonic resonance, rendering this system suitable for a formulation with the MIM, where the immobile density is modelled explicitly. For high Péclet numbers, i.e., when advection is dominant over diffusion in the system, we observe a cubic scaling of the MSD accompanied by nG distributions at short times. This cubic regime emerges for long immobilisations and for short immobilisations, if the Péclet number is sufficiently high. The plateau observed in the advection-free setting [D1] persists for arbitrary Péclet numbers for long immobilisations. In the long-time limit the diffusion is normal and the displacements follow a Gaussian distribution, where the diffusion coefficient is enhanced by advection. We explain this with the coupling of advection and the variance of total time spent in the mobile state.

My contributions to [D2] are the formal analysis including the calculations, investigation including the discovery of the cubic regime, methodology and validation. I wrote the original draft and edited the review. Moreover, I created all figures and performed all simulations.

In chapter 3 we consider geological systems with immobilisations, that do not follow single rate mass transfer. This work was published in

T. J. Doerries, A. V. Chechkin, R. Schumer, and R. Metzler, Rate equations, spatial moments, and concentration profiles for mobile-immobile models with power-law and mixed waiting time distributions, *Phys. Rev. E* **105**, 014105 (2022),

which is reference [D3] in this thesis. We begin in section 3.1 with a

short review of MRMT and the fractal MIM, which are common models in geoscience to describe power-law tailed BTCs. In [D3] we obtain exact expressions for the moments of fractal MIM and find a crossover from normal to anomalous diffusion for initially mobile tracers.

Due to the non-analytic behaviour of the kernel from the Caputo derivative, fractal MIM cannot be written using a proper trapping time density. To overcome this, we present the extended mobile-immobile model (EMIM) in section 3.2, that models tracers switching between a mobile and an immobile state, where any probability density can be used for the immobilisation time density. For an exponential immobilisation time density the MIM is recovered, while the EMIM with a ML trapping time density with a power-law tail $\simeq t^{-1-\mu}$, $0 < \mu < 1$, converges to a bi-fractional diffusion equation in the long-time limit. One order is μ and the other is one. The motion of initially mobile tracers crosses over from Brownian with linear MSD and a Gaussian distribution to a nG distribution and anomalous scaling of the MSD in the long-time limit. We use the EMIM to successfully fit the power-law tailed BTC of tracers passing through a karst aquifer under the Schwartzwasser valley, that was recorded 3500 m from the injection point. The fit with the EMIM follows the power-law decay seen in the data.

My contributions to [D3] are the formal analysis including the calculations, investigation, methodology and validation. I wrote the original draft and edited the review. Moreover, I created all figures and performed all simulations.

In chapter 4 we summarize our results and make concluding remarks. In Appendix A we provide lengthy expressions and Appendices B and C provide additional expressions and work that were not published in [D1–D3]. Finally, in Appendix D the full manuscripts [D1–D3] are printed.

Chapter 2

Single rate mobile/immobile model

This chapter is concerned with the mobile/immobile model, where the transition between the mobile and immobile states occurs with constant rates. This corresponds to the switching of a telegraph process. We introduce the model equations in section 2.1. Then, we discuss results independent of whether advection is present. Moreover, we show how to solve the model using Fourier-Laplace transforms in section 2.1.1 and subordination in section 2.1.2. In section 2.2 we analyse the densities and MSDs for the advection-free case, followed by section 2.3, where we repeat the steps for the case with advection. In section 2.4 we compare our results to the results obtained for the CTRW with (bi-)exponential sojourn times.

2.1 Formulation of the model

The main idea of the MIM is to split the total density of tracers $n_{\text{tot}}(x, t)$ into the mobile density $n_{\text{m}}(x, t)$ and the immobile density $n_{\text{im}}(x, t)$, such that $n_{\text{tot}}(x, t) = n_{\text{m}}(x, t) + n_{\text{im}}(x, t)$ with units $[n_{\text{tot}}(x, t)] = 1/\text{m}$. The dynamics

is defined by the model equations

$$\begin{aligned}\frac{\partial}{\partial t}n_m(x,t) &= -\frac{1}{\tau_m}n_m(x,t) + \frac{1}{\tau_{im}}n_{im}(x,t) - v\frac{\partial}{\partial x}n_m(x,t) + D\frac{\partial^2}{\partial x^2}n_m(x,t) \\ \frac{\partial}{\partial t}n_{im}(x,t) &= -\frac{1}{\tau_{im}}n_{im}(x,t) + \frac{1}{\tau_m}n_m(x,t),\end{aligned}\tag{2.1}$$

with mean mobile residence time τ_m , mean immobile residence time τ_{im} , advection velocity v and diffusion coefficient D . Equations (2.1) model a tracer that switches between a mobile and an immobile state, where the switching follows a Markov telegraph process [91]. Our model (2.1) can be seen as the special case of the "multi-trapping" model for a single trap, which was developed to describe the motion of charge carriers in dielectric materials [28]. Models similar to (2.1) have been used in biological settings to explain the motion of tau proteins [38] or glucocorticoid receptors [92]. In biological contexts transport with intermittent immobilisations, such as in the MIM, is referred to as "stick and diffuse" [30] or "reaction-diffusion" [38, 92], where a reversible binding reaction is present. In our model (2.1) we consider the initial conditions $n_m(x, 0) = f_m^0\delta(x)$ and $n_{im}(x, 0) = f_{im}^0\delta(x)$, where f_m^0 and f_{im}^0 represent the fractions of mobile and immobile tracers at $t = 0$, respectively, subject to a normalization condition of $f_m^0 + f_{im}^0 = 1$. This normalization to unity corresponds to the single particle picture.

The linear rates in (2.1) correspond to exponential trapping time distributions [93, 94]. To demonstrate this, we formally solve for $n_{im}(x, t)$ in (2.1) and plug the result into the differential equation for $n_m(x, t)$ in (2.1). This gives the new integro-differential equation for the mobile density

$$\frac{\partial}{\partial t}n_m(x,t) = -\frac{1}{\tau_m}n_m(x,t) + \int_0^t \frac{1}{\tau_{im}}e^{-(t-\tau)/\tau_{im}}\frac{n_m(x,\tau)}{\tau_m}d\tau + L(x)n_m(x,t)\tag{2.2}$$

with the advection-dispersion operator $L(x) = -v\partial/\partial x + D\partial^2/\partial x^2$. The immobilisation term remains unchanged with a linear rate $1/\tau_m$ and we identify the trapping time¹ distribution $\gamma(t) = \exp(-t/\tau_{im})/\tau_{im}$. The physical pic-

¹We use the terms "trapping time" and "immobilisation time" interchangeably, and make a clear distinction from the "sojourn time", that we solely use for the CTRW.

ture of expression (2.2) is as follows. In the interval $[\tau, \tau + d\tau]$ the fraction $d\tau/\tau_m$ of mobile tracers immobilise. Later, at time t they were immobile for the duration $t - \tau$. This fraction of tracers is multiplied with $\gamma(t - \tau)$ and the tracers are added back to the mobile density. From this it can be seen that $\gamma(t - \tau)$ is the probability density to leave the immobile state after waiting the duration $t - \tau$, i.e., being immobile for the duration $t - \tau$. Exponential immobilisation time densities have been measured for instance in single particle tracking experiments in biological experiments of the Sox2 DNA-binding protein [95] and transcription factor p53 [96]. We note that a similar expression to (2.2) can be obtained for the immobile density, which reveals that the mobile residence times are distributed exponentially, as well. A more general model is introduced in [97], where a tracer switches between a state with diffusivity D_- and D_+ . The residence times in each state follow PDFs $\psi_{\pm}(t)$ with mean residence times $\langle\tau\rangle_{\pm}$ and the fraction of tracers in each state is in equilibrium at all times [57]. An advantage of our model (2.1) is that we can freely choose the fraction of initially mobile tracers and thereby expanding the range of possible experimental applications.

In geoscience an approach slightly different to ours (2.1) is commonly used, which is defined by the set of equations [16, 19, 21, 22, 35, 98]

$$\frac{\partial}{\partial t} C_m(x, t) + \beta \frac{\partial}{\partial t} C_{im}(x, t) = L(x) C_m(x, t) \quad (2.3a)$$

$$\frac{\partial}{\partial t} C_{im}(x, t) = \omega(C_m(x, t) - C_{im}(x, t)). \quad (2.3b)$$

Instead of single particle position densities in (2.1), where the total density is normalized $\int_{-\infty}^{\infty} n_{tot}(x, t) dx = 1$, we have concentrations $C_m(x, t)$ and $C_{im}(x, t)$ with units $[C_m(x, t)] = [C_{im}(x, t)] = \mu\text{g/L}$. The mobile mass $M_m(t) = \theta_m \int_{-\infty}^{\infty} C_m(x, t) dx$ and immobile mass $M_{im}(t) = \theta_{im} \int_{-\infty}^{\infty} C_{im}(x, t) dx$ follow the total normalization $M_0 = M_m(t) + M_{im}(t)$. The capacity coefficient β defines the ratio of the immobile to mobile pore volumes $\beta = \theta_{im}/\theta_m$. By formally choosing $M_0 = 1$, $\beta\omega = 1/\tau_m$ and $\omega = 1/\tau_{im}$ we obtain the equivalence of $C_m(x, t)$ and $n_m(x, t)$. At the same time the immobile density is the scaled immobile concentration $n_{im}(x, t) = \beta C_{im}(x, t)$ for this particular choice of parameters. Therefore, if only the mobile density is measured, it

does not matter whether model (2.1) or (2.3) is chosen. Next, we show how to solve the model equations (2.1) using Fourier-Laplace transforms.

2.1.1 Solution in Laplace space

We apply the Fourier-Laplace transform defined by the expression $f(k, s) = \int_{-\infty}^{\infty} dk \int_0^{\infty} ds f(x, t) \exp(ikx - st)$ to the model equation (2.1) and solve for $n_m(k, s)$, $n_{im}(k, s)$ and $n_{tot}(k, s)$. In these expressions, the Fourier wave number k is associated to the real space distance x , while the Laplace variable s is associated with time t . This is a common approach to solve diffusion equations, and it is done similarly in [23, 58, 59, 79]. In this thesis we denote expressions in Fourier- or Laplace space solely by replacing the respective arguments. Details of the calculations in Fourier-Laplace space for our model (2.1) can be found in [D1–D3]. The relations established in Fourier-Laplace domain presented in Appendix A can be inverted using the inverse Fourier transform, which yields the following expressions in Laplace domain

$$n_m(x, s) = \left(f_m^0 + \frac{f_{im}^0}{1 + s\tau_{im}} \right) \frac{\exp\left(\frac{vx}{2D}\right)}{\sqrt{v^2 + 4\phi(s)D}} \exp\left(-\sqrt{v^2 + 4\phi(s)D} \frac{|x|}{2D}\right) \quad (2.4)$$

$$n_{im}(x, s) = \frac{\tau_{im}/\tau_m}{1 + s\tau_{im}} \left(f_m^0 + \frac{f_{im}^0}{1 + s\tau_{im}} \right) \frac{\exp\left(\frac{vx}{2D}\right)}{\sqrt{v^2 + 4\phi(s)D}} \\ \times \exp\left(-\sqrt{v^2 + 4\phi(s)D} \frac{|x|}{2D}\right) + f_{im}^0 \frac{\tau_{im}}{1 + s\tau_{im}} \delta(x) \quad (2.5)$$

as functions of x and s with $\phi(s) = s[1 + \tau_{im}\tau_m^{-1}/(1 + s\tau_{im})]$. By performing a numerical Laplace inversion, the densities can be obtained for any desired time and position. The n -th moment of the total density $n_{tot}(x, t) = n_m(x, t) + n_{im}(x, t)$ can be obtained from the expression in Fourier-Laplace space

$$\langle x^n(s) \rangle = (-i)^n \left(\frac{\partial}{\partial k} n_{tot}(k, s) \right)^n \Big|_{k=0}. \quad (2.6)$$

Expression (2.6) holds, because $n_{tot}(k, s)$ can be interpreted as the characteristic function of a probability density $n_{tot}(x, s)$ due to the normalization [14]. We cannot directly apply expression (2.6) to the mobile and immobile den-

sities, because in general they are not normalized. We obtain the fractions $f_m(t) = \int_{-\infty}^{\infty} dx n_m(x, t)$ and $f_{im}(t) = \int_{-\infty}^{\infty} dx n_{im}(x, t)$ of mobile and immobile tracers from Laplace inversion of $n_m(k=0, s)$ and $n_{im}(k=0, s)$. The expressions are given by

$$f_m(t) = \frac{\tau_m}{\tau_m + \tau_{im}} + \frac{f_m^0 \tau_{im} - f_{im}^0 \tau_m}{\tau_m + \tau_{im}} \exp(-[\tau_m^{-1} + \tau_{im}^{-1}]t), \quad (2.7)$$

$$f_{im}(t) = \frac{\tau_{im}}{\tau_m + \tau_{im}} - \frac{f_m^0 \tau_{im} - f_{im}^0 \tau_m}{\tau_m + \tau_{im}} \exp(-[\tau_m^{-1} + \tau_{im}^{-1}]t), \quad (2.8)$$

with $f_m(t) + f_{im}(t) = 1$. The fractions of mobile and immobile tracers change over time in general and reach the respective stationary values $f_m^{\text{eq}} = \tau_m / (\tau_m + \tau_{im})$ and $f_{im}^{\text{eq}} = \tau_{im} / (\tau_m + \tau_{im})$ in the long-time limit $t \gg \tau_m, \tau_{im}$. This can be seen in figure 2.1, where $f_m(t)$ is shown as a grey line for the parameters $f_m^0 = 1$, $\tau_m = 1$ and $f_{im} = 100$ used in [D2]. Immobilisations are the physical process behind the nG displacements and anomalous scaling of the MSD, that we discuss in the following sections. Therefore, we illustrate the immobilisations in figure 2.1 by colouring the areas under the curve for $f_m(t)$ according to the fraction of tracers with specific numbers of immobilisations N_{im} . We obtain N_{im} by integrating the corresponding expressions in [30]. For $t \ll \tau_m = 1$ almost all tracers have never immobilised and the area under the curve is coloured black. At around $t = 10$ the majority of mobile tracers has immobilised once, as shown by the red area. For longer times both the mean number of immobilisations and the variance of immobilisations increases.

In order to obtain the p -th moment of the mobile and immobile density, we first calculate the non-normalized moments

$$(-i)^p \left. \frac{\partial^p}{\partial k^p} n_j(k, s) \right|_{k=0} = \langle x^p(s) \rangle_{j,u} \quad (2.9)$$

with $j \in \{m, im\}$, where we denote the moments as unnormalized using the subscript u . Then we calculate the Laplace inversion, which can be done exactly for the single rate model (2.1). In time-domain we normalize the

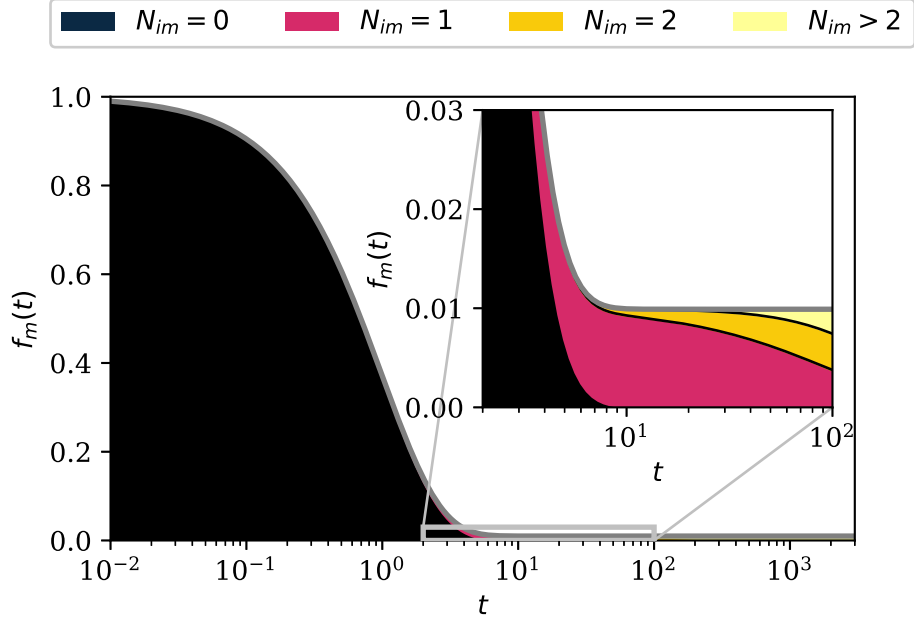


Figure 2.1: Semilog plot of the fraction of mobile tracers $f_m(t)$ over time shown as a grey line for $\tau_m = 1$, $\tau_{im} = 100$ and initially mobile tracers. In the long-time limit $t \gg \tau_m, \tau_{im}$ the equilibrium fraction $f_m^{eq} = \tau_m / (\tau_m + \tau_{im})$ is reached. The areas are coloured according to the number of immobilisation events N_{im} , where the black area corresponds to mobile tracers that have never immobilised, while the tracers immobilised and mobilised once in the red area.

unnormalized moments (2.9) as follows

$$\langle x^p(t) \rangle_j = \frac{\langle x^p(t) \rangle_{j,u}}{f_j(t)}, \quad (2.10)$$

as was done similarly in [36]. While the fractions $f_j(t)$ of mobile and immobile tracers are independent of advection, the moments (2.6) and (2.10) behave differently depending on the presence of advection. Therefore, we consider the two cases separately in sections (2.2) and (2.3), respectively. Next, we present the subordination method, which is especially suited to solving the model including advection.

2.1.2 Solution using subordination

Solving the model (2.1) in Fourier-Laplace space is a direct path to obtaining the moments and densities in Laplace space, which can be (numerically) transformed to time-domain solutions. In this section we introduce another approach, that does not require transforming to a conjugated variable and gives direct insights into the physical mechanisms of the MIM.

Bochner introduced the concept of subordination [99], which involves a process $X[\tau_o(t)]$. The operational time τ_o has non-negative increments and corresponds to the number of steps in many random walk contexts [100]. In the laboratory frame the time t is measured and the increments of $\tau_o(t)$ follow a known stochastic process for a given system. In our case, the stochasticity arises from the stochastic immobilisations. During an immobile period $\tau_o(t)$ remains constant, and it increases linearly during mobile periods. The process $X(\tau_o)$ follows Brownian motion with drift and can be written as the following Langevin equation [54, 64, 65, 101]

$$\frac{d}{d\tau_o}x(\tau_o) = v + \sqrt{2D}\xi(\tau_o) \quad (2.11a)$$

$$\frac{d}{dt}\tau_o(t) = i(t), \quad (2.11b)$$

where $\xi(\tau_o)$ denotes Gaussian white noise with correlation $\langle \xi(\tau)\xi(\tau') \rangle = \delta(\tau - \tau')$. Equation (2.11a) corresponds to a Langevin equation of a particle subject to a constant force and diffusion. The increments $i(t)$ follow a two-state telegraph Markov process with values zero and one, where the mean residence times are given by τ_{im} and τ_m , respectively. The subordinator $P(\tau_o, t)$ gives the probability density of the operational time τ_o at time t , and it is known exactly [30, 91]. The operational time τ_o is equivalent to the total mobile duration in our model. With the Gaussian propagator $G(x, t)$ corresponding to advection-diffusion we obtain the total density

$$n_{tot}(x, t) = \int_0^\infty P(\tau_o, t)G(x, \tau_o)d\tau_o, \quad (2.12)$$

which was reported similarly in [57] for a switching diffusion process. We note

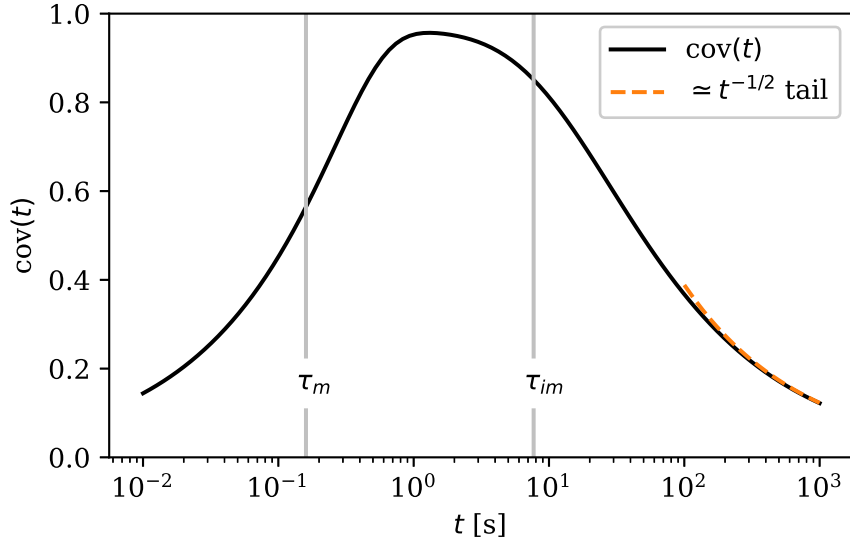


Figure 2.2: Semilog plot of the coefficient of variation $\text{cov}(t)$ (2.14) of the subordinator $P(\tau_o, t)$ for initially mobile tracers. The parameters $\tau_m = 0.16$ s and $\tau_{im} = 7.7$ s are taken from [38] and reflect the immobilisations of tau proteins in neurons. For short times $t \ll \tau_m, \tau_{im}$ and long times $t \gg \tau_m, \tau_{im}$ the coefficient of variation takes on small values, suggesting a distribution close to a Gaussian distribution. The long-time asymptote $\simeq t^{-1/2}$ is shown as a dashed orange line. For intermediate times $\tau_m \ll t \ll \tau_{im}$, $\text{cov}(t)$ takes on higher values, implying nG densities.

that expression (2.12) can be obtained from the expression for $n_{\text{tot}}(x, s)$ (2.5) in Laplace space. From equation (2.12) it can be inferred, that a wide distribution $P(\tau_o, t)$ yields a nG distribution due to non identically distributed increments consisting of a mix of Gaussians with a range of variances, while a sufficiently sharp distributed $P(\tau_o, t)$ generates a Gaussian distribution. One possible approach to obtaining $P(\tau_o, t)$ is to formally set $v = 1$ and $D = 0$ in the MIM (2.1) and identifying $P(\tau_o, t)$ with $n_{\text{tot}}(\tau_o, t)$ [D2]. This is possible, because in the diffusion-free case the position x of a tracer is directly proportional to the total mobile duration $x = v\tau_o$. For $v = 1$ we can formally identify $x = \tau_o$. This allows obtaining the moments of $P(\tau_o, t)$ from the moments of $n_{\text{tot}}(x, t)$, that we know exactly [D2]. Namely, we have

$$\langle \tau_o^n(t) \rangle = \int_0^\infty \tau_o^n P(\tau_o, t) d\tau_o = \langle x^n(t) \rangle_{\text{tot}} \Big|_{x=\tau_o, v=1, D=0}. \quad (2.13)$$

Now we can quantify the relative width of $P(\tau_o, t)$ using the coefficient of variation [102]

$$\text{cov}(t) = \frac{\sqrt{\langle [\tau_o - \langle \tau_o \rangle]^2 \rangle}}{\langle \tau_o \rangle} \quad (2.14)$$

that is a dimensionless quantity relating the standard deviation to the mean value. In Appendix C we show that (2.14) is equal to the square root of the ergodicity breaking parameter. The coefficient of variation (2.14) is shown in figure 2.2 for initially mobile tracers. For the mean mobile and immobile times the values $\tau_m = 0.16$ s and $\tau_{\text{im}} = 7.7$ s are chosen, that match the immobilisation behaviour of tau proteins in neurons [38, D1]. The coefficient of variation takes on small values for short times $t \ll \tau_m, \tau_{\text{im}}$ and long times $t \gg \tau_m, \tau_{\text{im}}$. The long-time scaling $\simeq t^{-1/2}$ is obtained in [D2] and shown as a dashed orange line in figure 2.2. This implies relatively sharp distributions of the subordinator $P(\tau_o, t)$ in these limits and therefore a particle density $n_{\text{tot}}(x, t)$ close to a Gaussian distribution. At intermediate times $\tau_m \leq t \leq \tau_{\text{im}}$ the subordinator is not a narrow function, as demonstrated by the relatively large value of $\text{cov}(t)$ shown in figure 2.2. This implies nG displacements, that we systematically study in the following section.

2.2 Results for the advection-free model

In this section we discuss the main results of

T.J. Doerries, A.V. Chechkin, and R. Metzler, Apparent anomalous diffusion and non-Gaussian distributions in a simple mobile-immobile transport model with Poissonian switching, *J. R. Soc. Interface* **19**, 20220233 (2022),

where we consider the advection-free model, i.e., we set $v = 0$ in the model equation (2.1). The advection-free MIM corresponds to biological systems with exponentially distributed immobilisations, such as synaptic vesicles in hippocampal neurons [30], glucocorticoid receptors in the nucleus [92] or DNA binding proteins such as the tumour suppressor p53 [103–105], the damage detection complex Rad4-Rad23 [103, 106] or the architectural DNA binding protein Fis, that slides along the DNA and transiently binds to it [49]. The latter is schematically depicted in figure 1.3. The motion of tau proteins has been described with a differential equation corresponding to the MIM (2.1) for $v = 0$ in [38]. Tau proteins plays a vital role in facilitating the assembly and enhancing the stability of microtubules, thereby aiding in the effective functioning of neurons, as schematically shown in figure 1.2 [37]. The relevance of tau proteins becomes clear from the association of Alzheimer’s disease with reduced tau proteins binding capacity [37, 107]. We use parameters obtained in [38] for tau proteins, i.e., $D = 13.9(\mu\text{m})^2\text{s}^{-1}$, $\tau_m = 0.16\text{ s}$ and $\tau_{im} = 7.7\text{ s}$ in this section. The residence times in the immobile state are long compared to the mobile residence times $\tau_m \approx 48\tau_{im}$. This gives rise to three time regimes that we will analyse, namely the short-time regime $t \ll \tau_m \ll \tau_{im}$, the intermediate time regime $\tau_m \ll t \ll \tau_{im}$ and the long-time limit $\tau_m \ll \tau_{im} \ll t$. These three time regimes together with the mobile, immobile and total density and the three fractions of initially mobile tracers $f_m \in \{0, f_m^{\text{eq}}, 1\}$ give a total of 27 cases, that are considered in [D1]. Here we highlight only some results and start with the displacement distributions.

2.2.1 Displacement distributions

In this section we discuss asymptotic expressions of the displacement distributions. We use the term displacement distribution instead of the more common term PDF, because the mobile and immobile densities in MIM are not normalized. We obtain the short-time asymptote by applying the Tauberian theorem, which relates the short-time behaviour for $t \ll \tau_m, \tau_{im}$ to the large s behaviour of the density in Laplace space for $s \gg 1/\tau_m, 1/\tau_{im}$ [108]. Similar results hold for the long-time limit [108]. We verify our asymptotics with computer simulations, as shown in [D1]. In this section we start with initially mobile tracers followed by initially immobile tracers and an equilibrium fraction of initially mobile tracers. For initially mobile tracers $f_m^0 = 1$, we obtain the Gaussian

$$n_{\text{tot}}(x, t) \sim \frac{1}{\sqrt{4\pi Dt}} \exp\left(-\frac{x^2}{4Dt}\right) \quad (2.15)$$

in the short time limit $t \ll \tau_m, \tau_{im}$. The Gaussian (2.15) corresponds to the density of free Brownian motion. Now we relax the condition $t \ll \tau_m$ to $t \ll \tau_{im}$ and hence allow immobilisations. As described in 2.1, the mobile residence time distribution is an exponential distribution with mean τ_m . Now two mechanisms are interacting. First, the spread of the tracers due to the Brownian diffusion and second the immobilisations. Both mechanisms combined yield the immobile density²

$$n_{\text{im}}(x, t \ll \tau_{im}) \sim \int_0^t \frac{\exp(-t'/\tau_m)/\tau_m}{\sqrt{4\pi Dt'}} \exp\left(-\frac{x^2}{4Dt'}\right) dt' . \quad (2.16)$$

This means the increments are not identically distributed, and we obtain a nG distribution. The integral in (2.16) can be solved analytically, revealing that a Laplace distribution $\exp(-\text{const}|x|)/(2\text{const})$ emerges in the centre $|x| \ll \tau_{im}\sqrt{D/\tau_m}$, as shown in [D1]. The Laplacian shape persists wider than the standard deviation of the distribution $\sqrt{2D\tau_m}$, rendering the Laplacian centre pronounced. This is different from e.g., the PDF reported for CTRW under relatively mild conditions, where exponential tails emerge far from

²Expression (2.16) can be obtained by solving the model equations (2.1) for $1/\tau_{im} = 0$

the Gaussian centre [71]. To state it more precisely, at intermediate times $\tau_m \ll t \ll \tau_{im}$ the Laplace distribution

$$n_{\text{tot}}(x, t) \sim \frac{1}{\sqrt{4D\tau_m}} \exp\left(-\frac{|x|}{\sqrt{D\tau_m}}\right) \quad (2.17)$$

emerges. Notably, (2.17) does not depend on time. We obtain the long-time asymptote

$$n_{\text{tot}}(x, t) \sim \frac{1}{\sqrt{4\pi D_{\text{eff}}^0 t}} \exp\left(-\frac{x^2}{4D_{\text{eff}}^0 t}\right) \quad (2.18)$$

for $t \gg \tau_m, \tau_{im}$ using the Tauberian theorem for $s \ll 1/\tau_m, 1/\tau_{im}$ with $\phi(s) \sim s(1 + \tau_{im}/\tau_m)$, where³ $D_{\text{eff}}^0 = D\tau_m/(\tau_m + \tau_{im})$. The total density matches Brownian motion slowed down by the fraction of mobile tracers, and it holds for any fraction of initially mobile tracers f_m^0 . In this long-time limit, the mobile and immobile density have the same shape where the weights are given by f_m^{eq} and f_{im}^{eq} , respectively. The occurrence of a Gaussian distribution is expected, because all timescales are finite in the MIM with linear rates (2.1), and we expect the central limit theorem to hold for $t \gg \tau_m, \tau_{im}$. Moreover, the relative width of the subordinator vanishes asymptotically, as shown in figure 2.2.

Now we consider initially immobile tracers. Initially immobile tracers remain at the origin until they mobilise. For short times $t \ll \tau_m, \tau_{im}$ the tracers mobilise with the constant rate $1/\tau_{im}$. Once released, the tracers behave the same as mobile tracers with a constant source at origin. This means that in contrast to initially mobile tracers the displacements are not identically distributed due to varying mobile durations, and we obtain a nG distribution

$$n_{\text{tot}}(x, t) \sim \frac{2t/\tau_{im}}{\sqrt{4\pi Dt}} e^{-\frac{x^2}{4Dt}} - \frac{|x| \left(1 - \text{erf}\left(\frac{|x|}{\sqrt{4Dt}}\right)\right)}{2D\tau_{im}} + \left(1 - \frac{t}{\tau_{im}}\right) \delta(x), \quad (2.19)$$

for $t \ll \tau_m, \tau_{im}$ and initially immobile tracers. We obtain the scaled Laplace

³We use D_{eff}^0 with the superscript 0 to distinguish this result for $v = 0$ from the more general expression (2.25) that includes advection.

distribution

$$n_{\text{tot}}(x, t) \sim \frac{t/\tau_{\text{im}}}{\sqrt{4D\tau_{\text{m}}}} \exp\left(-\frac{|x|}{\sqrt{D\tau_{\text{m}}}}\right) + \left(1 - \frac{t}{\tau_{\text{im}}}\right) \delta(x), \text{ for } \tau_{\text{m}} \ll t \ll \tau_{\text{im}} \quad (2.20)$$

at intermediate times, which is the same Laplace density as for initially mobile tracers (2.15) but with growing weight t/τ_{im} and an additional narrow peak at the origin. In the long-time limit initially immobile tracers follow the same Gaussian (2.15) with effective diffusion coefficient D_{eff}^0 , as initially mobile tracers.

Now we choose an equilibrium fraction of initially mobile tracers $f_{\text{m}}^0 = f_{\text{m}}^{\text{eq}}$. The model equations (2.1) are linear, therefore the distributions from equilibrium initial conditions is the weighted sum of the results for initially mobile and initially immobile tracers. For the timescale separation $\tau_{\text{m}} \ll \tau_{\text{im}}$ this implies that for short to intermediate times most of the tracers are immobile and concentrated in the delta peak at the origin, accompanied by a Gaussian with variance $2Dt$ arising from initially mobile tracers. The mass of the nG distribution arising from initially immobile tracers that have mobilised, i.e., (2.19) is negligible in comparison. At intermediate times $n_{\text{tot}}(x, t)$ is given by the Laplacian and delta peak (2.20). In [42] the displacement distributions of acetylcholine receptors on live cell membranes was measured. It has a distinct Laplacian shape with a delta peak at the origin, similar to the total density at intermediate times of initially immobile tracers (2.20) up to the coefficient t/τ_{im} . In another experiment the displacement distributions of Fis DNA binding proteins can be fitted with two Gaussians, where the standard deviation of one is below experimental resolution [49]. Therefore, this distribution could correspond to the short-time total density with an equilibrium fraction of initially mobile tracers, that consists of a delta peak and a Gaussian distribution. Another possible explanation for this nG distribution could be given by the intermediate time distribution of the MIM with a delta peak and a Laplace distribution.

In [57] the short-time distribution of a switching diffusion model with diffusivities D and zero is analysed for arbitrary residence time distributions with finite means restricted to an equilibrium fraction of tracers in state

D . The PDF scales like $\sim C_1(t) - C_2|x|$ for small $x > 0$, which is called a cusp [57]. In [D1] we report a different short-time distribution for an equilibrium fraction of initially mobile tracers, because we focused on the leading terms with the biggest weight. Taking all terms of $n_{\text{tot}}(x, t)$ into account, i.e. the weighted sum of [D1, Eq. (4.1)] and [D1, Eq. (3.1)] gives the same expression, as [57, Eq. (26)] in the limit $\tau_m \ll \tau_{\text{im}}$. In addition to the short-time limit we find a clear cusp in the total density at intermediate times $\tau_m \ll t \ll \tau_{\text{im}}$ in the form of a Laplace distribution. In the following section we characterise the width of the particle densities using the MSD.

2.2.2 Mean squared displacements

We obtain exact expressions for the MSD by performing a Laplace inversion of expressions (2.6) and (2.10). For the total density we obtain the mean squared displacement

$$\langle x^2(t) \rangle = 2D_{\text{eff}}^0 t + 2D\tau_{\text{im}} \frac{f_m^0 \tau_{\text{im}} / \tau_m - f_{\text{im}}^0}{(1 + \tau_{\text{im}} / \tau_m)^2} \left(1 - e^{-(\tau_m^{-1} + \tau_{\text{im}}^{-1})t} \right). \quad (2.21)$$

The shape of the MSD (2.21) depends on the fraction of initially mobile tracers f_m^0 . We start with the case of initially mobile tracers $f_m^0 = 1$. In this case the MSD grows linearly $\sim 2Dt$, which is the same as for free Brownian motion for short times $t \ll \tau_m, \tau_{\text{im}}$. At intermediate times strong subdiffusive behaviour is observed, where a plateau emerges for $\tau_m \ll t \ll \tau_{\text{im}}$. The plateau arises at the same time as the Laplace distribution (2.17) with a fixed scale parameter for $\tau_m \ll t \ll \tau_{\text{im}}$. The initially fast spread of tracers is slowed down due to immobilisations, resulting in the plateau at intermediate times. In the long-time limit $t \gg \tau_m, \tau_{\text{im}}$ the MSD grows linearly $\langle x^2(t) \rangle \sim 2D_{\text{eff}}^0 t$ with $D_{\text{eff}}^0 = D\tau_m / (\tau_m + \tau_{\text{im}})$, as discussed in the previous section. In the long-time limit only the fraction $\tau_m / (\tau_m + \tau_{\text{im}})$ of all tracers is mobile, therefore the spread is slowed down. We note that a result similar to (2.21) has been found in a two-dimensional setting restricted to $f_m^0 = 1$ where a distribution similar to a Laplace distribution emerges at intermediate timescales [109].

Now we show how to interpret the transition of the MSD from linear to a plateau to linear as a cooling effect. As described in Appendix B, the MSD

follows the expression

$$\frac{d}{dt}\langle x^2(t) \rangle = 2 \frac{k_B T f_m(t)}{\gamma} = 2D f_m(t), \quad (2.22)$$

exactly and we identify the effective temperature $T_{\text{eff}}(t) = T f_m(t)$. At short times $t \ll \tau_m \ll \tau_{\text{im}}$ the fraction $f_m(t)$ remains almost constant, yielding a linear MSD at short times with a high effective temperature $T_{\text{eff}} \sim T$. For $t \geq \tau_m$ the number of mobile tracers rapidly decreases leading to decreasing increments of the MSD. This gives the plateau at intermediate timescales $\tau_m \ll t \ll \tau_{\text{im}}$. In the long-time limit $t \gg \tau_m, \tau_{\text{im}}$ the fraction $f_m(t)$ takes on the constant value f_m^{eq} and the MSD is linear, corresponding to the temperature $T_{\text{eff}} \sim f_m^{\text{eq}} T \ll T$.

The transition of the MSD from linear at short times to a plateau at intermediate times to a linear MSD at long times has been observed in other contexts. One example is given by the diffusion of tracers in a heterogeneous medium with compartments, that are bounded by semipermeable barriers [47]. The same behaviour of the MSD was observed in a two-dimensional experiment of tracers transiently confined in a random matrix of obstacles [45]. Another experiment was carried out in [110], where a nanoparticle diffuses in a porous cavity with repulsive particle-wall interactions. An exponential distribution of sojourn times in these cavities was observed, that corresponds to a release of tracers with a constant rate, as in the MIM (2.1). Moreover, the MSD displayed linear growth at short times followed by a plateau and close to linear long-time growth [110]. In these models the linear MSD at short times arises due to the particle diffusing before encountering the boundary. In our model this corresponds to tracer diffusing freely before immobilising. The plateau arises in our model due to immobile tracers, while it originates from moving tracers that cannot move further from the initial position because of the confinement in [47, 110]. Due to the transient nature of the confinements, tracers travel from one compartment to another and the MSDs grow in the long-time limit. In our model the MSD grows linearly in the long-time limit due to the finite mean immobile time, i.e., the tracers keep moving after an immobile period.

Now we turn to initially immobile tracers, which yield a quadratic growth of the MSD $\langle x^2(t) \rangle \sim Dt^2/\tau_{\text{im}}$ at short times $t \ll \tau_{\text{m}}, \tau_{\text{im}}$. The quadratic term appears because mass is shifted from the delta peak at the origin to the mobile density proportional to t and the diffusion time increases. This is discussed in detail in [D1]. The quadratic growth can be understood as heating by identifying a linearly growing effective temperature $\simeq t$ in (2.22). A short-time quadratic growth of the MSD emerges in another model, as well. It has been observed for a diffusing diffusivity model, where the initial diffusion coefficient is set to zero [55], which resembles initially immobile tracers.

For an equilibrium fraction of initially mobile tracers the MSD follows $\langle x^2(t) \rangle = 2D_{\text{eff}}^0 t$ at all times. Together with the nG distribution at short to intermediate times this gives rise to FnG diffusion. A similar result has been observed for a three-dimensional trapping model similar to the MIM in [111]. In another setting an experiment of colloidal beads diffusing along a linear phospholipid bilayer tube FnG diffusion revealed, demonstrating that FnG may be observed in experiments [52]. The MSD was observed to be linear at all times, while the displacement distribution of tracers transitions from a Laplace distribution to a Gaussian distribution. In contrast to our result the variance of the Laplace distribution grows linearly in [52]. Our result is closer to the experiments on Fis DNA-binding proteins, where the FnG is reported [49]. The nG distribution is split into a sharp peak of immobile tracers at the origin and a wider distribution [49]. As described above, the latter could be explained with a Gaussian in our model in the short-time limit $t \ll \tau_{\text{m}}, \tau_{\text{im}}$ or a Laplace distribution at intermediate timescales $\tau_{\text{m}} \ll t \ll \tau_{\text{im}}$, that both arise for an equilibrium fraction of initially mobile tracers [D1].

So far, we have focused on the timescale separation of long immobile times $\tau_{\text{im}} \gg \tau_{\text{m}}$. For short immobilisations $\tau_{\text{im}} \ll \tau_{\text{m}}$ the long-time diffusion coefficient does not deviate from the diffusion coefficient of free Brownian particles, because almost all tracers are mobile. Therefore, the plateau observed for long immobilisation does not occur for $\tau_{\text{im}} \ll \tau_{\text{m}}$, and the diffusion is almost indistinguishable from Brownian motion for $t \gg \tau_{\text{im}}$, regardless of the fraction of initially mobile tracers.

To summarize, we use the MIM known from geoscience to describe the

motion of single tracers in biological experiments, where we focus on the MSD and displacement distributions. In addition, in Appendix C, we discuss time averaged mean squared displacements, which become relevant when only few trajectories are obtained from experiments. We find that the TAMSDs obtained from MIM vary significantly at intermediate measurement lengths even for vanishing delay and equilibrium initial conditions. This matches what has been reported before for a switching diffusion model [112]. Using the subordination technique we are able to provide an exact distribution of TAMSDs for short time-lags. In the next section 2.3, we consider advection and discover anomalous diffusion and nG distributions that emerge also for short immobilisations in contrast to the advection-free setting.

2.3 Results for the model including advection

In this section we discuss the main results of

T.J. Doerries, R. Metzler, and A.V. Chechkin, Emergent anomalous transport and non-Gaussianity in a simple mobile-immobile model: the role of advection, NJP **25**, 063009 (2023),

which we cite as [D2]. We consider the full MIM (2.1) including advection and we propose to model the motion of biomolecules in a biosensor in [D2]. The biomolecules bind to specific receptors in the sensor, leading to transient immobilisations. We do not compare our model to experimental data and we therefore use dimensionless parameters in this section to study various parameter regimes. The MIM including advection has been analysed in geoscience to describe the motion of tracers in porous media already in the 1960s intensively, often in the formulation of the MIM with capacity coefficients (2.3) [16–18, 22–24, 98]. It has been used to describe sorbing tracers [79, 113] and chemicals in chromatography [114]. In geoscience the observable is often the breakthrough curve (BTC), which is the concentration of tracers at a fixed position over time [16–19, 21, 26, 74, 76, 98]. The MSD of the MIM has been obtained for various fractions of initially mobile tracers [23, 35, 36]. We now systematically investigate the MSD and analyse how advection affects

the plateau that is present in the advection-free case for long immobilisations. In addition, we find a new regime at intermediate timescales with a cubic scaling of the MSD. We immediately proceed with the MSD instead of the first moment, because the first moment is related to the second moment of the advection-free case $\langle x^2(t) \rangle_0$ with the second Einstein relation [115]

$$\langle x(t) \rangle = \frac{v}{2D} \langle x^2(t) \rangle_0, \quad (2.23)$$

as can be seen by evaluating the expression for the moments in Laplace space (2.9).

As we demonstrate now, there exists a timescale before which advection plays a negligible role. In the mobile state tracers are displaced with $\Delta x_v = vt$ due to advection and $\Delta x_D = \sqrt{2Dt}$ due to diffusion. Comparing Δx_v and Δx_D gives the timescale $\tau_v = 2D/v^2$ before which advection plays a negligible role. This means that for $t \ll \tau_v$ the system subject to advection behaves the same as in the advection free setting in the previous section. As laid out in the following sections, we find a novel intermediate time regime with a clear anomalous scaling of the MSD paired with a nG displacement distribution for times longer than τ_v , if τ_v is smaller than τ_m and τ_{im} .

Using τ_v , we define the Péclet number $Pe = \tau_m/\tau_v = v^2\tau_m/(2D)$. Péclet numbers are dimensionless numbers that indicate if a transport process is advection- or diffusion dominated [116]. Usually it is defined as $Pe = vL/D$ with a typical length scale L , for which we choose $L = v\tau_m/2$. The model equations (2.1) depend on the four parameters τ_m , τ_{im} , v and D . We transform (2.1) to the dimensionless variables $t' = t/\tau_m$ and $x' = x/\sqrt{D\tau_m}$ and obtain the equations

$$\begin{aligned} \frac{\partial}{\partial t'} n_m(x', t') &= -n_m(x', t') + \frac{\tau_m}{\tau_{im}} n_{im}(x', t') \\ &\quad - \sqrt{2Pe} \frac{\partial}{\partial x'} n_m(x', t') + \frac{\partial^2}{\partial x'^2} n_m(x', t') \end{aligned} \quad (2.24a)$$

$$\frac{\partial}{\partial t'} n_{im}(x', t') = -\frac{\tau_m}{\tau_{im}} n_{im}(x', t') + n_m(x', t'), \quad (2.24b)$$

which only depend on the ratio τ_{im}/τ_m and the Pe . The dependence of the

dimensionless model (2.24) on two parameters only is worth to emphasize. The dimensionless formulation of pure advection-diffusion without immobilisations depends on one parameter. Our model adds only one additional parameter τ_m/τ_{im} , which defines the relative length of immobilisations. Therefore, the dimensionless model (2.24) has the minimum number of parameters needed to cover advection and diffusion dominated transport, as well as short and long immobilisations. In [98] the dimensionless formulation of the MIM is presented for the approach common in geoscience (2.3), that incorporates the capacity coefficient β instead of mean mobile and immobile durations τ_m and τ_{im} .

The long-time asymptote of the densities is independent of the fraction of initially mobile tracers and we therefore discuss it next before going to the preasymptotic regimes that depend on this fraction.

2.3.1 Long-time asymptote

The long-time asymptote is independent of the fraction of initially mobile tracers. Therefore, we consider it separately from the preasymptotic results for the concentration profiles and MSDs. The long-time effective diffusion coefficient obtained from the exact moments by $\lim_{t \rightarrow \infty} \langle [x(t) - \langle x(t) \rangle]^2 \rangle / 2t$ is given by the expression

$$D_{\text{eff}} = D \frac{\tau_m}{\tau_m + \tau_{im}} + v^2 \frac{\tau_m^2 \tau_{im}^2}{(\tau_m + \tau_{im})^3} \quad (2.25)$$

and becomes v dependent, if advection is present. This result is in contrast to the solution of the advection-diffusion equation, where v is absent in the central moments. Expression (2.25) has been reported before [23, 35]. We provide a physical explanation for the occurrence of advection in D_{eff} (2.25) here. In order to explain this effect, we discretize the advection-diffusion process into discrete steps of size Δx_l , that follow a normal distribution $\mathcal{N}(v\Delta t, 2D\Delta t)$ for some small timescale $\Delta t \ll \tau_m, \tau_{im}$. Each tracer performs a random number of steps n , that follows a Gaussian distribution $\mathcal{N}(\mu/\Delta t, \sigma^2/(\Delta t)^2)$ in the long-time limit $t \gg \tau_m, \tau_{im}$. Here μ and σ^2 denote the first moment and the second central moment of the subordinator obtained

from (2.13), as described in detail in [D2]. After these n steps, the tracer is located at $x = \sum_{l=1}^n \Delta x_l$. Using the independence of the step lengths Δx_l and the number of steps n , we obtain the variance of positions [117]

$$\begin{aligned} \langle [x(t) - \langle x(t) \rangle]^2 \rangle &= \langle n \rangle \langle [\Delta x_l - \langle \Delta x_l \rangle]^2 \rangle + (\langle \Delta x_l \rangle)^2 \langle [n - \langle n \rangle]^2 \rangle \\ &\sim 2 \left(D \frac{\tau_m}{\tau_m + \tau_{im}} + \frac{v^2 \tau_m^2 \tau_{im}^2}{(\tau_m + \tau_{im})^3} \right) t \end{aligned} \quad (2.26)$$

in the long-time limit $t \gg \tau_m, \tau_{im}$. On the one hand equation (2.26) illustrates that when there is diffusion without advection, the only factor influencing the MSD is the average mobile duration. On the other hand the relation (2.26) demonstrates that advection couples to the variance of the total mobile durations of the tracers.

In the long-time limit $t \gg \tau_m, \tau_{im}$ the total density follows the Gaussian

$$n_{\text{tot}}(x, t) \sim \frac{1}{\sqrt{4\pi D_{\text{eff}} t}} \exp\left(-\frac{(x - v_{\text{eff}} t)^2}{4D_{\text{eff}} t}\right) \quad (2.27)$$

with the effective advection speed $v_{\text{eff}} = v\tau_m/(\tau_m + \tau_{im})$. The Gaussian form is expected from the narrow form of the subordinator at long times and is checked with simulations in [D2]. With the expression for D_{eff} the specific form of v_{eff} follows directly from the Einstein relation (2.23). Next, we present nG displacements at intermediate timescales.

2.3.2 Displacement distributions

First, we will consider initially mobile tracers in this section. We start with long immobilisations $\tau_{im} \gg \tau_m$, for good comparability with the advection-free case in the previous section with the same timescale separation. Compared to the advection-free case a new advection dominated regime emerges for $\tau_v \ll t \ll \tau_m$, where the total density is given by

$$n_{\text{tot}}(x, t) \sim \left(1 - \frac{t}{\tau_m}\right) \frac{\exp\left(-\frac{(x-vt)^2}{4Dt}\right)}{\sqrt{4\pi Dt}} + \begin{cases} \frac{1}{\tau_m v} & \text{for } 0 < x < vt \\ 0 & \text{otherwise} \end{cases}, \quad (2.28)$$

where the scaled Gaussian corresponds to the mobile density and the uniform density to the immobile tracers. The physical mechanism for the uniform part of the distribution can be understood as follows. The fraction of mobile mass is close to unity due to $t \ll \tau_m$. This implies, that we effectively have a Gaussian with almost constant weight translating with constant speed v . From this mobile density tracers immobilise with a constant rate, giving rise to the uniform immobile distribution.

At intermediate times $\tau_m \ll t \ll \tau_{im}$, initially mobile tracers follow the density

$$n_{\text{tot}}(x, t) \sim \frac{\exp\left(\frac{vx}{2D}\right)}{\sqrt{v^2\tau_m^2 + 4D\tau_m}} \exp\left(-\sqrt{v^2\tau_m^2 + 4D\tau_m} \frac{|x|}{2D\tau_m}\right), \quad (2.29)$$

which is an asymmetric density with exponential decay with different constants for the positive and negative x direction. The density (2.29) does not depend on time, the same as in the advection-free case (2.17), because the physical mechanism remains the same: Almost all initially mobile tracers have immobilised once.

Still for initially mobile tracers, let us consider short immobilisations $\tau_{im} \ll \tau_m$, which results in Gaussian Brownian motion in the advection-free case. By including advection, we observe a nG distribution close to the origin for $x \ll vt$ and $v^2\tau_{im} \gg D$

$$n_{\text{tot}}(x, t) \sim \frac{t}{\tau_m} \frac{\exp\left(-\frac{t}{\tau_{im}} + \frac{x}{v\tau_{im}}\right)}{v\tau_{im}}, \quad \text{for } \tau_{im} \ll t \ll \tau_m \text{ and } 0 < x \ll vt. \quad (2.30)$$

The tail approximation is only applicable in the vicinity of the origin, and as a result, it is not normalized. This exponential tail (2.30) is similar to the exponential tail reported in [118] for a CTRW with exponentially distributed sojourn times and advection.

Now we turn to initially immobile tracers. For short immobilisation du-

rations $\tau_{\text{im}} \ll \tau_{\text{m}}$, we observe a tail similar to (2.30) given by

$$n_{\text{tot}}(x, t) \sim \delta(x) \exp\left(-\frac{t}{\tau_{\text{im}}}\right) + \frac{1}{v\tau_{\text{im}}} \exp\left(\frac{x}{v\tau_{\text{im}}} - \frac{t}{\tau_{\text{im}}}\right) \text{ for } 0 < x \ll vt, \quad (2.31)$$

for $v^2\tau_{\text{im}} \gg D$ and $\tau_v \ll t \ll \tau_{\text{m}}$, where an additional delta peak of immobile tracers is located at the origin. This asymptote is valid in the advection-dominated regime $\tau_v \ll t \ll \tau_{\text{im}}$. Going to long immobilisations $\tau_{\text{im}} \gg \tau_{\text{m}}$ we find that initially immobile tracers have the same delta peak at the origin in the short-time limit with an additional uniform distribution of mobile tracers

$$n_{\text{tot}}(x, t) \sim \left(1 - \frac{t}{\tau_{\text{im}}}\right) \delta(x) + \begin{cases} \frac{1}{\tau_{\text{m}}v} & \text{for } 0 < x < vt \\ 0 & \text{otherwise} \end{cases} \text{ for } \tau_v \ll t \ll \tau_{\text{m}}, \quad (2.32)$$

in the advection dominated regime $\tau_v \ll t \ll \tau_{\text{m}}$. The appearance of the uniform density of mobile tracers of initially immobile tracers and the similarity of this term to the second term in (2.28) is no surprise. In general the distribution of mobile tracers that were initially immobile is proportional to immobile tracers of initially mobile tracers [D1].

At intermediate times in the immobilisation dominated regime an asymmetric Laplace distribution with the same time-dependent weight as for $v = 0$ emerges. For an equilibrium fraction of initially mobile tracers, the densities are given by the weighted sum of the results for the mobile and immobile initial tracers, due to the linearity of the system. In summary, we have found an advection-dominated nG regime for both initially mobile and initially immobile tracers. This regime emerges for short immobilisations $\tau_{\text{im}} \ll \tau_{\text{m}}$ and for long immobilisations $\tau_{\text{m}} \ll \tau_{\text{im}}$. In the next section we see that this regime emerges in the MSD as well, although the lower bound of the corresponding timespan differs in some cases.

2.3.3 Mean squared displacements

From exact expressions in time-domain we obtain the Taylor expansion for $t \ll \tau_{\text{m}}, \tau_{\text{im}}$. For simplicity, we only consider the MSD of the total density here. Expressions for the mobile and immobile densities are provided in [D2].

We start with the MSD of initially mobile tracers

$$\langle [x(t) - \langle x(t) \rangle]^2 \rangle \sim 2Dt + \frac{v^2}{3\tau_m} t^3 \text{ for } t \ll \tau_m, \tau_{\text{im}}, \quad (2.33)$$

which shows superballistic scaling of the MSD with a cubic exponent for $\tau_\star = \sqrt{3\tau_v\tau_m} \ll t \ll \tau_m, \tau_{\text{im}}$ regardless of the ratio τ_m/τ_{im} for a sufficiently high Péclet number. In the previous section, we have seen that the distribution for short immobilisations is different compared to the distribution of long immobilisations. Both densities give rise to the cubic scaling of the MSD. The physical mechanism behind the cubic scaling for initially mobile tracers can be understood by going to the reference frame moving along the Gaussian peak of mobile tracers with $x' = vt$. From this co-moving reference frame the immobilised tracers appear to move ballistically, which gives a quadratic scaling of the MSD. In addition, the number of tracers that appear to be moving ballistically grows linearly. This gives the cubic scaling of the MSD.

The MSD of initially immobile tracers scales as follows

$$\langle [x(t) - \langle x(t) \rangle]^2 \rangle \sim \frac{Dt^2}{\tau_{\text{im}}} + \frac{v^2}{3\tau_{\text{im}}} t^3 \text{ for } t \ll \tau_m, \tau_{\text{im}}, \quad (2.34)$$

where the cubic term dominates for $\tau_v \ll t \ll \tau_m, \tau_{\text{im}}$. This cubic regime occurs for short and for long immobilisations for sufficiently large Péclet numbers. Note that in the Appendix of [D2] we discuss the parameter space where the cubic scaling emerges in detail.

Another new behaviour compared to the advection-free case in the MSD can be observed for short immobilisations, where "advection induced subdiffusion" is observed. With this terminology we refer to a plateau in the MSD for $\tau_{\text{im}} \ll t \ll \tau_m$ for $\text{Pe} \gg \tau_m/\tau_{\text{im}}$. This arises because initially immobile tracers mobilise fast and are subject to strong drift. This means that for short times the MSD grows fast (cubically, as described before). Once all tracers are mobile, they stay mobile for $t \ll \tau_m$. The spread due to diffusion is negligible compared to the initial spread and the distribution of tracers is translated without changing its shape significantly. Therefore, a plateau in the MSD emerges.

The MSD is a non-linear function of the first and second moment. Therefore, the MSD with an equilibrium fraction of initially mobile tracers is not simply given by a linear combination of the MSD for initially mobile and MSD for initially immobile tracers. Moreover, the Taylor expansion of the MSD

$$\langle [x(t) - \langle x(t) \rangle]^2 \rangle \sim 2Df_m^{\text{eq}}t + v^2 f_m^{\text{eq}} f_{\text{im}}^{\text{eq}} t^2 \text{ for } t \ll \tau_m, \tau_{\text{im}}, \quad (2.35)$$

contains a quadratic regime in the MSD for $\tau_v/f_{\text{im}}^{\text{eq}} \ll t \ll \tau_m, \tau_{\text{im}}$ in contrast to FnG in the advection-free case. The ballistic regime emerges for long immobilisations $\tau_{\text{im}} \gg \tau_m$ for $\text{Pe} \gg 1$ and for short immobilisations $\tau_{\text{im}} \ll \tau_m$ for $\text{Pe}^{-1/2} \ll \tau_{\text{im}}/\tau_m$.

Now that we have discussed the displacement distributions and the MSD for the MIM, we compare the results to the CTRW, which is a common model for systems with trapping.

2.4 Comparison to the continuous time random walk

The continuous time random walk (CTRW) was initially introduced to describe the motion of charge carriers in an amorphous semiconductor subject to an electric field [59]. It is widely used in geoscience [19, 23, 72, 79, 86] and biophysics [39–41, 61] to describe diffusing tracers that get trapped. The CTRW is a two-step process. First, a tracer waits for a random duration τ_s , called the sojourn time. Second, it instantaneously jumps a random distance Δx , where in general both quantities are drawn from a transition density $\psi(\Delta x, \tau_s)$. In Fourier-Laplace space the PDF is given by the Montroll Weiss equation [59]

$$p_{\text{CTRW}}(k, s) = \frac{1 - \psi(s)}{s} \frac{1}{1 - \psi(k, s)}, \quad (2.36)$$

with $\psi(\tau_s) = \int_{-\infty}^{\infty} \psi(\Delta x, \tau_s) d\Delta x$. A prevalent feature of the sojourn time densities is the asymptotic scaling $\psi(\tau_s) \simeq \tau_s^{-1-\alpha}$ with $0 < \alpha < 1$ [13]. This leads to a PDF with infinite mean, which can occur e.g., for expo-

nentially distributed energy pots [119]. Other examples where a diverging mean occurs include small-scale heterogeneities in porous sand packs [78] and the Kv2.1 potassium channel diffusing in the plasma membrane of living cells [39]. In chapter 3.2, we introduce an extension of the MIM, that allows for power-law immobilisation time distributions. For the present model (2.1), it is more instructive to compare our results to CTRWs with sojourn time distributions that have finite moments. Recently, (bi-)exponential sojourn time distributions gained attention [70, 71]. The relation between the MIM and its extensions on one hand and CTRW on the other hand has been discussed in detail, for instance, in [23, 79, 81], mainly on a general level of integro-differential equations. In this section, we make a direct comparison of CTRWs with (bi-)exponential sojourn time distributions and MIM on the level of PDFs and MSDs. In section 3.4 we extend the discussion to the sojourn time distributions, that arise from the formal equivalence on the level of integro-differential equations.

We start with a CTRW with an exponentially distributed sojourn time distribution $\psi(t) = \exp(-t/\tau_\psi)/\tau_\psi$ and a Gaussian displacement distribution $\lambda(x)$ with mean μ and variance σ^2 . This constitutes the model analysed in [118]. We modify the solution of this model found in [71] to account for non-zero mean displacements μ and obtain

$$p_{\text{CTRW}}(x, t) = \sum_{j=1}^{\infty} \frac{(t/\tau_\psi)^j \exp\left(-\frac{t}{\tau_\psi}\right) \exp\left(-\frac{(x-j\mu)^2}{2j\sigma^2}\right)}{j! \sqrt{2\pi j\sigma^2}}. \quad (2.37)$$

If t is of the same order as τ_ψ , only a few number of immobilisations will have taken place and the resulting PDF (2.37) takes on a ripple-like form with peaks centred around $x = j\mu$ for integer values of j . This distribution differs from a Gaussian distribution and is different from the nG distributions with spatially uniform tails or exponential tails, that we discuss for our model in section 2.3.2. From $p(x, t)$ (2.37) we obtain the MSD

$$\langle [x(t) - \langle x(t) \rangle]^2 \rangle = \frac{\sigma^2}{\tau_\psi} t + \frac{\mu^2}{\tau_\psi} t, \quad (2.38)$$

which is linear at all times. This is in contrast to the results obtained from our model, where the MSD deviates a lot from a purely linear MSD due to a cubic scaling and a subsequent plateau at intermediate timescales for $\tau_v \ll \tau_m \ll \tau_{im}$. It is no surprise that the MSD (2.38) does not contain many regimes, because the underlying CTRW contains a single timescale τ_ψ only.

Next, we compare MIM to a two-state CTRW with two timescales, that was introduced in [120]. In this CTRW it is drawn from $\psi_1(x, t)$ and $\psi_2(x, t)$ alternatingly. The transition densities are chosen as

$$\psi_i(x, t) = \frac{1}{\sqrt{4\pi D_i t}} \exp\left(-\frac{(x - v_i t)^2}{4D_i t}\right) \psi_i(t), \quad i = 1, 2 \quad (2.39)$$

with average speeds v_i and diffusion constants D_i . In the long-time limit the MSD is linear with the diffusion coefficient [120]

$$D_{\text{eff}} = \frac{D_1 \tau_1 + D_2 \tau_2}{\tau_1 + \tau_2} + \frac{1}{2(\tau_1 + \tau_2)} \left[\sigma_1^2 \left(v_1 - \frac{v_1 \tau_1 + v_2 \tau_2}{\tau_1 + \tau_2} \right) + \sigma_2^2 \left(v_2 - \frac{v_1 \tau_1 + v_2 \tau_2}{\tau_1 + \tau_2} \right) \right] \quad (2.40)$$

with $\tau_i = \int_0^\infty t \psi_i(t) dt$ and $\sigma_i^2 = \int_0^\infty t^2 \psi_i(t) dt - \tau_i^2$, $i = 1, 2$. By formally choosing $D_1 = D$, $v_1 = v$, $D_2 = 0$, $v_2 = 0$, $\psi_1(t) = \exp(-t/\tau_m)/\tau_m$ and $\psi_2(t) = \exp(-t/\tau_{im})/\tau_{im}$, we obtain the same effective diffusion coefficient, as in the MIM (2.25). This means that in the long-time limit the continuous paths in the mobile state can be replaced with instantaneous jumps. For short times the distribution is different in the MIM due to the continuous trajectories.

The next CTRW we consider effectively mimics the mobile state of the MIM with short jumps paired with short sojourn times. We consider the CTRW used in [70], where the sojourn time distribution function consists of a weighted sum of two exponential distributions

$$\psi(t) = p_D \frac{\exp\left(-\frac{t}{\tau_D}\right)}{\tau_D} + (1 - p_D) \frac{\exp\left(-\frac{t}{\tau_B}\right)}{\tau_B}, \quad (2.41)$$

where $\tau_D \leq \tau_B$ and $p_D \in (0, 1)$. This can be interpreted as drawing from

an exponential distribution with mean τ_D with probability p_D and from an exponential distribution with mean τ_B otherwise. We consider a Gaussian jump length distribution function

$$\lambda(x) = \frac{1}{\sqrt{2\pi\sigma^2}} \exp\left(-\frac{(x-\mu)^2}{2\sigma^2}\right), \quad (2.42)$$

with mean μ and variance σ^2 . Note that this is an extension of the displacement distribution in [70], where only the case $\mu = 0$ is considered. This model can mimic the MIM, if we formally choose the parameters $\tau_B = \tau_{\text{im}}$, $p_D = 1 - \tau_D/\tau_{\text{m}}$, $\mu = v\tau_D$, $\sigma = \sqrt{2D\tau_D}$ and $\tau_D \ll \tau_B, \tau_{\text{im}}, \tau_{\text{m}}$, as we elucidate in the following. The value of p_D is close to unity. Therefore, the probability to draw from the exponential distribution with mean τ_D is very high. This means that many steps will be taken with mean sojourn time τ_D . The smallest timescale is τ_D . Therefore, the jump lengths with mean $\mu = v\tau_D$ and variance $\sigma^2 = 2D\tau_D$ are also small. This large number of steps with small step sizes mimics the mobile state of the MIM. With probability $1 - p_D$ the sojourn time is drawn from $\exp(-t/\tau_{\text{im}})/\tau_{\text{im}}$ with $\tau_{\text{im}} = \tau_B$. This corresponds to the immobile state of the MIM. The probability $1 - p_D$ directly translates to an immobilisation rate of $1/\tau_{\text{m}}$. In figure 2.3 we compare the MSD of the CTRW with a bi-exponential sojourn time density shown as disc markers to the MIM shown as solid lines using dimensionless parameters for demonstration purposes. For the MIM we choose the parameters $\tau_{\text{m}} = 1$, $\tau_{\text{im}} = 100$, $D = 1$ and $v = 0$ or $v = 10$. For the CTRW we choose the parameters $\tau_D = 2 \times 10^{-2}$, $\tau_B = \tau_{\text{im}}$, $\mu = v\tau_D$ and $\sigma^2 = 2D\tau_D$. The MSDs for the advection-free case $v = 0$ match, as shown by the blue line and grey markers. In the case of advection, the MSD of the CTRW shown with black markers grows faster compared to MIM shown as an orange line for short times $t \leq \tau_D$. As described in detail in [D2, Appendix L.3], this arises due to the stochastic number of steps in the "mobile state" of the CTRW for a given mobile duration. In contrast, in the discretized version of the MIM, which we introduced in section 2.3.1, the number of steps is exactly proportional to time in the mobile state.

So far, we have analysed the relation of the MSDs from the MIM and

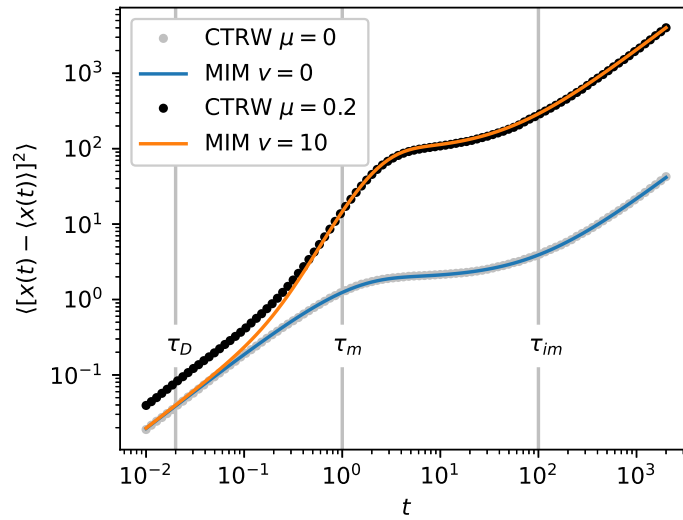


Figure 2.3: Double-logarithmic plot of the MSD with a comparison of the MIM shown as solid lines and CTRW with a bi-exponential sojourn time distribution shown as disc markers. The parameters of CTRW are chosen to mimic MIM. See text for details. In the advection-free case ($v = \mu = 0$) the MSD of MIM and CTRW exactly overlap, as shown by the blue curve and the grey markers. In the case with advection the MSD of CTRW grows faster for short times due stochastic number of steps in the "mobile state" for a given mobile duration. Parameters: $\tau_D = 10^{-2}$, $\tau_m = 1$, $\tau_{im} = \tau_B = 100$ and $D = 1$. Reprinted without changes from [D2] under the licence <https://creativecommons.org/licenses/by/3.0>.

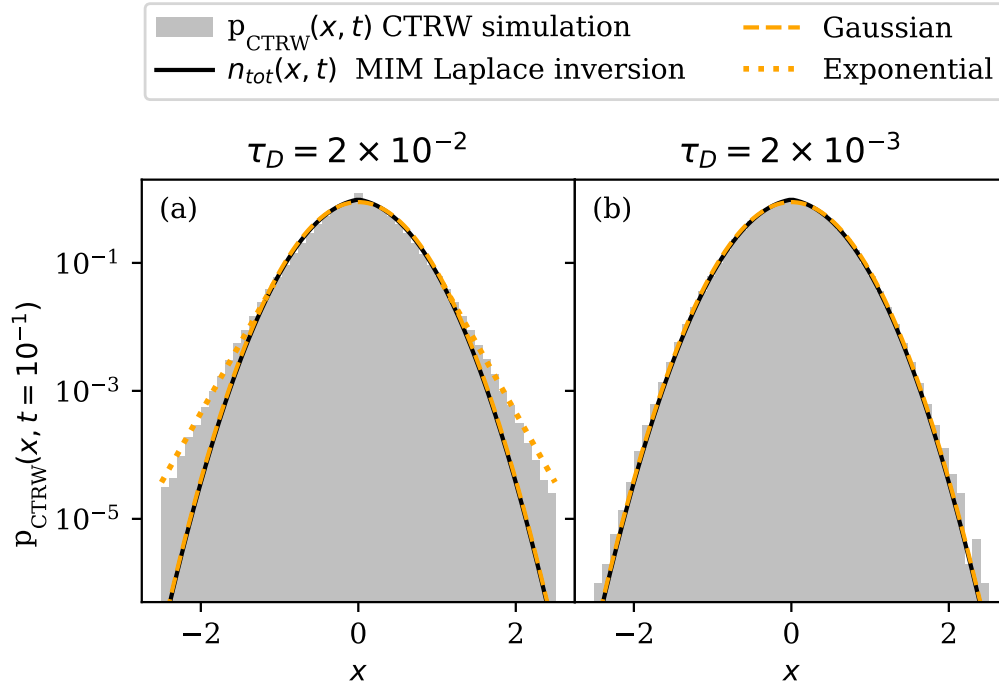


Figure 2.4: Semilog plot of the total density $n_{\text{tot}}(x, t)$ of the MIM and the PDF $p_{\text{CTRW}}(x, t)$ of the CTRW without advection. The CTRW has a bi-exponential sojourn time distribution and the same parameters as in figure 2.3. The histograms for the CTRW are obtained from simulations with 10^7 tracers and $n_{\text{tot}}(x, t)$ shown as a solid black line is obtained from Laplace inversions of $n_{\text{m}}(x, s) + n_{\text{im}}(x, s)$ (2.4-2.5). We use $\tau_{\text{D}} = 2 \times 10^{-2}$ in panel (a) and $\tau_{\text{D}} = 2 \times 10^{-3}$ in panel (b). As a guide to the eye a Gaussian is shown as a dashed line, which matches the centre of the distributions. An exponential guide to the eye is shown as a dotted line. The exponential tail only appears for the CTRW in panel (a).

the CTRW as laid out in [D2]. A matching MSD does not imply identical distributions, as shown in figure 2.4. For the advection-free case we use the same parameters, as in figure 2.3 with the goal to mimic MSD using a CTRW. The total densities of MIM are obtained from Laplace inversions of $n_m(x, s) + n_{im}(x, s)$ (2.4-2.5) and the position densities $p_{CTRW}(x, t)$ of CTRW are obtained via simulations with 10^7 tracers at $t = 10^{-1}$. In panel (a) we use $\tau_D = 2 \times 10^{-2}$ and in panel (b) we use $\tau_D = 2 \times 10^{-3}$. Even though the full MSDs match for $\tau_D = 2 \times 10^{-2}$, as shown in figure 2.3, the densities of CTRW and MIM at $t = 10^{-1}$ do not match in panel (a). Both densities share a Gaussian centre demonstrated by the Gaussian guide to the eye shown as a dashed line. A deviation can be seen at the tails, where the CTRW follows exponential tails as shown by the dotted lines, which are exponential guides to the eye. These exponential tails match what has been reported in [71] for the tails of CTRWs. In a CTRW the sojourn times are randomly drawn from a distribution. Therefore, it may occur that few tracers jump considerably more often than the average. These tracers move further than the majority of tracers, leading to the exponential tails. In order to obtain a better match of the densities of MIM and CTRW using the bi-exponential CTRW, the variance of step numbers in the "mobile state" should be as small as possible. As described in [D2], the mean number of steps at time t is t/τ_D and the variance of step numbers is given by the same quantity. The number of steps is narrowly distributed, if the coefficient of variation is small, i.e. the ratio of standard deviation to mean obeys $\sqrt{\tau_D}/t \ll 1$. Therefore, the exponential tails vanish in panel (b) for $\tau_D = 2 \times 10^{-3}$ for $t = 10^{-1}$ in the part of the density shown in figure 2.4.

In conclusion, if we choose a bi-exponential sojourn time distribution (2.41) where τ_D is chosen sufficiently small, the MSD and density obtained from the CTRW match the results for the total density of the MIM. A fundamental difference between CTRW and the MIM persists. Namely, in CTRW tracers are always immobile and perform instantaneous jumps. In contrast, in MIM the trajectory is continuous and interrupted by immobilisations. Furthermore, the total density is split into a mobile and an immobile density in the MIM. This distinction might become relevant, if only one of the two

populations can be measured. One example is given by a biosensor, where only bound molecules are detected. The splitting of tracers into a mobile and an immobile population is observed for the passive motion of tracers in mucin gels [121, 122] or acetylcholine receptors in live cell membrane [42].

In this section we have compared the MIM to the bi-exponential CTRW in [70]. We continue the discussion of the relation between CTRW and the MIM in section 3.4, where we see that this bi-exponential sojourn time distribution naturally arises from the formal equivalence of the MIM and CTRW on the level of integro-differential equations.

Chapter 3

The extended mobile/immobile model

In this chapter we discuss the main results of

T. J. Doerries, A. V. Checkin, R. Schumer, and R. Metzler, Rate equations, spatial moments, and concentration profiles for mobile-immobile models with power-law and mixed waiting time distributions, *Phys. Rev. E* **105**, 014105 (2022),

which we reference with [D3]. Here we introduce the extended MIM (EMIM). It is an extension of the MIM in the sense that it explicitly incorporates a residence time distribution in the immobile state, that can be chosen freely, e.g., with a power-law tail. In section 3.1 we introduce common models used in geoscience that go beyond single rate mass transfer to show how the EMIM can be seen as an extension of these established models. The full model is introduced in section 3.2, where we additionally discuss the mobile mass decay. In section 3.3 we discuss the concentration profiles and MSD. Finally, we dedicate section 3.4 to a discussion of the relation between CTRW and the EMIM.

3.1 Mobile/immobile models beyond single rates

In many settings particles do not mobilise with a constant rate, i.e., the immobile residence times do not follow an exponential distribution in these settings. An example is given by variations in aquifer properties, such as the types of minerals, the geometry of pores or the quantity of organic material [22]. Another example is given by power law residence times of tracers in the hyporheic zone, which is the region of aquifers near a stream, that is in exchange with the stream [27]. Another motivation to generalize the MIM is to account for a mobile mass decay with a power-law tail that was measured in the MADE-1 experiment [88]. This power-law tail cannot be modelled with the single-rate model (2.1).

In this section we give a brief overview over common models used in geoscience and start by introducing the multi-rate mass transfer model (MRMT) [89] followed by the fractal MIM from [21]. These models provide motivation for the introduction of the extended MIM introduced in [D3] and give insight into the relation of EMIM and previously established models.

The Multirate mass transfer model

In this section we follow the steps presented in [22] and introduce the multirate mass transfer model (MRMT). In the following we show how MRMT emerges from the physical picture of multiple immobile zones. The starting equation for the mobile concentration $c_m(x, t)$ is given by¹

$$\frac{\partial}{\partial t} c_m(x, t) = - \sum_{l=1}^N \beta_l \alpha_l (c_m(x, t) - c_{\text{im},l}(x, t)) + L(x) c_m(x, t) \quad (3.1)$$

with the advection-dispersion operator $L(x) = -v\partial/\partial x + D\partial^2/\partial x^2$. Instead of a single immobile density, as in the MIM (2.1), we now have N immobile zones with concentrations $c_{\text{im},l}(x, t)$ with transition rates α_l with $l = 1, \dots, N$ in (3.1). The capacity coefficients β_l denote the fraction of immobile volume

¹We use the lower case letter c for the concentration of MRMT to distinguish the formulas from the formulas for the EMIM in the following sections, where we use the upper case letter C for the concentration.

with index l to the mobile volume. Each immobile concentration follows the rate equation

$$\frac{\partial}{\partial t} c_{\text{im},l}(x, t) = \alpha_l (c_{\text{m}}(x, t) - c_{\text{im},l}(x, t)) . \quad (3.2)$$

We define the sum of all immobile concentrations $c_{\text{im}}(x, t) = \sum_{l=1}^N c_{\text{im},l}(x, t)$. For the initial condition $c_{\text{m}} = c_{\text{m}}^0 \delta(x)$ and $c_{\text{im},l}(x, t = 0) = 0$ we can formally solve each immobile concentration $c_{\text{im},l}(x, t)$ and insert the result into (3.1), leading to the expression

$$\begin{aligned} \frac{\partial}{\partial t} c_{\text{m}}(x, t) = \int_0^t \sum_{l=1}^N \beta_l \alpha_l e^{-\alpha_l(t-\tau)} \frac{\partial c_{\text{m}}(x, \tau)}{\partial \tau} d\tau + \sum_{l=1}^N \beta_l \alpha_l e^{-\alpha_l t} \delta(x) \\ + L(x) c_{\text{m}}(x, t). \end{aligned} \quad (3.3)$$

The second sum arises from an integration by parts. Now we make the limit $N \rightarrow \infty$ and go from a discrete set of variables α_l to a continuous variable α . The distribution of capacities β_l becomes a function $\beta(\alpha)$. Instead of the sums we obtain integrals

$$\frac{\partial}{\partial t} c_{\text{m}}(x, t) = \int_0^t \int_0^\infty \beta(\alpha) \alpha e^{-\alpha(t-\tau)} \frac{\partial c_{\text{m}}(x, \tau)}{\partial \tau} d\alpha d\tau + \int_0^\infty \beta(\alpha) \alpha e^{-\alpha t} \delta(x) d\alpha. \quad (3.4)$$

Now we notice that the inner integral can be understood as a Laplace transform [25]

$$g(t) = \int_0^\infty b(\alpha) \alpha e^{-\alpha t} d\alpha \quad (3.5)$$

of $\alpha b(\alpha)$. The function $g(t)$ is often referred to as the "memory function" [21, 25, 123]. Using $g(t)$, the equation of motion for the mobile concentration is given by

$$\frac{\partial}{\partial t} c_{\text{m}}(x, t) = - \int_0^t g(t - \tau) \frac{\partial c_{\text{m}}(x, \tau)}{\partial \tau} d\tau - c_{\text{m}}^0 \delta(x) g(t) + L(x) c_{\text{m}}(x, t). \quad (3.6)$$

If the mobile concentration is known, the immobile concentration can be obtained from the relation $c_{\text{im}}(x, t) = \int_0^t g(t - \tau) c_{\text{m}}(x, \tau) d\tau$, which arises

from conservation of mass [21]. The total density follows [21]

$$\frac{\partial}{\partial t} c_{\text{tot}}(x, t) = - \int_0^t g(t - \tau) \frac{\partial c_{\text{tot}}(x, \tau)}{\partial \tau} d\tau + L(x) c_{\text{tot}}(x, t). \quad (3.7)$$

The convolution in (3.7) is called the source-sink term $\Gamma(x, t)$, which is the rate of loss or gain of mobile mass due to exchange with the immobile zones [25]. Next, we study MRMT (3.7) for a specific choice of $g(t)$.

Fractal MIM

In [21], a choice similar to $g(t) = t^{-\mu}/\Gamma(1 - \mu)\tau_*^\mu$ is made² with $0 < \mu < 1$, which gives rise to the bi-fractional diffusion equation

$$\frac{\partial}{\partial t} c_{\text{m}}(x, t) = \tau_*^\mu \int_0^t \frac{(t - \tau)^{-\mu}}{\Gamma(1 - \mu)} \frac{\partial c_{\text{m}}(x, \tau)}{\partial \tau} d\tau - c_{\text{m}}^0 \frac{\tau_*^\mu}{\Gamma(1 - \mu)\tau^\mu} + L(x) c_{\text{m}}(x, t) \quad (3.8)$$

where a Caputo fractional derivative of order μ emerges in addition to the first derivative with respect to t [68]. This choice of $g(t)$ together with the equation for the total concentration (3.7) is called the fractal MIM, which leads to power-law tails in the BTCs and mobile mass [21].

The immobile residence time distribution corresponding to MRMT (3.7) can be obtained by rewriting the source-sink term as follows [25]

$$\Gamma(x, t) = \int_0^t c_{\text{m}}(x, t - \tau) \frac{\partial g(\tau)}{\partial \tau} d\tau + g(0) c_{\text{m}}(x, t) - g(t) c_{\text{m}}(x, 0), \quad (3.9)$$

where $\partial g(t)/\partial t$ can be interpreted as the immobile residence time distribution, as we describe in section 2.1 in detail. However, $\Gamma(x, t)$ cannot be rewritten as (3.9) with the choice $g(t) = t^{-\mu}/\Gamma(1 - \mu)\tau_*^\mu$, because $\partial g(t)/\partial t$ diverges with the power-law $t^{-1-\mu}$ for $t \rightarrow 0$. This leads to a diverging integral. To solve this issue we developed the extended MIM as presented in the following section, where arbitrary residence time distributions can be used, i.e., all distributions that are defined for $t \geq 0$.

²We introduce the timescale τ_* here to account for the dimensions in $g(t)$ and keep β dimensionless.

3.2 Formulation of the model

In [D3] we introduce the extended MIM (EMIM), defined by the set of equations

$$\frac{\partial}{\partial t} C_m(x, t) = -\beta\omega C_m(x, t) + \int_0^t \gamma(t - \tau) \beta\omega C_m(x, \tau) d\tau + L(x) C_m(x, t), \quad (3.10a)$$

$$\frac{\partial}{\partial t} C_{im}(x, t) = \omega C_m(x, t) - \int_0^t \gamma(t - \tau) \omega C_m(x, \tau) d\tau. \quad (3.10b)$$

The total concentration $C_{\text{tot}}(x, t) = C_m(x, t) + \beta C_{im}(x, t)$ is split into the mobile concentration $C_m(x, t)$ and immobile concentration $C_{im}(x, t)$ with units $[C_m(x, t)] = [C_{im}(x, t)] = \mu\text{g}/\text{L}$. We consider the initial conditions $C_m(x, 0) = M_0\delta(x)$ and $C_{im}(x, 0) = 0$ for simplicity and because it reflects the experimental situations in groundwater research, where the chemical is typically injected into the mobile water [19]. The capacity coefficient β is defined by the ratio of immobile to mobile pore volume. Similar to the single-rate MIM (2.1), only the equation for the mobile concentration is subject to advection and diffusion, as denoted by the advection-dispersion operator $L(x)$. Tracers immobilise with the rate $\beta\omega$. The residence times in the immobile state are distributed with $\gamma(\tau)$. The integral in (3.10a) can be understood the same way as described in section 2.1. The EMIM model equations (3.10) can be seen as an extension of the non-Markovian rate equations used to describe the photoluminescence in semiconductor nanoplatelets [94]. In [D3] we add transport to the mobile state using $L(x)$. We note that in [79] the rate equation for the immobile concentration (3.10b) was proposed as a balance equation for sorbing tracers. The rate equation for the mobile concentration (3.10a) including $L(x)$ is new compared to the model in [79].

We consider only initially mobile tracers in [D3] and mainly focus on the evolution of the mobile concentration in this chapter. The solution for the

mobile concentration in Laplace space is given by [D3]

$$C_m(x, s) = M_0 \frac{\exp\left(\frac{vx}{2D}\right)}{\sqrt{v^2 + 4\phi_{\text{EMIM}}(s)D}} \exp\left(-\sqrt{v^2 + 4\phi_{\text{EMIM}}(s)D} \frac{|x|}{2D}\right), \quad (3.11)$$

with $\phi_{\text{EMIM}}(s) = s + \beta\omega(1 - \gamma(s))$. Expression (3.11) is the same as for the single-rate model (2.4), if we formally set $f_m^0 = M_0$, $f_{\text{im}}^0 = 0$ and $\phi(s) = \phi_{\text{EMIM}}$. The mobile concentration (3.11) fits the observation in [79], that the mobile concentration is equivalent to the concentration of non-immobilising tracers $C(x, s)$ with a replaced argument in Laplace space $C_m(x, s) = C(x, \phi(s))$.

In [D3] we consider five immobile residence time distributions. First, we choose an exponential residence time distribution

$$\gamma_{\text{exp}}(t) = \omega \exp(-\omega t) \quad (3.12)$$

with $\omega > 0$, which renders the model (3.10) equivalent to the MIM in the formulation used in geoscience (2.3). We use the term "exponential model" for EMIM with immobilisation density $\gamma_{\text{exp}}(t)$. Second, we consider a bi-exponential distribution. This is a linear combination of two exponentials (3.12) with distinct values for ω_1 and ω_2 . We focus on the third choice for the immobile residence time distribution, which is the Mittag-Leffler distribution

$$\gamma_{\text{ML}}(t) = \frac{(t/\tau_\star)^\mu}{t} E_{\mu, \mu}(-[t/\tau_\star]^\mu) \quad (3.13)$$

with $0 < \mu < 1$ and $\tau_\star > 0$. The main feature of this distribution is the power-law tail $\simeq t^{-1-\mu}$, that generates a diverging mean. We use the term "ML model" for EMIM with immobilisation density $\gamma_{\text{ML}}(t)$. For ML trapping and $t \gg \tau_\star$, the EMIM (3.10) converges to a bi-fractional diffusion equation (3.7), as shown in [D3, section IV]. Note, that this does not necessarily imply a long-time limit, because the timescale $1/(\beta\omega)$ of the mobile residence times may be longer than τ_\star .

In [124] a model similar to EMIM is applied. The tracer is mobile for a fixed duration Δt and is displaced. Afterwards a time step is draw from a

Lévy stable distribution. The total density obtained in this way obeys the fractal MIM in the long-time limit, as well.

A two-dimensional version of the EMIM (3.10) with immobilisation density $\gamma_{\text{ML}}(t)$ has been adapted in [90] to describe the diffusion of excitons in layered perovskites and transition metal dichalcogenides.

All experimental systems have a finite size. Therefore, a largest trapping time exists, which is often taken into account by tempering with an exponential cut-off [19, 23, 80, 86, 125]. In [D3] we do this by choosing

$$\gamma_{\text{temp}}(t) = \frac{\exp(-t/\tau_t)\gamma(t)}{\int_0^\infty \exp(-\tau/\tau_t)\gamma(\tau)d\tau}, \quad (3.14)$$

with the tempering timescale τ_t . We insert $\gamma_{\text{ML}}(t)$ into (3.14) and obtain the mean

$$\langle t \rangle = \frac{\tau_*^\mu \mu}{\tau_t^{\mu-1} (1 + (\tau_*/\tau_t)^\mu)}. \quad (3.15)$$

The fifth immobile residence time distribution we consider is a linear combination of a ML distribution (3.13) and an exponential distribution (3.12). To compare the dynamics induced by each immobile residence time distribution we perform a fit of the mobile mass $M(t)$ to experimental data obtained in the MADE-1 experiment and shown in figure 3.1 using disc markers [21, 87, 88]. The measured mobile mass monotonically decreases and does not take on an equilibrium value. At around $t = 300$ d a shoulder is visible. We obtain the mobile mass by performing numerical Laplace inversions of the expression

$$M_m(s) = \int_{-\infty}^{\infty} C_m(x, s) dx = \frac{M_0}{\phi_{\text{EMIM}}(s)}, \quad (3.16)$$

which agrees with the result of the non-Markovian rate equations in [94]. The results of the Laplace inversions are shown in figure 3.1 as solid lines. In [88] the relative mobile mass is reported, which is the fraction of recovered mass to injected mass M_0^{exp} in the experiment. Notably, this fraction is higher than unity for three data points. Therefore, we use the normalized data points $M_m(t)/M_0^{\text{exp}}$ from [88], which are dimensionless and use $M_0 = M(t \rightarrow 0)/M_0^{\text{exp}}$ as a dimensionless fitting parameter, as described in [D3].

The ML model fits the data well with a value of $R^2 = 0.992$, as shown in panel (a). The fit follows the apparent power-law decay $\simeq t^{-0.58}$ of the mobile mass starting from around $t = 100$ d. This is in contrast to the mobile mass obtained for the exponential immobile residence time distribution shown in panel (b), which takes on a plateau value starting from $t = 100$ d. The mobile mass for the truncated ML distribution in panel (c) fits the data better with $R^2 = 0.994$ at the cost of an additional parameter. The mobile mass for a bi-exponential immobile residence time distribution in panel (d) does not qualitatively change compared to the single exponential case in panel (b). Except for the last data point it describes the data better than the single exponential case with $R^2 = 0.989$. The mobile mass obtained for a linear combination of a ML density and an exponential density describes the data best with an $R^2 = 0.998$, as shown in panel (e). This is the only choice of the immobile residence time distribution, that we consider that follows the shoulder in the data. Finally, we show the mobile mass obtained from the fractal MIM (3.8), which we obtain in the limit $\tau_* \rightarrow 0$. The qualitative functional form matches that of the ML density in panel (a), the fit is slightly worse with $R^2 = 0.988$. We note that fits for the fractal MIM and $\gamma_{\text{exp}}(t)$ were performed in [21] with similar results.

From now on, we focus on $\gamma_{\text{exp}}(t)$ (3.12) and $\gamma_{\text{ML}}(t)$ (3.13) as immobile residence time distributions. These are two prototypical choices for a distribution with finite mean on the one hand and for a distribution with a power-law tail leading to an infinite mean on the other hand. Another reason to consider these two distributions is that they have less parameters than the composite distributions. Furthermore, whenever we compare our results with $\gamma_{\text{ML}}(t)$ to the results for $\gamma_{\text{exp}}(t)$, we compare the EMIM to the classical MIM used in geoscience (2.3) [16, 21, 22, 35, 98].

In figure 3.2 we compare immobilisations of the EMIM with $\gamma_{\text{exp}}(t)$ in panel (a) to EMIM with $\gamma_{\text{ML}}(t)$ in panel (b). The parameters are chosen identical to the fits in figure 3.1. In figure 3.2 the mobile mass is shown using a grey line. The coloured areas correspond to the fraction of tracers with a specific number of immobilisation events N_{im} obtained from simulations. Moreover, the black area denotes tracers, that never immobilised and dark

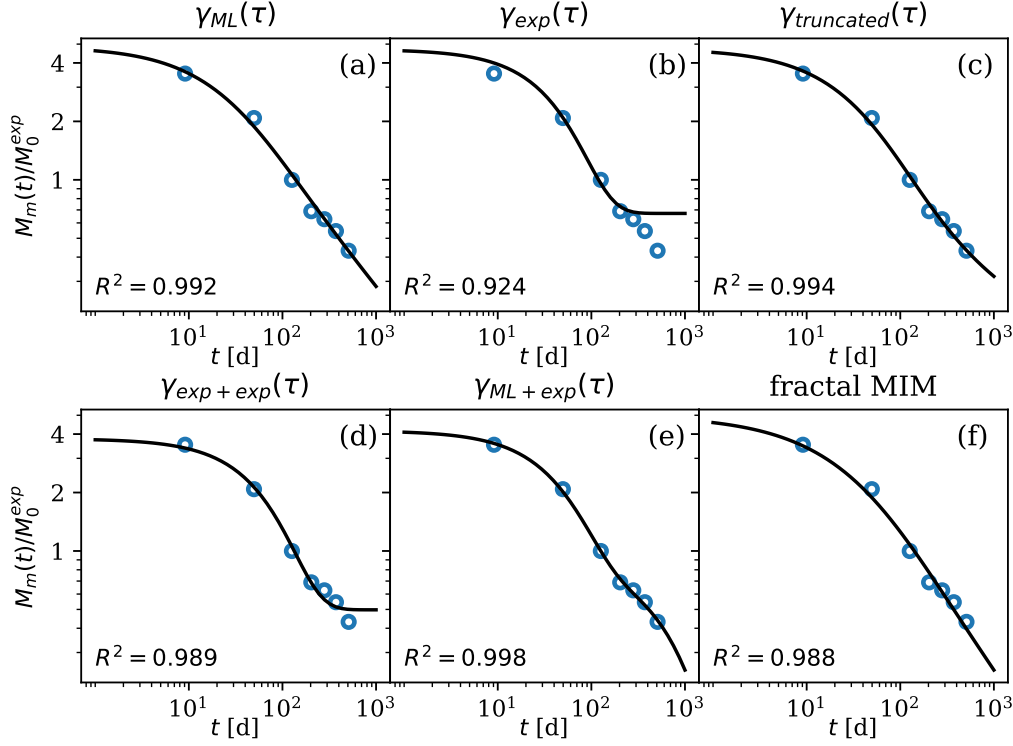


Figure 3.1: Double logarithmic plot of the normalized mobile mass over time. Disc markers show the normalized measured mobile mass in the MADE-1 experiment [88]. All panels show fits of the mobile mass obtained from Laplace inversion of $M_m(s)$ (3.16) with various choices for the immobile residence time distribution. In panel (a) the Mittag-Leffler immobile residence time distribution (3.13) is used. It has a $t^{\mu-1} = t^{-0.58}$ tail. The exponential residence time in (b) results in a stationary value of $M(t \rightarrow \infty)/M_0^{\text{exp}} = 0.67$ with fit parameters taken from [21]. In panel (c) an ML density with exponential cut-off at $\tau_t = 12 \times 10^3$ is used. For $t \ll \tau_t$ it is similar to the ML model. In panel (d) the weighted sum of two exponentials is used, which does not differ qualitatively from the single exponential case in (b). The linear combination of the ML and exponential density shown in panel (e) is the only fit that follows the "shoulder" of the data around $t = 300$. Panel (f) shows the fractal MIM from [21], which is the asymptotic limit of the ML model in the limit $\tau_* \rightarrow 0$. For the fit parameters obtained in [21], that are also used here, the tail follows $t^{-0.67}$.

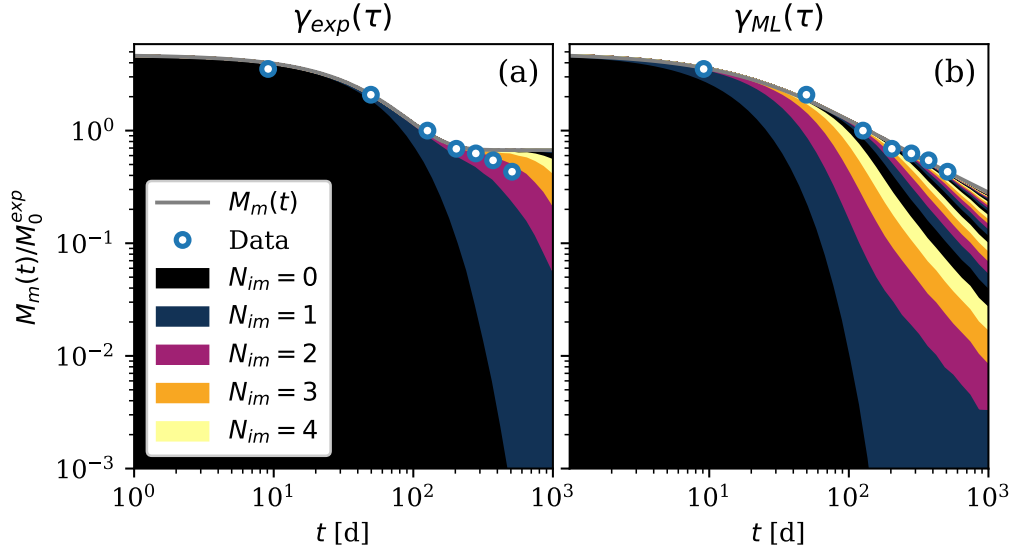


Figure 3.2: Double logarithmic plot of the normalized mobile mass as a function of time. The disc markers show the normalized mobile mass obtained in the MADE-1 experiment [88]. In panel (a) the exponential immobile residence time distribution is used with the same fit parameters, as in figure 3.1. Similar to figure 2.1, the stacked coloured areas correspond to the fraction of tracers that have immobilised N_{im} times, i.e., the black area denotes tracers that were never immobile, the dark violet area corresponds to tracers that have immobilised exactly once and are back in the mobile state. In panel (b) we show the same information, but for the ML immobile residence time density and the fit parameters from figure 3.1. In panel (b) the colours are cyclic, meaning, that starting from $N_{im} = 5$ the colours repeat. In contrast to the exponential case in (a) tracers immobilise significantly more often. The number of immobilisations is obtained from simulations.

3.3. RESULTS FOR THE EXTENDED MOBILE/IMMOBILE MODEL 61

violet denotes tracers that immobilised exactly once. We proceed to compare the immobilisation events in the exponential model to the ML model. The most apparent difference is the significantly higher number of immobilisations in the ML model. To accommodate this the colour-coding in panel (b) is cyclic, meaning that $N_{\text{im}} = 5$ is shown in black and $N_{\text{im}} = 6$ is shown in dark violet. One reason for this higher number of immobilisations when using $\gamma_{\text{ML}}(t)$ is the shorter mean mobile time, which is roughly a third of the value when using $\gamma_{\text{exp}}(t)$. Another reason is that short immobilisations are more likely with a Mittag-Leffler immobilisation time density. Namely, for the fitted parameters the median of $\gamma_{\text{ML}}(t)$ is 4.7 d compared to 19 d for $\gamma_{\text{exp}}(t)$. This means that short immobilisations are more likely in the ML model. In addition, long immobilisations are more likely in the ML model. Moreover, the 90th percentile of $\gamma_{\text{exp}}(t)$ is 79 d compared to 829 d for $\gamma_{\text{ML}}(t)$. The high value for $\gamma_{\text{ML}}(t)$ arises due to the power-law tail with diverging mean, which also leads to an asymptotic decay of mobile tracer numbers in contrast to the plateau value for the exp model. In conclusion, a tracer following the dynamics of the EMIM with $\gamma_{\text{ML}}(t)$ compared to $\gamma_{\text{ex}}(t)$ immobilises often for short times and will asymptotically be trapped for a long time. In the following section we discuss the concentration profiles and MSDs for the ML model.

3.3 Results for the extended mobile/immobile model

In this section we discuss the concentration profiles and the MSD of the EMIM for a Mittag-Leffler immobilisation duration distribution.

3.3.1 Concentration profiles

We apply the Tauberian theorem to obtain the short-time asymptotes of the mobile and immobile concentration. Up to a factor M_0 we find the same Gaussian result of the mobile concentration as for exponential trapping times in [D2]. The same relation holds for the immobile concentration. In

contrast to the long-time limit of the single rate model (2.1) the long-time asymptote of the mobile and immobile density remain non-Gaussian for a ML immobilisation distribution. The explicit forms are obtained in [D3] and are given by the expressions

$$C_m(x, t) \sim M_0 \frac{\beta\omega\tau_*^\mu}{v^2} e^{\frac{v}{2D}(x-|x|)} |x| t^{-1-\mu} M_\mu \left(\frac{\beta\omega\tau_*^\mu}{v} |x| t^{-\mu} \right), \text{ for } t \gg \tau_*, 1/\beta\omega, \quad (3.17)$$

and

$$C_{im}(x, t) \sim M_0 \frac{\beta\omega\tau_*^\mu}{v} e^{\frac{v}{2D}(x-|x|)} t^{-\mu} M_\mu \left(\frac{\beta\omega\tau_*^\mu}{v} |x| t^{-\mu} \right), \text{ for } t \gg \tau_*, 1/\beta\omega, \quad (3.18)$$

with the initially mobile mass M_0 and auxiliary function of Wright type $M_\mu(z)$ [126]. We compare the long-time asymptotes (3.17) and (3.18) shown as grey lines with markers in figure 3.3 to the Laplace inversions of the EMIM with various trapping time densities shown as black lines, where we formally set $M_0 = 1$ for simplicity. The solid black line is obtained for $\gamma_{ML}(t)$ (3.13), the dashed black line is obtained from the fractal MIM (3.8) and the dotted line corresponds to the EMIM with $\gamma_{exp}(t)$ (3.12). The parameters for the distributions are identical to the fits of the mobile mass decay measured in the MADE-1 experiment shown in figure (3.1). For the transport of tracers the parameters $v = 0.8 \text{ m/day}$ and $D = 4 \text{ m}^2/\text{day}$ are chosen, as described in [D3]. For $t = 1000 \text{ d}$ the asymptotes of $C_m(x, t)$ (3.17) and $C_{im}(x, t)$ (3.18) display a good estimate of the ML and limit model. A notable feature of $C_{im}(x, t)$ is the cusp at the origin, which is similar to the results obtained for the fractional advection-diffusion equation [127]. In the next section we see that these distributions lead to long-time subdiffusive or superdiffusive MSDs depending on the value of μ and v .

3.3.2 Mean squared displacements

We obtain the moments from the expressions in Fourier-Laplace space the same way, as described in section 2.1.1 for MIM. Regardless of the immobilisation time density, the short-time asymptote of the first moment and the

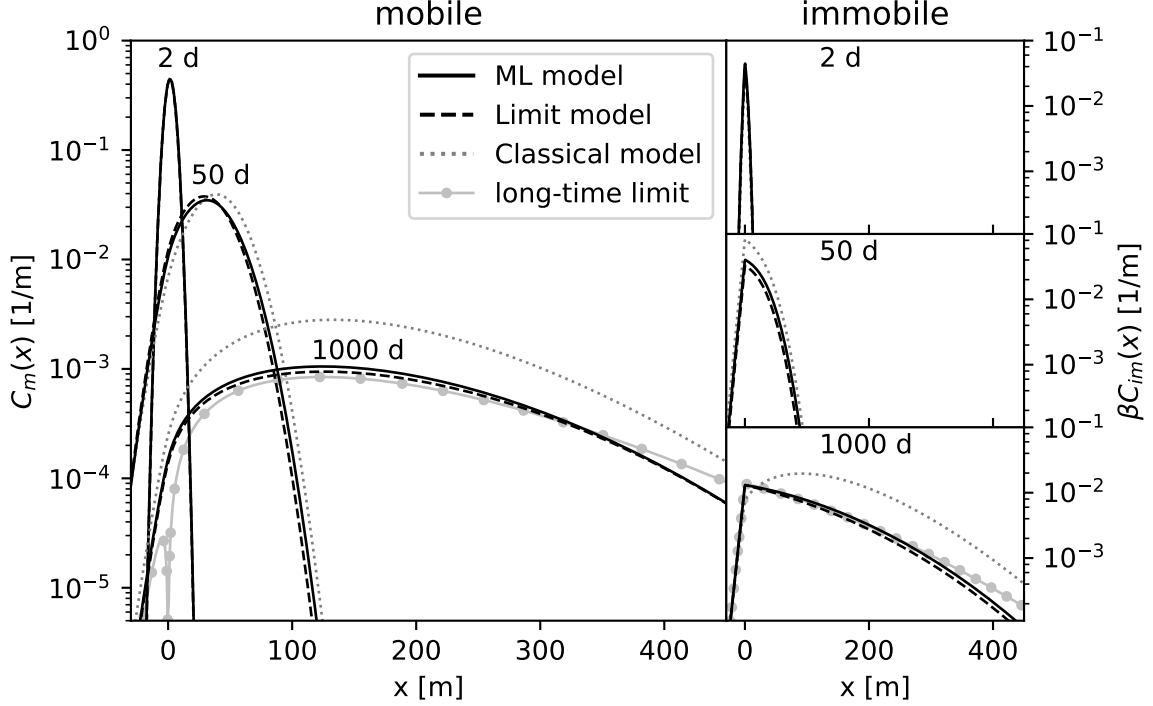


Figure 3.3: Semilog plot of the mobile concentration (left) and immobile concentration (right). The main panel (left) displays the concentrations of mobile particles at 2, 50, and 500 days after injection, while the right panel illustrates the concentrations of immobile particles at the same time intervals. Black lines denote Laplace inversions with a ML trapping time density (solid line), fractal MIM (dashed line, called limit model in the legend) and exponential trapping time density (dotted line). The parameters of the trapping time distributions are identical to the fitting of the mobile mass decay depicted in figure 3.1. For short durations, all models exhibit a mobile distribution that follows a Gaussian distribution, which becomes increasingly skewed as time progresses. In contrast, the distribution of immobile particles is non-Gaussian throughout the entire duration. Notably, cusps are prominently observed at $x = 0$, which is a characteristic feature of transportation systems with trapping times that diverge [128,129]. The long-term asymptotes, as depicted by equations (3.17) and (3.18), are represented by the grey lines accompanied by markers. These asymptotes estimate the ML model and fractal MIM well. We utilize values of 0.8 m/day and 4 m²/day for the parameters v and D , respectively. Reprinted figure with permission from [T.J. Doerries, A.V. Chechkin, R. Schumer and R. Metzler, Phys. Rev. E 105, 014105-18 (2022).] Copyright (2023) by the American Physical Society.

MSD of the mobile and total concentration are linear

$$\langle x(t) \rangle_{\text{m}} \sim vt \quad \text{for } t \ll 1/\beta\omega, \quad (3.19)$$

$$\langle (x(t) - \langle x(t) \rangle_{\text{m}})^2 \rangle_{\text{m}} \sim 2Dt \quad \text{for } t \ll 1/\beta\omega, \quad (3.20)$$

due to Brownian motion with advection before the first immobilisation, as shown in [D3]. We focus on the long-time asymptote of the mobile concentration using the ML model, where the first moment follows

$$\langle x \rangle_{\text{m}} \sim \frac{vt^\mu}{\beta\omega\tau_\star^\mu} \frac{\Gamma(\mu)}{\Gamma(2\mu)} \text{ for } t \rightarrow \infty, \quad (3.21)$$

as obtained via the Tauberian theorem in [D3]. Similar to the subdiffusive case of CTRW [63], the first moment (3.21) is non-linear. The MSD of the mobile density in the long-time limit is given by the expression

$$\begin{aligned} \langle (x(t) - \langle x(t) \rangle_{\text{m}})^2 \rangle_{\text{m}} = & 2D\Gamma(\mu) \frac{t^\mu}{\beta\omega\tau_\star^\mu\Gamma(2\mu)} \\ & + v^2\Gamma(\mu) \frac{t^{2\mu}}{(\beta\omega\tau_\star^\mu)^2} \left(\frac{2}{\Gamma(3\mu)} - \frac{\Gamma(\mu)}{\Gamma^2(2\mu)} \right) \text{ for } t \rightarrow \infty. \end{aligned} \quad (3.22)$$

Expression (3.22) implies subdiffusion for $\mu < 1/2$ and superdiffusion for $\mu > 1/2$, which is known for systems with scale-free trapping times and advection [59, 63]. This can be explained with tracers being trapped close to the origin, i.e., in figure 3.3 the immobile density has a visible peak close to the origin, mobile tracers move forward and immobile tracers mobilise close to the origin. The short-time and long-time asymptotics of the moments obtained in [D3] including expressions (3.20-3.22) agree with the calculations of the moments for the two-dimensional advection-free case for the EMIM in [90]. Furthermore, the asymptotics match what has been reported before for the fractal MIM in [130]. We note that in addition to the first and second moment we discuss the skewness and kurtosis in [D3].

For $t \gg \tau_\star$, the EMIM (3.10) with ML trapping density (3.13) converges to the fractal MIM model (3.7) with $g(t) = t^{-\mu}/\Gamma(1-\mu)\tau_\star^\mu$. In [D3] we go beyond the asymptotes calculated in [130] and obtain exact expressions for the first moments and MSDs of the mobile and immobile density. We present

the results for the mobile densities here, which are given by the first moment

$$\langle x(t) \rangle_m = \frac{vt E_{1-\mu,2}^2(-\beta\omega\tau_*^\mu t^{(1-\mu)})}{E_{1-\mu}(-\omega\beta\tau_*^\mu t^{(1-\mu)})} \quad (3.23)$$

and the MSD

$$\begin{aligned} \langle (x(t) - \langle x(t) \rangle_m)^2 \rangle_m &= 2Dt \frac{E_{1-\mu,2}^2(-\beta\omega\tau_*^\mu t^{(1-\mu)})}{E_{1-\mu}(-\beta\omega\tau_*^\mu t^{(1-\mu)})} + 2v^2 t^2 \frac{E_{1-\mu,3}^3(-\beta\omega\tau_*^\mu t^{(1-\mu)})}{E_{1-\mu}(-\beta\omega\tau_*^\mu t^{(1-\mu)})} \\ &\quad - v^2 t^2 \left(\frac{E_{1-\mu,2}^2(-\beta\omega\tau_*^\mu t^{(1-\mu)})}{E_{1-\mu}(-\beta\omega\tau_*^\mu t^{(1-\mu)})} \right)^2. \end{aligned} \quad (3.24)$$

The long-time asymptotes of the exact expressions (3.23) and (3.24) can be obtained by rewriting the three-parameter Mittag-Leffler functions in terms of two-parameter Mittag-Leffler functions [131] and approximating them up to second order using [132, Eq. (6.11)]. The asymptotes obtained this way match the asymptotes (3.21) and (3.22), respectively.

In the advection-free setting the MSD behaves similar to a cooling system with the effective temperature $T_{\text{eff}}(t) = T_0 M_m(t)/M_0$ in the same way as described for the MIM in Appendix B. This implies that already from the mobile mass decay with a power-law tail $t^{\mu-1}$ we can deduce the long-time scaling of the MSD from

$$\frac{\partial}{\partial t} \langle x^2(t) \rangle = \frac{2K_B T_0 M_m(t)}{\gamma M_0} \simeq t^{\mu-1} \text{ for } t \rightarrow \infty, \quad (3.25)$$

where integrating gives the expression

$$\langle x^2(t) \rangle \simeq t^\mu \text{ for } t \rightarrow \infty. \quad (3.26)$$

This "cooling" is similar to what is known for granular gases, where inelastic collisions decrease the mean kinetic energy due to energy dissipation into internal degrees of freedom, where the cooling $T(t) = T_0/(1 + t/\tau_0)^2$ is used [133–135].

In [56] a switching diffusion model is used, where the residence times follow distinct power-law tailed distributions in each state. For finite residence

times in the diffusive state and diverging mean residence times in the slow state with $D_- \rightarrow 0$ the same scaling as (3.26) was observed in the MSD. Long-time power-law scaling of the MSD is commonly described with the CTRW [13, 39]. In the next section we expand the discussion of the relation between the MIM and CTRW presented in section 2.4 to include the EMIM.

3.4 Relation between our model and the continuous time random walk

We start the discussion of the relation between CTRW and the EMIM by showing that the total density of the EMIM and MRMT are formally equivalent to the PDF of the CTRW, as shown in [23, 28]. By adding the two model equations of EMIM in (3.10) we obtain the following expression

$$\frac{\partial}{\partial t} C_{\text{tot}}(x, t) = -v \frac{\partial}{\partial x} C_{\text{m}}(x, t) + D \frac{\partial^2}{\partial x^2} C_{\text{m}}(x, t), \quad (3.27)$$

which is a differential equation for $C_{\text{tot}}(x, t)$ that involves $C_{\text{m}}(x, t)$ on the right side. We apply the Laplace transform to (3.27) and obtain the expression

$$sC_{\text{tot}}(x, s) - C_{\text{tot}}(x, t = 0) = -v \frac{\partial}{\partial x} C_{\text{m}}(x, s) + D \frac{\partial^2}{\partial x^2} C_{\text{m}}(x, s). \quad (3.28)$$

From the solutions in Fourier-Laplace space (A.2) and (A.3) we obtain the relation

$$C_{\text{m}}(x, s) = \frac{s}{\phi_{\text{EMIM}}(s)} C_{\text{tot}}(x, s), \quad (3.29)$$

for initially mobile tracers. We insert relation (3.29) into expression (3.28) and obtain

$$sC_{\text{tot}}(x, s) - C_{\text{tot}}(x, t = 0) = \frac{s}{\phi_{\text{EMIM}}(s)} \left(-v \frac{\partial}{\partial x} C_{\text{tot}}(x, s) + D \frac{\partial^2}{\partial x^2} C_{\text{tot}}(x, s) \right). \quad (3.30)$$

Now we define $M(s) = s/\phi_{\text{EMIM}}(s)$ ³ and apply the reverse Laplace transform to expression (3.30)

$$\frac{\partial}{\partial t} C_{\text{tot}}(x, t) = \int_0^t M(t-t') \left(-v \frac{\partial}{\partial x} + D \frac{\partial^2}{\partial x^2} \right) C_{\text{tot}}(x, t') dt', \quad (3.31)$$

This expression has the same form that can be derived from CTRW and $M(t)$ is called memory function in geoscience [74, 136]. Using MIM (2.1), the same expression as (3.31) can be derived for $n_{\text{tot}}(x, t)$. The memory function is related to the trapping time density of the CTRW $\psi(t)$ by [28]

$$M(s) = s\bar{\tau} \frac{\psi(s)}{1 - \psi(s)} \quad (3.32)$$

in Laplace space with a timescale $\bar{\tau}$. Together with $M(s) = s/\phi_{\text{EMIM}}(s)$ this gives the relation [28, Eq (107)]

$$\psi(s) = \frac{1}{1 + \bar{\tau}\phi_{\text{EMIM}}(s)}. \quad (3.33)$$

We check the normalization of $\psi(s)$ and note that since $\gamma(s=0) = 1$, we have $\phi_{\text{EMIM}}(s=0) = 0$. This implies $\psi(s=0) = 1$, i.e., normalization.

The relation between MRMT and CTRW has been established on the level of $M(s)$ and the total density before [23, 82]. Now we investigate what this implies for the sojourn time distribution. We now choose $\bar{\tau}$ such that it is the smallest timescale of the system. In figure 3.4 $\psi(\tau)$ is shown for an exponential immobilisation time distribution in panel (a). The sojourn time distribution $\psi(\tau)$ can be split into two parts. The first part for $\tau < \bar{\tau}$ is an exponential distribution with mean $\bar{\tau}$. The second part for $t > \bar{\tau}$ behaves as $\bar{\tau}/\tau_m \gamma(\tau)$, i.e., the trapping time distribution of the MIM scaled by the factor $\bar{\tau}/\tau_m$. We interpret the shape of $\psi(\tau)$ as follows. Short waiting times drawn from $\exp(-\tau/\bar{\tau})/\bar{\tau}$ mimic steps in the mobile state of the MIM. With probability $\bar{\tau}/(\bar{\tau} + \tau_m)$ a longer trapping time is drawn from $\gamma(\tau)$ corresponding to trapping in an immobile zone. This means, that starting from the formal equivalence of the MIM and CTRW on the level of the integro-differential

³Not to be confused with the mobile mass $M_m(t)$, that is written with a subscript.

equation (3.31), we obtain the CTRW with a bi-exponential sojourn time distribution from [70], that we have discussed in section 2.4 for $\tau_D = \bar{\tau}$. This implies that we can interpret $\bar{\tau}$ as the mean sojourn time in the mimiced mobile state. As discussed in section 2.4, the timescale $\bar{\tau}$ needs to be sufficiently small for an equivalence. By choosing an ML immobilisation time distribution in the EMIM we find the same splitting of $\psi(\tau)$ into two parts. The first part of $\psi(\tau)$ follows an exponential $\exp(-\tau/\bar{\tau})/\bar{\tau}$ for small τ , as shown in figure 3.4(b). The second part follows the power-law tail $\sim \tau^{-1-\mu}$ from the ML density. This suggests writing the sojourn time density as

$$\psi_{\star}(\tau) = \frac{\tau_m}{\tau_m + \bar{\tau}} \frac{\exp(-\tau/\bar{\tau})}{\bar{\tau}} + \frac{\bar{\tau}}{\tau_m + \bar{\tau}} \gamma(\tau) \quad (3.34)$$

with the immobilisation time density $\gamma(\tau)$ from the EMIM. We note that equation (3.34) is based on the observation in figure 3.4 of numerical Laplace inversions. In future projects it could be interesting to derive expression (3.34) more rigorously and prove on that level that CTRW can mimic the total density of the EMIM. The CTRW does not reproduce one of the main features of the (E)MIM, which is the splitting of the tracer density into mobile and immobile densities. We conclude this thesis with a summary and outlook in the following chapter.

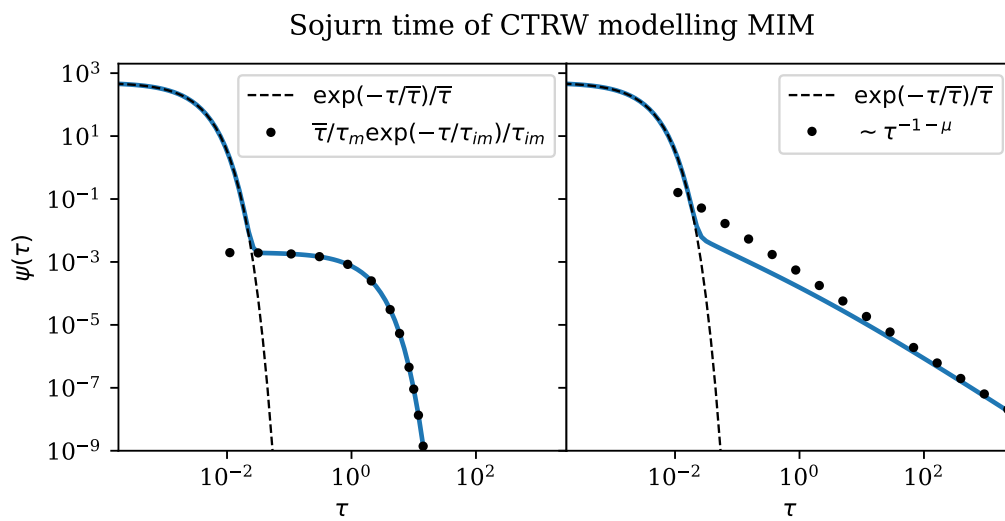


Figure 3.4: Double logarithmic plot of the sojourn time density of CTRW that mimics the MIM. In the left panel the single-rate model (2.1) is mimicked, i.e., $\phi(s) = s(1 + \tau_{im}/\tau_m)/(1 + s\tau_{im})$ is used in expression (3.33). In the right panel EMIM with $\gamma_{ML}(t)$ (3.13) is used in expression (3.33). In both panels the resulting trapping time density $\psi(\tau)$ contains two parts. The first part has an exponential shape with mean $\bar{\tau}$ that corresponds to a step in the mobile domain. The second part follows approximately the trapping time in the immobile domain $\bar{\tau}/\tau_m\gamma(\tau)$ scaled by the factor $\bar{\tau}/\tau_m$, as shown by the dotted lines.

Chapter 4

Summary and outlook

In this chapter we will summarize the main results of this thesis and give an outlook on possible future research directions and applications. The mobile/immobile model (MIM) was typically used in geoscience to describe the motion of contaminants in groundwater subject to advection and diffusion already in the 1960s [16–18]. Contaminants effectively transiently immobilise due to diffusion into dead-end pores or adsorption on surfaces. In the MIM the immobilisation durations are distributed exponentially. This implies that the increments of the tracers are not distributed identically at intermediate timescales. Breaking of the central limit theorem is the result, which readily implies non-Gaussian (nG) distributions in the MIM. A key assumption of the MIM is to split the total density of tracers into a mobile and an immobile density. In some experiments only one of the two is measured, rendering the distinction of mobile and immobile tracers in the MIM beneficial. Examples for such experiments pose geological experiments, where contaminants move through an aquifer and effectively immobilise in pores. Only the mobile tracers exit the aquifer and can be measured. At the site of measurement the pores are not present and the immobile density is not sampled. In another setting the immobile density is sampled, namely those bio molecules, that bind to specific receptors in a bio sensor, as discussed in [D2]. The observable in typical geoscience experiments is the contaminant concentration over time at a fixed location, which is called the breakthrough curve (BTC) [16, 17, 22–26]. In biophysics the mean squared displacement

(MSD) is a typical observable, which has been calculated for the MIM before [23, 31–36]. The goal of this thesis was to identify nG displacement distributions and anomalous scaling regimes in the MSD of the MIM. To do so, we systematically studied the MSD and displacement distributions of the mobile, immobile and total density of tracers. Moreover, we have considered three fractions of initially mobile tracers, namely all tracers initially mobile, initially immobile and an equilibrium fraction. Together with various relevant time regimes this constitutes around twenty cases to be discussed, and we therefore present only selected highlights of nG displacements and anomalous scaling of the MSD here. We found clear anomalous scaling regimes at relevant short and intermediate timescales with a strong dependence on the fraction of initially mobile tracers.

We started with the advection-free case, which we used to model the motion of tau proteins in neurons [D1]. Single particle tracking experiments of tau proteins tagged with a fluorescent marker revealed transient immobilisations due to binding of tau proteins to microtubules [137]. A further experiment on tau proteins obtained long binding times $\tau_{\text{im}} = 7.7\text{sec}$ of the tau proteins to the microtubules compared to the mean mobile duration $\tau_{\text{m}} = 0.16\text{sec}$ [38]. The reaction-diffusion equation used in [38] is equivalent to our formulation of the MIM, which allowed us to use the results of MIM to describe the motion of tau proteins [D1]. The displacement distribution of initially mobile tracers follows a Laplace distribution at intermediate timescales $\tau_{\text{m}} \ll t \ll \tau_{\text{im}}$ paired with a plateau in the MSD.

Another application of the advection-free MIM pose Fis DNA-sliding proteins in Escherichia Coli bacteria, that transiently bin to the DNA. In single particle tracking experiments a Fickian yet non-Gaussian (FnG) diffusion was observed [49]. Our model was able to give two alternative explanations for the FnG diffusion assuming an equilibrium fraction of initially mobile tracers. In both cases the sharp peak in the centre arises from immobile tracers. The remaining part of the distribution may stem from the Gaussian displacements at short timescales $t \ll \tau_{\text{m}}$ or from a Laplace distribution at intermediate timescales $\tau_{\text{m}} \ll t \ll \tau_{\text{im}}$.

In [D2] we included advection and found a cubic scaling regime of the

MSD paired with nG displacements. It persists for initially mobile and for initially immobile tracers, regardless of the ratio $\tau_{\text{im}}/\tau_{\text{m}}$ for sufficiently high Péclet numbers $\text{Pe} = v^2\tau_{\text{m}}/D$. We systematically studied the dependence of anomalous scaling regimes on the ratio $\tau_{\text{im}}/\tau_{\text{m}}$ and Pe in Appendix of [D2]. It would be interesting to perform single particle tracking experiments of tracer particles in a bio sensor to confirm the predicted MSDs and nG distributions.

To describe immobilisations that are not exponentially distributed, we introduced the extended MIM (EMIM) in [D3], which was applied to the diffusion of excitons in layered perovskites and transition metal dichalcogenides [90]. We restricted ourselves to the case of initially mobile tracers, which led to Brownian motion with a linear MSD at short times regardless of the immobilisation time distribution. Among others, we used a Mittag-Leffler (ML) immobilisation time distribution function with a power-law tail $\simeq t^{-1-\mu}$ with $0 < \mu < 1$ and a diverging mean. We obtain an exact expression for the mobile mass decay with a long time power-law tail $\simeq t^{\mu-1}$. We fitted our model to experimental data of the MADE-1 experiment of bromide diffusing in a heterogeneous aquifer [88], where we obtained $\mu = 0.42$. In the advection-free case this results in long-time subdiffusion $\simeq t^\mu$. This could readily be deduced from the power-law decay of the mobile mass $M_{\text{m}}(t)$ due to the relation $d\langle x^2(t) \rangle/dt = 2DM_{\text{m}}(t)/M_0$. In Appendix B we derived this expression following the steps of Langevin's original paper [8] by defining an effective temperature $T_{\text{eff}} = TM_{\text{m}}(t)/M_0$. Integration of $\lim_{t \rightarrow \infty} M_{\text{m}}(t) \simeq t^{\mu-1}$ gave the expected MSD $\langle x^2(t) \rangle \simeq t^\mu$ for the long-time limit. In future projects it would be interesting to understand the connection between the MIM and an effective temperature further and see if it can be done for systems including advection, as well.

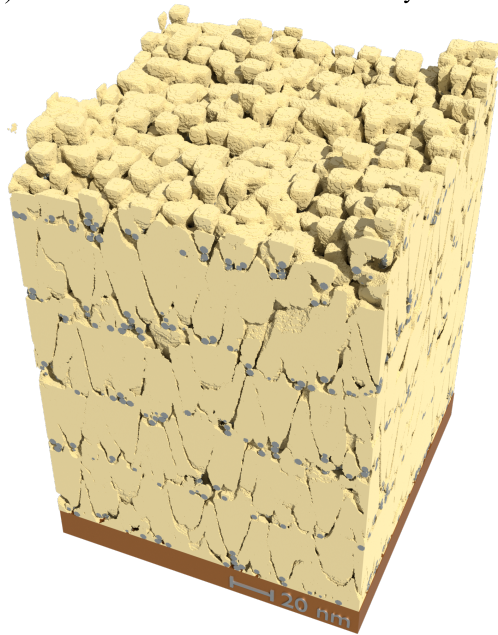
When including advection in the EMIM, we found a crossover from a linear MSD to an asymptotic scaling $\simeq t^{2\mu}$, which is subdiffusive or superdiffusive for $0 < \mu < 1/2$ and $1/2 < \mu < 1$, respectively. The displacement distribution crosses over from a Gaussian to a nG distribution, which persists in the long-time limit. In the long-time limit mobile tracers lead immobile tracers. Moreover, the first moment and second moment of the mobile moment is a multiple of the respective total and immobile moments in the

long-time limit. This is in contrast to the case of exponential trapping times, where the moments of all densities overlap in the long-time limit.

The EMIM is formulated using the capacity coefficient β taking different volumes for the mobile and immobile phase into account, as is typically done in geoscience, e.g., for the fractal MIM [21, 22]. In the limit $t \gg \tau_*$, where τ_* denotes a timescale of the ML distribution, our model converges to the fractal MIM, for which we obtain exact analytical expressions for the first moment and non-linear MSD in terms of Mittag-Leffler functions. In addition, we fitted the density obtained through Laplace inversions of the EMIM to a BTC of an experiment where dye moves through karst aquifers using an exponential and an ML immobilisation time distribution. We found $\mu = 0.77$ for the ML distribution, implying long-time superdiffusive spread of the tracers and long immobilisation times. In the time regime where the fitted BTC was measured the resulting MSDs of both immobilisation time distributions almost coincide and display a superdiffusive MSD.

In this thesis we have analysed the MSD and nG displacements of the MIM. The time averaged MSD (TAMSD) is another quantity that is well suited for single particle tracking experiments or molecular dynamics simulations, where only a few trajectories may be obtained [31, 32, 39, 43, 62]. The TAMSD averages the squared increments with delay Δ along a single trajectory with length T [13]. Due to the stochastic nature of single trajectories, the TAMSD is a random quantity. For ergodic systems such as Brownian motion the TAMSDs converge to a deterministic function for $\Delta \ll T$. In contrast, TAMSDs obtained from a continuous time random walk (CTRW) with power-law sojourn times remain stochastic even in the limit $\Delta \ll T$ and $T \rightarrow \infty$. In the light of the comparison of the MIM and CTRW in this thesis it would be interesting to study the TAMSDs of the MIM. In [112] the TAMSD is analysed for a switching model, where the diffusivity switches between two diffusivities D_1 and D_2 with linear rates. In Appendix C we reproduced the results for $D_1 = 0$ using the subordination approach. The subordinator is the distribution of total mobile durations at a given time in our model. We showed that for finite T the TAMSDs do not converge for $\Delta \ll T$ and have a finite spread, even for an equilibrium fraction of initially

(a) Modelled anode of a lithium battery



(b) Pore structure

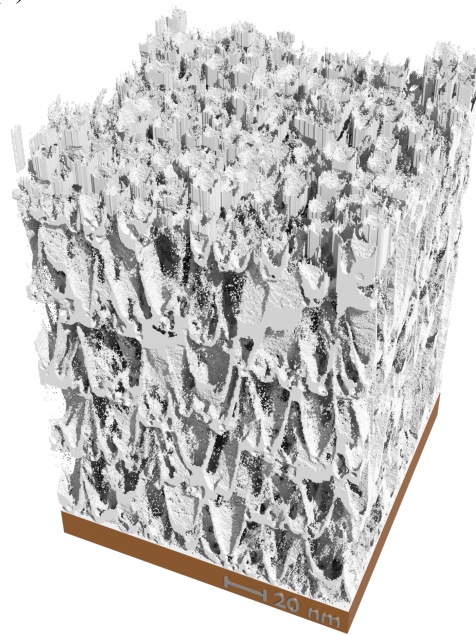


Figure 4.1: (a) Raytracing image of a lattice model with size $512 \times 512 \times 1000$ of a multilayered silicon anode with an embedded tantalum nanoparticle scaffold for lithium-ion batteries based on the experiment in [138]. The scale bar has a size of 20 nm. On top of a copper plane tantalum nanospheres with diameter 3 nm are placed using soft deposition followed by sputtering of silicon atoms for five layers. The resulting medium has around 15 percent of connected porosity. The pores are shown in the panel (b), where lithium atoms can diffuse on the surface. It would be interesting to identify dead-end pores, where the lithium effectively immobilises and apply the EMIM as an effective one-dimensional model. Simulations by Andrés Fernando and figure by Timo Doerries.

mobile tracers, where the MSD is linear at all times. Moreover, we provide a relatively simple analytical exact formula for the distribution of the TAMSD for $\Delta \ll \tau_m, \tau_{im}, T$, which is new compared to the results in [112]. This distribution is directly related to the subordinator. It would be interesting to investigate the TAMSDs of the MIM further and compare the results to experimental single particle tracking data e.g. of Fis or tau proteins.

Furthermore, it might be interesting to identify immobile zones in data of porous media and obtain the residence time distributions in the respective zones. One example for such data is shown in figure 4.1. A stochastic lattice deposition model of a lithium-ion battery anode corresponding to the experiment in [138] is shown in figure 4.1(a). The pore structure is shown in panel (b) of figure 4.1, where the lithium atoms can diffuse on the surface. To answer how lithium atoms move in batteries with a typical size known from everyday life the EMIM could provide an effective one-dimensional model. This would require identifying effectively "immobile" dead-end pores, as was done e.g. in [139] for sandstone using a model similar to the EMIM. An idea to improve the methodology in [139] could be a more physical definition of an immobile zone.

In conclusion, the MIM is suitable for systems where the population of tracers splits into mobile and immobile populations. We found Fickian yet non-Gaussian diffusion for an equilibrium fraction of initially mobile tracers without advection. In all other cases except for short immobilisations $\tau_{im} \ll \tau_m$ in the advection-free case it is subject to nG displacements and an anomalous scaling of the MSD at intermediate timescales. These results are relevant e.g. to provide a possible explanation of the nG distribution of Fis DNA binding proteins in single particle tracking experiments [49,D1]. In the EMIM the anomalous scaling of the MSD and the nG displacements persist also in the long-time limit for power-law immobilisation time distributions.

Appendix A

Expressions in Fourier-Laplace space

We apply the Fourier-Laplace transform

$$f(k, s) = \int_{-\infty}^{\infty} \int_0^{\infty} e^{-st+ikx} f(x, t) dt dx \quad (\text{A.1})$$

to the model equations (2.1) and rearrange to obtain the expressions

$$n_m(k, s) = \left(f_m^0 + f_{im}^0 \frac{1}{1 + s\tau_{im}} \right) \frac{1}{\phi(s) - ikv + k^2 D} \quad (\text{A.2})$$

$$n_{im}(k, s) = f_{im}^0 \frac{\tau_{im}}{1 + s\tau_{im}} + \frac{\tau_{im}/\tau_m}{1 + s\tau_{im}} \left(f_m^0 + f_{im}^0 \frac{1}{1 + s\tau_{im}} \right) \frac{1}{\phi(s) - ikv + k^2 D} \quad (\text{A.3})$$

as well as

$$n_{tot}(k, s) = n_m(k, s) + n_{im}(k, s) = \frac{f_m + f_{im}^0 \frac{1}{1 + s\tau_{im}}}{s} \frac{\phi(s)}{\phi(s) - ikv + k^2 D} + f_{im}^0 \frac{\tau_{im}}{1 + s\tau_{im}} \quad (\text{A.4})$$

with $\phi(s) = s[1 + \tau_{im}\tau_m^{-1}/(1 + s\tau_{im})]$. Fourier inversion of (A.2) and (A.3) gives expressions (2.4) and (2.5).

Appendix B

Following the steps of Langevin to obtain the MSD

In this chapter we follow the steps of Langevin [8] to obtain an expression for the MSD of (E)MIM in the advection-free setting. We start with the underdamped Langevin equation

$$m \frac{d^2x}{dt^2} = -\gamma \frac{dx}{dt} + \xi(t) \quad (\text{B.1})$$

of a tracer with mass m , friction coefficient γ and a random force $\xi(t)$ with $\langle x(t)\xi(t) \rangle = 0$. We multiply (B.1) with x and obtain the expression

$$\frac{1}{2}m \frac{d^2x^2}{dt^2} - m \left(\frac{dx}{dt} \right)^2 = -\frac{\gamma}{2} \frac{dx^2}{dt} + x(t)\xi(t). \quad (\text{B.2})$$

Averaging over the random force realizations we obtain

$$\left\langle \frac{1}{2}m \frac{d^2x^2}{dt^2} \right\rangle - \left\langle m \left(\frac{dx}{dt} \right)^2 \right\rangle = -\frac{\gamma}{2} \left\langle \frac{dx^2}{dt} \right\rangle, \quad (\text{B.3})$$

where we used $\langle x(t)\xi(t) \rangle = 0$. Now we can identify $\left\langle m \left(\frac{dx}{dt} \right)^2 \right\rangle / 2$ with the mean kinetic energy $\langle E_{\text{kin}} \rangle$. Using the equipartition theorem $\langle E_{\text{kin}} \rangle = \frac{1}{2}k_B T$

and a constant temperature Langevin arrives at the relation

$$\frac{d}{dt}\langle x^2(t) \rangle = \frac{4\langle E_{\text{kin}} \rangle}{\gamma} + c \exp\left(-\frac{\gamma}{m}t\right), \quad (\text{B.4})$$

where c is a constant depending on the initial velocity. In the limit $t \gg m/\gamma$, when the initial momentum has relaxed, the expression (B.4) simplifies to

$$\frac{d}{dt}\langle x^2(t) \rangle = \frac{2K_B T}{\gamma}, \quad (\text{B.5})$$

which implies $\langle x^2(t) \rangle = 2Dt$ for $t \gg m/\gamma$.

Now we modify this derivation to incorporate immobilisations. We define the new random force $\xi'(t) = \xi(t)i(t)$ with the indicator function $i(t)$, which takes on the value one if the tracer is mobile at time t and zero otherwise. We have introduced $i(t)$ in the context of subordination in section 2.1. Only mobile tracers contribute to the mean kinetic energy, therefore the kinetic energy of MIM is given by $k_B T f_m(t)/2$, where we have used the relation $\langle i(t) \rangle = f_m(t)$. If $f_m(t)$ is a slowly varying function on the timescale of m/γ , we can replace $\langle E_{\text{kin}} \rangle$ with $k_B T f_m(t)/2$ in equation (B.4), which eventually gives

$$\frac{d}{dt}\langle x^2(t) \rangle = \frac{2K_B T f_m(t)}{\gamma} \text{ for } t \gg m/\gamma \quad (\text{B.6})$$

for slowly varying $f_m(t)$. Expression (B.6) is an exact expression for (E)MIM, valid at all timescales. In order to apply it to EMIM $f_m(t)$ needs to be replaced with $M_m(t)/M_0$. Integrating expression (B.6) gives the MSD in the advection-free setting. We can interpret $T_{\text{eff}}(t) = T f_m(t)$ as an effective temperature of the system due to $\langle E_{\text{kin}}(t) \rangle = \frac{1}{2}k_B T_{\text{eff}}(t)$.

Appendix C

Time averaged mean squared displacement

In many single particle tracking experiments the time averaged mean squared displacement (TAMSD)

$$\overline{\delta^2(\Delta)} = \frac{1}{T - \Delta} \int_0^{T-\Delta} [x(t + \Delta) - x(t)]^2 dt \quad (\text{C.1})$$

is calculated for each trajectory with length T [13, 39, 112]. The TAMSD averages over all squared increments with time lag Δ and it is a random quantity for finite T . For example, simple Brownian motion has stochastic TAMSDs, as shown in figure C.1(a). For large Δ the integration domain for the TAMSD (C.1) shrinks and it is averaged over less values, increasing the stochasticity. We define the ensemble averaged TAMSD

$$\langle \overline{\delta^2(\Delta)} \rangle = \left\langle \frac{1}{T - \Delta} \int_0^{T-\Delta} [x(t + \Delta) - x(t)]^2 dt \right\rangle, \quad (\text{C.2})$$

which is given by $2D\Delta$ for Brownian motion, as shown in figure C.1(a) as a blue line. Almost all TAMSDs overlap with this averaged TAMSD for $\Delta \ll 1$. The spread of the TAMSDs is often characterized using the ergodicity breaking parameter [13, 140]

$$EB_T(\Delta) = \langle \xi^2 \rangle - 1, \quad (\text{C.3})$$

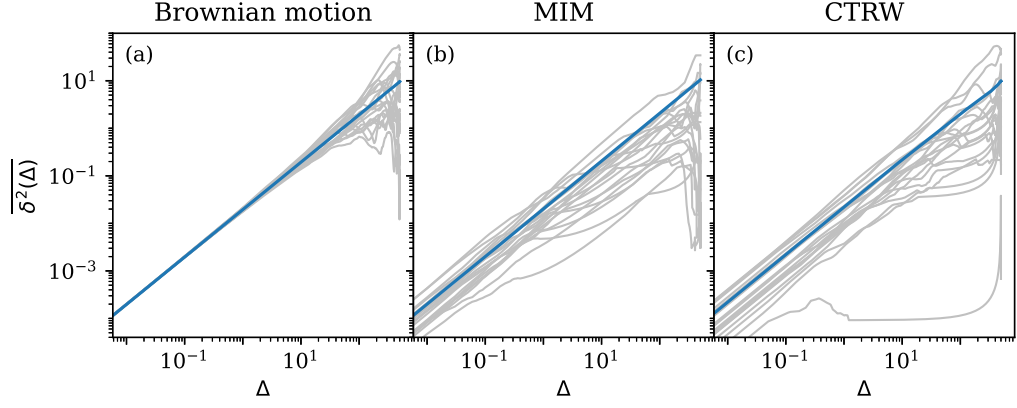


Figure C.1: Double logarithmic plots of the time averaged mean squared displacement (C.1) for $T = 500$. Panel (a) is plotted for Brownian motion, panel (b) for MIM ($\tau_m = 1$, $\tau_{im} = 100$) and panel (c) for a CTRW with a sojourn time density with power-law tail $\simeq t^{-1.646}$. Blue lines display ensemble averaged TAMSDs.

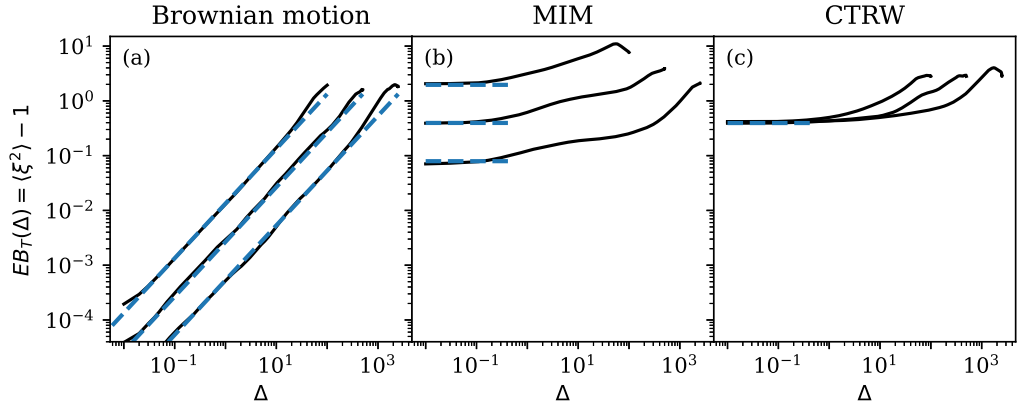


Figure C.2: Double logarithmic plot of the ergodicity breaking parameter (C.3). In panel (a) Brownian motion is used, in panel (b) MIM is used with parameters $\tau_m = 1$, $\tau_{im} = 100$ and in panel (c) a CTRW is used with a sojourn time density with power-law tail $\simeq t^{-1.646}$. The three black lines in each panel are obtained for $T =$, $T =$ and $T =$ from left to right, respectively. Blue dashed lines in panel (a) show $4\Delta/3T$ and expression (C.11) in panel (b).

where the dimensionless quantity $\xi = \overline{\delta^2(\Delta)}/\langle\overline{\delta^2(\Delta)}\rangle$ denotes the TAMSD normalized by the ensemble averaged TAMSD. For Brownian motion it is known that $EB_T(\Delta) \sim 4\Delta/3T$, as shown in figure C.2(a) [140]. This means that for small ratios Δ/T the spread of TAMSDs vanishes and the TAMSDs converge to the MSD $2D\Delta$.

Now we consider TAMSDs of MIM for $D = 1$, $v = 0$, $\tau_m = 1$ and $\tau_{im} = 100$ and an equilibrium fraction of mobile tracers. The MSD $2Df_m^{\text{eq}}t$ is linear at all times, as shown in chapter 2. As shown in figure C.1(b), the TAMSDs of MIM shown as grey lines do not converge to the ensemble averaged TAMSD shown as a blue line in the limit $\Delta/T \rightarrow 0$. A clear spread of TAMSDs is visible for the whole range of values of shown Δ . Now we calculate the spread of TAMSDs for small Δ , i.e., $EB_T(\Delta \rightarrow 0^+)$. We start by introducing the total mobile duration T_m , which is drawn from the subordinator $P(T_m, T)$. We start with expression (C.1). The increments for each trajectory are distributed according to $2D\Delta$ in the mobile state, while they are zero in the immobile state. Then, we only integrate over parts of the trajectory, where the tracer is mobile. This gives

$$\lim_{\Delta \rightarrow 0^+} \overline{\delta^2(\Delta)} = \lim_{\Delta \rightarrow 0^+} \frac{1}{T} \int_0^{T_m} 2D\Delta dt \quad (\text{C.4})$$

$$\sim \frac{1}{T} 2DT_m\Delta \text{ for } \Delta \ll T. \quad (\text{C.5})$$

From expression (C.5) we obtain the ensemble averaged TAMSD

$$\lim_{\Delta \rightarrow 0^+} \langle\overline{\delta^2(\Delta)}\rangle \sim \frac{2D}{T} \langle T_m \rangle \Delta \quad (\text{C.6})$$

Using the fraction of expressions (C.5) and (C.6) we can obtain the distribution $\phi(\xi)$. First, we rewrite ξ in terms of the mobile total mobile durations of each tracer particle T_m as follows

$$\xi = \frac{\overline{\delta^2(\Delta)}}{\langle\overline{\delta^2(\Delta)}\rangle} \sim \frac{2DT_m\Delta/T}{2D\Delta\langle T_m \rangle/T} \text{ for } \Delta \ll T \quad (\text{C.7})$$

$$\sim \frac{T_m}{\langle T_m \rangle} \text{ for } \Delta \ll T. \quad (\text{C.8})$$

84 APPENDIX C. TIME AVERAGED MEAN SQUARED DISPLACEMENT

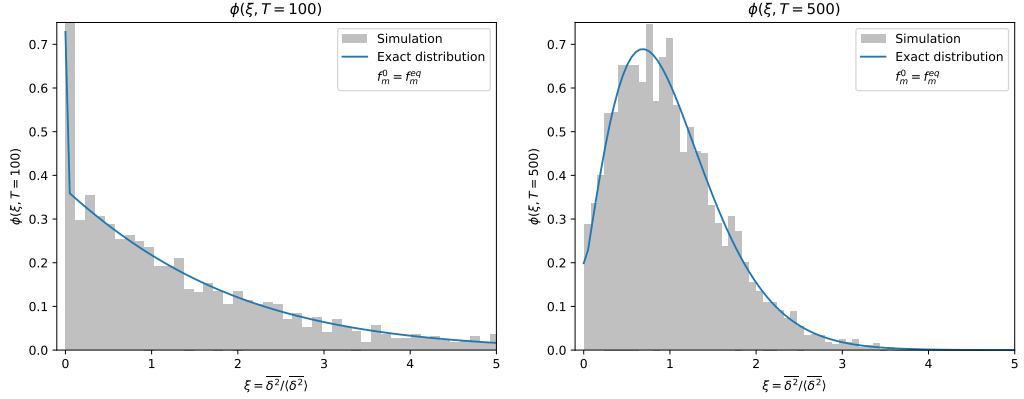


Figure C.3: Distribution of $\xi = \overline{\delta^2(\Delta)}/\langle\overline{\delta^2(\Delta)}\rangle$ for $\Delta \rightarrow 0^+$. The analytical solution (C.9) shown as a solid line is compared to a histogram from simulations.

This gives the distribution

$$\phi(\xi, T) \sim P(\xi \langle T_m \rangle, T) \langle T_m \rangle, \text{ for } \Delta \ll T, \quad (\text{C.9})$$

with the subordinator $P(T_m, T)$, that we introduce in chapter 2. We compare expression (C.9) to simulations in figure C.3 for an equilibrium fraction of initially mobile tracers, where we use $\langle T_m \rangle = f_m^{\text{eq}} T$. The full analytic expression (C.9) is relevant, as can be seen from the fact that the same distribution was obtained numerically, e.g., in [57].

Now we calculate the ergodicity breaking parameter EB [13], which we express using the first and second moment of the mobile duration T_m

$$\lim_{\Delta \rightarrow 0^+} EB_T(\Delta) = \langle \xi^2 \rangle - 1 \quad (\text{C.10})$$

$$= \frac{\langle T_m^2 \rangle - \langle T_m \rangle^2}{\langle T_m \rangle^2}. \quad (\text{C.11})$$

The moments of T_m can be obtained using (2.13). In [D2] we obtain exact expressions for $\langle T_m \rangle$ and $\langle T_m^2 \rangle$ for arbitrary fractions of initially mobile tracers. We point out that expression (C.11) is the squared coefficient of variation of the mobile durations $\text{cov}(t)$ (2.14) considered in the main text.

The ergodicity breaking parameter $EB_T(\Delta)$ has a non-zero value for $\Delta \rightarrow 0^+$ in contrast to the case of Brownian motion. It takes on a plateau value

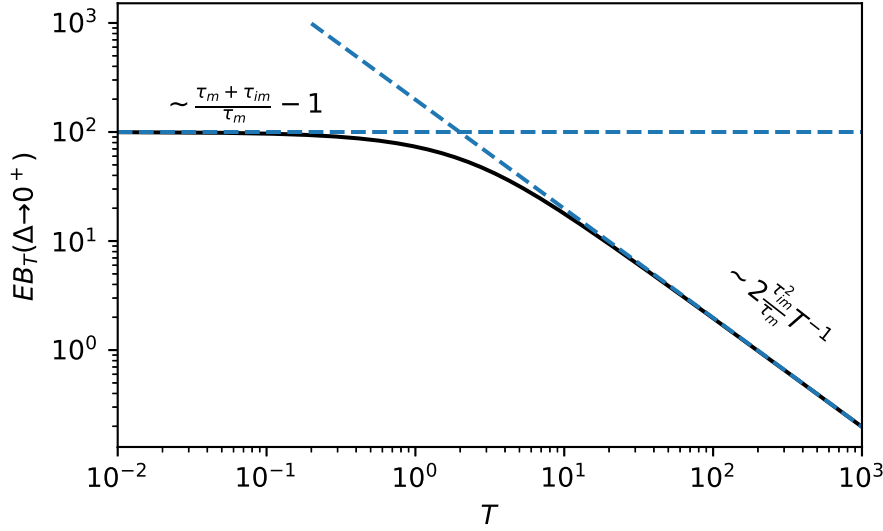


Figure C.4: Ergodicity breaking parameter for MIM in the limit $\Delta \rightarrow 0^+$ goes to zero with $2\tau_{\text{im}}^2/(\tau_{\text{m}}T)$ which means for ergodicity $T \gg 2\tau_{\text{im}}^2/\tau_{\text{m}}$.

for small Δ , as shown in figure C.2. Expression (C.11) is shown as a solid black line in figure C.4 as a function of the trajectory length T .

We insert the asymptotic expression of $\langle T_{\text{m}}^2 \rangle$ for $T \ll \tau_{\text{m}}, \tau_{\text{im}}$, namely $\lim_{T \rightarrow 0} \langle T_{\text{m}}^2 \rangle = f_{\text{m}}^{\text{eq}} T^2$ this gives $\lim_{T \rightarrow 0^+} EB_T(0^+) = 1/f_{\text{m}}^{\text{eq}} - 1$. This result is shown as a horizontal dashed line, which overlaps with the line for (C.11). For long trajectories $T \gg \tau_{\text{m}}, \tau_{\text{im}}$, we obtain in the same way the asymptote $\lim_{T \rightarrow \infty} EB_T(0^+) = 2\tau_{\text{im}}^2/T^{-1}$, which is shown as a dashed line in figure C.4, which agrees well with the full solution (C.11). This means that the ergodicity breaking parameter for $\Delta \rightarrow 0^+$ vanishes for long trajectories.

To conclude, on the level of TAMSDs MIM displays some features of Brownian motion, where $EB_T(\Delta)$ at $\Delta \rightarrow 0^+$ decreases for long trajectories T . Similarly to CTRW with power-law tailed sojourn time distributions, the value of $EB_T(\Delta)$ remains non-zero for $\Delta \rightarrow 0^+$. For illustration, some TAMSDs of a CTRW are shown in figure C.1(c)). As shown in figure C.2(c), $EB_T(\Delta \rightarrow 0)$ remains the same for increasing T in CTRW in contrast to MIM. The same scaling of $EB_T(\Delta)$, that we find, has been reported before in [112]. In [112] a tracer particle switches between two diffusion coefficients D_1 and D_2 with linear rates similar to MIM. In [112] the two-point correlation

function was used to obtain the moments of the TAMSD. In contrast, we use the subordination technique, which allows us to obtain not only $EB_T(\Delta)$, but also the distribution of ξ . This distribution was obtained numerically in [112] and [70], which stresses the relevance of this distribution¹. We point out the TAMSDs have a significant spread even at $T = 500$, which is five times the longest timescale $\tau_{\text{im}} = 100$ of the system.

¹We note that in [70] a CTRW is used with a bi-exponential sojourn time distribution. As described in chapter 2, this can mimic MIM for certain parameters.

Appendix D

Collection of papers

T.J. Doerries, A.V. Checkkin, and R. Metzler, Apparent anomalous diffusion and non-Gaussian distributions in a simple mobile-immobile transport model with Poissonian switching, *J. R. Soc. Interface* **19**, 20220233 (2022).

Used with permission of The Royal Society (U.K.), from Apparent anomalous diffusion and non-Gaussian distributions in a simple mobile-immobile transport model with Poissonian switching, T.J. Doerries, A.V. Checkkin, and R. Metzler, **19**, 20220233 (2022).

<https://doi.org/10.1098/rsif.2022.0233>

INTERFACE

royalsocietypublishing.org/journal/rsif

Research



Cite this article: Doerries TJ, Chechkin AV, Metzler R. 2022 Apparent anomalous diffusion and non-Gaussian distributions in a simple mobile–immobile transport model with Poissonian switching. *J. R. Soc. Interface* **19**: 20220233.
<https://doi.org/10.1098/rsif.2022.0233>

Received: 22 March 2022

Accepted: 15 June 2022

Subject Category:

Life Sciences–Physics interface

Subject Areas:

biophysics, environmental science

Keywords:

diffusion, mobile–immobile model, tau proteins

Author for correspondence:

Ralf Metzler

e-mail: rmetzler@uni-potsdam.de

Apparent anomalous diffusion and non-Gaussian distributions in a simple mobile–immobile transport model with Poissonian switching

Timo J. Doerries¹, Aleksei V. Chechkin^{1,2,3} and Ralf Metzler¹¹Institute of Physics and Astronomy, University of Potsdam, 14476 Potsdam, Germany²Faculty of Pure and Applied Mathematics, Hugo Steinhaus Center, Wrocław University of Science and Technology, Wyspińskiego 27, 50-370 Wrocław, Poland³Akhiezer Institute for Theoretical Physics, National Science Center ‘Kharkiv Institute of Physics and Technology’, 61108 Kharkiv, Ukraine

RM, 0000-0002-6013-7020

We analyse mobile–immobile transport of particles that switch between the mobile and immobile phases with finite rates. Despite this seemingly simple assumption of Poissonian switching, we unveil a rich transport dynamics including significant transient anomalous diffusion and non-Gaussian displacement distributions. Our discussion is based on experimental parameters for tau proteins in neuronal cells, but the results obtained here are expected to be of relevance for a broad class of processes in complex systems. Specifically, we obtain that, when the mean binding time is significantly longer than the mean mobile time, transient anomalous diffusion is observed at short and intermediate time scales, with a strong dependence on the fraction of initially mobile and immobile particles. We unveil a Laplace distribution of particle displacements at relevant intermediate time scales. For any initial fraction of mobile particles, the respective mean squared displacement (MSD) displays a plateau. Moreover, we demonstrate a short-time cubic time dependence of the MSD for immobile tracers when initially all particles are immobile.

1. Introduction

Already in the 1960s, there was considerable interest in the transport of chemical tracers, especially pesticides, nitrates and heavy metals through water-carrying layers of soil [1]. A typical description for such contaminant transport was the diffusion–advection equation (sometimes called the convective–dispersive equation) [2]

$$\frac{\partial}{\partial t} C(x, t) = D \frac{\partial^2}{\partial x^2} C(x, t) - v \frac{\partial}{\partial x} C(x, t), \quad (1.1)$$

where $C(x, t)$ is the contaminant concentration at distance x after time t , v is an advection velocity chosen as zero in the following and D is the diffusion constant (dispersion coefficient typically measured in units of $\text{cm}^2 \text{d}^{-1}$). Measurements revealed, however, that not all of the contaminant concentration was mobile at any given time, but that a fraction could be (transiently) trapped in stagnant volumes. Building on earlier models by Deans [3] and Coats & Smith [4], van Genuchten & Wierenga [5] analysed the exchange between mobile ($C_m(x, t)$) and immobile ($C_{im}(x, t)$) fractions. The mobile–immobile model under advection–diffusion conditions has been investigated intensively in the literature over the last 50 years [3,4,6–8]. Application of the mobile–immobile model includes the advective–diffusive transport of contaminants in the mobile domain of porous media [3,4,6–8], electrons in photoconductors [9], chemicals in chromatography [10] and adsorbing solutes in soil [11]. In many

geophysical systems equations of the type (1.1) are modified to account for anomalous transport, in which molecular transport no longer follows the linear time dependence $\langle \Delta x^2(t) \rangle = \langle x^2(t) \rangle - \langle x(t) \rangle^2 = 2Dt$ of Brownian motion, but follows laws of the type $\langle \Delta x^2(t) \rangle = 2D_\alpha t^\alpha$, for which $\alpha \neq 1$ [12]. Indeed, such transport anomalies were found on large field experiments, up to kilometre scales [13,14]. In such systems, the mobile-immobile transport model is replaced by models in which generalized transport terms are incorporated [15,16]. This type of model, in contrast to equation (1.1), is characterized by non-Gaussian distributions [12].

Motivated by concrete biological examples, we here study a seemingly simple version of the mobile-immobile transport model, in which particles switch between a freely diffusive phase and an immobile, stagnant phase. Even for the Poissonian switching dynamics considered here between the mobile and immobile phases and for biologically relevant parameters, we demonstrate the existence of a significant, transient anomalous-diffusive regime with a distinct non-Gaussian displacement distribution.

In fact, various components of biological cells, including tau proteins, synaptic vesicles in hippocampal neurons, glucocorticoid receptors, calcium-sensing proteins and transcription factors at the junction of the endoplasmic reticulum and the plasma membrane, undergo diffusion with transient immobilization [17–24]. Another example is given by the diffusion and target search of DNA-binding proteins along DNA molecules. For instance, the core domain of the tumour suppressor p53, the damage detection complex Rad4-Rad23 and the architectural DNA-binding protein Fis repeatedly attach to and detach from the DNA during the target search [25–29]. We here focus on tau proteins, which transiently bind to microtubules in axons of neuronal cells and are immobilized in the bound state, as schematically depicted in figure 1. Tau proteins stabilize microtubules that give structure to cells [30]. Alzheimer’s disease is associated with tau proteins losing the ability to bind to microtubules [30,31]. This effectively destabilizes the microtubules and leads to neurodegeneration [30,31]. Owing to the extremely elongated shape of the axon, the motion of tau proteins can be effectively described in one dimension [17]. If the immobilization time follows an exponential distribution with mean τ_{im} and tracers immobilize with rate τ_{im}^{-1} , i.e. a Poissonian dynamics, as assumed in [17], the motion can be described by the mobile-immobile model

$$\left. \begin{aligned} \frac{\partial}{\partial t} n_m(x, t) &= -\frac{1}{\tau_m} n_m(x, t) + \frac{1}{\tau_{im}} n_{im}(x, t) + D \frac{\partial^2}{\partial x^2} n_m(x, t) \\ \text{and } \frac{\partial}{\partial t} n_{im}(x, t) &= -\frac{1}{\tau_{im}} n_{im}(x, t) + \frac{1}{\tau_m} n_m(x, t). \end{aligned} \right\} \quad (1.2)$$

Here, $n_m(x, t)$ and $n_{im}(x, t)$ denote the line densities of mobile and bound tau proteins, respectively, with physical dimension [1/length]. The diffusion coefficient of the mobile tracers is D . Since we are dealing with a system of non-interacting particles, we use a probabilistic formulation according to which the total concentration $n_{tot}(x, t) = n_m(x, t) + n_{im}(x, t)$ is normalized to unity, $\int_{-\infty}^{\infty} n_{tot}(x, t) dx = 1$. The line densities $n_m(x, t)$ and $n_{im}(x, t)$ are then the respective fractions. Equations (1.2) were analysed in three dimensions for an equilibrium fraction of initially mobile tracers, finding Fickian yet non-Gaussian diffusion [32]. Accordingly, the mean squared

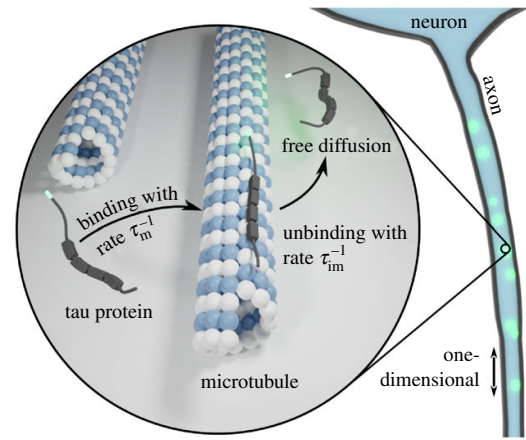


Figure 1. Schematic of tau protein dynamics in axons of neuronal cells. Diffusing tau proteins bind to longitudinally aligned microtubules inside the axon with the rate τ_m^{-1} . Upon binding, they remain immobile for the average duration τ_{im} and unbind with the rate τ_{im}^{-1} . The green markers represent fluorescent proteins attached to the tau proteins. Because of the elongated shape of the axons, the tau protein dynamic can effectively be described in one dimension. In our model, we assume a homogeneous binding site density.

displacement (MSD) of the total concentration n_{tot} grows linearly at all times, and under certain conditions a non-Gaussian distribution emerges [32].

Such Fickian yet non-Gaussian diffusion has been shown to occur for the motion of colloidal beads on phospholipid bilayer tubes, molecules at surfaces and colloids in a dense matrix of micropillars, where the colloids can get trapped in pockets [33–35]. Fickian yet non-Gaussian diffusion with a finite correlation time beyond which the displacement probability density function (PDF) crosses over to a Gaussian with an effective diffusivity arises in diffusing-diffusivity models, in which the diffusivity of individual tracers varies stochastically over time [36–41]. Direct examples for such randomly evolving diffusion coefficients (mobilities) are indeed known from lipids in protein-crowded bilayer membranes [42], shape-shifting protein molecules [43] or (de)polymerizing oligomer chains [44,45]. In other systems, an intermittent plateau emerges in the MSD; for instance, for two-dimensional fluids confined in a random matrix of obstacles or a porous cavity, in which trapping in finite pockets plays a key role [46–48]. We also mention plateaus in the MSD of both two- and three-dimensional isotropic Lennard-Jones binary liquids [49]. In most of the systems mentioned here, the PDF crosses over from an exponential (Laplace) PDF to a Gaussian. In the following, we explicitly show how a Laplace distribution with fixed scale parameters arises at intermediate time scales in our mobile-immobile model, paired with transient anomalous diffusion.

In what follows, we consider three initial conditions: an equilibrium fraction of mobile tracers and a scenario in which initially all tracers are mobile or immobile. These experimentally feasible situations significantly change the diffusion at short and intermediate time scales, at which apparent anomalous diffusion arises with slow-down and plateau-like behaviour, or ballistic diffusion, respectively. Together with the transient non-Gaussian displacement PDF, this behaviour is remarkably rich, given the simplicity of the governing equation (1.2). We individually analyse the motion of the

mobile and immobile population of tracers, made possible by the formulation of separate densities for mobile and immobile particles in this modelling approach. One physical incentive to do so is that the function of the tau proteins depends on their binding state [30]. Only bound tau proteins stabilize microtubules, or transcription factors modulate gene expression when bound to the DNA [21,30]. In some situations, only the mobile or immobile tracers can be measured. An example is given by combining total internal reflection fluorescence microscopy with fluorescently labelled single-stranded DNA, which binds to the microscope coverslip [50].

We present general results for the mobile and immobile concentrations and the MSD for arbitrary fractions of initially mobile tracers in §2. Sections 3–5 present concrete results and detailed discussions for different fractions of initial mobile particle concentrations; respectively, we start with the cases when all tracers are initially mobile and immobile and commence with an equilibrium fraction of mobile tracers. We conclude in §6.

2. Model and general solutions

We consider the mobile–immobile model equations (1.2) for the initial conditions $n_m(x, 0) = f_m \delta(x)$ and $n_{im}(x, 0) = f_{im} \delta(x)$, where f_m and f_{im} denote the fractions of initially mobile and immobile tracers, respectively, with the normalization $f_m + f_{im} = 1$. This formulation is suitable for typical single-particle tracking experiments used in biological and soft matter systems. They are also relevant for geophysical experiments, in which point-like injection of tracers is used. In this section, we keep the fractions f_m and f_{im} arbitrary and choose specific values in the following three sections.

In what follows, we use the concrete parameters $D = 13.9$ ($\mu\text{m}^2 \text{s}^{-1}$), $\tau_m = 0.16 \text{ s}$ and $\tau_{im} = 7.7 \text{ s}$ from [17] in all figures and neglect the vanishingly small advection velocity $v = 0.002 \mu\text{m s}^{-1}$. The values were obtained from experiments using the fluorescent decay after the photoactivation technique [17]. Let us briefly address the experimental origin of the time-scale separation between τ_m and τ_{im} . From single-particle tracking experiments of single-stranded DNA or tau proteins, immobilization times during the particle motion can be extracted [18,50]. The experiments for the tau proteins in [18] provided two-dimensional information and revealed relatively short residence times of the tau proteins on the microtubules, when compared with mobile times [18]. By contrast, the fluorescence decay after photoactivation (FDAP) experiment in one dimension along the axon direction, here denoted as the x variable, revealed long residence times and short mobile periods: $\tau_{im} \approx 48 \tau_m$ [17]. This seeming contradiction can be resolved when examining more closely the two-dimensional trajectories in the electronic supplementary material of [18]. Namely, the microtubules inside the axon are aligned in parallel with the axon axis, as also shown in figure 1. While a single binding event is short, an unbound particle quickly rebinds to a parallel, nearby microtubule after a short distance covered by diffusion perpendicular to the axon axis. This perpendicular motion does not contribute to the one-dimensional motion in the x -direction and thus, while individual binding times are relatively short, *effective* binding times appear much longer in the projection to one dimension. Since we are only interested in the one-dimensional motion, we use the parameters of [17] and hence long immobilization times.

2.1. Mobile and immobile concentration profiles

We consider the Fourier–Laplace transform of the concentrations and solve for $n_m(k, s)$, $n_{im}(k, s)$ and $n_{tot}(k, s)$ in expressions (A 1) and (A 2), in which the Fourier wavenumber k corresponds to the distance x in real space and the Laplace variable s is conjugated to time t ; see appendix A for details. We denote functions in Fourier or Laplace space solely by replacing the explicit dependencies on the respective arguments. The relations in the Fourier–Laplace domain can be Fourier-inverted, and we obtain the expressions in the Laplace domain,

$$n_m(x, s) = \left(f_m + f_{im} \frac{1}{1 + s\tau_{im}} \right) \frac{1}{\sqrt{4\phi(s)D}} e^{-\sqrt{\phi(s)D}|x|}, \quad (2.1)$$

$$n_{im}(x, s) = \left(f_m + f_{im} \frac{1}{1 + s\tau_{im}} \right) \times \frac{\tau_{im}/\tau_m}{1 + s\tau_{im}} \frac{1}{\sqrt{4\phi(s)D}} e^{-\sqrt{\phi(s)D}|x|} + f_{im} \frac{\tau_{im}}{1 + s\tau_{im}} \delta(x) \quad (2.2)$$

and

$$n_{tot}(x, s) = \frac{f_m + f_{im}}{1 + s\tau_{im}} \frac{1}{\phi(s)} e^{-\sqrt{4\phi(s)D}|x|} + f_{im} \frac{\tau_{im}}{1 + s\tau_{im}} \delta(x), \quad (2.3)$$

as functions of x and s with $\phi(s) = s[1 + \tau_m \tau_m^{-1}/(1 + s\tau_m)]$. These expressions are valid for all s and hence for all times t . A numerical Laplace inversion then provides the densities for any specified time. Remarkably, it turns out that the density of mobile tracers, which were initially immobile, is proportional to the density of immobile tracers, which were initially mobile. This can be seen by setting $f_m = 0$ or $f_{im} = 0$ in (2.1) and (2.2), respectively. This proportionality holds for all s and hence at all times. We obtain the long-time Gaussian limit of the full concentration in B.3,

$$n_{tot}(x, t) \sim \frac{1}{\sqrt{4\pi D_{\text{eff}} t}} \exp\left(-\frac{x^2}{4D_{\text{eff}} t}\right), \quad t \gg \tau_m, \tau_{im}, \quad (2.4)$$

with $D_{\text{eff}} = D/(1 + \tau_m/\tau_{im})$. Note that, for asymptotic equalities, we use the \sim symbol. In fact, independent of the ratio f_m and f_{im} we asymptotically obtain a Gaussian distribution in which the diffusivity is reduced to the effective diffusivity D_{eff} . The mobile and immobile concentrations are asymptotically equivalent to (2.4) up to a scalar f_j^{eq} defined below [16].

2.2. Moments

In general, the fractions \bar{n}_m and \bar{n}_{im} of mobile and immobile tracers, initially fixed as f_m and f_{im} , change over time. To obtain the respective numbers, we integrate the tracer densities over space. This corresponds to setting $k=0$ in the Fourier–Laplace transforms $n_m(k, s)$ and $n_{im}(k, s)$ of the densities. After Laplace inversion, we find

$$\bar{n}_m(t) = \frac{\tau_m}{\tau_m + \tau_{im}} + \frac{f_m \tau_{im} - f_{im} \tau_m}{\tau_m + \tau_{im}} \exp(-[\tau_m^{-1} + \tau_{im}^{-1}]t) \quad (2.5)$$

and

$$\bar{n}_{im}(t) = \frac{\tau_{im}}{\tau_m + \tau_{im}} - \frac{f_m \tau_{im} - f_{im} \tau_m}{\tau_m + \tau_{im}} \exp(-[\tau_m^{-1} + \tau_{im}^{-1}]t), \quad (2.6)$$

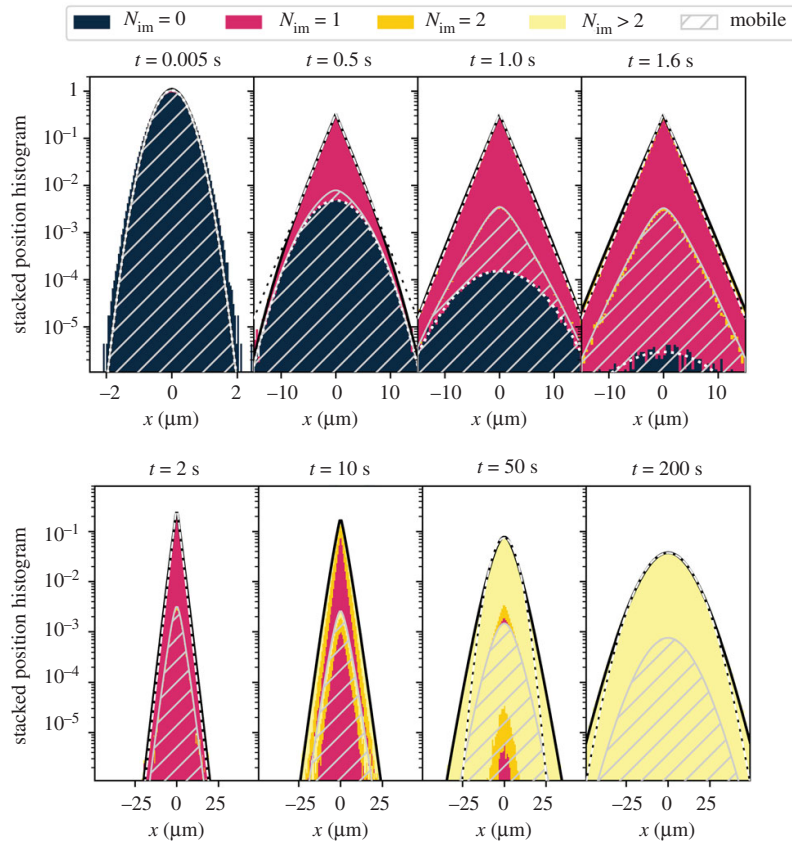


Figure 2. Concentration profiles for mobile initial conditions. The solid black line shows $n_{\text{tot}}(x, t)$ and the grey striped area $n_m(x, t)$, obtained via Laplace inversion of relations (2.1) and (2.3). Colours indicate the number of immobilization events of particles from a Brownian dynamics simulation with 5×10^6 trajectories in a stacked histogram. The striped area denotes mobile particles and the white dotted line denotes initially mobile tracers that have not yet been immobilized up to the indicated time t (3.2); this result almost coincides with the full concentration in the top left panel. For $t = 0.5$ s to 2 s, the white dashed line shows the Laplacian (3.5); for $t = 50$ s and 200 s, it shows the long-time Gaussian (2.4).

with $\bar{n}_m(t) + \bar{n}_{\text{im}}(t) = 1$. In the long-time limit $t \gg \tau_m, \tau_{\text{im}}$, the fractions of mobile and immobile tracers reach the stationary values $f_m^{\text{eq}} = \tau_m / (\tau_m + \tau_{\text{im}})$ and $f_{\text{im}}^{\text{eq}} = \tau_{\text{im}} / (\tau_m + \tau_{\text{im}})$, respectively. Our approach of splitting the total concentration into mobile and immobile fractions allows us to calculate the moments of the unbound, bound and total tau protein distributions individually,

$$\langle x^2(t) \rangle_j = \frac{1}{\bar{n}_j(t)} \int_{-\infty}^{\infty} x^2 n_j(x, t) dx, \quad (2.7)$$

where j stands for m , im and tot [16]. To shorten the notation, we use $\langle x^2(t) \rangle = \langle x^2(t) \rangle_{\text{tot}}$ in the remainder of this work. Using the Laplace inversion of

$$\left. \frac{\partial^2}{\partial k^2} n_{\text{tot}}(k, s) \right|_{k=0} = \langle x^2(s) \rangle, \quad (2.8)$$

we obtain the expression

$$\langle x^2(t) \rangle = 2D_{\text{eff}}t + 2D\tau_{\text{im}} \frac{f_m \tau_{\text{im}} / \tau_m - f_{\text{im}}}{(1 + \tau_{\text{im}} / \tau_m)^2} \left(1 - e^{-(\tau_m + \tau_{\text{im}})t} \right) \quad (2.9)$$

for the second moment. In the next section, we consider the initial conditions, when all tracers are initially mobile. This is chosen for didactic purposes, as this initial condition shows the plateau in

the MSD and intermittent Laplace distribution most clearly. In §4, we consider immobile initial conditions and finally consider equilibrium initial conditions in §5, where the effects discussed in earlier sections are present at the same time.

3. All tracers initially mobile

We now consider the initial condition when all tracers are mobile, i.e. $n_m(x, 0) = \delta(x)$ and $n_{\text{im}}(x, 0) = 0$. This initial condition does not correspond to the experiment carried out by Igaev *et al.* [17]. However, this situation could be realized experimentally, e.g. by using the method of injection of fluorescently labelled tau proteins [53]. In what follows, we repeatedly use the time-scale separation $\tau_m \ll \tau_{\text{im}}$ observed for tau proteins and also relevant to other systems.

3.1. Concentration

We calculate the densities at short, intermediate and long times. In B.1, we obtain the Gaussian

$$n_{\text{tot}}(x, t) \sim \frac{1}{\sqrt{4\pi Dt}} \exp\left(-\frac{x^2}{4Dt}\right) \quad (3.1)$$

in the short-time limit $t \ll \tau_m, \tau_{\text{im}}$. The Gaussian (3.1) can be seen in figure 2 in the top left panel. In this figure $n_m(x, t)$,

$n_{\text{tot}}(x, t)$ and a histogram are shown. The densities are obtained from Laplace inversions of the expressions in Laplace space (2.3), while the histogram is obtained from simulations, and colours denote the number of immobilization events N_{im} . Initially, all particles are mobile and diffuse freely, as denoted by the black colouring.

The concentration of freely diffusing particles that have not immobilized yet, i.e. have zero immobilization events $N_{\text{im}}=0$, is given by the PDF of free Brownian motion multiplied by the probability of not having immobilized, i.e.

$$n_{\text{m}}(x, t | N_{\text{im}} = 0) = \frac{\exp(-t/\tau_{\text{m}})}{\sqrt{4\pi Dt}} \exp\left(-\frac{x^2}{4Dt}\right). \quad (3.2)$$

These mobile tracers immobilize with the position-dependent rate $n_{\text{m}}(x, t | N_{\text{im}}=0)/\tau_{\text{m}}$. Integrating from $t'=0$ to $t'=t$, we obtain in the limit $t \ll \tau_{\text{im}}$ (i.e. at short and intermediate times) that

$$\begin{aligned} n_{\text{im}}(x, t \ll \tau_{\text{im}}) &\sim \int_0^t \frac{\exp(-t'/\tau_{\text{m}})/\tau_{\text{m}}}{\sqrt{4\pi Dt'}} \exp\left(-\frac{x^2}{4Dt'}\right) dt' \\ &= \frac{\exp(-|x|/\sqrt{D\tau_{\text{m}}})}{\sqrt{4D\tau_{\text{m}}}} \frac{1 - \text{erf}\left(|x|/\sqrt{4Dt} - \sqrt{t/\tau_{\text{m}}}\right)}{2} \\ &\quad - \frac{\exp(|x|/\sqrt{D\tau_{\text{m}}})}{\sqrt{4D\tau_{\text{m}}}} \frac{1 - \text{erf}\left(|x|/\sqrt{4Dt} + \sqrt{t/\tau_{\text{m}}}\right)}{2}. \end{aligned} \quad (3.3)$$

Comparing (3.3) with the Laplace inversion of $n_{\text{im}}(x, s)$ (2.3) in figure 8, we find very good agreement in the relevant range $t \ll \tau_{\text{im}}^2$. For the total density, we obtain by adding $n_{\text{m}}(x, t)$ (3.1) and $n_{\text{im}}(x, t)$ (3.3)

$$\begin{aligned} n_{\text{tot}}(x, t) &\sim \frac{\exp(-t/\tau_{\text{m}})}{\sqrt{4\pi Dt}} \exp\left(-\frac{x^2}{4Dt}\right) + n_{\text{im}}(x, t \ll \tau_{\text{im}}), \\ t &\ll \tau_{\text{im}} \end{aligned} \quad (3.4)$$

for the full tracer density. For $t \ll \tau_{\text{m}}$, we recover the Gaussian (3.1) from (3.4), while for $\tau_{\text{m}} \ll t \ll \tau_{\text{im}}$ the distribution is distinctly non-Gaussian, as shown in figure 2. Up to around $t=0.6$ s, the motion of the free tracers is dominated by the Gaussian $n_{\text{m}}(x, t | N_{\text{im}}=0)$ (see (3.2)), which spreads like free Brownian particles, shown as a white dotted line in figure 2. At around $t=1.6$ s, most of the tracers with $N_{\text{im}}=0$ immobilized and the majority of mobile tracers were immobile exactly once ($N_{\text{im}}=1$) and transitioned back to the mobile zone, as shown by the red area. Because of the immobilization, these tracers have moved less than the free particles with $N_{\text{im}}=0$ and a Laplace distribution emerges in the centre. For $x \ll t\sqrt{D/\tau_{\text{m}}}$ and $t \gg \tau_{\text{m}}$, we can use the asymptotic $\lim_{x \rightarrow \infty} \text{erf}(x) = -\lim_{x \rightarrow -\infty} \text{erf}(-x) = 1$ in $n_{\text{im}}(x, t \ll \tau_{\text{im}})$ (equation (3.3)), and obtain from $n_{\text{tot}}(x, t)$ (3.4) the expression

$$n_{\text{tot}}(x, t) \sim \frac{1}{\sqrt{4D\tau_{\text{m}}}} \exp\left(-\frac{|x|}{\sqrt{D\tau_{\text{m}}}}\right), \quad (3.5)$$

in the intermediate-time regime $\tau_{\text{m}} \ll t \ll \tau_{\text{im}}$. Combining the conditions $t \ll \tau_{\text{m}}$ and $x \ll t\sqrt{D/\tau_{\text{m}}}$ leads to $x \ll \tau_{\text{im}}\sqrt{D/\tau_{\text{m}}} = 71 \mu\text{m}$, which is large compared with the standard deviation $\sqrt{2D\tau_{\text{m}}} = 2.1 \mu\text{m}$ of the Laplace distribution (3.5). This means that the distribution follows such a Laplace shape for a large range of positions. The total concentration, in turn, therefore follows a Laplace distribution with fixed parameters. This is a pronounced deviation from a Gaussian distribution. This result can also be obtained from

calculations in Laplace space, as shown in B.2. By contrast, for times significantly longer than τ_{im} , many immobilizations take place, as shown by the bright yellow area in figure 2, where the distribution follows the Gaussian (2.4) with the effective diffusivity $D_{\text{eff}} = D/(1 + \tau_{\text{im}}/\tau_{\text{m}})$.

3.2. Mean squared displacement

For the general expression for the MSD (2.9) for immobile initial conditions, we obtain the expression

$$\langle x^2(t) \rangle = \frac{2D}{1 + \tau_{\text{im}}/\tau_{\text{m}}} \left[t + \frac{\tau_{\text{im}}^2/\tau_{\text{m}}}{1 + \tau_{\text{im}}/\tau_{\text{m}}} \left(1 - e^{-(\tau_{\text{m}}^{-1} + \tau_{\text{im}}^{-1})t} \right) \right]. \quad (3.6)$$

At intermediate times, the MSD (expression (3.6)) exhibits a plateau-like behaviour with the constant MSD

$$\langle x^2(t) \rangle \sim 2D\tau_{\text{m}}, \quad \tau_{\text{m}} \ll t \ll \tau_{\text{im}}, \quad (3.7)$$

corresponding to free Brownian particles that moved for the duration τ_{m} . This requires the condition $\tau_{\text{m}} \ll \tau_{\text{im}}$, which is satisfied in the tau protein case [17], with $\tau_{\text{m}} = 0.16$ s and $\tau_{\text{im}} = 7.7$ s. Such plateaus are often found when tracers diffuse in porous media or for dynamics in crowded membranes or environments with obstacles, in which the tracer can be transiently confined [38,46,48,54,55]. The MSD (3.6) is shown in figure 3a as the black solid line.

When calculating the moments of the mobile and immobile tracers (2.7), the time-dependent normalizations of the tracer densities (2.6),

$$\bar{n}_{\text{m}}(t) = \frac{\tau_{\text{m}}}{\tau_{\text{m}} + \tau_{\text{im}}} \left[\frac{1 + \tau_{\text{im}}}{\tau_{\text{m}} e^{-(\tau_{\text{m}}^{-1} + \tau_{\text{im}}^{-1})t}} \right] \quad (3.8)$$

and

$$\bar{n}_{\text{im}}(t) = \frac{\tau_{\text{im}}}{\tau_{\text{m}} + \tau_{\text{im}}} [1 - e^{-(\tau_{\text{m}}^{-1} + \tau_{\text{im}}^{-1})t}], \quad (3.9)$$

need to be taken into account, yielding the moments of the mobile and immobile densities (2.7) [16]

$$\begin{aligned} \langle x^2(t) \rangle_{\text{m}} &= \frac{2D}{(1 + \tau_{\text{im}}/\tau_{\text{m}})(1 + \tau_{\text{im}}/\tau_{\text{m}} e^{-(\tau_{\text{m}}^{-1} + \tau_{\text{im}}^{-1})t})} \left[t \left(1 + \frac{\tau_{\text{im}}^2}{\tau_{\text{m}}^2} e^{-(\tau_{\text{m}}^{-1} + \tau_{\text{im}}^{-1})t} \right) \right. \\ &\quad \left. + \frac{2\tau_{\text{im}}^2/\tau_{\text{m}}}{1 + \tau_{\text{im}}/\tau_{\text{m}}} (1 - e^{-(\tau_{\text{m}}^{-1} + \tau_{\text{im}}^{-1})t}) \right] \end{aligned} \quad (3.10)$$

and

$$\begin{aligned} \langle x^2(t) \rangle_{\text{im}} &= \frac{2D}{1 - e^{-(\tau_{\text{m}}^{-1} + \tau_{\text{im}}^{-1})t}} \left[\frac{t}{1 + \tau_{\text{im}}/\tau_{\text{m}}} \left(1 - \frac{\tau_{\text{im}}}{\tau_{\text{m}}} e^{-(\tau_{\text{m}}^{-1} + \tau_{\text{im}}^{-1})t} \right) \right. \\ &\quad \left. + \frac{\tau_{\text{im}}^2/\tau_{\text{m}} - \tau_{\text{im}}}{(1 + \tau_{\text{im}}/\tau_{\text{m}})^2} (1 - e^{-(\tau_{\text{m}}^{-1} + \tau_{\text{im}}^{-1})t}) \right]. \end{aligned} \quad (3.11)$$

As shown in figure 3, the mobile second moment exhibits a peak at around $t=0.6$ s, followed by a plateau. This peak arises as the density of mobile tracers initially consists of mobile tracers that have never immobilized. Once $t \gg \tau_{\text{m}}$, the mobile density mainly consists of tracers that were immobile (at least) once and mobilized, as discussed above. Since the latter had less time to move, they have spread less and the MSD temporarily decreases.

The immobile MSD (3.11) has the short-time behaviour $\langle x^2(t) \rangle_{\text{im}} \sim Dt$ for $t \ll \tau_{\text{m}}, \tau_{\text{im}}$. The factor $\frac{1}{2}$ when compared

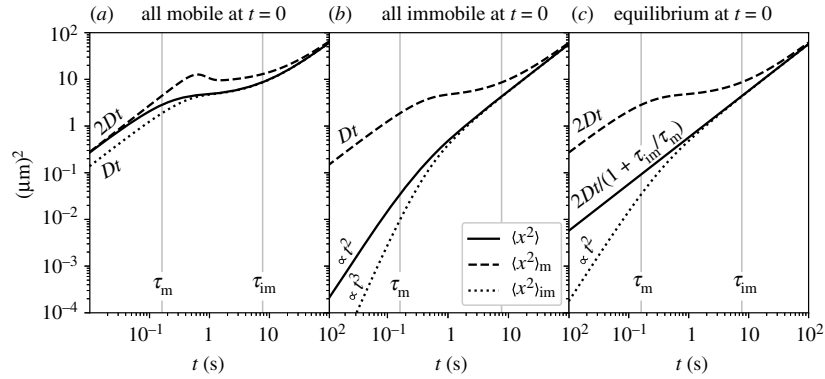


Figure 3. Second moments for different initial conditions on a log–log scale. In (a), all tracers are initially mobile, as in §3. After a linear growth, the second moment $\langle x^2(t) \rangle$ of all tracers (equation (3.6)) shows a plateau for $\tau_m \ll t \ll \tau_{im}$. The second moment of the mobile particles (equation (3.10)) in (a) has a peak immediately before the total particle moment and the mobile particle moment reach a plateau value. Immobile tracers spread $\sim Dt$ at short times, and the second moment (3.11) has a plateau at intermediate times. In (b), all tracers are initially immobile, as in §4. The second moment of all tracers (equation (4.3)) grows $\sim Dt^2/\tau_{im}$ at short times, owing to the decaying number of particles located at $x=0$. The immobile tracers spread $\sim Dt^3/(3\tau_m\tau_{im})$ at short times, while the full expression is given in equation (4.3). The mobile tracers in (b) spread exactly like the immobile tracers in (a), where all tracers are initially mobile. (c) The equilibrium case, §5, in which the second moment grows like $2Dt/(1 + \tau_{im}/\tau_m)$ (equation (5.3)) for all times. The mobile and immobile moments exactly match the moments of the total distribution with mobile and immobile initial conditions, respectively.

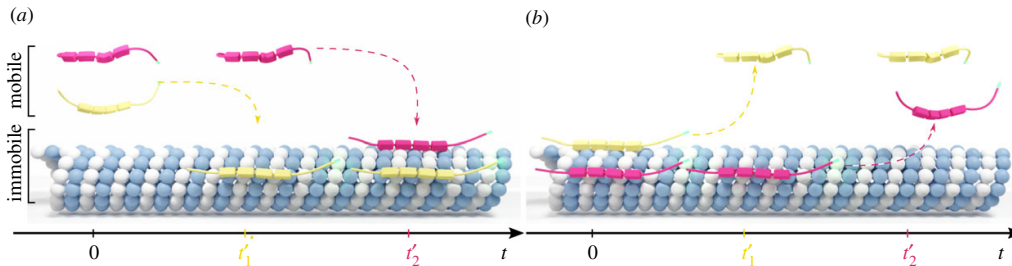


Figure 4. Schematic showing the short-time behaviour of tracers for mobile (a) and immobile initial conditions (b) at three snapshots of time. In both panels, the tracers change the mobilization state at times t'_1 and t'_2 , respectively. For mobile initial conditions in (a), the number of immobile tracers grows $\sim t/\tau_m$ at short times. Namely, the later a tracer immobilizes, the longer it was previously mobile. In (b), the number of mobile tracers grows $\sim t/\tau_{im}$. Namely, the earlier a tracer mobilizes in (b), the longer it is mobile.

with the mobile tracers arises because immobile tracers effectively average over the history of the mobile tracers. Namely, for $t \ll \tau_m, \tau_{im}$, mobile particles immobilize with the constant rate $p(t') = 1/\tau_m$. A particle that immobilized at time t' before moved for the duration t' and thus contributes $2Dt'$ to the second moment for $t > t'$; see figure 4a for a schematic drawing. When averaging over different mobile periods t' and normalizing with the fraction of immobile tracers $\int_0^t p(t') dt'$, we obtain

$$\langle x^2(t) \rangle_{im} \sim 2D \frac{\int_0^t t' p(t') dt'}{\int_0^t p(t') dt'} = \frac{2D \int_0^t t'/\tau_m dt'}{t/\tau_m} = Dt, \quad \text{for } t \ll \tau_m, \tau_{im}. \quad (3.12)$$

As mentioned above, the long-time limits of the MSDs of all densities remain equal to $2D_{eff}t$, regardless of the fractions f_m and f_{im} .

4. All tracers initially immobile

We now discuss the case when all tracers are immobile at $t=0$, $n_{im}(x, 0) = \delta(x)$ and $n_m(x, 0) = 0$.

4.1. Concentration

In B.1, we obtain the short-time behaviour

$$n_{tot}(x, t) \sim \frac{2t/\tau_{im}}{\sqrt{4\pi Dt}} e^{-(x^2/4Dt)} - \frac{|x| \left(1 - \operatorname{erf} \left(\frac{|x|}{\sqrt{4Dt}} \right) \right)}{2D\tau_{im}} + \left(1 - \frac{t}{\tau_{im}} \right) \delta(x), \quad \text{for } t \ll \tau_m, \tau_{im} \quad (4.1)$$

by applying approximations for large s in Laplace space. Expression (4.1) is shown in the left panel of figure 5 as the black dashed line. In particular, note the distinctively non-Gaussian shape of the distribution in contrast to the case of mobile initial conditions. The Gaussian in equation (4.1) has the normalization $\sim 2t/\tau_{im}$, while the second term has the normalization $\sim t/\tau_{im}$, and thus the whole expression (4.1) is normalized to unity. In B.2, we obtain the total density at intermediate times $\tau_m \ll t \ll \tau_{im}$

$$n_{tot}(x, t) \sim \frac{t/\tau_{im}}{\sqrt{4D\tau_m}} \exp \left(-\frac{|x|}{\sqrt{D\tau_m}} \right) + \left(1 - \frac{t}{\tau_{im}} \right) \delta(x), \quad (4.2)$$

as shown in figure 5 in the top row (except for the leftmost panel) as a black–white striped line. Compared with the mobile initial

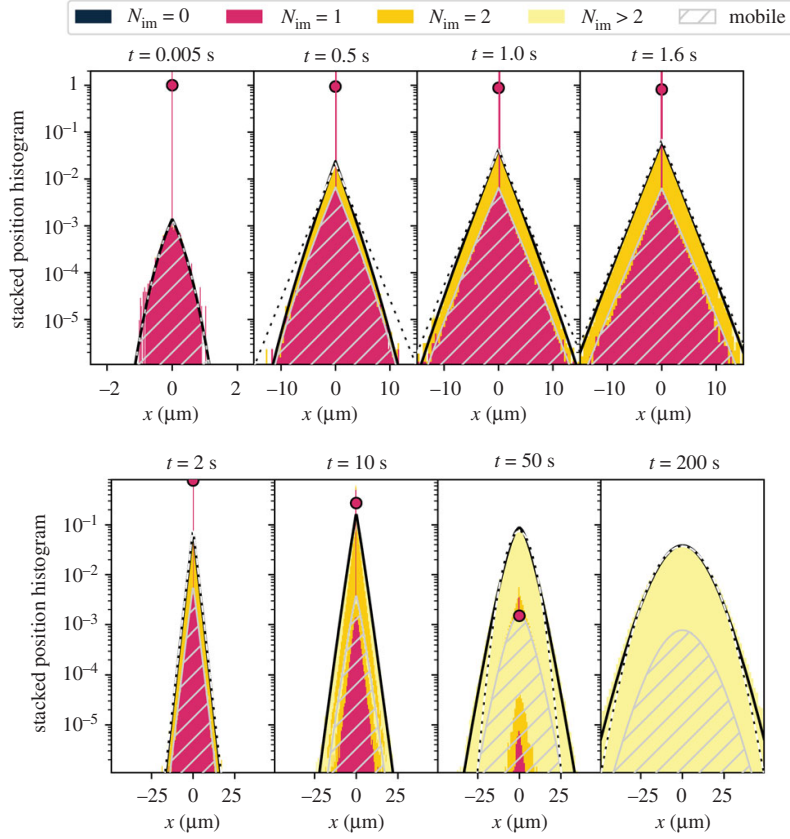


Figure 5. Concentration profiles for immobile initial conditions; for a description of the legend, see figure 2. The main difference from the case of mobile initial conditions poses the peak of immobile tracers at $x=0$ that have not moved up to time t , as shown by the circle. In addition, we here find a pronounced relative increase of mobile particle numbers and the very slow spread of immobile tracers at short times. The short-time approximation (4.1) is shown as the black dashed line in the top left panel. For $t=0.5$ – 10 s, the white dashed line shows the Laplacian (4.2) with growing weight; for $t=50$ s and 200 s, it shows the long-time Gaussian (2.4).

condition, the coefficient of the Laplace distribution has the linear growth t/τ_{im} . Most tracers remain immobile at the origin at $t=1.6$ s. In B.4, we find expression (B 11) for $n_{\text{tot}}(x, t)$, which is valid for $t \ll \tau_{\text{im}}$ and contains equations (4.1) and (4.2) as limits. In figure 5, the lower panels show the transition from the Laplace distribution to the Gaussian (2.4).

4.2. Mean squared displacement

From the general expression for the MSD (2.9), we obtain the expression

$$\langle x^2(t) \rangle = \frac{2D}{1 + \tau_{\text{im}}/\tau_{\text{m}}} \left[t - \frac{\tau_{\text{im}}}{1 + \tau_{\text{im}}/\tau_{\text{m}}} \left(1 - e^{-(\tau_{\text{m}}^{-1} + \tau_{\text{im}}^{-1})t} \right) \right]. \quad (4.3)$$

The MSD (4.3) has the ballistic short-time behaviour

$$\langle x^2(t) \rangle \sim \frac{Dt^2}{\tau_{\text{im}}} + O(t^3), \quad t \ll \tau_{\text{m}}, \tau_{\text{im}}. \quad (4.4)$$

The Landau symbol $O(\cdot)$ represents higher order terms. The ballistic behaviour at short times $t \ll \tau_{\text{im}}$ arises because the fraction $\exp(-t/\tau_{\text{im}}) \sim 1 - t/\tau_{\text{im}}$ of tracers are immobile at $x=0$ and hence do not contribute to the second moment. For $t' \ll \tau_{\text{m}} \ll \tau_{\text{im}}$, immobile particles mobilize with the constant rate $p(t')=1/\tau_{\text{im}}$. A particle that mobilized at time t' moved for

the duration $t-t'$ and thus contributes $2D(t-t')$ to the second moment for $t > t'$; see figure 4a for a schematic drawing. When integrating over different mobilization times t' , we find

$$\begin{aligned} \langle x^2(t) \rangle &\sim 2D \int_0^t (t-t')p(t') dt' = 2D \int_0^t \frac{t-t'}{\tau_{\text{im}}} dt' \\ &= D \frac{t^2}{\tau_{\text{im}}}, \quad t \ll \tau_{\text{m}} \ll \tau_{\text{im}}. \end{aligned} \quad (4.5)$$

We obtain the number of free and bound tracers from the general expression (2.6),

$$\bar{n}_{\text{m}}(t) = \frac{\tau_{\text{m}}}{\tau_{\text{m}} + \tau_{\text{im}}} \left[1 - e^{-(\tau_{\text{m}}^{-1} + \tau_{\text{im}}^{-1})t} \right] \quad (4.6)$$

and

$$\bar{n}_{\text{im}}(t) = \frac{\tau_{\text{im}}}{\tau_{\text{m}} + \tau_{\text{im}}} \left[\frac{1 + \tau_{\text{m}}}{\tau_{\text{im}} e^{-(\tau_{\text{m}}^{-1} + \tau_{\text{im}}^{-1})t}} \right]. \quad (4.7)$$

This produces the normalization of the immobile moment, and we find

$$\begin{aligned} \langle x^2(t) \rangle_{\text{im}} &= \frac{2Dt}{1 + \tau_{\text{m}}/\tau_{\text{im}}} \frac{1 + e^{-(\tau_{\text{m}}^{-1} + \tau_{\text{im}}^{-1})t}}{\tau_{\text{im}}/\tau_{\text{m}} + e^{-(\tau_{\text{m}}^{-1} + \tau_{\text{im}}^{-1})t}} \\ &- \frac{4D\tau_{\text{im}}^2/\tau_{\text{m}}}{(1 + \tau_{\text{im}}/\tau_{\text{m}})^2} \frac{1 - e^{-(\tau_{\text{m}}^{-1} + \tau_{\text{im}}^{-1})t}}{\tau_{\text{im}}/\tau_{\text{m}} + e^{-(\tau_{\text{m}}^{-1} + \tau_{\text{im}}^{-1})t}}. \end{aligned} \quad (4.8)$$

This MSD has the short-time behaviour $\langle x^2(t) \rangle_{\text{im}} \sim Dt^3 / (3\tau_{\text{im}}\tau_{\text{m}})$ for $t \ll \tau_{\text{mv}}, \tau_{\text{im}}$. The cubic scaling emerges as the only immobile tracers, which are not located at the origin, have previously mobilized and then immobilized again. The mobile concentration grows $\sim t/\tau_{\text{im}}$ at short times $t \ll \tau_{\text{im}}$. Integrating over the time t' spent in the mobile phase yields the cubic scaling

$$\begin{aligned} \langle x^2(t) \rangle_{\text{im}} &\sim 2D \int_0^t \frac{1}{\tau_{\text{m}}} n_{\text{m}}(t-t') t' dt' \\ &= \frac{2D}{\tau_{\text{m}}\tau_{\text{im}}} \int_0^t (t-t') t' dt' = D \frac{t^3}{3\tau_{\text{m}}\tau_{\text{im}}}, \end{aligned} \quad (4.9)$$

where, in the first step, we took the limit $t \ll \tau_{\text{m}}$. Since the mobile concentration with immobile initial conditions is proportional to the immobile concentration with mobile initial conditions, $\langle x^2(t) \rangle_{\text{m}}$ is equal to $\langle x^2(t) \rangle_{\text{im}}$ in (3.11) with mobile initial conditions. This can be seen in figure 3*a,b*. As for the mobile initial condition considered in §3, the MSDs of all densities grow $\sim 2D_{\text{eff}}t$ asymptotically.

5. Equilibrium initial fractions of initial mobile tracers

In this section, we use the equilibrium values $n_{\text{m}}(x, 0) = f_{\text{m}}^{\text{eq}}\delta(x)$ and $n_{\text{im}}(x, 0) = f_{\text{im}}^{\text{eq}}\delta(x)$ as initial conditions.

5.1. Concentration profiles

From the general expressions (2.1) and (2.3) for the densities $n_{\text{m}}(x, s)$ and $n_{\text{tot}}(x, s)$, we find that the mobile concentration of the equilibrium case discussed here is proportional to the total concentration for the mobile initial condition in §3 at all times. To understand why this is true, we note that both concentrations at all times contain mobile tracers that were initially mobile. Moreover, from equations (2.1) and (2.3), we see that the mobile concentration of the equilibrium case contains initially immobile tracers, while the total concentration contains immobile tracers that were initially mobile. In equations (2.1) and (2.3), the respective terms that appear in addition to the initially mobile fractions that are still mobile are proportional to each other at all times, as described in §2.1. An analogous relation holds between the immobile concentration with equilibrium initial conditions and the total concentration with immobile initial conditions, as can be seen in equations (2.1) and (2.3).

We consider the short-time approximation $t \ll \tau_{\text{mv}}, \tau_{\text{im}}$ for which initially immobile tracers have not yet mobilized and initially mobile tracers have not yet been trapped. Therefore, we can neglect the terms with the rates τ_{m}^{-1} and τ_{im}^{-1} in (1.2) and solve $n_{\text{m}}(x, t)$ and $n_{\text{im}}(x, t)$ separately, yielding

$$n_{\text{tot}}(x, t) \sim \frac{f_{\text{m}}^{\text{eq}}}{\sqrt{4\pi Dt}} \exp\left(-\frac{x^2}{4Dt}\right) + f_{\text{im}}^{\text{eq}}\delta(x), \quad t \ll \tau_{\text{mv}}, \tau_{\text{im}}, \quad (5.1)$$

with a Gaussian distribution describing free diffusion in addition to a Dirac- δ distribution of initially immobile tracers that have not yet moved. This behaviour can be seen in the top left panel of figure 6. The same result as (5.1) can be obtained by combining the short-time expressions for the mobile (3.1) and immobile (4.1) initial conditions for $t \ll \tau_{\text{mv}}, \tau_{\text{im}}$, as done in equation (B 5). At short times, the total density (5.1) behaves like the case of mobile initial conditions with

an additional delta peak. At intermediate times $\tau_{\text{m}} \ll t \ll \tau_{\text{im}}$, we obtain

$$n_{\text{tot}}(x, t) \sim \frac{t/\tau_{\text{im}}}{\sqrt{4D\tau_{\text{m}}}} \exp\left(-\frac{|x|}{\sqrt{D\tau_{\text{m}}}}\right) + \left(1 - \frac{t}{\tau_{\text{im}}}\right)\delta(x) \quad (5.2)$$

by combining the mobile (3.5) and immobile expression (4.2), respectively.³ In fact equation (5.2) is the same as expression (4.2) for the case of immobile initial conditions, in the intermediate-time regime. This result is shown in figure 6, where this approximation is compared with the full concentration from $t = 0.5$ to $t = 2$. This result is the one-dimensional equivalent to the findings in [32]. The lower right panels of figure 6 show the Gaussian long-time limit (2.4) as a black–white striped line.

5.2. Mean squared displacement

The number of mobile and immobile tracers remains constant for equilibrium initial conditions. At all times, the second moment of all tracers (2.9) thus simplifies to

$$\langle x^2(t) \rangle = \frac{2D}{1 + \tau_{\text{im}}/\tau_{\text{m}}}t. \quad (5.3)$$

The second moment is similar to that of a free Brownian particle, with the effective diffusion coefficient $D_{\text{eff}} = D/(1 + \tau_{\text{im}}/\tau_{\text{m}})$, as shown in figure 3. This is a known result from models for Fickian yet non-Gaussian diffusion [32]. The mobile and immobile moments, $\langle x^2(t) \rangle_{\text{m}}$ and $\langle x^2(t) \rangle_{\text{im}}$, are equivalent to the moments of the full density with mobile (3.6) and immobile (4.3) initial conditions, as can be seen in figure 3. This relation holds because the respective densities are proportional, as discussed above. The mobile and immobile moments show clear anomalous diffusion for $t \ll \tau_{\text{mv}}$ with a quite long crossover dynamics, as depicted in figure 3*c*. The mobile moment has a plateau in the intermediate regime $\tau_{\text{m}} \ll t \ll \tau_{\text{im}}$ and the immobile moment behaves ballistically at short times $t \ll \tau_{\text{m}}$.

In the long-time limit, all mobile and immobile second moments grow like the moments of the total concentration, i.e. $\langle x^2(t) \rangle_{\text{m}} \sim \langle x^2(t) \rangle_{\text{im}} \sim 2D_{\text{eff}}t$ for $t \gg \tau_{\text{mv}}, \tau_{\text{m}}$.

6. Discussion and conclusion

We considered a quite simple mobile–immobile model according to which tracer particles switch between a mobile diffusing state and an immobilized state. On average, the tracers remain mobile for the duration τ_{m} and immobile for τ_{im} . We considered the particular case, motivated by experiments on tau proteins binding to and unbinding from microtubules in axons of dendritic cells [17], when the two time scales are separated, $\tau_{\text{m}} \ll \tau_{\text{im}}$. We analysed three different initial conditions with varying fractions of mobile to immobile tracers at the origin, which can, in principle, all be realized in experiments. The initial condition of mobile tracers can be realized by injecting fluorescently labelled proteins [53]. Initially, immobile tracers could in principle be obtained in single-particle tracking experiments, by focusing on the tracks of immobile tracers. Equilibrium fractions of mobile tracers naturally occur when the tau proteins were in proximity to the microtubules for $t \gg \tau_{\text{mv}}, \tau_{\text{im}}$ before the start of the data acquisition.

First, we studied the case when all tracers are initially mobile, as described in the experiment in [53]. Second, we assumed all tracers to be initially immobile. Third, we considered an equilibrium fraction, corresponding to the experiment in [17]. For non-equilibrium fractions of initially mobile

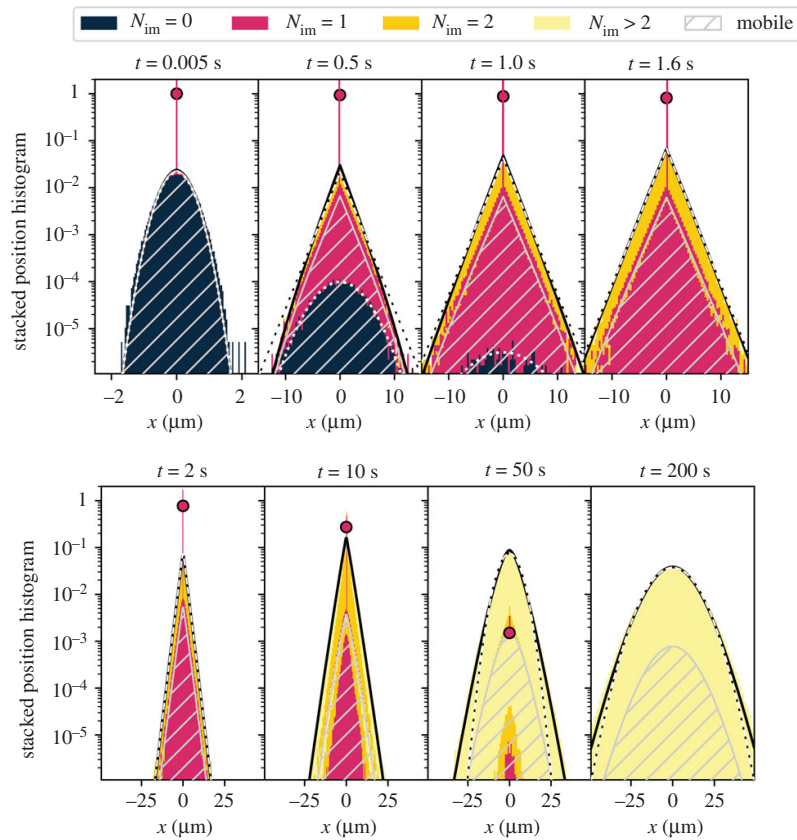


Figure 6. Concentration profiles for equilibrium initial conditions. At $t = 0$, all tracers are at $x = 0$ and the equilibrium fraction $\tau_{im}/(\tau_m + \tau_{im})$ is immobile. For a description of the legend, see figure 2. The top left panel shows the short-time behaviour consisting of a Gaussian and a δ -distribution (equation (5.1)). At $t = 1$, almost all initially mobile tracers immobilized at least once and the total concentration follows the Laplace distribution (5.2), as shown by the black–white striped line for $t = 0.5$ – 2 s. At longer times, after several immobilizations the concentration profiles cross over to a Gaussian, as witnessed by equation (2.4), shown as a black–white striped line for $t = 50$ s and $t = 200$ s.

tracers, we find anomalous diffusion at short and intermediate time scales, at which initially mobile tracers display a plateau in the MSD at intermediate times and initially immobile tracers spread ballistically at short times. At $t \ll \tau_m$ and an initial equilibrium fraction, the tracer density consists of a Gaussian and a delta peak. Initially, mobile tracers follow a Gaussian distribution at short times. When all tracers are initially immobile, the short-time distribution consists of a delta peak and a non-Gaussian distribution. At intermediate times $\tau_m \ll t \ll \tau_{im}$, the distribution is made up of a Laplace distribution and a delta distribution of initially immobile tracers that have not moved yet. The coefficients of the two distributions depend on the specific initial conditions. We additionally obtain expressions for the densities that are valid for the whole range $t \ll \tau_{im}$. We stress that the distribution is non-Gaussian at intermediate times, regardless of the initial conditions. By contrast, the distribution asymptotically at long times matches a Gaussian for all initial conditions. The densities of mobile and immobile tracers with equilibrium initial conditions match the total tracer densities of mobile and immobile initial conditions, respectively, at all times. Moreover, the immobile tracer density from mobile initial conditions is proportional to the mobile tracer density from immobile initial conditions at all times. As a special case for equilibrium initial conditions, our model corresponds to the one-dimensional version of the model used in [32] to describe Fickian yet non-Gaussian diffusion. We find the same linear

MSD for all times and obtain a closed expression for the Laplace distribution at intermediate time scales.

The model developed here is, of course, much more general. We provided the framework for any ratio of the characteristic time scales τ_m and τ_{im} , such that the model will be useful for scenarios ranging from geophysical experiments with Poissonian (im)mobilization statistics to molecular systems such as protein (un)binding to DNA in nanochannel set-ups. To the best of our knowledge, the transient Laplace distribution of tau proteins has not been observed yet. We now discuss possible experiments that could reveal the anomalous diffusion regime and the Laplace distribution, which depend on the time scales τ_m and τ_{im} . For the present analysis, we used the parameters $\tau_m = 0.16$ s and $\tau_{im} = 7.7$ s for tau proteins, which were obtained from an FDAP experiment [17]. FDAP experiments do not directly allow the observation of single-particle displacement densities and the moments thereof. However, a single-molecule tracking (SMT) study of tau proteins [18] with two-dimensional trajectories of 2.2 s length was conducted, where we expect the transient Laplace distribution to be visible in the marginal distribution, given that the sample size is large enough. From SMT experiments, the moments can be obtained, although, in [18], the moments of the distribution were not evaluated. Another example for a system with $\tau_{im} > \tau_m$ is given by synaptic vesicles [19]. In [19], fluorescence correlation spectroscopy reveals $\tau_{im} = (4.2 \pm 0.4)$ s and $\tau_m = (2.0 \pm 0.4)$ s. In addition,

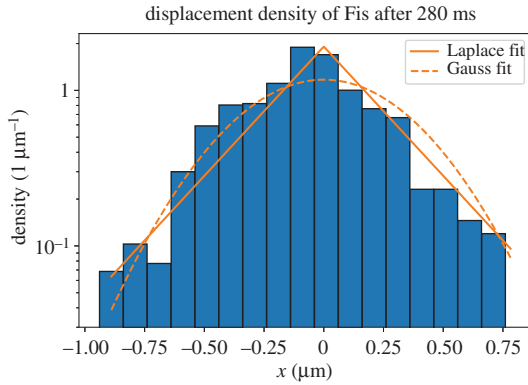


Figure 7. Displacement distribution of the Fis DNA-binding protein. The histogram depicts the data measured by Kamagata *et al.* [29]. The solid and dashed lines depict fits with a Laplace and a Gaussian distribution, respectively. The Laplace fit $\exp(-|x|/a)/2a$ yields $a = 0.27 \mu\text{m}$. The Gaussian fit $\exp(-x^2/(4Dt))/\sqrt{4\pi Dt}$ with $t = 0.28 \text{ s}$ yields $D = 0.21 \mu\text{m}^2 \text{ s}^{-1}$, which is within the margin of error of the value $(0.19 \pm 0.02) \mu\text{m}^2 \text{ s}^{-1}$ of the fast diffusion coefficient reported in [29]. The data were extracted from the PDF file of [29].

glucocorticoid receptors show long immobilization events with $\tau_{\text{im}} = 13 \text{ ms}$ compared with $\tau_{\text{m}} = 2 \text{ ms}$, as revealed by fluorescent recovery after a photobleaching experiment [20]. The Laplace distribution cannot be observed in this experiment, owing to the missing information on single tracers. SMT experiments of the transcription factor p53 [22] show a switched separation of time scales with $\tau_{\text{im}} = 1.80 \text{ s}$ and $\tau_{\text{m}} = 8.4 \text{ s}$. Here, SMT allows us to measure the exponential binding time distribution corresponding to a single binding rate, as in our model. The second moment is measured for up to 0.6 s , where longer trajectories would allow for a comprehensive comparison with the moments calculated in this work. For $\tau_{\text{m}} > \tau_{\text{im}}$, the Laplace distribution does not arise. We now look at another SMT experiment in more detail. In [29], the architectural DNA-binding protein Fis was observed to have a linear MSD and a non-Gaussian displacement distribution, as depicted in figure 7. The authors of [29] fitted two Gaussians to the distribution and deduced the presence of two sliding modes of Fis on the DNA. Since the motion during the slow sliding mode is within experimental accuracy, it is plausible to assume that the non-Gaussian distribution emerges as a result of immobilization. In figure 7, we show fits with a Laplace distribution and a Gaussian distribution in a logarithmic presentation. The Laplace distribution matches the general shape with few exceptions around $-0.4 \mu\text{m}$, while the Gaussian distribution does not capture the peak in the centre. We note that the Laplace distribution requires a single fitting parameter, compared with the two Gaussians with advection used in [29] requiring five parameters. The apparent Laplace distribution and linear MSD translate to equilibrium initial conditions in our model.

We note that (non-)exponential (im)mobilization has been studied using a Langevin equation with switching diffusivities [56,57] and the continuous time random walk framework, where the waiting time probability distribution function consists of a combination of two exponentials with different time scales [58]. It will be a topic of future research to study the effect of a drift velocity on the pre-asymptotic behaviour for different initial conditions, as well as what happens when non-exponential (im)mobilization is considered in a mobile-immobile model in connection with chemical reactions.

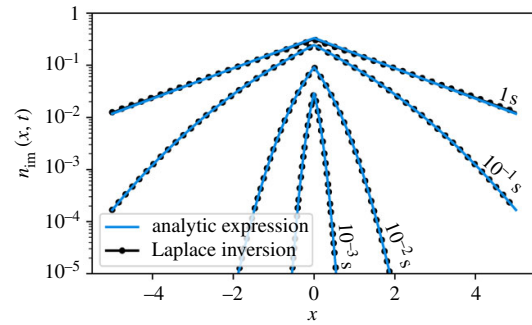


Figure 8. Comparison of the Laplace inversion of $n_{\text{im}}(x, s)$ (expression (2.3)) and the analytic expression for $n_{\text{im}}(x, t)$ (equation (3.3)) that holds for $t \ll \tau_{\text{im}}$. Both overlap almost perfectly for $t < \tau_{\text{im}} = 7.7 \text{ s}$.

Data accessibility. This article has no addition data.

Authors' contributions. T.J.D.: formal analysis, investigation, methodology, validation, visualization, writing—original draft, writing—review and editing; A.V.C.: conceptualization, formal analysis, investigation, supervision, writing—review and editing; R.M.: conceptualization, funding acquisition, project administration, supervision, validation, writing—original draft, writing—review and editing. All authors gave final approval for publication and agreed to be held accountable for the work performed herein.

Conflict of interest declaration. We declare we have no competing interests.

Funding. We acknowledge funding from the German Science Foundation (DFG, grant no. ME 1535/12-1). A.V.C. acknowledges the support of the Polish National Agency for Academic Exchange (NAWA).

Endnotes

¹The slow directed motion only plays a role when very long times are considered [17,51,52].

²Equations (3.2) and (3.3) can also be obtained by taking the limit $\tau_{\text{im}} \rightarrow \infty$ in (1.2) and solving the equations directly.

³An approximation for the whole range of $t \ll \tau_{\text{im}}$ can be obtained for any fractions of initially mobile tracers f_{m} by combining equations (3.4) and (B 11) from the mobile and immobile initial conditions, respectively. This yields equation (B 12) and is shown in figure 10.

Appendix A. General equations

Starting with equation (1.2), we apply the Fourier–Laplace transform $f(k, s) = \int_{-\infty}^{\infty} \int_0^{\infty} e^{-st+ikx} f(x, t) dt dx$ to the rate to obtain

$$\left. \begin{aligned} n_{\text{m}}(k, s) &= \frac{f_{\text{m}} + f_{\text{im}}(1/(1+s\tau_{\text{im}}))}{\phi(s) + k^2 D} \\ \text{and } n_{\text{im}}(k, s) &= \frac{\tau_{\text{im}}}{1+s\tau_{\text{im}}} \left(f_{\text{im}} + \tau_{\text{im}}^{-1} \frac{f_{\text{m}} + f_{\text{im}}(1/(1+s\tau_{\text{im}}))}{\phi(s) + k^2 D} \right) \end{aligned} \right\} \quad (\text{A } 1)$$

as well as

$$\begin{aligned} n_{\text{tot}}(k, s) &= n_{\text{m}}(k, s) + n_{\text{im}}(k, s) \\ &= \frac{f_{\text{m}} + f_{\text{im}}(1/(1+s\tau_{\text{im}}))}{s} \frac{\phi(s)}{\phi(s) + k^2 D} \\ &\quad + f_{\text{im}} \frac{\tau_{\text{im}}}{1+s\tau_{\text{im}}} \end{aligned} \quad (\text{A } 2)$$

with $\phi(s) = s[1 + \tau_{\text{im}}\tau_{\text{m}}^{-1}/(1 + s\tau_{\text{im}})]$.

Appendix B. Asymptotics calculated in Laplace space

We go from a short-time limit to a long-time limit.

B.1. Short-time limit

For $t \ll \tau_m, \tau_{im}$, we obtain $s\tau_m \gg 1$ and $s\tau_{im} \gg 1$. This yields $\phi(s) \sim s$ in this limit. With (A 1) for $f_m = 1$ and $f_{im} = 0$, we obtain the expression

$$n_m(k, s) \sim n_{tot}(k, s) \sim \frac{1}{s + k^2 D}, \quad (\text{B 1})$$

which produces the Gaussian (3.1). We now consider $f_{im} = 1$ and $f_m = 0$ and obtain the expression

$$n_{tot}(k, s) \sim \frac{1}{s\tau_{im}s + k^2 D} + \left(\frac{1}{s} - \frac{1}{s^2\tau_{im}}\right) \quad (\text{B 2})$$

from (A 2) in the limit $s\tau_m \gg 1$ and $s\tau_{im} \gg 1$. Fourier–Laplace inversion yields the expression

$$n_{tot}(x, t) \sim \frac{1}{\tau_{im}} \int_0^t \frac{1}{\sqrt{4\pi D t'}} e^{-(x^2/4D t')} dt' + (1 - t/\tau_{im})\delta(x) \quad (\text{B 3})$$

for $t \ll \tau_m \ll \tau_{im}$.

Solving the integral in (B 3) gives the expression

$$n_{tot}(x, t) \sim \frac{2t/\tau_{im}}{\sqrt{4\pi D t}} e^{-(x^2/4Dt)} - \frac{|x|(1 - \text{erf}(|x|/\sqrt{4Dt}))}{2D\tau_{im}} + \left(1 - \frac{t}{\tau_{im}}\right)\delta(x), \quad \text{for } t \ll \tau_m \ll \tau_{im}, \quad (\text{B 4})$$

where normalization is conserved. By combining expression (B 4) for immobile initial conditions and (3.1) for mobile initial conditions, we obtain the expression

$$n_{tot}(x, t) \sim \left(\frac{f_m + 2f_{im}t}{\tau_{im}}\right) \frac{1}{\sqrt{4\pi D t}} e^{-(x^2/4Dt)} - f_{im} \frac{|x|(1 - \text{erf}(|x|/\sqrt{4Dt}))}{2D\tau_{im}} + f_{im} \left(1 - \frac{t}{\tau_{im}}\right)\delta(x), \quad (\text{B 5})$$

for $t \ll \tau_m \ll \tau_{im}$ for arbitrary fractions of initially mobile tracers.

B.2. Density at intermediate time scales

We now investigate the intermediate time $\tau_m \ll t \ll \tau_{im}$, corresponding to $s\tau_m \ll 1$ and $s\tau_{im} \gg 1$. In this regime, we have

$$n_{tot}(x, t) \sim \int_0^t \frac{t + \tau_m - t'}{\tau_{im}\tau_m} \exp\left(\frac{-t'}{\tau_m}\right) \frac{\exp\left(-\frac{x^2}{4Dt'}\right)}{\sqrt{4Dt'}} dt' + (1 - t/\tau_{im})\delta(x) = \frac{e^{-(x^2/4Dt)}}{\sqrt{4\pi D t}} e^{-t/\tau_m} \frac{t}{\tau_{im}} + (1 - t/\tau_{im})\delta(x) + \frac{\exp(-|x|/\sqrt{D\tau_m})}{\sqrt{4D\tau_m}} \left(t/\tau_{im} - |x|\sqrt{\frac{\tau_m}{4D\tau_{im}^2}} + \tau_m/2\tau_{im}\right) \frac{1 - \text{erf}\left(|x|/\sqrt{4Dt} - \sqrt{t/\tau_m}\right)}{2} \quad (\text{B 10})$$

$$- \frac{\exp(|x|/\sqrt{D\tau_m})}{\sqrt{4D\tau_m}} \left(t/\tau_{im} + |x|\sqrt{\frac{\tau_m}{4D\tau_{im}^2}} + \tau_m/2\tau_{im}\right) \frac{1 - \text{erf}\left(|x|/\sqrt{4Dt} + \sqrt{t/\tau_m}\right)}{2}. \quad (\text{B 11})$$

Normalization is preserved, as can be seen by integrating (B 10) over x . The first summand in (B 10) then resolves to t/τ_{im} . In the limit $t \ll \tau_m, \tau_{im}$, we recover the short-time behaviour for $n_{tot}(x, t)$ (B 4), as shown in figure 9. For $\tau_m \ll t \ll \tau_{im}$ and

$\phi(s) \sim \tau_m^{-1}$, yielding the expression

$$n_{tot}(x, s) \sim \frac{f_m + f_{im}}{s} \frac{1}{s\tau_{im}} \frac{1}{\sqrt{4D\tau_m}} e^{-(|x|/\sqrt{D\tau_m})} + f_{im} \left(\frac{1}{s} - \frac{1}{s^2\tau_{im}}\right)\delta(x) \quad (\text{B 6})$$

from (2.3) for the total concentration. The inverse Laplace transform of (B 6) yields the expression

$$n_{tot}(x, s) \sim \left(\frac{f_m + f_{im}t}{\tau_{im}}\right) \frac{1}{\sqrt{4D\tau_m}} e^{-(|x|/\sqrt{D\tau_m})} + f_{im} \left(\frac{1-t}{\tau_{im}}\right)\delta(x) \quad (\text{B 7})$$

for $\tau_m \ll t \ll \tau_{im}$.

B.3. Density in the long-time limit

We obtain the long-time limit $t \gg \tau_m, \tau_{im}$ from $n_{tot}(k, s)$ (A 2) using $s \ll 1/\tau_{im}, 1/\tau_m$ and $\phi(s) \sim s(1 + \tau_{im}/\tau_m)$. This yields the expression

$$n_{tot}(x, t) \sim \frac{1}{\sqrt{4\pi D_{\text{eff}} t}} e^{-(x^2/4D_{\text{eff}} t)}, \quad \text{for } t \gg \tau_m, \tau_{im}, \quad (\text{B 8})$$

with $D_{\text{eff}} = D/(1 + \tau_{im}/\tau_m)$.

B.4. Density at short to intermediate time scales

Here, we analyse the regime $t \ll \tau_{im}$. The case $f_m = 1$ and $f_{im} = 0$ is considered in §3. We consider the case $f_{im} = 1$ and $f_m = 0$ here. From $n(x, s)$ (2.3), we obtain, with $s\tau_{im} \gg 1$ and $\phi(s) \sim s + 1/\tau_m$

$$n_{tot}(x, s) \sim \frac{s\tau_m + 1}{s^2\tau_{im}\tau_m} \frac{1}{\sqrt{4D(s + 1/\tau_m)}} e^{-\sqrt{(s+1/\tau_m)/D}|x|} + \left(\frac{1}{s} - \frac{1}{s^2\tau_{im}}\right), \quad \text{for } s\tau_{im} \gg 1. \quad (\text{B 9})$$

In the time domain in the limit $t \ll \tau_{im}$, this corresponds to the expression

$|x| \ll \sqrt{4D\tau_{im}^2/\tau_m}$, we recover the Laplacian intermediate regime in (B 7) with $f_{im} = 1$ and $f_m = 0$. In figure 9, we show a verification of (B 11). For arbitrary fractions of initially mobile tracers, we combine equation (B 11) for immobile initial

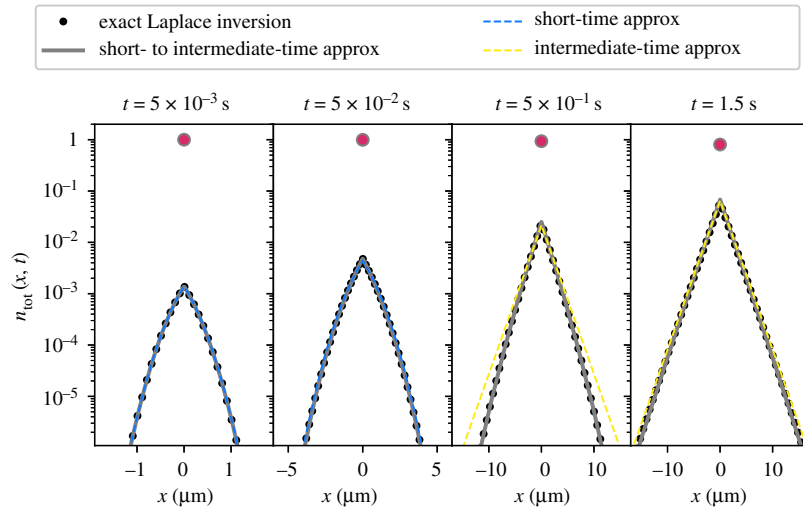


Figure 9. All tracers initially immobile. Comparison of the exact Laplace inversion of (2.3), the short-time approximation (B 4), the intermediate-time approximation (B 7) and the short- to intermediate-time approximation (B 11).

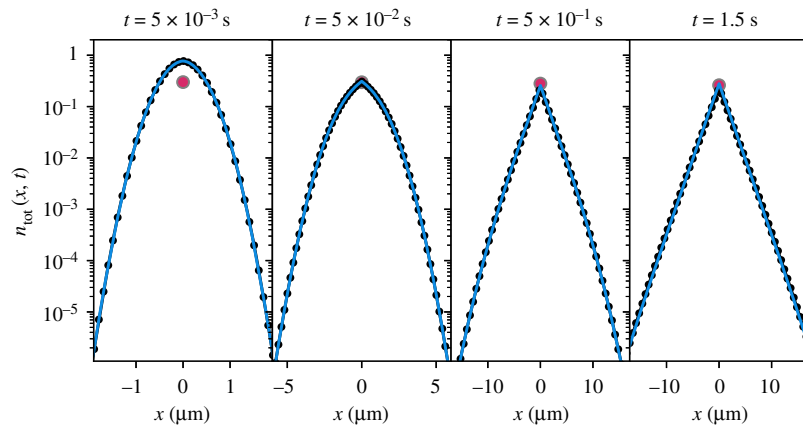


Figure 10. Total concentration $n_{\text{tot}}(x, t)$ for $f_{\text{im}} = 3/10$ and $f_m = 7/10$. Expression (B 12) is shown as the blue line and the Laplace inversion of $n_{\text{tot}}(x, s)$ (2.3) is shown as the black line with markers. Both overlap over five decades in amplitude, for all times shown. The red marker with the grey edge at $x = 0$ denotes the initially immobile tracers that have not yet moved. At short times, the distribution consists of the particles at $x = 0$ and a Gaussian. At $t = 1$ s, the distribution follows a Laplace distribution (linear tails in the log-linear plot), on top of the particles at $x = 0$.

conditions with equation (3.4) for mobile initial conditions, as follows:

$$\begin{aligned}
 n_{\text{tot}}(x, t) \sim & \frac{e^{-(x^2/4Dt)}}{\sqrt{4\pi Dt}} e^{-t/\tau_m} \left(f_m + f_{\text{im}} \frac{t}{\tau_{\text{im}}} \right) + f_{\text{im}}(1 - t/\tau_{\text{im}})\delta(x) \\
 & + \left[f_m + f_{\text{im}} \left(\frac{t}{\tau_{\text{im}}} - |x| \sqrt{\frac{\tau_m}{4D\tau_{\text{im}}^2}} + \tau_m/2\tau_{\text{im}} \right) \right] \\
 & \times \frac{\exp(-|x|/\sqrt{D\tau_m})}{\sqrt{4D\tau_m}} \frac{1 - \text{erf}\left(|x|/\sqrt{4Dt} - \sqrt{t/\tau_m}\right)}{2} \\
 & - \left[f_m + f_{\text{im}} \left(\frac{t}{\tau_{\text{im}}} + |x| \sqrt{\frac{\tau_m}{4D\tau_{\text{im}}^2}} + \tau_m/2\tau_{\text{im}} \right) \right] \\
 & \times \frac{\exp(|x|/\sqrt{D\tau_m})}{\sqrt{4D\tau_m}} \frac{1 - \text{erf}\left(|x|/\sqrt{4Dt} + \sqrt{t/\tau_m}\right)}{2}.
 \end{aligned}
 \tag{B 12}$$

In figure 10, expression (B 12) is compared with the Laplace inversion of the exact expression of $n_{\text{tot}}(x, s)$ (2.3).

References

1. Biggar JW, Nelson DR. 1967 Miscible displacement and leaching phenomena. In *Irrigation of agricultural lands* (ed. RM Hagen), pp. 254–274. Agronomy Monographs, vol. 11. Madison, WI: American Society of Agronomy.
2. Lapidus L, Amundson NR. 1952 Mathematica of adsorption in beds. VI. The effect of longitudinal diffusion in ion exchange and chromatographic columns. *J. Phys. Chem.* **56**, 984–988. (doi:10.1021/j150500a014)
3. Deans HH. 1963 A mathematical model for dispersion in the direction of flow of porous media. *Soc. Pet. Eng. J.* **3**, 49–52. (doi:10.2118/493-PA)
4. Coats KH, Smith BD. 1964 Dead-end pore volume and dispersion in porous media. *Soc. Pet. Eng. J.* **4**, 73–84. (doi:10.2118/647-PA)
5. Van Genuchten MT, Wierenga PJ. 1976 Mass transfer studies in sorbing porous media I. Analytical solutions. *Soil Sci. Soc. Am. J.* **40**, 473–480. (doi:10.2136/sssaj1976.03615995004000040011x)
6. Haggerty R, Gorelick SM. 1995 Multiple-rate mass transfer for modeling diffusion and surface reactions in media with pore-scale heterogeneity. *Water Res. Res.* **31**, 2383–2400. (doi:10.1029/95WR10583)
7. Dentz M, Berkowitz B. 2003 Transport behavior of a passive solute in continuous time random walks and multirate mass transfer. *Water Res. Res.* **39**, 1. (doi:10.1029/2001WR001163)
8. Sardin M, Schweich D, Leij FJ, van Genuchten MT. 1991 Modeling the nonequilibrium transport of linearly interacting solutes in porous media: a review. *Water Res. Res.* **27**, 2287–2307. (doi:10.1029/91WR01034)
9. Schmidlin FW. 1977 Theory of trap-controlled transient photoconduction. *Phys. Rev. B* **16**, 2362–2385. (doi:10.1103/PhysRevB.16.2362)
10. Villermaux J. 1987 A flexible method for representing complex phenomena from simple concepts. *J. Chromatogr.* **406**, 11–26. (doi:10.1016/S0021-9673(00)94014-7)
11. Roth K, Jury WA. 1993 Linear transport models for adsorbing solutes. *Water Res. Res.* **29**, 1195–1203. (doi:10.1029/92WR02537)
12. Metzler R, Klafter J. 2000 The random walk's guide to anomalous diffusion: a fractional dynamics approach. *Phys. Rep.* **339**, 1–77. (doi:10.1016/S0370-1573(00)00070-3)
13. Boggs JM, Young SC, Beard LM, Gelhar LW, Rehfeldt KR, Adams EE. 1992 Field study of dispersion in a heterogeneous aquifer: 1. Overview and site description. *Water Res. Res.* **28**, 3281–3291. (doi:10.1029/92WR01756)
14. Goepfert N, Goldscheider N, Berkowitz B. 2020 Experimental and modeling evidence of kilometer-scale anomalous tracer transport in an alpine karst aquifer. *Water Res.* **178**, 115755. (doi:10.1016/j.watres.2020.115755)
15. Schumer R, Benson DA, Meerschaert MM, Baeumer B. 2003 Fractal mobile/immobile solute transport. *Water Res. Res.* **39**, 13. (doi:10.1029/2003wr002141)
16. Doerries TJ, Chechkin AV, Schumer R, Metzler R. 2022 Rate equations, spatial moments, and concentration profiles for mobile-immobile models with power-law and mixed waiting time distributions. *Phys. Rev. E* **105**, 014105. (doi:10.1103/PhysRevE.105.014105)
17. Igaev M, Janning D, Sündermann F, Niewidok B, Brandt R, Junge W. 2014 A refined reaction-diffusion model of tau-microtubule dynamics and its application in FDAP analysis. *Biophys. J.* **107**, 2567–2578. (doi:10.1016/j.bpj.2014.09.016)
18. Janning D *et al.* 2014 Single-molecule tracking of tau reveals fast kiss-and-hop interaction with microtubules in living neurons. *Mol. Biol. Cell.* **25**, 3541–3551. (doi:10.1091/mbc.e14-06-1099)
19. Yeung C, Shtrahman M, Wu XL. 2007 Stick-and-diffuse and caged diffusion: a comparison of two models of synaptic vesicle dynamics. *Biophys. J.* **92**, 2271–2280. (doi:10.1529/biophysj.106.081794)
20. Sprague BL, Pego RL, Stavrea DA, McNally JG. 2004 Analysis of binding reactions by fluorescence recovery after photobleaching. *Biophys. J.* **86**, 3473–3495. (doi:10.1529/biophysj.103.026765)
21. Liu Z, Legant WR, Chen BC, Li L, Grimm JB, Lavis LD, Betzig E, Tjian R. 2014 3D imaging of Sox2 enhancer clusters in embryonic stem cells. *elife* **3**, e04236. (doi:10.7554/elife.04236)
22. Mazza D, Abernathy A, Golob N, Morisaki T, McNally JG. 2012 A benchmark for chromatin binding measurements in live cells. *Nucleic Acids Res.* **40**, e119. (doi:10.1093/nar/gks701)
23. Chen J *et al.* 2014 Single-molecule dynamics of enhanceosome assembly in embryonic stem cells. *Cell* **156**, 1274–1285. (doi:10.1016/j.cell.2014.01.062)
24. Wu MM, Covington ED, Lewis RS. 2014 Single-molecule analysis of diffusion and trapping of STIM1 and Orai1 at endoplasmic reticulum–plasma membrane junctions. *Mol. Biol. Cell* **25**, 3672–3685. (doi:10.1091/mbc.e14-06-1107)
25. Park S, Lee OC, Durang X, Jeon JH. 2021 A mini-review of the diffusion dynamics of DNA-binding proteins: experiments and models. *J. Korean Phys. Soc.* **78**, 408–426. (doi:10.1007/s40042-021-00060-y)
26. Tafvizi A, Miry LA, van Oijen AM. 2011 Dancing on DNA: kinetic aspects of search processes on DNA. *ChemPhysChem* **12**, 1418–1489. (doi:10.1002/cphc.201100112)
27. Tafvizi A, Huang F, Fersht AR, Miry LA, van Oijen AM. 2011 A single-molecule characterization of p53 search on DNA. *Proc. Natl. Acad. Sci. USA* **108**, 563–568. (doi:10.1073/pnas.1016020107)
28. Kong M *et al.* 2016 Single-molecule imaging reveals that Rad4 employs a dynamic DNA damage recognition process. *Mol. Cell* **64**, 376–387. (doi:10.1016/j.molcel.2016.09.005)
29. Kamagata K, Mano E, Uchi K, Kanabayashi S, Johnson RC. 2018 High free-energy barrier of 1D diffusion along DNA by architectural DNA-binding proteins. *J. Mol. Biol.* **430**, 655–667. (doi:10.1016/j.jmb.2018.01.001)
30. Kolarova M, García-Sierra F, Bartos A, Ricny J, Ripova D. 2012 Structure and pathology of tau protein in Alzheimer disease. *J. Alzheimer's Dis.* **2012**, 731526. (doi:10.1155/2012/731526)
31. Guo T, Noble W, Hanger DP. 2017 Roles of tau protein in health and disease. *Acta Neuropathol.* **133**, 665–704. (doi:10.1007/s00401-017-1707-9)
32. Mora S, Pomeau Y. 2018 Brownian diffusion in a dilute field of traps is Fickian but non-Gaussian. *Phys. Rev. E* **98**, 040101. (doi:10.1103/PhysRevE.98.040101)
33. Wang B, Anthony SM, Bae SC, Granick S. 2009 Anomalous yet Brownian. *Proc. Natl. Acad. Sci. USA* **106**, 15160–15164. (doi:10.1073/pnas.0903554106)
34. Skaug MJ, Mabry J, Schwartz DK. 2013 Intermittent molecular hopping at the solid-liquid interface. *Phys. Rev. Lett.* **110**, 256101. (doi:10.1103/PhysRevLett.110.256101)
35. Chakraborty I, Roichman Y. 2020 Disorder-induced Fickian, yet non-Gaussian diffusion in heterogeneous media. *Phys. Rev. Res.* **2**, 022020. (doi:10.1103/PhysRevResearch.2.022020)
36. Chechkin AV, Seno F, Metzler R, Sokolov IM. 2017 Brownian yet non-Gaussian diffusion: from superstatistics to subordination of diffusing diffusivities. *Phys. Rev. X* **7**, 021002. (doi:10.1103/physrevx.7.021002)
37. Chubynsky MV, Slater GW. 2014 Diffusing diffusivity: a model for anomalous, yet Brownian, diffusion. *Phys. Rev. Lett.* **113**, 098302. (doi:10.1103/PhysRevLett.113.098302)
38. Wang B, Kuo J, Bae SC, Granick S. 2012 When Brownian diffusion is not Gaussian. *Nat. Mater.* **11**, 481–485. (doi:10.1038/nmat3308)
39. Sposini V, Chechkin AV, Seno F, Pagnini G, Metzler R. 2018 Random diffusivity from stochastic equations: comparison of two models for Brownian yet non-Gaussian diffusion. *New J. Phys.* **20**, 043044. (doi:10.1088/1367-2630/aab696)
40. Lanoiselée Y, Grebenkov DS. 2018 A model of non-Gaussian diffusion in heterogeneous media. *J. Phys. A: Math. Theor.* **51**, 145602. (doi:10.1088/1751-8121/aab15f)
41. Jain R, Sebastian KL. 2016 Diffusion in a crowded, rearranging environment. *J. Phys. Chem. B* **120**, 3988–3992. (doi:10.1021/acs.jpcc.6b01527)
42. Javanainen M, Hammaren H, Monticelli L, Jeon JH, Metzler R, Vattulainen I. 2013 Anomalous and normal diffusion of proteins and lipids in crowded lipid membranes. *Faraday Discuss.* **161**, 397–417. (doi:10.1039/C2FD20085F)
43. Yamamoto E, Akimoto T, Mitsutake A, Metzler R. 2021 Universal relation between instantaneous diffusivity and radius of gyration of proteins in

- aqueous solution. *Phys. Rev. Lett.* **126**, 128101. (doi:10.1103/PhysRevLett.126.128101)
44. Baldovin F, Orlandini E, Seno F. 2019 Polymerization induces non-Gaussian diffusion. *Front. Phys.* **7**, 124. (doi:10.3389/fphy.2019.00124)
 45. Hidalgo-Soria M, Barkai E. 2020 The hitchhiker model for Laplace diffusion processes in the cell environment. *Phys. Rev. E* **102**, 012109. (doi:10.1103/PhysRevE.102.012109)
 46. Skinner TOE, Schnyder SK, Aarts DGAL, Horbach J, Dullens RPA. 2013 Localization dynamics of fluids in random confinement. *Phys. Rev. Lett.* **111**, 128301. (doi:10.1103/PhysRevLett.111.128301)
 47. Wang D, Wu H, Liu L, Chen J, Schwartz DK. 2019 Diffusive escape of a nanoparticle from a porous cavity. *Phys. Rev. Lett.* **123**, 118002. (doi:10.1103/PhysRevLett.123.118002)
 48. Słezak J, Burov S. 2021 From diffusion in compartmentalized media to non-Gaussian random walks. *Sci. Rep.* **11**, 1. (doi:10.1038/s41598-020-79139-8)
 49. Miotto JM, Pigolotti S, Chechkin AV, Roldán-Vargas S. 2021 Length scales in Brownian yet non-Gaussian dynamics. *Phys. Rev. X* **11**, 031002. (doi:10.1103/PhysRevX.11.031002)
 50. Peterson EM, Manhart MW, Harris JM. 2016 Single-molecule fluorescence imaging of interfacial DNA hybridization kinetics at selective capture surfaces. *Anal. Chem.* **88**, 1345–1354. (doi:10.1021/acs.analchem.5b03832)
 51. Scholz T, Mandelkow E. 2014 Transport and diffusion of Tau protein in neurons. *Cell. Mol. Life Sci.* **71**, 3139–3150. (doi:10.1007/s00018-014-1610-7)
 52. Mercken M, Fischer I, Kosik KS, Nixon RA. 1995 Three distinct axonal transport rates for tau, tubulin, and other microtubule-associated proteins: evidence for dynamic interactions of tau with microtubules in vivo. *J. Neurosci.* **15**, 8259–8267. (doi:10.1523/JNEUROSCI.15-12-08259.1995)
 53. Kreis TE, Birchmeier W. 1982 Microinjection of fluorescently labeled proteins into living cells with emphasis on cytoskeletal proteins. *Int. Rev. Cytol.* **75**, 209–227. (doi:10.1016/s0074-7696(08)61005-0)
 54. Ghosh SK, Cherstvy AG, Metzler R. 2015 Non-universal tracer diffusion in crowded media of non-inert obstacles. *Phys. Chem. Chem. Phys.* **17**, 1857–1858. (doi:10.1039/c4cp03599b)
 55. Javanainen M, Hammaren H, Monticelli L, Jeon J-H, Miettinen MS, Martinez-Seara H, Metzler R, Vattulainen I. 2013 Anomalous and normal diffusion of proteins and lipids in crowded lipid membranes. *Faraday Discuss.* **161**, 397–417. (doi:10.1039/C2FD20085F)
 56. Miyaguchi T, Akimoto T, Yamamoto E. 2016 Langevin equation with fluctuating diffusivity: a two-state model. *Phys. Rev. E* **94**, 012109. (doi:10.1103/PhysRevE.94.012109)
 57. Hidalgo-Soria M, Barkai E, Burov S. 2020 Cusp of non-Gaussian density of particles for a diffusing diffusivity model. *Entropy* **23**, 231. (doi:10.3390/e23020231)
 58. Vitaly S, Paradisi P, Pagnini G. 2022 Anomalous diffusion originated by two Markovian hopping-trap mechanisms. *J. Phys. A: Math. Theor.* **55**, 224012. (doi:10.1088/1751-8121/ac677f)

T.J. Doerries, R. Metzler, and A.V. Chechkin, Emergent anomalous transport and non-Gaussianity in a simple mobile-immobile model: the role of advection, *NJP* **25**, 063009 (2023).
<https://doi.org/10.1088/1367-2630/acd950>



OPEN ACCESS

RECEIVED

23 January 2023

REVISED

20 May 2023

ACCEPTED FOR PUBLICATION

26 May 2023

PUBLISHED

9 June 2023



Original Content from this work may be used under the terms of the [Creative Commons Attribution 4.0 licence](https://creativecommons.org/licenses/by/4.0/).

Any further distribution of this work must maintain attribution to the author(s) and the title of the work, journal citation and DOI.



PAPER

Emergent anomalous transport and non-Gaussianity in a simple mobile-immobile model: the role of advection

Timo J Doerries¹, Ralf Metzler^{1,2,*}  and Aleksei V Chechkin^{1,3,4} ¹ Institute of Physics & Astronomy, University of Potsdam, 14476 Potsdam, Germany² Asia Pacific Centre for Theoretical Physics, Pohang 37673, Republic of Korea³ Faculty of Pure and Applied Mathematics, Hugo Steinhaus Centre, Wrocław University of Science and Technology, Wyspińskiego 27, 50-370 Wrocław, Poland⁴ Akhiezer Institute for Theoretical Physics, 61108 Kharkov, Ukraine

* Author to whom any correspondence should be addressed.

E-mail: rmetzler@uni-potsdam.de

Keywords: diffusion, drift/advection, non-Gaussianity

Abstract

We analyse the transport of diffusive particles that switch between mobile and immobile states with finite rates. We focus on the effect of advection on the density functions and mean squared displacements (MSDs). At relevant intermediate time scales we find strong anomalous diffusion with cubic scaling in time of the MSD for high Péclet numbers. The cubic scaling exists for short and long mean residence times in the immobile state τ_{im} . For long τ_{im} the plateau in the MSD at intermediate times, previously found in the absence of advection, also exists for high Péclet numbers. Initially immobile tracers are subject to the newly observed regime of advection induced subdiffusion for short immobilisations and high Péclet numbers. In the long-time limit the effective advection velocity is reduced compared to advection in the mobile phase. In contrast, the MSD is enhanced by advection. We explore physical mechanisms behind the emerging non-Gaussian density functions and the features of the MSD.

1. Introduction

One of the simplest equations to describe the transport of tracers in subsurface aquifers (water-bearing layers or permeable rock or sediment) is the advection–diffusion equation [1, 2]

$$\frac{\partial}{\partial t} G(x, t) = D \frac{\partial^2}{\partial x^2} G(x, t) - v \frac{\partial}{\partial x} G(x, t), \quad (1)$$

where $G(x, t)$ denotes the probability density function of a tracer particle, v the constant advection velocity, and D the diffusion constant. The initial condition is $G(x, 0) = \delta(x)$, corresponding to a ‘point injection’ in geoscience. The probability density function encoded by equation (1) with initial condition $G(x, 0)$ is given by the Gaussian

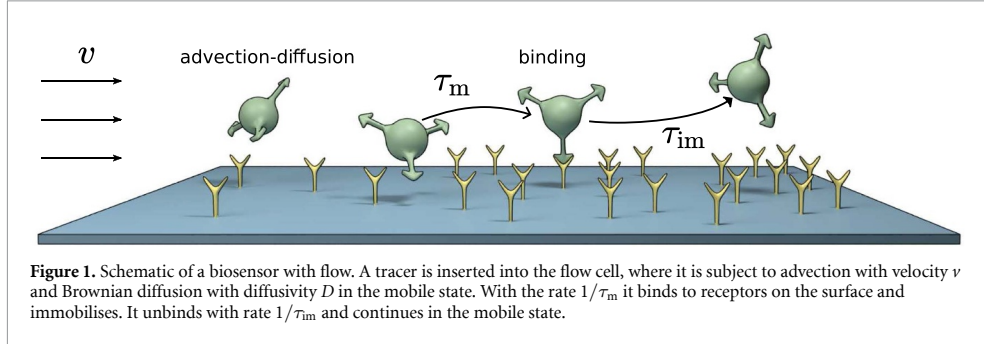
$$G(x, t) = \frac{1}{\sqrt{4\pi Dt}} \exp\left(-\frac{(x - vt)^2}{4Dt}\right), \quad (2)$$

with similarity variable $x - vt$, where the first moment $\langle x(t) \rangle = \int_{-\infty}^{\infty} xG(x, t)dx = vt$ and the mean squared displacement (MSD) $\langle [x(t) - \langle x(t) \rangle]^2 \rangle = 2Dt$ are linear at all times. The latter does not depend on v . The alternatively used mobile–immobile model (MIM) is a more elaborate model that takes pores into account, where a tracer can remain immobile for an exponentially random duration [3–5]. This linear first order mass transfer is often used to model sorbing solutes, as well [6–8]. In an MIM the concentration is split into a mobile density $n_{\text{m}}(x, t)$ and an immobile density $n_{\text{im}}(x, t)$. In the mobile state tracers are subject to advection and diffusion in the same way as in the advection–diffusion equation (1). MIMs have been used extensively in geophysical systems [3, 4, 8–18]. Apart from geophysical applications, we mention two other applications,

where motion interrupted by transient immobilisations has been studied. The first application pose biological systems, such as potassium channels in the membrane of living cells [19] and transcription factors [20]. Many systems such as tau proteins [21, 22], synaptic vesicles [23], complexes at the endoplasmic reticulum [24], the drug molecule doxorubicin in silica nanoslits [25] and DNA binding proteins [26–35] may be described in terms of an MIM, in which the residence times in the immobile state are distributed exponentially⁵. The corresponding experiments were conducted in flow cells [26, 32–35] or occur in live biological cells [27–30]. In such cellular systems advection may arise due to the action of molecular motors causing streaming in the cytoplasm [36]. Further examples of systems with advection, where in addition immobilisations occur, include DNA molecules in microfluidic setups and bio sensors [37, 38]. The second application, featuring transient immobilisations concerns charge carriers in semiconductors, where a recent focus lies on exciton diffusion in layered perovskites and transition metal dichalcogenides [39–42]. Often, MIMs are not formulated in terms of mean residence times but with a single rate for mass exchange and a solute capacity coefficient that takes different volumes of the mobile and immobile volume into account [3, 7, 11, 12, 43]. The moments for mobile, immobile and total density of the MIM have been calculated for various initial conditions while including effects of advection and diffusion [6, 7, 13]. We here focus on the densities and MSDs at relevant intermediate time scales and unveil interesting new properties in the transport dynamics. In the short time limit initially mobile tracers behave like free Brownian tracers (2) with an MSD $\sim 2Dt$. At long times the MSD is linear, with the effective diffusivity D_{eff} containing a term proportional to v^2 , that can yield $D_{\text{eff}} > D$ [7, 13]. This is in contrast to the solution (2) of the advection-dispersion equation (1), in which the MSD does not depend on v . Below we provide a physical explanation for how this enhanced effective diffusion coefficient is brought about. Another model often used to describe the motion of tracers with immobile periods is the continuous time random walk (CTRW) [39, 44, 45], for which it was shown that exponential tails emerge in the position density [46] when a drift is present [13, 18, 47–50]. CTRWs have also been analysed for systems with two states, characterised by two waiting time distributions, such that a specific distribution is chosen alternatingly or randomly [51, 52]. A similar approach to modelling motion interrupted by transient immobilisations was studied in [53]. In the present work we consider a MIM in the formulation with mean mobile residence time τ_m and mean immobile residence time τ_{im} similar to our previous work [54] in the absence of a drift. In [54], the mean immobile residence time τ_{im} and mean mobile residence time τ_m are well separated, $\tau_{\text{im}} \gg \tau_m$, corresponding to the one-dimensional motion of tau proteins without advection. At intermediate times $\tau_m \ll t \ll \tau_{\text{im}}$ a Laplace distribution of positions $\text{const} \times \exp(-\text{const}|x|)/2$ with fixed variance was shown to emerge whose prefactor depends on the initial condition, and the MSD of initially mobile tracers displayed a plateau at intermediate times. The main goal of the present work is to analyse how the Laplace distribution and the plateau in the MSD change when advection is added. The transition from the Brownian MSD $2Dt$ at short times to $2D_{\text{eff}}t$ implies a crossover regime, in which the MSD grows faster than linear given our finding $D_{\text{eff}} > D$. In fact, we find a sustained superdiffusive regime with a cubic anomalous diffusion exponent in the MSD at relevant intermediate time scales. For low advection velocities we recover the model from [54]. Therefore, to highlight new features, we focus on high Péclet numbers $\text{Pe} = v^2\tau_m/(2D) \gg 1$. An application of the MIM with a high Péclet number may occur for sufficiently long times in subsurface aquifers, in the hyporheic zone or in microfluidic setups. A specific example is the motion of biomolecules in bio sensors, as schematically depicted in figure 1. The biomolecules are inserted into a flow cell and bind to the surface reversibly [38]. The surface is coated with receptors that specifically bind to the molecule of interest. Only the bound molecules can be detected using e.g. surface plasmon resonance [38]. In our model we assume the detector to be completely covered with receptors and consider concentrations well below saturation.

In the next section we introduce the model equations and show two ways to solve the model. The direct way using Fourier–Laplace transform yields the densities in Laplace space and exact expressions for the MSD. Additionally, we show how to solve the advection-MIM using a subordination approach, that produces a physical explanation for the additional term in D_{eff} due to the variance of times the tracers spend in the mobile state. As mentioned in the following, we consider strong advection and obtain asymptotic expressions for the density and the MSD in the presence of a clear time scale separation, i.e. $\tau_m \ll \tau_{\text{im}}$ or $\tau_{\text{im}} \ll \tau_m$. For clarity we focus on the detailed behaviour of the MSD of the total density, while the results for the immobile and mobile fractions are summarised in the appendix. The dimensionless form of the model depends on the ratio τ_{im}/τ_m and the Péclet number only. We use these variables in a phase diagram to analyse the anomalous diffusion in the full parameter space including small Péclet numbers. Specifically, in section 2, we formulate and solve our model. In section 3 we consider tracers that are initially mobile and obtain asymptotic

⁵ We use the term ‘residence times’ in the mobile or immobile state to avoid confusion with the waiting times in a continuous time random walk.



expressions of the density functions and MSDs. Special focus is put on finding the parameter regimes where non-Gaussian displacement distributions and anomalous scaling of the MSD emerge. In section 4 we repeat the same analysis for initially immobile tracers. Finally, we summarise and conclude in section 5. The appendix provides details on the calculations and additional figures of the MSDs.

2. Formulation of the model

We employ the MIM with mean mobile residence time τ_m and mean immobile residence time τ_{im} in an (effectively) one-dimensional setting with position variable x ,

$$\begin{aligned}\frac{\partial}{\partial t} n_m(x, t) &= -\frac{1}{\tau_m} n_m(x, t) + \frac{1}{\tau_{im}} n_{im}(x, t) - v \frac{\partial}{\partial x} n_m(x, t) + D \frac{\partial^2}{\partial x^2} n_m(x, t) \\ \frac{\partial}{\partial t} n_{im}(x, t) &= -\frac{1}{\tau_{im}} n_{im}(x, t) + \frac{1}{\tau_m} n_m(x, t),\end{aligned}\quad (3)$$

where $n_m(x, t)$ and $n_{im}(x, t)$ denote the line densities of mobile and immobile tracers, respectively. Advection with velocity v and dispersion with diffusion constant D is exclusively affecting the mobile density. A single tracer switches between the mobile state and immobile state following a two state continuous time Markov process, i.e. it follows a Poissonian switching. The realisation (3) of the MIM corresponds to the model used in [54] with the residence time distribution in the mobile state $\gamma(\tau) = \exp(-\tau/\tau_m)/\tau_m$. We add a drift in the mobile state here and will show that this has significant consequences. Splitting the total density $n_{tot}(x, t) = n_m(x, t) + n_{im}(x, t)$ has the advantage that not always $n_{tot}(x, t)$ is measured in experiments. In a biophysics sensor as sketched in [38], solely the immobile tracers can be measured. In contrast, it is often the mobile density that is measured in geological experiments [12, 18]. In both cases it is thus essential to model the two densities separately. Step or delta injection into the mobile domain is common in geological experiments [10, 12, 55–57]. Our model (3) is very similar to the MIMs used in geoscience, with the difference that there usually the capacity coefficients and porosity, among others, are used instead of the mean residence times [6, 7, 13]. We consider the initial condition $n_m(x, 0) = f_m^0 \delta(x)$ and $n_{im}(x, 0) = f_{im}^0 \delta(x)$ where $\delta(x)$ denotes the Dirac- δ distribution. The factors f_m^0 and f_{im}^0 denote the fractions of initially mobile and immobile tracers with $f_m^0 + f_{im}^0 = 1$, which effects the normalisation of the total density, $\int_{-\infty}^{\infty} n_{tot}(x, t) dx = 1$. This corresponds to a single-particle picture with no interactions between the tracers, as is the case in model (3). In this work we consider the cases when all tracers are either initially mobile ($f_m^0 = 1$) or when all tracers are immobile ($f_{im}^0 = 1$). We briefly discuss an equilibrium fraction of initially mobile tracers in appendix K. Other mixed initial conditions are comparatively uninteresting and do not correspond to the experimental initial conditions we have in mind. The structure of this section is as follows. In section 2.1 solutions are derived using Fourier–Laplace transforms. The solution using a subordination approach is shown in section 2.2. In section 2.3 it is demonstrated that the dimensionless formulation of the model (3) model depends on two parameters only. Finally, we discuss the short- and long-time behaviour in sections 2.4 and 2.5.

2.1. Solution in Laplace space

Fourier–Laplace transform $f(k, s) \equiv \int_{-\infty}^{\infty} \int_0^{\infty} f(x, t) \exp(-st + ikx) dt dx$ of the model equations (3) allows solving for the densities, as shown in appendix A. Subsequent Fourier inversion of equations (A.2) and (A.3) produces the expressions

$$n_m(x, s) = \left(f_m^0 + f_{im}^0 \frac{1}{1 + s\tau_{im}} \right) \frac{\exp\left(\frac{vx}{2D}\right)}{\sqrt{\nu^2 + 4\phi(s)D}} \exp\left(-\sqrt{\nu^2 + 4\phi(s)D} \frac{|x|}{2D}\right) \quad (4)$$

$$n_{im}(x, s) = \frac{\tau_{im}/\tau_m}{1 + s\tau_{im}} \left(f_m^0 + f_{im}^0 \frac{1}{1 + s\tau_{im}} \right) \frac{\exp\left(\frac{vx}{2D}\right)}{\sqrt{\nu^2 + 4\phi(s)D}} \exp\left(-\sqrt{\nu^2 + 4\phi(s)D} \frac{|x|}{2D}\right) + f_{im}^0 \frac{\tau_{im}}{1 + s\tau_{im}} \delta(x) \quad (5)$$

as well as (see equation (A.4))

$$n_{tot}(x, s) = \frac{f_m + f_{im}^0 \frac{1}{1 + s\tau_{im}}}{s} \frac{\phi(s) \exp\left(\frac{vx}{2D}\right)}{\sqrt{\nu^2 + 4\phi(s)D}} \exp\left(-\sqrt{\nu^2 + 4\phi(s)D} \frac{|x|}{2D}\right) + f_{im}^0 \frac{\tau_{im}}{1 + s\tau_{im}} \quad (6)$$

with $\phi(s) = s[1 + \tau_{im}\tau_m^{-1}(1 + s\tau_{im})]$. The fraction $f_m(t) = \int_{-\infty}^{\infty} n_m(x, t) dx$ of free and the fraction $f_{im}(t) = \int_{-\infty}^{\infty} n_{im}(x, t) dx$ of immobile tracers are a function of time and the expressions are given in equation (A.8) in appendix A. From these relations we immediately deduce that the total density is normalised, $f_m(t) + f_{im}(t) = 1$. In the long-time limit, the equilibrium fraction $f_m^{eq} = \tau_m/(\tau_m + \tau_{im})$ of all tracers are mobile. We calculate the p th moment ($p \in \mathbb{N}$) using

$$\langle x^p(t) \rangle_j = \frac{1}{f_j(t)} \int_{-\infty}^{\infty} x^p n_j(x, t) dx, \quad (7)$$

where j stands for m , im , or tot [54]. To shorten the notation, we use $\langle x^2(t) \rangle = \langle x^2(t) \rangle_{tot}$ in the remainder of this work. The lengthy exact expressions for the MSD are given in appendix B. We will study their detailed behaviour below and in sections 3 and 4 for specific initial conditions. The first moment $\langle x(t) \rangle$ is related to the second moment $\langle x^2(t) \rangle_0$ in the advection-free setting with the second Einstein relation [58]

$$\langle x(t) \rangle = \frac{\nu}{2D} \langle x^2(t) \rangle_0. \quad (8)$$

This relation becomes obvious when we look at the moments in appendix B. Since $\langle x^2(t) \rangle_0$ was discussed in [54] in detail, we focus on the MSD here.

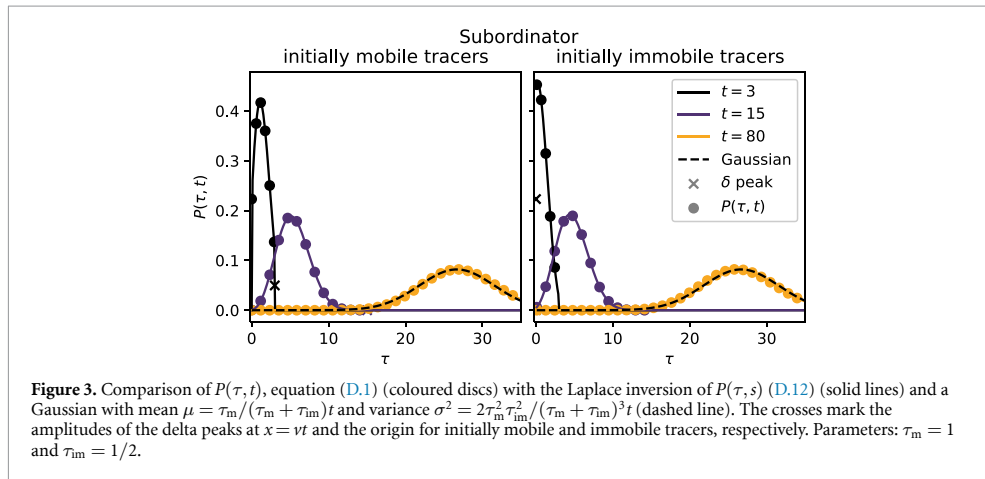
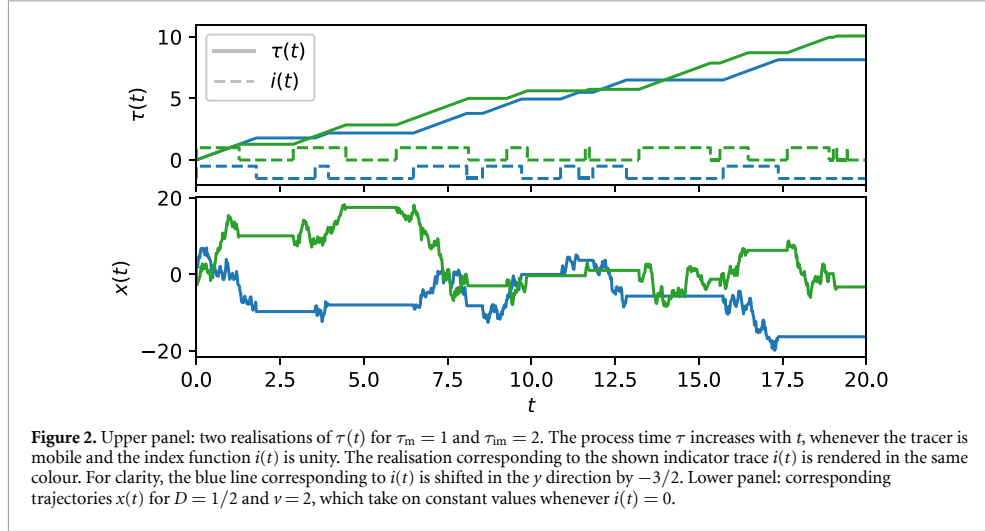
2.2. Subordination approach

The concept of subordination was originally introduced by Bochner [59] and refers to a process $X[\tau(t)]$ with the operational time τ (in many random walk contexts the number of jumps [44]), which has random non-negative increments. For the operational time τ the propagator is known, in our case the Gaussian $G(x, \tau)$ (2). Then, the subordinator relates the stochastic increases of τ to the process (laboratory) time t measured in the real-world observation. In our model the stochasticity comes from the immobilisations, where t increases even while τ is stalling. Assume that we know of a single tracer when it is mobile and when it is immobile. Let $i(t)$ be the index function that is unity if the tracer is mobile at time t and zero otherwise, as shown in figure 2. The index function follows a two-state continuous-time Markov process (telegraph process) with mean residence time τ_m in state 1 and mean residence time τ_{im} in state 0. As described in [60–62] (compare also [63]), this allows us to write a Langevin equation of the form

$$\frac{d}{d\tau} x(\tau) = \nu + \sqrt{2D} \xi(\tau) \quad (9)$$

$$\frac{d}{dt} \tau(t) = i(t), \quad (10)$$

with the operational time τ , that is a random quantity, and zero-mean white Gaussian noise with correlation $\langle \xi(\tau) \xi(\tau + \Delta\tau) \rangle = \delta(\Delta\tau)$. Figure 2 shows two samples of $\tau(t)$ for $\tau_m = 1$ and $\tau_{im} = 2$ in the upper panel. The lower panel shows the corresponding trajectory $x(t)$ for $D = 1/2$ and $\nu = 2$. The propagator with this new variable τ is given by $G(x, \tau)$ (2). In appendix D we show how to obtain the subordinator $P(\tau, t)$ and its moments using Laplace transforms. In figure 3 we show the numerical Laplace inversion of $P(\tau, s)$ (D.12) for three values of t and the parameters $\tau_m = 1$ and $\tau_{im} = 1/2$. In order to verify our approach, we compare the Laplace inversion to the solution $P(\tau, t)$ obtained in [23], that is presented in appendix D. We find good agreement between the two approaches, as shown in figure 3. In the long-time limit $P(\tau, t)$ converges to a Gaussian with mean $\mu = t\tau_m/(\tau_m + \tau_{im})$ and variance $\sigma^2 = 2\tau_m^2\tau_{im}^2/(\tau_m + \tau_{im})^3 t$, as shown by the dashed



line following a Gaussian with that mean and variance (see the moments above). With $P(\tau, t)$ we can eliminate $\tau(t)$ and find using the well established method of subordination [60–65]

$$n_{\text{tot}}(x, t) = \int_0^\infty P(\tau, t)G(x, \tau)d\tau, \quad (11)$$

where $G(x, t)$ denotes the propagator (18) in the mobile phase. Expression (11) can be written in the form (6) of $n_{\text{tot}}(x, s)$ by inserting the subordinator $P(\tau, s)$ in Laplace space. In appendix D we show how to obtain $n_m(x, t)$ and $n_{im}(x, t)$ in a similar way.

2.3. Dimensionless form

Our model (3) has the four parameters τ_m, τ_{im}, ν and D . We now show that in a dimensionless form the model depends only on two free parameters, which significantly reduces the space of parameters we need to consider in order to obtain a full picture of the model. Moreover, this highlights the conceptual simplicity of the model. To this end, we define the new dimensionless variables $t' = t/\tau_m$ and $x' = x/\sqrt{D\tau_m}$. In these variables the model (3) turns into the set of equations

$$\begin{aligned} \frac{\partial}{\partial t'} n_m(x', t') &= -n_m(x', t') + \frac{\tau_m}{\tau_{im}} n_{im}(x', t') \\ &\quad - \sqrt{2\text{Pe}} \frac{\partial}{\partial x'} n_m(x', t') + \frac{\partial^2}{\partial x'^2} n_m(x', t') \end{aligned} \quad (12)$$

$$\frac{\partial}{\partial t} n_{\text{im}}(x', t') = -\frac{\tau_{\text{m}}}{\tau_{\text{im}}} n_{\text{im}}(x', t') + n_{\text{m}}(x', t'), \quad (13)$$

which only depends on the immobilisation ratio $\tau_{\text{im}}/\tau_{\text{m}}$ and the Péclet number $\text{Pe} = v^2 \tau_{\text{m}}/(2D)$. The typical length scale for the latter is given by $v\tau_{\text{m}}$. The factor 1/2 in the Péclet number is introduced for convenience. To see this, we note that from the Péclet number we obtain the advection time scale $\tau_v = 2D/v^2$, which naturally arises from the solution to the advection-diffusion equation (2) as follows. The typical distance travelled due to advection and dispersion is given by $\Delta x_v = vt$ and $\Delta x_D = \sqrt{2Dt}$, respectively. Comparing these distances gives the time scale $\tau_v = 2D/v^2 = \tau_m/\text{Pe}$, after which displacements due to advection dominate over diffusive displacements.

2.4. Short-time behaviour

In the mobile phase tracers are being propagated with the Gaussian (2). As described above the displacements are diffusion dominated for $t \ll \tau_v$. This means that the tracers follow the same density as in the case without advection, which is described in detail in [54]. To emphasise the effects of advection we therefore choose $\tau_v \ll \tau_{\text{m}}, \tau_{\text{im}}$. This defines the short-time limit $t \ll \tau_v$.

2.5. Long-time asymptote

The densities of the total, mobile and immobile density are, up to a factor, the same in the long-time limit $t \gg \tau_{\text{m}}, \tau_{\text{im}}$ [5]. In absence of advection, the effective long-time diffusivity is given by $D_{\text{eff}} = D\tau_{\text{m}}/(\tau_{\text{m}} + \tau_{\text{im}})$ for $t \gg \tau_{\text{m}}, \tau_{\text{im}}$ [54]. Tracers disperse slower compared to the model of simple diffusion advection without immobilisation (1) with diffusivity D . We now obtain D_{eff} by analysing the asymptotic behaviour $t \gg \tau_{\text{m}}, \tau_{\text{im}}$ of the expressions for the MSD. The exact expressions for the first and second moments are stated in appendix B. These results provide the long-time asymptote of the MSD for all initial conditions, namely,

$$\langle [x(t) - \langle x(t) \rangle]^2 \rangle \sim 2 \left(D \frac{\tau_{\text{m}}}{\tau_{\text{m}} + \tau_{\text{im}}} + \frac{v^2 \tau_{\text{m}}^2 \tau_{\text{im}}^2}{(\tau_{\text{m}} + \tau_{\text{im}})^3} \right) t, \text{ for } t \gg \tau_{\text{m}}, \tau_{\text{im}}, \quad (14)$$

where \sim denotes asymptotic equivalence with an additional spread $\propto v^2 t$ compared to the case without advection. Remarkably, the asymptotic dispersion with the new effective diffusion coefficient

$$D_{\text{eff}} = D \frac{\tau_{\text{m}}}{\tau_{\text{m}} + \tau_{\text{im}}} + v^2 \frac{\tau_{\text{m}}^2 \tau_{\text{im}}^2}{(\tau_{\text{m}} + \tau_{\text{im}})^3} \quad (15)$$

can hence even be higher than the diffusivity D in the mobile state and overcompensate the slow-down of the spread due to immobile durations. In appendix H we explore the parameter regime that yields $D_{\text{eff}} > D$. As shown in figure H1, the increase of D_{eff} is highest, when τ_{m} and τ_{im} are of the same order. A physical intuition for the additional spread due to advection arises from the special case $D = 0$, for which $x = v\tau$ with the mobile duration τ . Due to the stochastic switching between the mobile and immobile state, an ensemble of tracers will have a distribution of mobile durations τ (the density $P(\tau, t)$ in section 2.2), and hence the positions will have a finite spread. This additional spread was derived before [6, 13], albeit without a more detailed physical justification. The anomalous transport regime at intermediate times that necessarily has to exist to effect the crossover between the two normal-diffusive regimes, and the important physical consequences will not be explained⁶. We explore the physical mechanism behind the additional dispersion due to advection in the long-time asymptote (14) of the MSD. We start by discretising the advection-diffusion process into discrete steps Δx_i that are normally distributed $\Delta x_i \stackrel{\text{d}}{=} \mathcal{N}(v\Delta t, 2D\Delta t)$, where each step takes a small duration $\Delta t \ll t, \tau_{\text{m}}, \tau_{\text{im}}$. After n steps the tracer position is given by $\sum_{i=1}^n \Delta x_i = x$. In the long-time limit the number of steps n follows a Gaussian $n \stackrel{\text{d}}{=} \mathcal{N}(\mu/\Delta t, \sigma^2/(\Delta t)^2)$, as described in section 2.2⁷. The number of steps n is independent of the steps Δx_i . With the expectation value \mathbb{E} and the variance var we obtain the expression [66]

$$\text{var}(x) = \mathbb{E}(n)\text{var}(\Delta x_i) + (\mathbb{E}(\Delta x_i))^2 \text{var}(n) \sim 2 \left(D \frac{\tau_{\text{m}}}{\tau_{\text{m}} + \tau_{\text{im}}} + \frac{v^2 \tau_{\text{m}}^2 \tau_{\text{im}}^2}{(\tau_{\text{m}} + \tau_{\text{im}})^3} \right) t, \quad (16)$$

⁶ Later we will demonstrate that the transient anomalous diffusion regime can assume substantial time spans with an approximately constant anomalous diffusion exponent.

⁷ The Gaussian distribution $n \stackrel{\text{d}}{=} \mathcal{N}(\mu/\Delta t, \sigma^2/(\Delta t)^2)$, that only applies in the long-time limit, in principle allows for negative numbers of steps. However, they asymptotically vanish, because the width of the distribution vanishes compared to the mean. We quantify this using the coefficient of variation of step numbers $\sqrt{\text{var}(n)}/\mathbb{E}(n) \sim \tau_{\text{im}}(\tau_{\text{im}} + \tau_{\text{m}})^{-1/2} t^{-1/2} \rightarrow 0$ for $t \gg \tau_{\text{m}}, \tau_{\text{im}}$. Note that here $\stackrel{\text{d}}{=}$ means equivalence in distribution.

for $t \gg \tau_m, \tau_{im}$. Equation (16) demonstrates that in the case of diffusion without advection only the mean mobile duration affects the MSD. In contrast, advection couples to the mean in the first moment and to the variance of the duration that the tracers spend in the mobile state in the MSD (14).

All time scales in the model are finite, and therefore the density converges to the Gaussian

$$n_{\text{tot}}(x, t) \sim \frac{1}{\sqrt{4\pi D_{\text{eff}}t}} \exp\left(-\frac{(x - v_{\text{eff}}t)^2}{4D_{\text{eff}}t}\right) \quad \text{for } t \gg \tau_m, \tau_{im} \quad (17)$$

in the long-time limit with the effective diffusion coefficient D_{eff} (equation (15)) and the effective advection velocity $v_{\text{eff}} = v\tau_m/(\tau_m + \tau_{im})$ (see appendix B.1). In the next two sections we analyse the densities and MSDs for the specific choice of initially mobile and immobile tracers, respectively.

3. Initially mobile tracers

In this section we assume all tracers to be initially mobile. This situation corresponds to many experimental realisations, when tracers are introduced into the system, such that they have not had a chance to immobilise. We consider the following four aspects. In section 3.1 we assume $\tau_v \ll \tau_m \ll \tau_{im}$, which corresponds to a high Péclet number and long immobilisations to emphasise the effect of advection compared to [54]. In section 3.2 we consider the density for short immobilisations and high Péclet numbers, $\tau_v \ll \tau_{im} \ll \tau_m$. The third section 3.3 is concerned with the MSD for which we obtain expressions for superdiffusion at intermediate time scales arising due to advection. In the final subsection appendix I.1 we analyse for which parameters the uncovered superdiffusive regime exists and how it is competing with the plateau regime in the MSD found in [54] for long immobilisations in the advection-free regime.

3.1. Densities for long immobilisations

Initially mobile tracers that have not yet immobilised follow a Gaussian distribution corresponding to free Brownian motion without advection for $t \ll \tau_m$. At short times $t \ll \tau_v$ advection is negligible in the Gaussian propagator and the density is the same Gaussian with mean $vt \ll \sqrt{2Dt}$ close to zero and variance $2Dt$. At intermediate times $\tau_v \ll t \ll \tau_m$ advection becomes relevant, and the mobile density takes on the Gaussian form

$$n_m(x, t) \sim \left(1 - \frac{t}{\tau_m}\right) \frac{\exp\left(-\frac{(x-vt)^2}{4Dt}\right)}{\sqrt{4\pi Dt}} \quad (18)$$

with $\int_{-\infty}^{\infty} n_m(x, t) dx \sim 1 - t/\tau_m$ corresponding to a scaled solution of the simple diffusion advection equation (1)⁸. The Gaussian (18) is shown as a dashed red line in the first two panels of figure 4, in which a stacked position histogram from simulations is shown in which the colours denote the number of immobilisation events N_{im} . The solid lines are obtained from Laplace inversion of $n_m(x, s)$, $n_{im}(x, s)$, and $n_{\text{tot}}(x, s)$ from equations (5) and (6). We use the parameters $\tau_m = 1$, $\tau_{im} = 100$, $D = 1/2$ and $v = 100$. These parameters are specifically chosen to be able to resolve the multiple time regimes. In the short to intermediate time regime $t \ll \tau_m, \tau_{im}$, where t can be shorter or longer than τ_v , the immobile density consists of tracers that immobilised at most once. In equation (F.2) in appendix F we arrive at the asymptotic expression

$$n_{im}(x, t) \sim \left[1 + \text{erf}\left(\frac{vt - |x|}{\sqrt{4Dt}}\right) + \exp\left(\frac{v|x|}{D}\right) \left(\text{erf}\left(\frac{vt + |x|}{\sqrt{4Dt}}\right) - 1\right)\right] \times \frac{\exp\left(\frac{vx - v|x|}{2D}\right)}{2v\tau_m} \quad (19)$$

for $t \ll \tau_m, \tau_{im}$. The mass corresponding to (19) is $\int_{-\infty}^{\infty} n_{im}(x, t) dx \sim t/\tau_m$, corresponding to 10^{-3} in the left panel of figure 4. This value is very small and hence the immobile density is not visible in the first panel.

The immobile density in figure 4 appears to be uniform at $t = 0.1$. Indeed, for $\tau_v \ll t$ the short-time density (19) approaches a uniform distribution. Using the properties of the error function we arrive at the asymptotic uniform distribution

$$n_{im}(x, t) \sim \begin{cases} \frac{1}{\tau_m v} & \text{for } 0 < x < vt \\ 0 & \text{otherwise} \end{cases}, \quad (20)$$

⁸ Equation (18) can be obtained by solving equation (3) for $\tau_m \rightarrow \infty$.

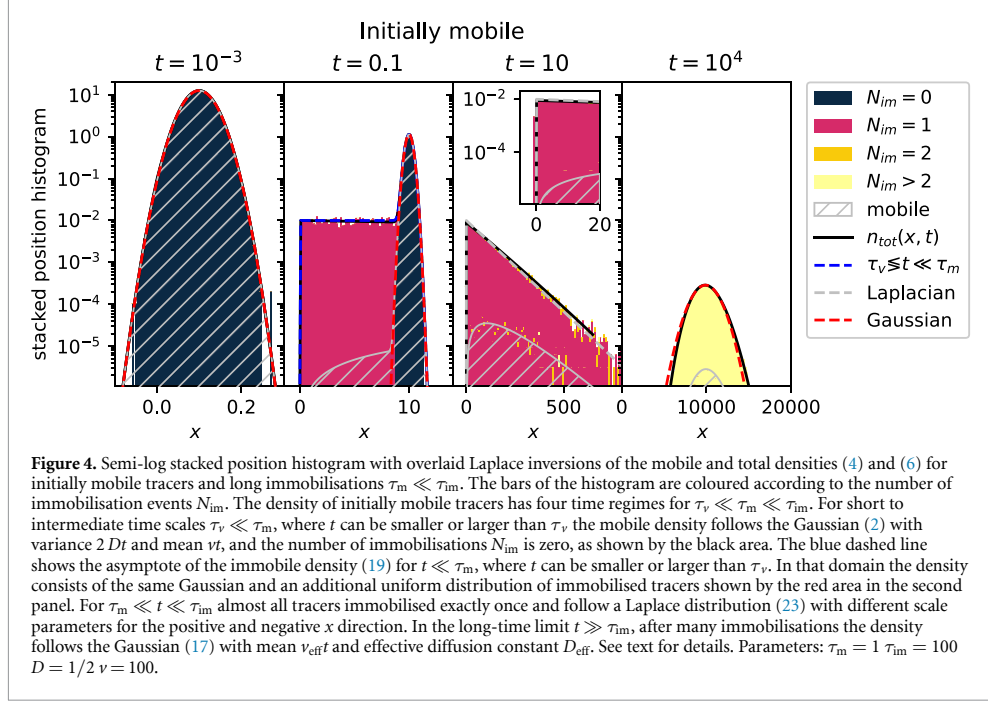


Figure 4. Semi-log stacked position histogram with overlaid Laplace inversions of the mobile and total densities (4) and (6) for initially mobile tracers and long immobilisations $\tau_m \ll \tau_{im}$. The bars of the histogram are coloured according to the number of immobilisation events N_{im} . The density of initially mobile tracers has four time regimes for $\tau_v \ll \tau_m \ll \tau_{im}$. For short to intermediate time scales $\tau_v \ll \tau_m$, where t can be smaller or larger than τ_v the mobile density follows the Gaussian (2) with variance $2Dt$ and mean vt , and the number of immobilisations N_{im} is zero, as shown by the black area. The blue dashed line shows the asymptote of the immobile density (19) for $t \ll \tau_m$, where t can be smaller or larger than τ_v . In that domain the density consists of the same Gaussian and an additional uniform distribution of immobilised tracers shown by the red area in the second panel. For $\tau_m \ll t \ll \tau_{im}$ almost all tracers immobilised exactly once and follow a Laplace distribution (23) with different scale parameters for the positive and negative x direction. In the long-time limit $t \gg \tau_{im}$, after many immobilisations the density follows the Gaussian (17) with mean $v_{eff}t$ and effective diffusion constant D_{eff} . See text for details. Parameters: $\tau_m = 1$ $\tau_{im} = 100$ $D = 1/2 v = 100$.

valid for $\tau_v \ll t \ll \tau_m, \tau_{im}$. This shape can indeed be seen in the second panel of figure 4, for which the immobile density remains almost constant for $0 < x < 10$. The approximation (19) is shown as the blue dashed line. In the same panel the Gaussian (18) is shown as the dashed red line. The total density is given by

$$n_{tot}(x, t) \sim \left(1 - \frac{t}{\tau_m}\right) \frac{\exp\left(-\frac{(x-vt)^2}{4Dt}\right)}{\sqrt{4\pi Dt}} + \begin{cases} \frac{1}{\tau_m v} & \text{for } 0 < x < vt \\ 0 & \text{otherwise} \end{cases} \quad (21)$$

for $\tau_v \ll t \ll \tau_m, \tau_{im}$ with $\int_{-\infty}^{\infty} n_{tot}(x, t) dx = 1$. The appearance of this regime is new, as compared to the case without advection [54]. A physical picture for the occurrence of the uniform density of immobile tracers is as follows. For $\tau_v \ll t \ll \tau_m$ advective transport dominates over diffusion. Indeed, the typical distance a tracer moved due to advection is given by the mean position vt , while the typical distance travelled due to diffusion is given by the standard deviation $\sqrt{2Dt}$. The mobile tracers hence move with a narrow Gaussian distribution while a fraction of tracers immobilises with the constant rate $1/\tau_m$, which generates the uniform part of the distribution (see figure 4 for $t = 0.1$).

Now we go to immobilisation dominated intermediate times $\tau_m \ll t \ll \tau_{im}$. This regime is easy to analyse when starting from the density in Laplace space. We have $\phi(s) \sim 1/\tau_m$ for $s\tau_m \ll 1 \ll s\tau_{im}$ and find the expression

$$n_{tot}(x, s) \sim \frac{1}{s} \frac{\exp\left(\frac{vx}{2D}\right)}{\sqrt{v^2\tau_m^2 + 4D\tau_m}} \exp\left(-\sqrt{v^2 + 4D/\tau_m} \frac{|x|}{2D}\right) \quad (22)$$

from $n_{tot}(x, s)$ (6), which in time-domain corresponds to

$$n_{tot}(x, t) \sim \frac{\exp\left(\frac{vx}{2D}\right)}{\sqrt{v^2\tau_m^2 + 4D\tau_m}} \exp\left(-\sqrt{v^2\tau_m^2 + 4D\tau_m} \frac{|x|}{2D\tau_m}\right), \quad (23)$$

for $\tau_m \ll t \ll \tau_{im}$. Expression (23) is a normalised distribution with time-independent parameters, that falls off exponentially in the positive and negative x direction with different coefficients. It is shown in the third panel in figure 4 for $t = 10$ as the grey dashed line. The density falls off quicker in the direction opposite to the advection velocity, as expected. Noteworthy, the Laplace distribution occurs for all values of the Péclet number, i.e. v can take on any value in the asymptote (23).

For long times $t \gg \tau_{\text{im}}$, we show the Gaussian (17) in figure 4 as a red dashed line for $t = 10^4$. The Gaussian (17) contains the effective advection $v_{\text{eff}} = v\tau_{\text{m}}/(\tau_{\text{m}} + \tau_{\text{im}})$ and the effective diffusivity (15), that we obtained in section 2.5.

3.2. Densities for short immobilisations

Now we turn to the case of short mean immobile residence times, $\tau_{\text{im}} \ll \tau_{\text{m}}$. For short times $t \ll \tau_{\text{v}}$ and intermediate times $\tau_{\text{v}} \ll t \ll \tau_{\text{im}} \ll \tau_{\text{m}}$ the mobile density follows the same Gaussian (18) as for long immobilisations. This can be seen in figure 5 in the first panel for $t = 0.1$. From simulations, we obtain position histograms that we colour-code according to the number of immobilisations. Most tracers have not immobilised at this time, as shown by the dominant black area that follows the Gaussian (18). The tracers that did immobilise follow the same asymptote (19) of $n_{\text{im}}(x, t)$ as for long immobilisations, as depicted by the dashed blue line. Beyond τ_{im} immobile tracers become mobile again and contribute to the mobile density. This can be seen in figure 5 in the second panel for $t = 1$ by the red area in the mobile density denoting tracers with a single immobilisation event. In figure 5, the total density appears to have an exponential tail in the opposite direction of the advection velocity for $t = 10$ and $t = 20$ in the third and fourth panel, respectively. We now investigate the origin of this phenomenon. For $t \ll \tau_{\text{m}}$, the fraction t/τ_{m} of mobile tracers is trapped for a short period τ drawn from $\gamma(\tau) = \exp(-\tau/\tau_{\text{im}})/\tau_{\text{im}}$. This is shown as the red area in figure 5 denoting a single immobilisation. Hence, these tracers were mobile for a total period of $t - \tau$. We convolute this with the propagator for advection diffusion. Together with tracers that have not immobilised this gives the total density for $\tau_{\text{m}} \ll t \ll \tau_{\text{im}}$,

$$n_{\text{tot}}(x, t) \sim \left(1 - \frac{t}{\tau_{\text{m}}}\right) \frac{\exp\left(-\frac{(x-vt')^2}{4Dt'}\right)}{\tau_{\text{m}}\sqrt{4\pi Dt'}} + \frac{t}{\tau_{\text{m}}} \int_0^t \frac{\exp\left(-\frac{(x-vt')^2}{4Dt'}\right)}{\tau_{\text{im}}\sqrt{4\pi Dt'}} e^{-(t-t')/\tau_{\text{im}}} dt'. \quad (24)$$

The integral on the right-hand side can be solved and is given by

$$\int_0^t \frac{\exp\left(-\frac{(x-vt')^2}{4Dt'}\right)}{\tau_{\text{im}}\sqrt{4\pi Dt'}} e^{-(t-t')/\tau_{\text{im}}} dt' \sim \frac{\exp\left(-\frac{t}{\tau_{\text{im}}}\right)}{2v\tau_{\text{im}}} \left[\exp\left(\frac{x}{v\tau_{\text{im}}}\right) \text{erfc}\left(\frac{x-tv}{2\sqrt{Dt}}\right) - \exp\left(\frac{vx}{D}\right) \text{erfc}\left(\frac{x+vt}{2\sqrt{Dt}}\right) \right], \quad (25)$$

for $v^2\tau_{\text{im}} \gg D$ with the complimentary error function $\text{erfc}(x) = 1 - \text{erf}(x)$. In appendix G we develop the full expression of the integral (25), that is also valid for $v^2\tau_{\text{im}} \sim D$, i.e. intermediate Péclet numbers. Approximation (24) is shown in figure 5 as the dashed dark-yellow line and follows the density for $x > 70$ at $t = 10$ and matches almost the entire density at $t = 20$. For $x \ll vt$ and $v^2\tau_{\text{im}} \gg D$ expression (24) simplifies to

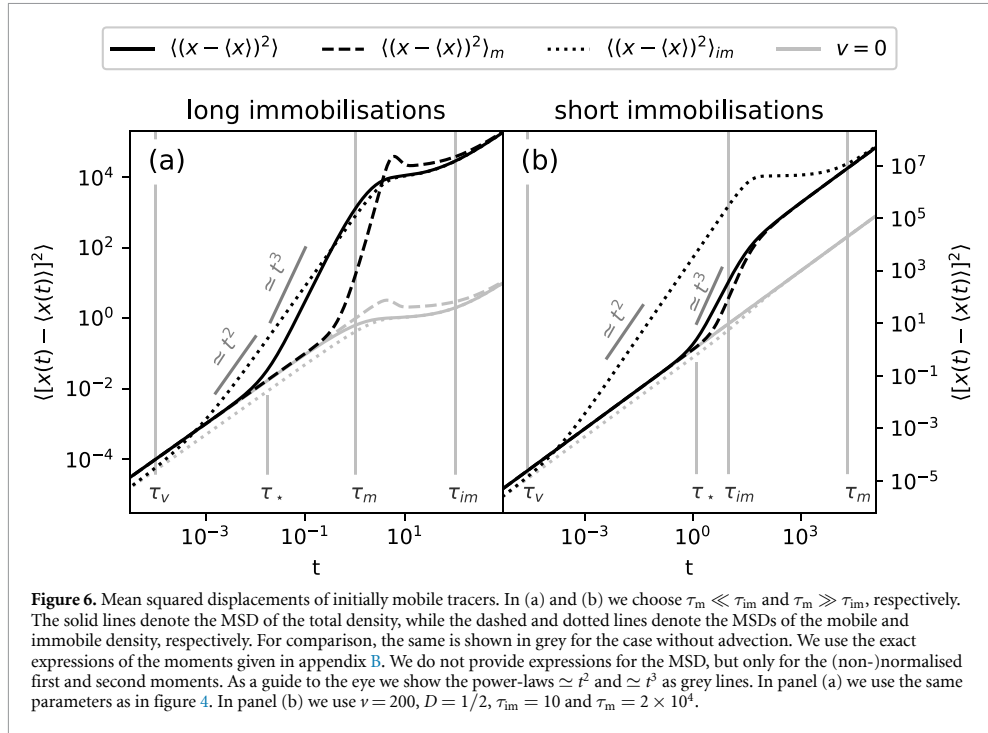
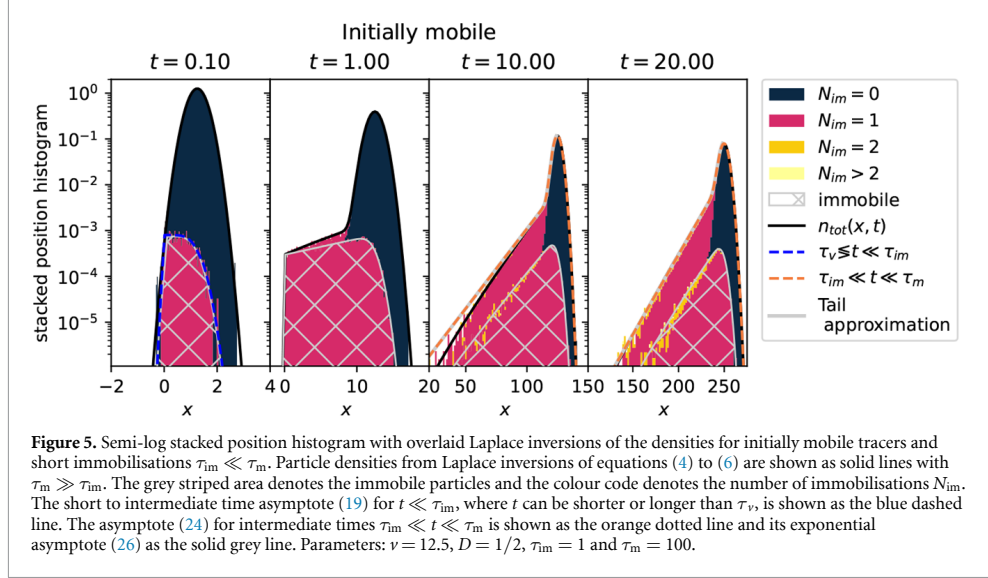
$$n_{\text{tot}}(x, t) \sim \frac{t}{\tau_{\text{m}}} \frac{\exp\left(-\frac{t}{\tau_{\text{im}}} + \frac{x}{v\tau_{\text{im}}}\right)}{v\tau_{\text{im}}}, \quad \text{for } \tau_{\text{im}} \ll t \ll \tau_{\text{m}} \text{ and } 0 < x \ll vt. \quad (26)$$

This tail approximation is only valid close the origin. For this reason it is not normalised. It is shown in figure 5 as the solid grey line. The tail overlaps with expression (24) shown as the dashed dark-yellow line. The second exponent in expression (26) reveals that the slope of the tail does not depend on time. The slope decreases for larger values of τ_{im} . As described in detail in section 2.5 the long-time asymptote $t \gg \tau_{\text{m}}$ of the density follows a Gaussian with an effective advection speed and an effective diffusivity.

3.3. Mean squared displacement

In this section we analyse the MSD of the total density. In appendices E.1.1 and E.1.2 we analyse the MSD of the immobile and mobile density, respectively. We now investigate how advection changes the MSD as compared to the results presented in [54]. Table C1 shows a series of the total, mobile and immobile MSDs for initially mobile and initially immobile tracers for $t \ll \tau_{\text{m}}, \tau_{\text{im}}$. In all cases, the leading order term does not depend on v . Therefore, for short times the MSDs are equivalent to the MSD without advection.

In figure 6(a) the MSD for initially mobile tracers is shown for long immobilisations, $\tau_{\text{m}} \ll \tau_{\text{im}}$, where the solid black line corresponds to the total density's MSD. In panel (b) we show the MSDs for short immobilisations, $\tau_{\text{im}} \ll \tau_{\text{m}}$. For comparison, we show the MSD for the case without advection in grey. It can be seen that the corresponding MSDs with and without advection overlap for $t \ll \tau_{\text{v}}$. After a linear



short-time behaviour for $t \ll \tau_*$ the MSD crosses over to a cubic scaling for $\tau_* \ll t \ll \tau_m, \tau_{im}$. Our goal is to quantify the cubic scaling and determine the value of τ_* . From a series expansion of the exact expression for the MSD (exact expressions for the moments are given in appendix B), we obtain the asymptotic MSD

$$\langle [x(t) - \langle x(t) \rangle]^2 \rangle \sim 2Dt + \frac{v^2}{3\tau_m} t^3, \text{ for } t \ll \tau_m, \tau_{im}. \quad (27)$$

In figure E2 we compare equation (27) to the full expression of the MSD and find very nice agreement. A cubic scaling of the MSD (27) emerges at intermediate times when the cubic term dominates over the linear term in equation (27). This corresponds to the relation $\tau_* \ll t \ll \tau_m$ with $\tau_* = \sqrt{3}\tau_v\tau_m$. Indeed, the cubic

scaling of the total MSD is shown in figure 6(a) in the domain $\tau_* \ll t \ll \tau_m$. Notably, it occurs also for $\tau_{im} \ll \tau_m$, as shown in figure 6(b). This cubic scaling is new compared to the case without advection. It lies within the domain where we found an advection dominated regime $\tau_v \ll t \ll \tau_m$ in the previous section, in which the density (21) consists of a uniform and a Gaussian distribution with time-dependent weights. In figure E1 we show the MSD and choose such parameters that emphasise that the intermediate cubic scaling can be more than a bare crossover but corresponds to a distinct anomalous regime. We now show that the anomalous diffusion arises from this distribution. First we consider the uniform distribution ranging from zero to vt . It has the first moment $\langle x(t) \rangle_{im} = \frac{vt}{2}$ and the second moment $\langle x(t)^2 \rangle = \frac{v^2 t^2}{3}$ with the MSD $\langle (x(t) - \langle x(t) \rangle)^2 \rangle_{im} = \frac{v^2 t^2}{12}$. This is the dominating term of the immobile density's MSD for $\tau_v \ll t \ll \tau_m, \tau_{im}$, as shown in figures 6(a) and (b), where the quadratic scaling can be observed. Second we recall the first and second moments of the mobile Gaussian distribution $\langle x(t) \rangle_m = vt$ and $\langle x(t)^2 \rangle = v^2 t^2 + 2Dt$. Now we consider the MSD of the total density by combining the moments with the normalisations t/τ_m and $1 - t/\tau_m$ for the uniform and Gaussian distribution, respectively. This leads to the same asymptotic MSD (27), as obtained by the series expansion, as the following calculation shows:

$$\begin{aligned} \langle x(t) \rangle &= \langle x(t) \rangle_{im} \frac{t}{\tau_m} + \langle x(t) \rangle_m \left(1 - \frac{t}{\tau_m}\right) = vt - \frac{vt^2}{2\tau_m} \\ \langle x(t)^2 \rangle &= \langle x(t)^2 \rangle_{im} \frac{t}{\tau_m} + \langle x(t)^2 \rangle_m \left(1 - \frac{t}{\tau_m}\right) = -\frac{2}{3} \frac{v^2 t^3}{\tau_m} + v^2 t^2 - 2D \frac{t^2}{\tau_m} + 2Dt \\ \langle [x(t) - \langle x(t) \rangle]^2 \rangle &= 2Dt - 2D \frac{t^2}{\tau_m} + \frac{v^2 t^3}{3\tau_m} - \frac{v^2 t^4}{4\tau_m^2} \\ &\sim 2Dt + \frac{v^2}{3\tau_m} t^3, \text{ for } t \ll \tau_m \ll \tau_{im}. \end{aligned} \quad (28)$$

The asymptotic expression is identical to what we found from the exact expressions (27). This shows indeed that the uniform distribution and the Gaussian distribution can indeed explain the cubic scaling. The cubic scaling of the MSD emerges for $\tau_* \ll t \ll \tau_m, \tau_{im}$. This means that for long immobilisations $\tau_m \ll \tau_{im}$ the advection needs to be sufficiently large such that $\tau_v = 2D/v^2 \ll \tau_m$, as shown in figure 6(a). The cubic scaling emerges for short immobilisations $\tau_{im} \ll \tau_m$, as well. In that case the Péclet number needs to satisfy $Pe \gg 3\tau_m^2/\tau_{im}^2$. In appendix I we discuss the parameter regimes for which cubic scaling emerges in detail.

Now we choose long immobilisations, $\tau_{im} \gg \tau_m$, and consider the intermediate immobilisation dominated regime $\tau_m \ll t \ll \tau_{im}$. In the absence of advection we found a plateau of the total MSD shown as the grey solid line in figure 6(a). Compared to [54] we here choose a high Péclet number, $v^2 \tau_m/2D \gg 1$, and keep the time scale separation $\tau_m \ll \tau_{im}$ here. The plateau still exists at $\tau_m \ll t \ll \tau_{im}$, although at a higher value as shown by the black solid line in figure 6(a). The existence of the plateau comes as no surprise, because the physical mechanism of the plateau remains unchanged. All tracers are initially mobile and have immobilised for $\tau_m \ll t \ll \tau_{im}$, as shown in figure 4 for $t = 10$. When all tracers are immobile the density does not change and hence the MSD remains constant. Analytically, this can be seen most easily from the expressions of the moments in Laplace space

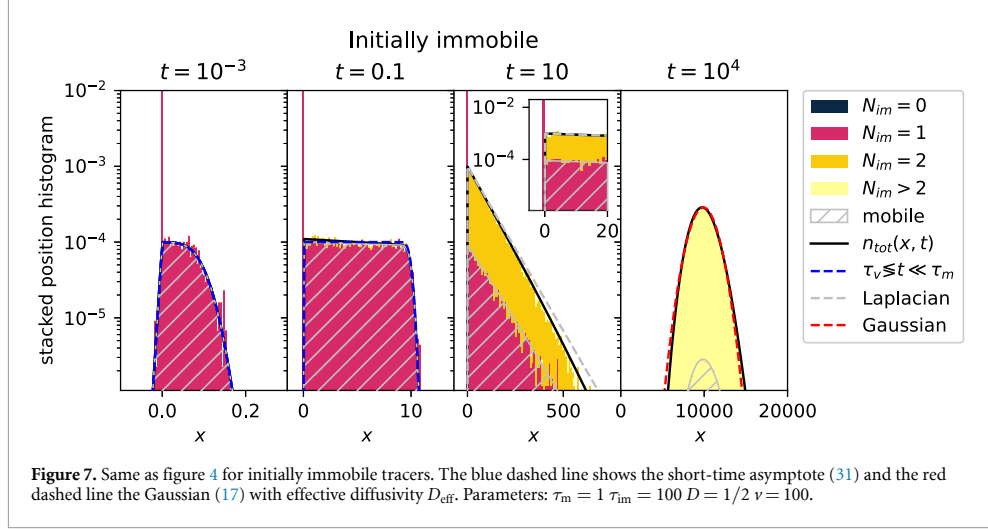
$$\langle x(s) \rangle = \frac{v}{s\phi(s)} \quad (29)$$

$$\langle x^2(s) \rangle = \frac{2v^2}{s\phi^2(s)} + \frac{2D}{s\phi(s)}, \quad (30)$$

that we obtain from expression (A.5). For $\tau_m \ll t \ll \tau_{im}$, we have $\phi(s) \sim 1/\tau_m$, which is a constant. Since the Laplace inverse $\mathcal{L}^{-1}[1/s] = 1$ we obtain a constant MSD in this time-domain $\tau_m \ll t \ll \tau_{im}$, where we observe the asymmetric Laplace distribution (23). We emphasise that the plateau exists regardless of the values of v and D . At long times $t \gg \tau_m, \tau_{im}, \tau_v$ the MSD grows linearly with the effective diffusion coefficient $D_{\text{eff}} = D \frac{\tau_m}{\tau_m + \tau_{im}} + v^2 \frac{\tau_m^2 \tau_{im}^2}{(\tau_m + \tau_{im})^3}$, as described in section 2.5.

4. Initially immobile tracers

In this section we consider initially immobile tracers. Experimentally, this may correspond to the situation when tracers are released into a microfluidic setup and (part of them) allowed to bind to the sensor receptors. Subsequently, the mobile tracers are flushed out, and then the recording is started. In section 4.1 we report the density for long immobilisations, $\tau_m \ll \tau_{im}$, and high Péclet numbers. In section 4.2 we repeat the same steps for short immobilisations, $\tau_{im} \ll \tau_m$. Section 4.3 is concerned with the MSD, and in the



fourth subsection appendix J.1 we analyse for which parameters a cubic scaling of the MSD emerges at intermediate time scales.

4.1. Density for long immobilisations

We assume long immobilisations, $\tau_m \ll \tau_{\text{im}}$, corresponding to the case studied in [54]. We choose a high Péclet number to emphasise the effect of advection, in contrast to the $v = 0$ case in [54]. At short times $t \ll \tau_v$ the propagator for mobile tracers is the same Gaussian as for the case $v = 0$. Therefore, we obtain the same short-time densities as in the $v = 0$ case, i.e. a δ -peak at the origin and an additional non-Gaussian distribution.

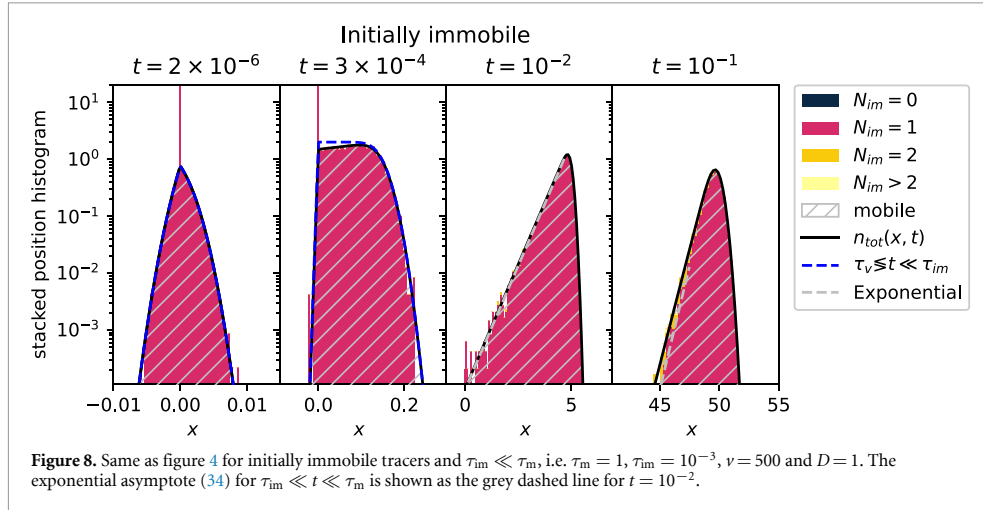
At short to intermediate times, $t \ll \tau_m, \tau_{\text{im}}$, at which t can be shorter or longer than τ_v , most initially immobile tracers are concentrated at the origin and only gradually mobilise. This gives rise to the immobile density $n_{\text{im}}(x, t) \sim (1 - t/\tau_{\text{im}})\delta(x)$. As described in detail in [54], immobile tracers that were initially mobile follow the same density as mobile tracers that were initially immobile, equation (19), up to a factor τ_m/τ_{im} . Therefore, we arrive at the total density for short to intermediate times

$$n_{\text{tot}}(x, t) \sim \left(1 - \frac{t}{\tau_{\text{im}}}\right) \delta(x) + \frac{\exp\left(\frac{vx - v|x|}{2D}\right)}{2v\tau_{\text{im}}} \times \left[1 + \text{erf}\left(\frac{vt - |x|}{\sqrt{4Dt}}\right) + \exp\left(\frac{v|x|}{D}\right) \left(\text{erf}\left(\frac{vt + |x|}{\sqrt{4Dt}}\right) - 1\right)\right] \quad (31)$$

for $t \ll \tau_m, \tau_{\text{im}}$. The asymptote of the second summand corresponding to the mobile density in expression (31) is shown in figure 7 as the blue dashed line, which nicely matches the simulations and the Laplace inversions for $t = 10^{-3}$ and $t = 10^{-1}$. We note that $n_{\text{tot}}(x, t)$ is always normalised, $\int_{-\infty}^{\infty} n_{\text{tot}}(x, t) dx = 1$, by construction. The same arguments as presented for initially mobile tracers explain the uniform density that appears at intermediate time scales for $\tau_v \ll t \ll \tau_m, \tau_{\text{im}}$, corresponding to the second panel in figure 7. In the immobilisation dominated intermediate time domain $\tau_m \ll t \ll \tau_{\text{im}}$ the Laplace distribution with additional δ -peak

$$n_{\text{tot}}(x, t) = \frac{t}{\tau_{\text{im}}} \frac{\exp\left(\frac{vx}{2D}\right)}{\sqrt{v^2\tau_m^2 + 4D\tau_m}} \exp\left(-\sqrt{v^2\tau_m^2 + 4D\tau_m} \frac{|x|}{2D\tau_m}\right) + \left(1 - \frac{t}{\tau_{\text{im}}}\right) \delta(x) \quad (32)$$

emerges with the same scale parameter as for initially mobile tracers (23). The prefactor of the asymmetric Laplace distribution is now t/τ_{im} , and this asymmetric Laplace distribution is shown in figure 7 as the grey dashed line. The long-time limit does not depend on the initial conditions and follows the same density as the initially mobile tracers, equation (17), as shown by the red dashed line in figure 7 at $t = 10^4$.



4.2. Density for short immobilisations

We now consider short immobilisations, $\tau_{im} \ll \tau_m$. At short to intermediate time scales $t \ll \tau_{im} \ll \tau_m$, at which t can be shorter or longer than τ_v , the same expression (31) holds as for long immobilisations. This can be seen in figure 8, where the asymptote (31) is shown as the blue dashed line. We find excellent agreement between the histogram based on the simulations and the density (31) for $t \ll \tau_{im}, \tau_m$, see the first and second panels in figure 8 for $t = 2 \times 10^{-6}$ and $t = 3 \times 10^{-4}$, respectively. In contrast to the case $v = 0$ in [54], a new regime $\tau_{im} \ll t \ll \tau_m$ emerges, that we call *advection induced subdiffusion*. The total density follows an exponential distribution, as can be seen from the linear shape of the density in the semi-log plot for $t = 10^{-2}$. To explain this shape we solve the model equations (3) for the advection induced subdiffusion regime times $t \ll \tau_m$, where t can be longer or shorter than τ_v . This produces the total density

$$n_{tot}(x, t) \sim \delta(x)e^{-t/\tau_{im}} + \int_0^t \frac{e^{-t'/\tau_{im}} \exp\left(-\frac{(x-vt')^2}{4Dt'}\right)}{\tau_{im} \sqrt{4\pi Dt'}} dt', \text{ for } t \ll \tau_m, \quad (33)$$

where the integral is identical to expression (25) for immobile tracers that were initially mobile. We obtain the expression

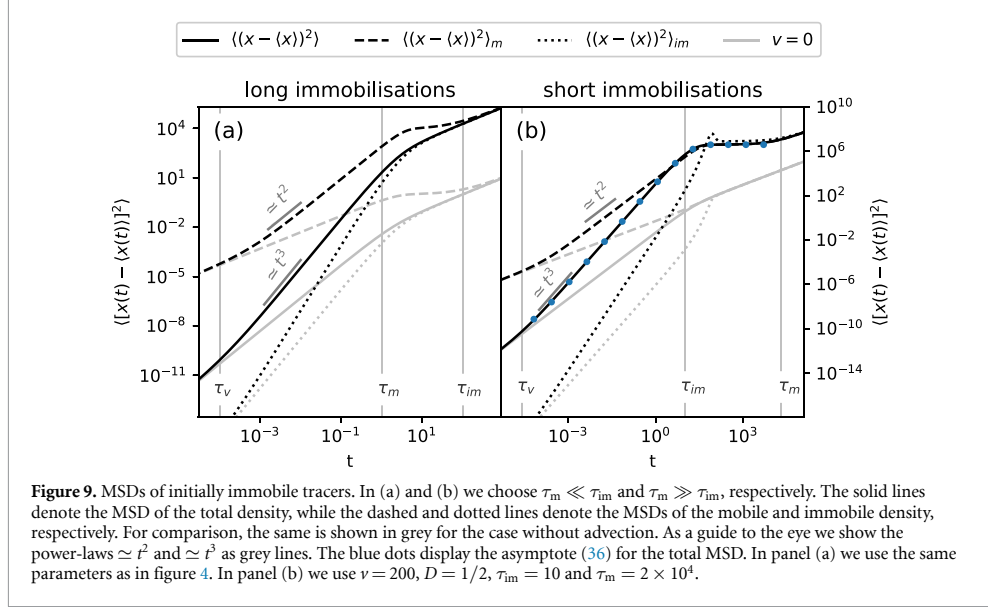
$$n_{tot}(x, t) \sim \delta(x) \exp\left(-\frac{t}{\tau_{im}}\right) + \begin{cases} \frac{1}{v\tau_{im}} \exp\left(\frac{x}{v\tau_{im}} - \frac{t}{\tau_{im}}\right) & \text{for } 0 < x \ll vt \\ 0 & \text{otherwise} \end{cases}, \quad (34)$$

for $v^2\tau_{im} \gg D$ and $t \ll \tau_m$. This comes as no surprise, as in both cases we have the same Gaussian propagator, in which the tracers have varying immobile durations. In the case of initially mobile tracers the immobile duration stems from an immobilisation at $t > 0$. In the present case of initially immobile tracers the immobile duration arises from the slow release at the origin at $t = 0$. In both cases the immobile duration is drawn from an exponential distribution with mean τ_{im} . The first term in (34) corresponds to initially immobile tracers that have not mobilised up to time t . The second term accounts for the slow release with rate $\tau_{im}^{-1} \exp(-t/\tau_{im})$ and motion in the mobile zone with advection only. The exponential distribution (34) is shown in figure 8 at $t = 2 \times 10^{-2}$ as the grey dashed line, and we find good agreement with the Laplace inversion of $n_{tot}(x, s)$ and simulations.

4.3. Mean squared displacement

We now analyse the MSD of the total density. In appendices E.2.1 and E.2.2 we analyse the MSD of the immobile and mobile density, respectively. We show the MSDs for long and short immobilisations in panels (a) and (b) of figure 9, respectively. From a series expansion of the MSD at $t = 0$ we obtain the asymptotic MSD at short to intermediate times,

$$\langle [x(t) - \langle x(t) \rangle]^2 \rangle \sim \frac{Dt^2}{\tau_{im}} + \frac{v^2}{3\tau_{im}} t^3, \text{ for } t \ll \tau_m, \tau_{im}, \quad (35)$$



in which t can be smaller or larger than τ_v . We compare the asymptote (35) to the full expression of the MSD in figure E2(b) and find very nice agreement. At short times $t \ll \tau_v$, the quadratic term dominates and we observe the same MSD as in the case without advection. This can be seen in figures 9(a) and (b). At intermediate times $\tau_v \ll t \ll \tau_m, \tau_{im}$ the cubic term in the asymptotic MSD (35) dominates. As shown in figure 9 the cubic scaling emerges for short and long immobilisations.

Now we go to the case of short immobilisation, $\tau_{im} \ll \tau_m$, for which advection induced subdiffusion emerges for $\tau_{im} \ll t \ll \tau_m$. As described in section 4.2, the total density follows an exponential distribution (34) and a δ -peak at the origin for $\tau_v \ll t \ll \tau_m$. The MSD of that distribution is given by

$$\langle [x(t) - \langle x(t) \rangle]^2 \rangle = v^2 \tau_{im} \left(\tau_{im} - 2t \exp\left(-\frac{t}{\tau_{im}}\right) - \tau_{im} \exp\left(-2\frac{t}{\tau_{im}}\right) \right), \quad (36)$$

for $\tau_v \ll t \ll \tau_m$ and $\tau_{im} \ll \tau_m$, which is shown in figure 9(b) as the blue line. From expression (36) we recover the intermediate time asymptote

$$\langle [x(t) - \langle x(t) \rangle]^2 \rangle \sim \frac{v^2 t^3}{3\tau_{im}}, \quad \text{for } \tau_v \ll t \ll \tau_{im}, \quad (37)$$

implying the same cubic scaling for $\tau_v \ll t \ll \tau_{im}$ as we found from the series expansion of the full MSD (35) for the advection dominated regime. This can be seen in the MSD in figure 9(b). The cubic scaling of the MSD emerges in the domain $\tau_v \ll t \ll \tau_m, \tau_{im}$, which limits the parameters to $\tau_v \ll \tau_m, \tau_{im}$. In terms of the Péclet number this implies $Pe \gg 1$ for long immobilisations $\tau_m \ll \tau_{im}$ and $Pe \gg \tau_m/\tau_{im}$ for short immobilisations $\tau_{im} \ll \tau_m$. A detailed discussion of the parameter regimes and the coexistence of the plateau regime is presented in appendix J.

In the advection induced subdiffusion domain the MSD (36) reaches the plateau value

$$\langle [x(t) - \langle x(t) \rangle]^2 \rangle \sim v^2 \tau_{im}^2, \quad \text{for } \tau_{im} \ll t \ll \tau_m. \quad (38)$$

These two anomalous scaling regimes shown in figure 9(b), namely, the cubic scaling and the plateau behaviour can be explained as follows. For $\tau_v \ll t \ll \tau_{im}$ the MSD grows due to the slow release and fast advection, where the spread due to diffusion is negligible. When all tracers mobilised at $t \gg \tau_{im}$, this spread due to advection vanishes, and the distribution moves along the direction of advection without changing the

Table 1. Main results of anomalous scaling of the MSD. In the second column the short-time asymptotes of the total density's MSD is shown for initially mobile and initially immobile tracers. The cubic term dominates for the time regime given in the third column, with $\tau_v = 2D/v^2$ and $\tau_* = \sqrt{3\tau_v\tau_m}$. In the fourth column the time regimes of the plateaus are given. For initially immobile tracers this advection induced subdiffusion occurs for large Péclet numbers only.

tracers initially	$t \ll \tau_m, \tau_{im}$	cubic regime	plateau regime
mobile	$2Dt + \frac{v^2}{3\tau_m} t^3$	$\tau_* \ll t \ll \tau_m, \tau_{im}$	$\tau_m \ll t \ll \tau_{im}$
immobile	$\frac{D}{\tau_{im}} t^2 + \frac{v^2}{3\tau_{im}} t^3$	$\tau_v \ll t \ll \tau_m, \tau_{im}$	$\tau_{im} \ll t \ll \tau_m$ for $Pe \gg \frac{\tau_m}{\tau_{im}}$

shape significantly. This explains the plateau in the MSD for $\tau_{im} \ll t \ll \tau_m$. We highlight that this advection induced subdiffusion is a new behaviour compared to the case without advection. For comparison, we show the MSD for $v = 0$ in figure 9(b) as the grey solid line. It crosses over from the short-time scaling $\sim Dt^2/\tau_{im}$ to the long-time asymptote $\sim 2D_{eff}t$ without any intermediate regime.

5. Conclusion

We analysed the densities along with the first and second moments of the MIM with exponential Poissonian switching between the mobile and immobile states in the presence of a drift velocity v . The whole dynamic is characterised by the mean mobile duration τ_m , the mean immobile duration τ_{im} and the time scale $\tau_v = 2D/v^2$, which is related to the Péclet number $Pe = \tau_m/\tau_v$. For $t \ll \tau_v$ advection plays a negligible role and the process is diffusion dominated, yielding the same results as in [54], where the diffusion regimes were analysed for the advection-free case. In order to highlight the role of advection we choose $\tau_v \ll \tau_m, \tau_{im}$, for which an advection dominated regime emerges for $\tau_v \ll t \ll \tau_m, \tau_{im}$. Relatively high Péclet numbers can be achieved in microfluidic setups and in certain geophysical systems. The first moment is proportional to the second moment of the advection-free model, as shown by the second Einstein relation. The second moment of the advection-free model has been discussed in detail in [54]. Therefore, we here concentrated on the discussion of the MSD. In general, for any fraction of initially mobile tracers and an arbitrary fraction τ_{im}/τ_m , we found the same long-time behaviour for $t \gg \tau_m, \tau_{im}$. The total density follows a Gaussian with an effective advection speed $v_{eff} = v\tau_m/(\tau_m + \tau_{im})$ and an effective diffusivity $D_{eff} = D\frac{\tau_m}{\tau_m + \tau_{im}} + v^2\frac{\tau_m^2\tau_{im}^2}{(\tau_m + \tau_{im})^3}$. Compared to the advection v in the free phase, v_{eff} is always smaller. The effective diffusivity D_{eff} is always larger than the effective diffusivity in the advection-free case due to the velocity-dependent term. Specifically, for sufficiently high Péclet numbers the effective diffusivity can significantly exceed the diffusivity D in the mobile domain. While D_{eff} was reported before [7, 13], we here provided a physical explanation for the additional dispersion due to the variance of durations the tracers spent in the mobile state.

We analysed two specific initial conditions with fully mobile and fully immobile tracers in detail. For initially mobile tracers the advection dominated regime contains two parts. In the first part, $\tau_v \ll t \ll \tau_* = \sqrt{3\tau_v\tau_m}$, the MSD grows linearly in time. In the second part of the advection-dominated regime, $\tau_* \ll t \ll \tau_m, \tau_{im}$, the MSD grows cubically. This regime is valid for any ratio τ_{im}/τ_m . This can be seen in table 1, where we summarise the main results of the anomalous scaling of the MSD.

For long immobilisations $\tau_{im} \gg \tau_m$ for initially mobile tracers, and in the advection dominated regime, the density consists of a Gaussian shape of mobile tracers plus a spatially uniform distribution of immobilised tracers. At longer times, $\tau_m \ll t \ll \tau_{im}$, we recovered a plateau in the MSD of initially mobile tracers reported in [54], regardless of the presence of advection. In this immobilisation dominated regime the distribution follows an asymmetric Laplace distribution, which decays rapidly in the direction opposite of the advection velocity and falls of slowly in the direction of the advection velocity. In the opposite case of short immobilisations, $\tau_{im} \ll \tau_m$, the total density follows a decreasing Gaussian shape with an increasing exponential tail in the direction opposite of the advection velocity in the whole advection dominated regime $\tau_v \ll t \ll \tau_{im}$. This exponential tail is similar to what was found for CTRWs with advection [46].

For initially immobile tracers the advection-dominated regime emerges, as well. This can be seen in table 1, where the series expansion of the MSD is shown. Here, the cubic scaling of the MSD appears in the whole regime $\tau_v \ll t \ll \tau_m, \tau_{im}$ for any ratio of τ_m/τ_{im} and a sufficiently high Péclet number. This is in contrast to the advection-free case reported in [54], where the MSD is close to the Brownian case for short immobilisations, $\tau_{im} \ll \tau_m$. For such short immobilisations the density follows a growing and drifting exponential distribution with an additional peak of immobile tracers at the origin. For later times, we found an advection induced subdiffusion regime $\tau_{im} \ll t \ll \tau_m$ for high Péclet numbers and short immobilisations.

This regime has not been reported previously. Here, the density consists of an exponential distribution with fixed scale parameters, where the mean is moving at a constant speed. For long immobilisations $\tau_m \ll \tau_{im}$, the density follows a spatially uniform distribution for $\tau_v \ll t \ll \tau_m$. For completeness, we consider an equilibrium fraction of initially mobile tracers in, which naturally occur in experiments, in appendix K, where a ballistic scaling of the MSD emerges at intermediate times.

Now we put our work into some context. A CTRW with an exponential sojourn time distribution with mean τ and a Gaussian displacement density with non-zero mean μ and variance σ^2 was considered in [46]. This model may appear similar to our model with exponentially distributed residence times in the immobile state and advection–diffusion in the mobile state. However, the MSD $\langle [x(t) - \langle x(t) \rangle]^2 \rangle = \sigma^2 t / \tau + \mu^2 t / \tau$ is linear at all times for the CTRW, as shown in appendix L.1. This contrasts the anomalous scaling at intermediate times of the MSD found here. Another formulation of CTRW is the two-state CTRW, in which two transition densities are considered from which steps are drawn in an alternating way [51]. In [51] the long-time asymptotic diffusion coefficient is obtained, which matches our result for a specific choice of parameters. We also mention the case in [52] in which a CTRW is analysed, whose waiting time distribution function is the weighted sum of two exponentials. If one of the exponential distributions has a weight close to unity and a mean that is significantly shorter than τ_m , this model generates the same MSD as the MSD of the total density from the MIM. We stress that the MIM provides additional information in the form of separate mobile and immobile densities. Thus the MIM is not simply the long-space-time limit of the model in [52]. A detailed analysis of the similarities and differences between the MIM and the processes in [51, 52] deserves a separate study.

In contrast to the advection-free case of MIM, where intermittent anomalous diffusion solely arises for mobile tracers for long immobilisations, the anomalous transport behaviours reported here occur for both long and short immobilisations. A condition for this anomalous behaviour is a high Péclet number, which occurs for example in experiments with biomolecules in biosensors [38]. Short immobilisations may occur unintentionally due to unwanted binding to the surface of a flow cell or other experimental boundaries. The resulting transport will be anomalous at intermediate time scales, even if the tracers are only subject to Brownian motion with drift in the mobile state. While the anomalous diffusion and non-Gaussian densities occur at intermediate time scales only, the measurement time is finite in experiments, and the effects may therefore erroneously appear to be an asymptotic phenomenon. In conclusion, we found a variety of anomalous diffusion regimes and non-Gaussian displacement distributions at relevant intermediate time scales in a simple MIM. We emphasise that the model's simplicity is attributed to its dependency on merely two parameters in its dimensionless representation. We finally note that persistent-intermittent anomalous scaling behaviours of the MSD as reported here for seemingly simple Poissonian mobile–immobile dynamics may be relevant for numerous experimental settings. Such scenarios should therefore be included in contemporary data analysis methods by classical observables and machine learning approaches [67–69].

Data availability statement

No new data were created or analysed in this study.

Acknowledgments

We acknowledge funding from the German Science Foundation (DFG, Grant No. ME 1535/12-1). AVC acknowledges the support of the Polish National Agency for Academic Exchange (NAWA).

Appendix A. Solving the MIM model in Fourier-Laplace space

We apply the Fourier–Laplace transform

$$f(k, s) = \int_{-\infty}^{\infty} \int_0^{\infty} e^{-st + ikx} f(x, t) dt dx \quad (\text{A.1})$$

to equations (3) and obtain the expressions

$$n_m(k, s) = \left(f_m^0 + f_{im}^0 \frac{1}{1 + s\tau_{im}} \right) \frac{1}{\phi(s) - ik_x v + k^2 D} \quad (\text{A.2})$$

$$n_{\text{im}}(k, s) = f_{\text{im}}^0 \frac{\tau_{\text{im}}}{1 + s\tau_{\text{im}}} + \frac{\tau_{\text{im}}/\tau_{\text{m}}}{1 + s\tau_{\text{im}}} \left(f_{\text{m}}^0 + f_{\text{im}}^0 \frac{1}{1 + s\tau_{\text{im}}} \right) \frac{1}{\phi(s) - ikv + k^2D} \quad (\text{A.3})$$

as well as

$$\begin{aligned} n_{\text{tot}}(k, s) &= n_{\text{m}}(k, s) + n_{\text{im}}(k, s) \\ &= \frac{f_{\text{m}} + f_{\text{im}}^0 \frac{1}{1 + s\tau_{\text{im}}}}{s} \frac{\phi(s)}{\phi(s) - ik_x v + k^2 D} + f_{\text{im}}^0 \frac{\tau_{\text{im}}}{1 + s\tau_{\text{im}}} \end{aligned} \quad (\text{A.4})$$

with $\phi(s) = s[1 + \tau_{\text{im}}\tau_{\text{m}}^{-1}/(1 + s\tau_{\text{im}})]$. Fourier inversion directly produces expressions (4) to (6).

From the densities (A.2) to (A.4) we obtain the p th moment ($p \in \mathbb{N}$)

$$(-i)^p \frac{\partial^p}{\partial k^p} n_{\text{tot}}(k, s) \Big|_{k=0} = \langle x^p(s) \rangle, \quad (\text{A.5})$$

in Laplace space. In order to obtain the mobile and immobile moments, we first calculate the non-normalised moments

$$(-i)^p \frac{\partial^p}{\partial k^p} n_j(k, s) \Big|_{k=0} = \langle x^p(s) \rangle_{j,u} \quad (\text{A.6})$$

with $j \in \{\text{m}, \text{im}, \text{tot}\}$. We then normalise the moment (A.6) in the time-domain with the fractions of mobile and immobile densities,

$$f_{\text{m}}(t) = \frac{\tau_{\text{m}}}{\tau_{\text{m}} + \tau_{\text{im}}} + \frac{f_{\text{m}}^0 \tau_{\text{im}} - f_{\text{im}}^0 \tau_{\text{m}}}{\tau_{\text{m}} + \tau_{\text{im}}} \exp(-[\tau_{\text{m}}^{-1} + \tau_{\text{im}}^{-1}]t), \quad (\text{A.7})$$

$$f_{\text{im}}(t) = \frac{\tau_{\text{im}}}{\tau_{\text{m}} + \tau_{\text{im}}} - \frac{f_{\text{m}}^0 \tau_{\text{im}} - f_{\text{im}}^0 \tau_{\text{m}}}{\tau_{\text{m}} + \tau_{\text{im}}} \exp(-[\tau_{\text{m}}^{-1} + \tau_{\text{im}}^{-1}]t), \quad (\text{A.8})$$

which we obtain by setting $k = 0$ in the densities (A.2)–(A.3) in Fourier–Laplace space and calculating the Laplace inversion.

Appendix B. Expressions of the moments

In this section we present the exact expressions of the first and second moments, which are obtained from expression (A.6).

B.1. First moments

For mobile initial conditions we find

$$\langle x(t) \rangle_{\text{tot}, f_m^0=1} = \frac{v}{1 + \tau_{\text{im}}/\tau_{\text{m}}} \left[t + \frac{\tau_{\text{im}}^2/\tau_{\text{m}}}{1 + \tau_{\text{im}}/\tau_{\text{m}}} \left(1 - e^{-(\tau_{\text{m}}^{-1} + \tau_{\text{im}}^{-1})t} \right) \right], \quad (\text{B.1})$$

$$\begin{aligned} \langle x(t) \rangle_{\text{m}, f_m^0=1} &= \frac{v}{(1 + \tau_{\text{im}}/\tau_{\text{m}}) \left(1 + \tau_{\text{im}}/\tau_{\text{m}} e^{-(\tau_{\text{m}}^{-1} + \tau_{\text{im}}^{-1})t} \right)} \left[t \left(1 + \frac{\tau_{\text{im}}^2}{\tau_{\text{m}}^2} e^{-(\tau_{\text{m}}^{-1} + \tau_{\text{im}}^{-1})t} \right) \right. \\ &\quad \left. + \frac{2\tau_{\text{im}}^2/\tau_{\text{m}}}{1 + \tau_{\text{im}}/\tau_{\text{m}}} \left(1 - e^{-(\tau_{\text{m}}^{-1} + \tau_{\text{im}}^{-1})t} \right) \right], \end{aligned} \quad (\text{B.2})$$

and

$$\langle x(t) \rangle_{\text{im}, f_m^0=1} = \frac{\nu}{1 - e^{-(\tau_m^{-1} + \tau_{\text{im}}^{-1})t}} \left[\frac{t}{1 + \tau_{\text{im}}/\tau_m} \left(1 - \frac{\tau_{\text{im}}}{\tau_m} e^{-(\tau_m^{-1} + \tau_{\text{im}}^{-1})t} \right) + \frac{\tau_{\text{im}}^2/\tau_m - \tau_{\text{im}}}{(1 + \tau_{\text{im}}/\tau_m)^2} \left(1 - e^{-(\tau_m^{-1} + \tau_{\text{im}}^{-1})t} \right) \right]. \quad (\text{B.3})$$

For initially immobile tracers we find

$$\langle x(t) \rangle_{\text{tot}, f_{\text{im}}^0=1} = \frac{\nu}{1 + \tau_{\text{im}}/\tau_m} \left[t - \frac{\tau_{\text{im}}}{1 + \tau_{\text{im}}/\tau_m} \left(1 - e^{-(\tau_m^{-1} + \tau_{\text{im}}^{-1})t} \right) \right], \quad (\text{B.4})$$

$$\langle x(t) \rangle_{\text{im}, f_{\text{im}}^0=1} = \frac{\nu t}{1 + \tau_m/\tau_{\text{im}}} \frac{1 + e^{-(\tau_m^{-1} + \tau_{\text{im}}^{-1})t}}{\tau_{\text{im}}/\tau_m + e^{-(\tau_m^{-1} + \tau_{\text{im}}^{-1})t}} - \frac{3\nu\tau_{\text{im}}^2/\tau_m}{(1 + \tau_{\text{im}}/\tau_m)^2} \frac{1 - e^{-(\tau_m^{-1} + \tau_{\text{im}}^{-1})t}}{\tau_{\text{im}}/\tau_m + e^{-(\tau_m^{-1} + \tau_{\text{im}}^{-1})t}}, \quad (\text{B.5})$$

and

$$\langle x(t) \rangle_{\text{m}, f_{\text{im}}^0=1} = \frac{\nu}{1 - e^{-(\tau_m^{-1} + \tau_{\text{im}}^{-1})t}} \left[\frac{t}{1 + \tau_{\text{im}}/\tau_m} \left(1 - \frac{\tau_{\text{im}}}{\tau_m} e^{-(\tau_m^{-1} + \tau_{\text{im}}^{-1})t} \right) + \frac{\tau_{\text{im}}^2/\tau_m - \tau_{\text{im}}}{(1 + \tau_{\text{im}}/\tau_m)^2} \left(1 - e^{-(\tau_m^{-1} + \tau_{\text{im}}^{-1})t} \right) \right]. \quad (\text{B.6})$$

B.2. Second moments

Consider initially mobile tracers ($f_m^0 = 1$ and $f_{\text{im}}^0 = 0$). Then we obtain

$$\langle x(t)^2 \rangle_{\text{tot}, f_m^0=1} = \frac{2D}{1 + \tau_{\text{im}}/\tau_m} \left[t + \frac{\tau_{\text{im}}^2/\tau_m}{1 + \tau_{\text{im}}\tau_m} \left(1 - e^{-(\tau_m^{-1} + \tau_{\text{im}}^{-1})t} \right) \right] + \frac{\nu^2 t^2 \tau_m^2}{(\tau_m + \tau_{\text{im}})^2} + \frac{\tau_{\text{im}}^2 \tau_m^2 \nu^2}{(\tau_m + \tau_{\text{im}})^3} \left[2t \left(2 - e^{-(\tau_m^{-1} + \tau_{\text{im}}^{-1})t} \right) \frac{\tau_{\text{im}}}{\tau_m} - 2 \frac{2\tau_{\text{im}}\tau_m - \tau_{\text{im}}^2}{\tau_m + \tau_{\text{im}}} + 2e^{-(\tau_m^{-1} + \tau_{\text{im}}^{-1})t} \frac{(2\tau_{\text{im}}\tau_m) - \tau_{\text{im}}^2}{\tau_m + \tau_{\text{im}}} \right] \quad (\text{B.7})$$

and

$$f_m(t) \langle x(t)^2 \rangle_{\text{m}, f_m^0=1} = \frac{2D}{(1 + \tau_{\text{im}}/\tau_m)(1 + \tau_{\text{im}}/\tau_m e^{-(\tau_m^{-1} + \tau_{\text{im}}^{-1})t})} \times \left[t \left(1 + \frac{\tau_{\text{im}}^2}{\tau_m^2} e^{-(\tau_m^{-1} + \tau_{\text{im}}^{-1})t} \right) + \frac{2\tau_{\text{im}}^2/\tau_m}{1 + \tau_{\text{im}}/\tau_m} \left(1 - e^{-(\tau_m^{-1} + \tau_{\text{im}}^{-1})t} \right) \right] + \frac{\nu^2 t^2}{(\tau_m + \tau_{\text{im}})^3} \left(\tau_m^3 + \tau_{\text{im}}^3 e^{-(\tau_m^{-1} + \tau_{\text{im}}^{-1})t} \right) + \frac{6\nu^2 t \tau_{\text{im}}^2 \tau_m^2}{(\tau_m + \tau_{\text{im}})^4} \left(\tau_m - \tau_{\text{im}} e^{-(\tau_m^{-1} + \tau_{\text{im}}^{-1})t} \right) + \frac{6\nu^2 \tau_{\text{im}}^3 (\tau_{\text{im}}\tau_m^3 - \tau_m^4)}{(\tau_m + \tau_{\text{im}})^5} \left(1 - e^{-(\tau_m^{-1} + \tau_{\text{im}}^{-1})t} \right), \quad (\text{B.8})$$

along with

$$\begin{aligned}
 f_{\text{im}}(t) \langle x(t)^2 \rangle_{\text{im}, f_{\text{im}}^0=1} &= \frac{2D}{1 - e^{-(\tau_{\text{m}}^{-1} + \tau_{\text{im}}^{-1})t}} \left[\frac{t}{1 + \tau_{\text{im}}/\tau_{\text{m}}} \left(1 - \frac{\tau_{\text{im}}}{\tau_{\text{m}}} e^{-(\tau_{\text{m}}^{-1} + \tau_{\text{im}}^{-1})t} \right) \right. \\
 &+ \frac{\tau_{\text{im}}^2/\tau_{\text{m}} - \tau_{\text{im}}}{(1 + \tau_{\text{im}}/\tau_{\text{m}})^2} \left(1 - e^{-(\tau_{\text{m}}^{-1} + \tau_{\text{im}}^{-1})t} \right) \\
 &+ \frac{2v^2\tau_{\text{im}}}{\tau_{\text{m}}} \left[\frac{t^2\tau_{\text{m}}(\tau_{\text{m}}^2 - e^{-(\tau_{\text{m}}^{-1} + \tau_{\text{im}}^{-1})t}\tau_{\text{im}}^2)}{2(\tau_{\text{m}} + \tau_{\text{im}})^3} + \frac{t\tau_{\text{im}}}{(\tau_{\text{m}} + \tau_{\text{im}})^4} \right. \\
 &\times \left((2\tau_{\text{im}}\tau_{\text{m}}^3 - \tau_{\text{m}}^4) - e^{-(\tau_{\text{m}}^{-1} + \tau_{\text{im}}^{-1})t}\tau_{\text{im}}(\tau_{\text{im}}\tau_{\text{m}}^2 - 2\tau_{\text{m}}^3) \right) \\
 &\left. \left. + \frac{\tau_{\text{im}}^4\tau_{\text{m}}^3 - 4\tau_{\text{im}}^3\tau_{\text{m}}^4 + \tau_{\text{im}}^2\tau_{\text{m}}^5}{(\tau_{\text{m}} + \tau_{\text{im}})^5} \left(1 - e^{-(\tau_{\text{m}}^{-1} + \tau_{\text{im}}^{-1})t} \right) \right] \right]. \quad (\text{B.9})
 \end{aligned}$$

For initially immobile tracers the moments read

$$\begin{aligned}
 \langle x(t)^2 \rangle_{\text{tot}, f_{\text{im}}^0=1} &= \frac{2D}{1 + \tau_{\text{im}}/\tau_{\text{m}}} \left[t - \frac{\tau_{\text{im}}}{1 + \tau_{\text{im}}/\tau_{\text{m}}} \left(1 - e^{-(\tau_{\text{m}}^{-1} + \tau_{\text{im}}^{-1})t} \right) \right] \\
 &+ \frac{v^2 t^2 \tau_{\text{m}}^2}{(\tau_{\text{im}} + \tau_{\text{m}})^2} + 2 \frac{tv^2 \tau_{\text{im}}^2 \tau_{\text{m}}^2}{(\tau_{\text{im}} + \tau_{\text{m}})^3} \left(1 - \frac{\tau_{\text{m}}}{\tau_{\text{im}}} + e^{-(\tau_{\text{m}}^{-1} + \tau_{\text{im}}^{-1})t} \right) \\
 &- 2 \frac{v^2 (2\tau_{\text{im}}^3 \tau_{\text{m}}^3 - \tau_{\text{im}}^2 \tau_{\text{m}}^4)}{(\tau_{\text{m}} + \tau_{\text{im}})^4} \left(1 - e^{-(\tau_{\text{m}}^{-1} + \tau_{\text{im}}^{-1})t} \right), \quad (\text{B.10})
 \end{aligned}$$

$$\begin{aligned}
 f_{\text{im}}(t) \langle x(t)^2 \rangle_{\text{m}, f_{\text{im}}^0=1} &= \frac{2D}{1 - e^{-(\tau_{\text{m}}^{-1} + \tau_{\text{im}}^{-1})t}} \left[\frac{t}{1 + \tau_{\text{im}}/\tau_{\text{m}}} \left(1 - \frac{\tau_{\text{im}}}{\tau_{\text{m}}} e^{-(\tau_{\text{m}}^{-1} + \tau_{\text{im}}^{-1})t} \right) \right. \\
 &+ \frac{\tau_{\text{im}}^2/\tau_{\text{m}} - \tau_{\text{im}}}{(1 + \tau_{\text{im}}/\tau_{\text{m}})^2} \left(1 - e^{-(\tau_{\text{m}}^{-1} + \tau_{\text{im}}^{-1})t} \right) \\
 &+ \frac{v^2 t^2 \tau_{\text{m}}}{(\tau_{\text{m}} + \tau_{\text{im}})^3} \left(\tau_{\text{m}}^2 - \tau_{\text{im}}^2 e^{-(\tau_{\text{m}}^{-1} + \tau_{\text{im}}^{-1})t} \right) \\
 &+ \frac{2v^2 t \tau_{\text{im}} \tau_{\text{m}}^3}{(\tau_{\text{im}} + \tau_{\text{m}})^4} \left(2\tau_{\text{im}} - \tau_{\text{m}} - e^{-(\tau_{\text{m}}^{-1} + \tau_{\text{im}}^{-1})t} \tau_{\text{im}} \left(\frac{\tau_{\text{im}}}{\tau_{\text{m}}} - 2 \right) \right) \\
 &\left. + \frac{2v^2 \tau_{\text{im}}^2 \tau_{\text{m}}^3 ((\tau_{\text{im}} - \tau_{\text{m}})^2 - 2\tau_{\text{im}}\tau_{\text{m}})}{(\tau_{\text{m}} + \tau_{\text{im}})^5} \left(1 - e^{-(\tau_{\text{m}}^{-1} + \tau_{\text{im}}^{-1})t} \right) \right] \quad (\text{B.11})
 \end{aligned}$$

and

$$\begin{aligned}
 f_{\text{im}}(t) \langle x(t)^2 \rangle_{\text{im}, f_{\text{im}}^0=1} &= \frac{2Dt}{1 + \tau_{\text{m}}/\tau_{\text{im}}} \frac{1 + e^{-(\tau_{\text{m}}^{-1} + \tau_{\text{im}}^{-1})t}}{\tau_{\text{im}}/\tau_{\text{m}} + e^{-(\tau_{\text{m}}^{-1} + \tau_{\text{im}}^{-1})t}} \\
 &- \frac{4D\tau_{\text{im}}^2/\tau_{\text{m}}}{(1 + \tau_{\text{im}}/\tau_{\text{m}})^2} \frac{1 - e^{-(\tau_{\text{m}}^{-1} + \tau_{\text{im}}^{-1})t}}{\tau_{\text{im}}/\tau_{\text{m}} + e^{-(\tau_{\text{m}}^{-1} + \tau_{\text{im}}^{-1})t}} \\
 &+ 2v^2 \frac{\tau_{\text{im}}}{\tau_{\text{m}}} \left[\frac{t^2 \tau_{\text{m}}^2}{2(\tau_{\text{m}} + \tau_{\text{im}})^3} \left(\tau_{\text{m}} + \tau_{\text{im}} e^{-(\tau_{\text{m}}^{-1} + \tau_{\text{im}}^{-1})t} \right) \right. \\
 &+ \frac{t\tau_{\text{im}}}{(\tau_{\text{m}} + \tau_{\text{im}})^4} \left((\tau_{\text{im}}\tau_{\text{m}}^3 - 2\tau_{\text{m}}^4) + e^{-(\tau_{\text{m}}^{-1} + \tau_{\text{im}}^{-1})t} (2\tau_{\text{im}}\tau_{\text{m}}^3 - \tau_{\text{m}}^4) \right) \\
 &\left. - \frac{3\tau_{\text{im}}^3 (\tau_{\text{im}}\tau_{\text{m}}^4 - \tau_{\text{m}}^5)}{(\tau_{\text{m}} + \tau_{\text{im}})^5} \left(1 - e^{-(\tau_{\text{m}}^{-1} + \tau_{\text{im}}^{-1})t} \right) \right]. \quad (\text{B.12})
 \end{aligned}$$

Appendix C. Series expansion of moments

The series expansion of the MSDs is shown in table C1.

Table C1. Short to intermediate time expansions for $t \ll \tau_m, \tau_{im}$ of the MSD for different fractions of initially mobile tracers f_m^0 .

j	series of $\langle [x(t) - \langle x(t) \rangle]^2 \rangle_j$ for $t \ll \tau_m, \tau_{im}$
	$f_m^0 = 1$
tot	$2Dt - \frac{Dt^2}{\tau_m} + \left[v^2 + D \left(\frac{1}{\tau_m} + \frac{1}{\tau_{im}} \right) \right] \frac{t^3}{3\tau_m} - \left[2v^2 \left(\frac{2}{\tau_m} + \frac{1}{\tau_{im}} \right) + D \left(\frac{1}{\tau_m} + \frac{1}{\tau_{im}} \right)^2 \right] \frac{t^4}{12\tau_m}$
m	$2Dt - \frac{Dt^2}{3\tau_m\tau_{im}} + \left[\frac{v^2}{12} + D \left(\frac{1}{6\tau_{im}} - \frac{1}{6\tau_m} \right) \right] \frac{t^3}{\tau_m\tau_{im}} + \left[3v^2(\tau_{im} - \tau_m) + D \left(14 - \frac{3\tau_{im}}{\tau_m} - \frac{3\tau_m}{\tau_{im}} \right) \right] \frac{t^4}{60\tau_m^2\tau_{im}^2}$
im	$Dt + \left[\frac{v^2}{12} + D \left(\frac{1}{6\tau_{im}} - \frac{1}{6\tau_m} \right) \right] t^2 + \left[v^2 \left(2 - \frac{3\tau_m}{\tau_{im}} - \frac{3\tau_{im}}{\tau_m} \right) + 2D(\tau_{im} - \tau_m) \left(\frac{1}{\tau_{im}} + \frac{1}{\tau_m} \right)^2 \right] \frac{t^3}{720\tau_m\tau_{im}}$
	$f_{im}^0 = 1$
tot	$\frac{Dt^2}{\tau_{im}} + \frac{v^2 - D \left(\frac{1}{\tau_m} + \frac{1}{\tau_{im}} \right)}{3\tau_{im}} t^3$
m	$Dt + \left[\frac{v^2}{12} + D \left(\frac{1}{6\tau_{im}} - \frac{1}{6\tau_m} \right) \right] t^2$
im	$\frac{Dt^2}{3\tau_m\tau_{im}} + \left[\frac{v^2}{12} + D \left(\frac{1}{6\tau_{im}} - \frac{1}{6\tau_m} \right) \right] \frac{t^3}{\tau_m\tau_{im}}$

Appendix D. Details on subordination

The probability density function $P(\tau, t)$ of $\tau(t) = \int_0^t i(t') dt'$ is calculated in [23] and reads

$$P(\tau, t) = f_m^0 \sum_{q=1}^{\infty} (P_{q,q-1}^u(\tau, t) + P_{q,q}^u(\tau, t)) + f_{im}^0 \sum_{q=1}^{\infty} (P_{q,q}^b(\tau, t) + P_{q-1,q}^b(\tau, t)). \quad (D.1)$$

Here, $P_{q,r}^u(\tau, t)$ and $P_{q,r}^b(\tau, t)$ denote the probability of initially mobile and immobile tracers, respectively, to spend in total the duration τ mobile in q mobile periods. The tracer remains immobile for the total duration $t - \tau$ in r immobile periods. The expressions for $P_{q,r}^u(\tau, t)$ and $P_{q,r}^b(\tau, t)$ are given by

$$P_{q+1,q}^u(s, t) = \begin{cases} \frac{1}{\tau_{im}} \frac{1}{q!(q-1)!} \left(\frac{s}{\tau_m} \right)^q \left(\frac{t-s}{\tau_{im}} \right)^{q-1} \exp\left(-\frac{s}{\tau_m} - \frac{t-s}{\tau_{im}}\right) & \text{for } q \geq 1 \\ \exp\left(-\frac{s}{\tau_m}\right) & \text{for } q = 0 \end{cases}, \quad (D.2)$$

$$P_{q,q}^u(s, t) = \frac{1}{\tau_m} \frac{1}{((q-1)!)^2} \left(\frac{s(t-s)}{\tau_m\tau_{im}} \right)^{q-1} \exp\left(-\frac{s}{\tau_m} - \frac{t-s}{\tau_{im}}\right) \text{ for } q \geq 1, \quad (D.3)$$

$$P_{q,q}^b(s, t) = \frac{1}{\tau_{im}} \frac{1}{((q-1)!)^2} \left(\frac{s(t-s)}{\tau_m\tau_{im}} \right)^{q-1} \exp\left(-\frac{s}{\tau_m} - \frac{t-s}{\tau_{im}}\right), \quad (D.4)$$

and

$$P_{q,q+1}^b(s, t) = + \begin{cases} \frac{1}{\tau_m} \frac{1}{q!(q-1)!} \left(\frac{t-s}{\tau_{im}} \right)^q \exp\left(-\frac{s}{\tau_m} - \frac{t-s}{\tau_{im}}\right) & \text{for } q \geq 1 \\ \exp\left(-\frac{t}{\tau_{im}}\right) & \text{for } q = 0 \end{cases}. \quad (D.5)$$

In geological experiments, typically the mobile density is measured [18]. Similarly to expression (11), we obtain the mobile density

$$n_m(x, t) = \int_0^t P_m(t', t) \frac{e^{-\frac{(x-vt')^2}{4Dt'}}}{\sqrt{4\pi Dt'}} dt', \quad (D.6)$$

with the probability $P_m(t', t)$ to be mobile for a total duration t' at time t conditioned to be in the mobile phase at time t . From expression (D.1) we simply need to remove the terms with an additional immobilisation to obtain

$$P_m(s, t) = \sum_{q=1}^{\infty} (f_m^0 P_{q,q-1}^u(s, t) + f_{im}^0 P_{q,q}^b(s, t)). \quad (D.7)$$

The immobile density $n_{\text{im}}(x, y, t)$ and $P_{\text{im}}(s, t)$ can be defined analogously to expressions (D.6) and (D.7) with

$$P_{\text{im}}(s, t) = \sum_{q=1}^{\infty} (f_{\text{m}}^0 P_{q,q}^u(s, t) + f_{\text{im}}^0 P_{q-1,q}^b(s, t)). \quad (\text{D.8})$$

The subordinator $P(s, t)$ can also be obtained in another way, as we show now. Since $i(t)$ follows a telegraph process, it is easy to see that the probability density functions $P_{\text{m}}(\tau, t) \equiv P(\tau, t|i(t) = 1)$ and $P_{\text{im}}(\tau, t) \equiv P(\tau, t|i(t) = 0)$ for the operational time obey the following set of equations

$$\begin{aligned} \frac{\partial}{\partial t} P_{\text{m}}(\tau, t) &= -\frac{P_{\text{m}}(\tau, t)}{\tau_{\text{m}}} + \frac{P_{\text{im}}(\tau, t)}{\tau_{\text{im}}} - \frac{\partial}{\partial \tau} P_{\text{m}}(\tau, t), \\ \frac{\partial}{\partial t} P_{\text{im}}(\tau, t) &= \frac{P_{\text{m}}(\tau, t)}{\tau_{\text{m}}} - \frac{P_{\text{im}}(\tau, t)}{\tau_{\text{im}}}, \end{aligned} \quad (\text{D.9})$$

where $P_{\text{m}}(\tau, t)$ and $P_{\text{im}}(\tau, t)$ denote the subordinator $P(\tau, t)$ conditioned on the tracer being mobile or immobile at time t , respectively, with $P(\tau, t) = P_{\text{m}}(\tau, t) + P_{\text{im}}(\tau, t)$. Double Laplace transform $\int_0^{\infty} dt \int_0^{\infty} d\tau f(\tau, t) \exp(-st - u\tau) = f(u, s)$ of $P(\tau, t)$ yields

$$P(u, s) = \frac{f_{\text{m}}^0 + f_{\text{im}}^0 \frac{1}{1+s\tau_{\text{im}}}}{s} \frac{\phi(s)}{\phi(s) + u} + f_{\text{im}}^0 \frac{\tau_{\text{im}}}{1 + s\tau_{\text{im}}}, \quad (\text{D.10})$$

with $\phi(s) = s[1 + \tau_{\text{im}}\tau_{\text{m}}^{-1}/(1 + s\tau_{\text{im}})]$. From $P(u, s)$ (D.10) we obtain the first and second moments in Laplace space

$$\langle \tau^p(s) \rangle = (-1)^p \left. \frac{\partial^p}{\partial u^p} P(u, s) \right|_{u=0}, \quad (\text{D.11})$$

for $p = 1$ and $p = 2$, respectively. We do not provide the lengthy expressions in time domain here. In the long-time $t \gg \tau_{\text{m}}, \tau_{\text{im}}$ the first moment is given by $\langle \tau(t) \rangle \sim t\tau_{\text{m}}/(\tau_{\text{m}} + \tau_{\text{im}})$ and the second central moment is given by $\langle [\tau(t) - \langle \tau(t) \rangle]^2 \rangle \sim 2\tau_{\text{m}}^2\tau_{\text{im}}^2/(\tau_{\text{m}} + \tau_{\text{im}})^3 t$. Laplace-inversion of $P(u, s)$ (D.10) gives the expression

$$P(\tau, s) = \frac{f_{\text{m}}^0 + f_{\text{im}}^0 \frac{1}{1+s\tau_{\text{im}}}}{s} \phi(s) \exp(-\tau\phi(s))\theta(s) + f_{\text{im}}^0 \delta(\tau) \frac{\tau_{\text{im}}}{1 + s\tau_{\text{im}}}, \quad (\text{D.12})$$

with the Heaviside step function $\theta(s)$.

Appendix E. Additional figures and asymptotes of the MSD

In this section we show additional figures of the MSD and develop asymptotic expressions of the mobile and immobile densities. In figure E1 the MSD is shown in addition to the instantaneous diffusion exponent $\alpha(t)$ for initially mobile tracers. For instance the cubic scaling can be seen in panels (c) and (d), where $\alpha(t)$ takes on values close to three for extended periods. In figure E2 we compare the expressions obtained for intermediate time scales to the exact expressions of the MSD.

E.1. Mobile initial conditions

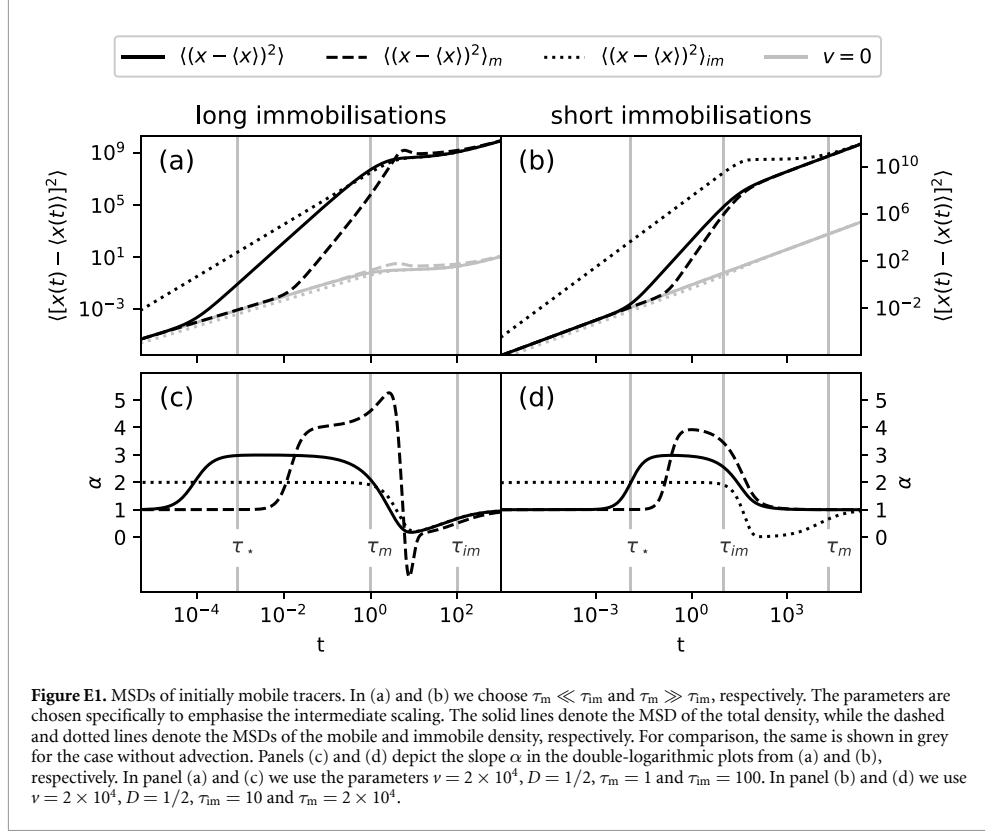
We assume initially mobile tracers and obtain asymptotic expressions in sections appendices E.1.1 and E.1.2.

E.1.1. MSD of the immobile density

Now we turn to the MSD of the immobile density. A series expansion of the exact MSD produces

$$\langle [x(t) - \langle x(t) \rangle]^2 \rangle_{\text{im}} \sim Dt + \frac{v^2}{12} t^2, \text{ for } t \ll \tau_{\text{m}} \ll \tau_{\text{im}}. \quad (\text{E.1})$$

Expression (E.1) implies a ballistic scaling of the immobile MSD for $6\tau_v \ll t \ll \tau_{\text{m}}, \tau_{\text{im}}$. This matches the MSD of the uniform distribution (20) of $n_{\text{im}}(x, t)$ shown in figure 4 where the right border moves at a constant speed. The immobile MSD with the ballistic scaling is shown in figure 6(a) as the dotted line.



Panel (c) depicts the anomalous diffusion exponent α , which is close to two for $6\tau_v \ll t \ll \tau_m$. Figure 6(a) shows the MSD of the mobile density as a dashed black line. For almost all times $t \ll \tau_m$ it coincides with $2Dt$ corresponding to the case without advection and Brownian diffusion. The reason for this is that at $t < \tau_m \ll \tau_{im}$ almost all mobile tracers have never immobilised, as shown in figure 4.

E.1.2. MSD of the mobile density

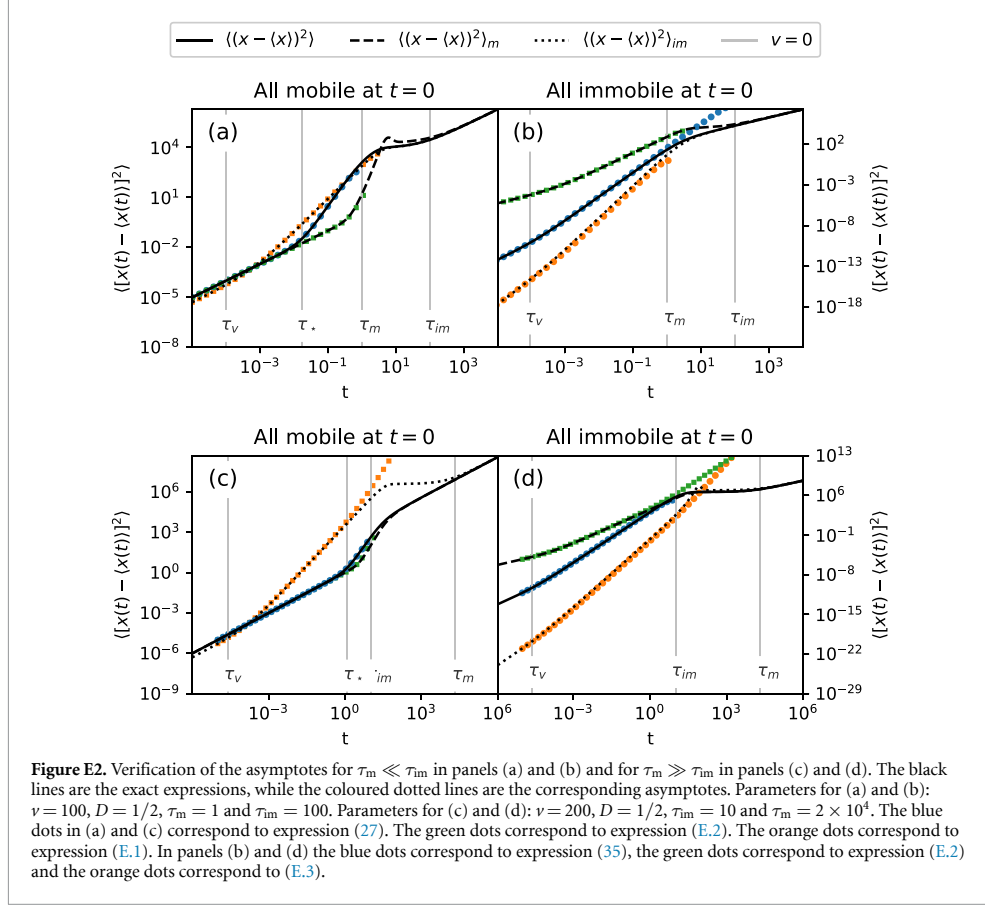
The MSD of the mobile density has the series expansion

$$\langle [x(t) - \langle x(t) \rangle]^2 \rangle = 2Dt + \frac{\nu^2}{12\tau_m\tau_{im}}t^4, \text{ for } t \ll \tau_m, \tau_{im}. \quad (\text{E.2})$$

The short-time behaviour $2Dt$ dominates up to $(2D\tau_m\tau_{im}/\nu^2)^{1/3}$, as shown in figures 6(a) and (b). The time scale $(2D\tau_m\tau_{im}/\nu^2)^{1/3}$ is very close to τ_m in panel (a) and close to τ_{im} in panel (b), therefore the t^4 scaling is not observed in figure 6. In the appendix in figure E1(a), we choose a higher Péclet number, for which the t^4 scaling is distinct. After τ_m the MSD has a peak and decreases afterwards for some time. This can be explained similarly to the advection free case in [54]. Up to τ_m , most of the mobile density consists of mobile tracers that have never immobilised. This can be seen in the histogram for $t = 0.1$ in figure 4, where most of the mobile density follows a Gaussian which is coloured black corresponding to zero immobilisation events $N_{im} = 0$. When the mobile density mostly consists of tracers that were immobile once the MSD decreases because the leading Gaussian peak is missing.

E.2. Immobile initial conditions

We assume initially immobile tracers and obtain asymptotic expressions in sections appendices E.2.1 and E.2.2.



E.2.1. MSD of the immobile density

From a series expansion of the immobile MSD we obtain the short to intermediate time asymptote of the immobile population,

$$\langle [x(t) - \langle x(t) \rangle]^2 \rangle_{im} \sim \frac{Dt^3}{3\tau_{im}\tau_m} + \frac{v^2}{12\tau_{im}\tau_m}t^4, \text{ for } t \ll \tau_m, \tau_{im}, \quad (\text{E.3})$$

where t can be shorter or longer than τ_v . In figure E2(b) we verify this asymptote and it shows good agreement with the full analytical solution. For a high Péclet number $Pe = \frac{v^2\tau_m}{2D} \gg 1$ the quartic term in the asymptotic MSD (E.3) dominates for $\tau_v \ll t \ll \tau_m, \tau_{im}$, as shown in figures 9(a) and (b).

E.2.2. MSD of the mobile density

The MSD of the mobile density with immobile initial conditions is the same as the MSD (E.1) of the immobile density with mobile initial conditions [54]. In the long-time limit $t \gg \tau_v, \tau_m, \tau_{im}$, the MSD is linear with effective diffusion coefficient (15).

Appendix F. Calculations for long immobilisations

We consider $s\tau_{im}, s\tau_m \gg 1$ in $n_{im}(x, s)$ (5), and find the expression

$$n_{im}(x, s) = \left(\frac{1}{s\tau_m} \right) \frac{\exp\left(\frac{vx}{2D}\right)}{\sqrt{v^2 + 4\phi(s)D}} \exp\left(-\sqrt{v^2 + 4\phi(s)D} \frac{|x|}{2D}\right), \quad (\text{F.1})$$

which corresponds in time-domain to the integral

$$n_{\text{im}}(x, t) \sim \frac{1}{\tau_m} \int_0^t \frac{\exp\left(-\frac{(x-vt')^2}{4Dt'}\right)}{\sqrt{4\pi Dt'}} dt' \quad (\text{F.2})$$

$$\sim \frac{\exp\left(\frac{vx-v|x|}{2D}\right)}{2v\tau_m} \left[1 + \operatorname{erf}\left(\frac{tv-|x|}{\sqrt{4Dt}}\right) + \exp\left(\frac{v|x|}{D}\right) \left(\operatorname{erf}\left(\frac{tv+|x|}{\sqrt{4Dt}}\right) - 1 \right) \right]. \quad (\text{F.3})$$

The integral (F.2) has the physical interpretation of mobile tracers following a Gaussian and immobilising with the constant rate $1/\tau_m$.

Appendix G. Density with short immobilisations

For $t \ll \tau_m$, the fraction t/τ_m of mobile tracers is trapped for a short period τ drawn from $\gamma(\tau) = \exp(-\tau/\tau_m)/\tau_m$. This is shown as the red area in figure 5 denoting one immobilisation. Hence, these tracers were mobile for a total period of $t - \tau$. We convolute this with the propagator for advection diffusion and obtain the expression

$$\begin{aligned} a(x, t) &= \int_0^t \frac{\exp\left(-\frac{(x-vt')^2}{4Dt'}\right)}{\sqrt{4\pi Dt'}} e^{-(t-t')/\tau_m} dt' \\ &= \frac{\exp\left(-\frac{t}{\tau_m} + \frac{vx}{2D}\right)}{2\sqrt{v^2 - \frac{4D}{\tau_m}}} \left(\exp\left(-|x|\sqrt{\frac{v^2}{4D^2} - \frac{1}{D\tau_m}}\right) \operatorname{erfc}\left(\frac{x-t\sqrt{v^2 - \frac{4D}{\tau_m}}}{2\sqrt{Dt}}\right) \right. \\ &\quad \left. - \exp\left(|x|\sqrt{\frac{v^2}{4D^2} - \frac{1}{D\tau_m}}\right) \operatorname{erfc}\left(\frac{x+t\sqrt{v^2 - \frac{4D}{\tau_m}}}{2\sqrt{Dt}}\right) \right) \end{aligned} \quad (\text{G.1})$$

with the complimentary error function $\operatorname{erfc}(x)$. Note that (G.1) is also valid for $v^2 < 4D/\tau_m$, i.e. also for the case without advection. The seemingly imaginary parts cancel out. Expression (G.1) can be rewritten as $a(x, t) = \operatorname{Im}\left(\operatorname{erf}\left(\frac{ibt-|x|}{\sqrt{Dt}}\right) \exp(-ib|x|/2D)\right) - \sin(b|x|/2D)/b$, which is strictly positive with $ib = \sqrt{v^2 - 4D/\tau_m}$, and it does not oscillate. The $-\sin(\dots)$ rather removes the oscillatory part of the $\operatorname{Im}(\exp(-ib|x|/2D))$ and the error function approaches unity for large x .

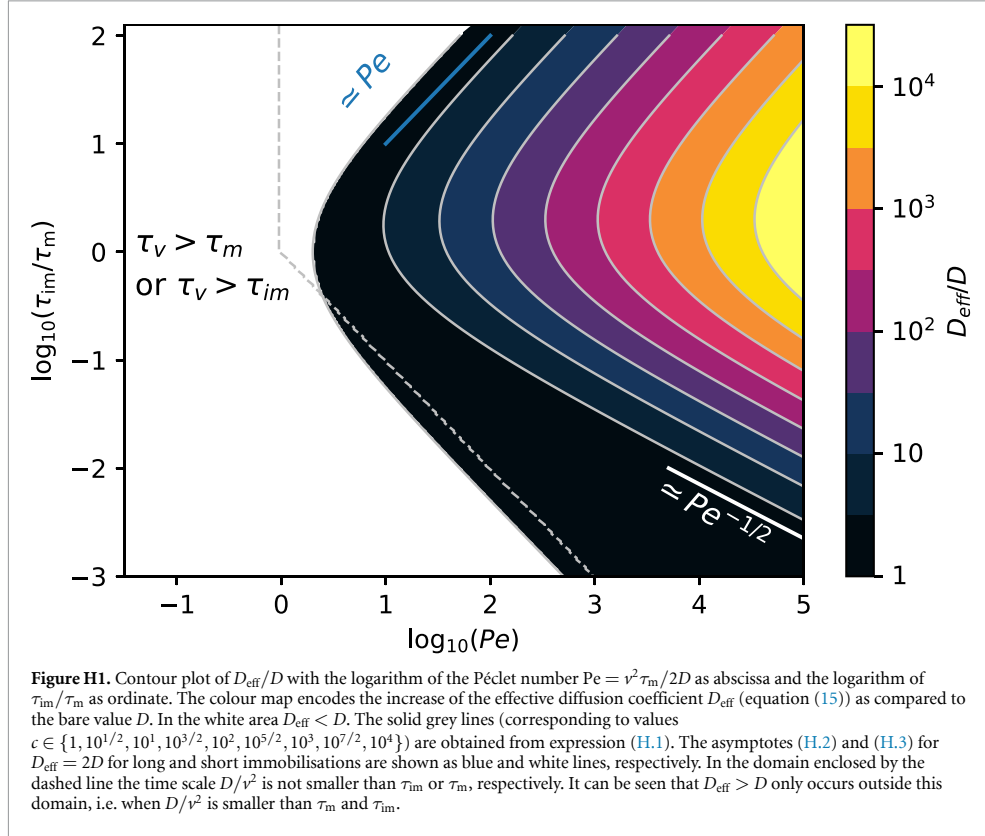
Appendix H. Dependence of D_{eff} on the model parameters

We now analyse the dependence of the effective diffusion coefficient on the model parameters. In section 2.3 we show that only two dimensionless parameters characterise the model, namely the Péclet number and τ_{im}/τ_m . We use the decadic logarithms of these parameters as the abscissa and ordinate in figure H1. The logarithmic colour map encodes the ratio D_{eff}/D for $D_{\text{eff}} > D$. Outside that region D_{eff} is smaller than D , as in the case without advection in [54]. For high Péclet numbers D_{eff} takes on high values depending on τ_{im}/τ_m . Now we analyse this dependence in more detail. For $D > 0$ we now analyse the ratio $D_{\text{eff}}/D = c(\text{Pe}, \tau_m/\tau_{\text{im}})$, that depends on Pe and τ_m/τ_{im} . For $c \geq 1$ we find the expression

$$\text{Pe} = \frac{c-1}{2} \left(1 + \frac{\tau_m}{\tau_{\text{im}}}\right)^2 + \frac{c}{2} \left(1 + \frac{\tau_m}{\tau_{\text{im}}}\right) \left(1 + \frac{\tau_{\text{im}}}{\tau_m}\right), \quad (\text{H.1})$$

which is the Péclet number as a function of τ_{im}/τ_m . It is shown for a range of c values in figure H1 as solid grey lines and matches the colour plot. We obtain the asymptotes

$$\text{Pe} \sim c \frac{\tau_{\text{im}}}{2\tau_m}, \text{ for } \tau_m \ll \tau_{\text{im}}, \quad (\text{H.2})$$



and

$$Pe \sim \begin{cases} \frac{\tau_m}{2\tau_{\text{im}}}, & \text{for } \tau_m \gg \tau_{\text{im}} \text{ and } c = 1 \\ \frac{c-1}{2(\tau_{\text{im}}/\tau_m)^2}, & \text{for } \tau_m \gg \tau_{\text{im}} \text{ and } c > 1 \end{cases}, \quad (\text{H.3})$$

from expression (H.1). The asymptote (H.2) is shown as the blue line at the top of the map in figure H1. For the lower bound in the map we choose $c = 2$ and depict the asymptote $Pe^{-1/2}$ as a white line in figure H1. Both asymptotes are parallel to the exact expressions shown as grey lines.

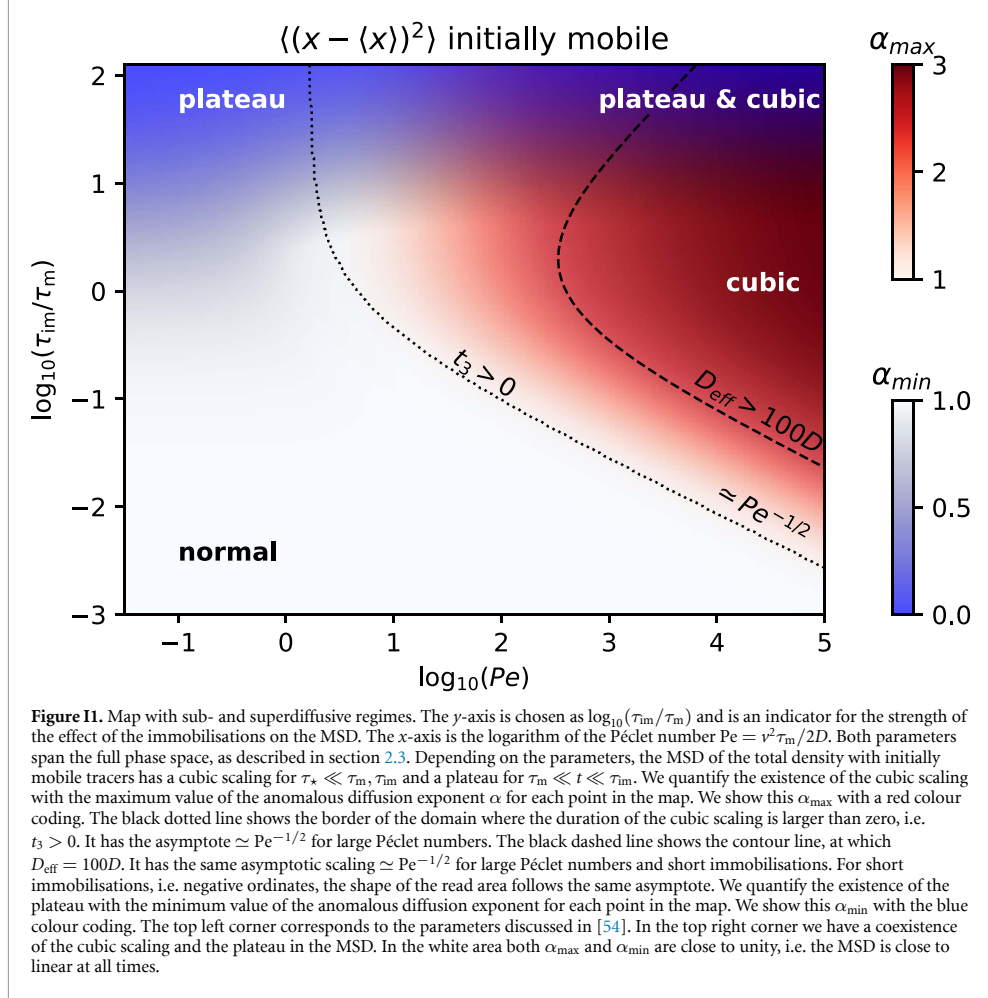
Appendix I. Parameter regimes for anomalous diffusion for initially mobile tracers

I.1. Parameter regimes for superdiffusion

Here we analyse for which parameter regimes the cubic scaling (27) of the total MSD appears for initially mobile tracers. First, long immobilisations are assumed in section appendix I.2 $\tau_m \ll \tau_{\text{im}}$, followed by short immobilisations in section appendix I.3.

I.2. Long immobilisations

A necessary condition for the cubic regime to emerge is that the lower bound τ_* of the time regime is smaller than the upper bound τ_m . We define t_3 as the duration between the upper and lower bound. This restricts the parameter space in which the cubic regime appears to positive values of the time difference t_3 . As shown in section 2.3, the whole parameter space can be spanned by the Péclet number $Pe = v^2 \tau_m / 2D$ and the ratio τ_{im}/τ_m . We use the decadic logarithm of these quantities as axis for a map in figure II, similar to figure H1. The border of the region with $t_3 > 0$ in the top right of figure H1 is shown as a black dotted line. We notice that $Pe > 1$ is a necessary condition for $t_3 > 0$. We analyse the parameter space for $\tau_{\text{im}} > \tau_m$ first and for



$\tau_{\text{im}} < \tau_{\text{m}}$ afterwards. Rearranging the condition $\tau_{\star} < \tau_{\text{m}}$ for the Péclet number reveals the lower bound $27/16 < \text{Pe}$ independent of $\tau_{\text{im}}/\tau_{\text{m}}$. Indeed, the black dotted line for $t_3 = 0$ is vertical in the map (11) for $\tau_{\text{im}} \gg \tau_{\text{m}}$, indicating no dependence on $\tau_{\text{im}}/\tau_{\text{m}}$ in that regime.

So far, we looked at the necessary condition that the lower bound for the interval of the cubic regime is lower than the upper bound. Another approach is to analyse the instantaneous anomalous diffusion exponent $\alpha(t)$. It can be obtained by calculating the slope in a double-logarithmic plot. This is shown in figure E1(c), where α remains close to unity for $t < \tau_{\star}$ and reaches the value three for $\tau_{\star} \ll t \ll \tau_{\text{m}}, \tau_{\text{im}}$. The alternative criterion for the cubic regime to exist is then simply that the maximum value of α_{max} is close to three. With this definition of $\alpha(t)$, superdiffusive parameter regimes are shown with the red colour-coding ranging from one to three in figure 11. This means that the more intense the red in an area is, the closer the parameters are to the asymptotic limits in which the cubic regime emerges. We notice that the red area lies entirely in the region with $t_3 > 0$ and its border follows the same asymptote $\text{Pe}^{-1/2}$ for $\tau_{\text{m}} \gg \tau_{\text{im}}$. The cubic regime appears both for $D_{\text{eff}} > D$ and for $D_{\text{eff}} \lesssim D$ for long immobilisations $\tau_{\text{im}} \gg \tau_{\text{m}}$ and for $\text{Pe} \gg 1$, as shown in the top right corner of the map in figure 11. For reference, a contour plot of D_{eff}/D is shown in figure H1. The reason for the appearance of the cubic regime regardless of the ratio D_{eff}/D is the existence of the plateau for $\tau_{\text{im}} \gg \tau_{\text{m}}$, which we explain now in detail. We know that regardless of the ratio $\tau_{\text{im}}/\tau_{\text{m}}$ the MSD of initially mobile tracers has the asymptote $2Dt$ for short times $t \ll \tau_{\text{m}}, \tau_{\text{im}}, \tau_{\text{v}}$. In the long-time limit it has the asymptote $2D_{\text{eff}}t$. The MSD of the total density is a strictly monotonic function. This means that if $D_{\text{eff}} < D$, any growth faster than linear must be compensated by a regime with a sublinear growth. This

slower than linear growth arises for long immobilisations only and constitutes the plateau for a sufficiently large ratio $\tau_{\text{im}}/\tau_{\text{m}}$.

1.3. Short immobilisations

Finally, we analyse the case of short immobilisations, $\tau_{\text{im}} \ll \tau_{\text{m}}$. The same series expansion of the total MSD holds as in the case with long immobilisations (27). The difference between the upper and lower bound of the cubic scaling is therefore $t_3 = \tau_{\text{im}} - \tau_*$. Notably, the duration of the cubic regime is shorter as compared to the case with long immobilisations in figure 6(a), because $\tau_* = \sqrt{6D\tau_{\text{m}}/v^2}$ is close to the lower bound τ_{im} for $\tau_{\text{m}} \gg \tau_{\text{im}}$. We emphasise that the cubic regime appears for short immobilisations, whereas for the case without advection the MSD is close to normal, as shown by the grey line in figure 6(b). For $\tau_{\text{im}} \ll \tau_{\text{m}}$, i.e. for negative ordinates in figure H1, the condition $\tau_* \ll \tau_{\text{im}}$ simplifies to $\sqrt{\frac{D}{v^2\tau_{\text{m}}}} = (2\text{Pe})^{-1/2} \ll \sqrt{2/3} \frac{\tau_{\text{im}}}{\tau_{\text{m}}}$. This means that for each ratio $\tau_{\text{im}}/\tau_{\text{m}}$ there exists a lower bound for the Péclet number for the cubic regime to exist. Indeed, the black dotted line on the map in figure 11 for $t_3 > 0$ has the asymptotic scaling $\text{Pe}^{-1/2}$ for $\tau_{\text{m}} \gg \tau_{\text{im}}$. The cubic regime appears for $t_3 > 0$ only, i.e. only in the top right part from the black dashed line in figure 11. In figure 11 the red colour denotes the maximum anomalous diffusion coefficient α_{max} . The condition $D_{\text{eff}} > 100D$ has the same asymptotic regime $\text{Pe}^{-1/2}$ for $\tau_{\text{m}} \gg \tau_{\text{im}}$, as shown by the black dashed line in figure 11. For $\tau_{\text{m}} \gg \tau_{\text{im}}$ the dark red region with α_{max} close to three is almost entirely contained within this region. This means that for $\tau_{\text{m}} \gg \tau_{\text{im}}$ the cubic regime always coexists with $D_{\text{eff}} \gg D$. In contrast, we found that the cubic regime appears regardless of the ratio D_{eff}/D for long immobilisations.

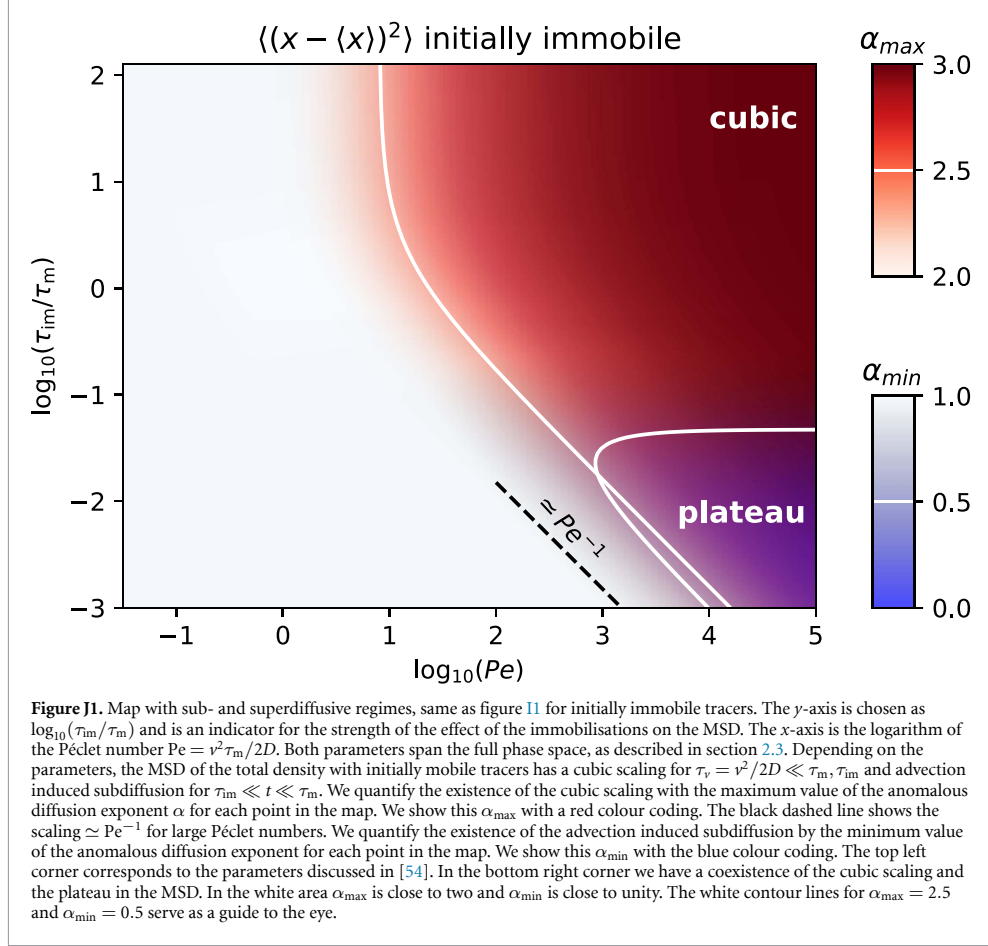
In addition to the maximum value of the instantaneous anomalous diffusion exponent, we consider the minimum value α_{min} in figure 11, in which values close to zero correspond to very slow intermediate growth, i.e. a plateau. This allows us to analyse how the plateau at $\tau_{\text{m}} \ll t \ll \tau_{\text{im}}$ is influenced by the presence of advection and the cubic regime. The coexistence of the cubic regime and the plateau can be seen in the MSD in figure 6(a). The top left blue corner in figure 11 corresponds to the case considered in [54] with long immobilisations and (almost) no advection. The blue subdiffusive area does not significantly change for growing Péclet numbers and it overlaps with the red superdiffusive region in the top right corner of the map in figure 11. In the lower left part of figure 11(a) white area dominates, in which diffusion is close to normal, with both α_{min} and α_{max} close to unity. This can be seen from the solid grey line in figure 6(b).

Appendix J. Parameter regimes for anomalous diffusion with initially immobile tracers

J.1. Parameter regimes for cubic MSD and advection induced subdiffusion

In section 4.3 we found an anomalous scaling of the MSD, and now we analyse for which values of the Péclet number and the characteristic time scales the cubic scaling of the MSD (35) emerges at intermediate times. The cubic term dominates for $\tau_v \ll t \ll \tau_{\text{m}}, \tau_{\text{im}}$. This implies the time scale separation $\tau_v \ll \tau_{\text{m}}, \tau_{\text{im}}$. For long immobilisations $\tau_{\text{im}} \gg \tau_{\text{m}}$ the parameter space for the cubic scaling to occur is therefore restricted to $\text{Pe} \gg 1$. This can be seen in figure J1 in the top right corner, where we show the decadic logarithm of the Péclet number as the abscissa and $\log_{10}(\tau_{\text{im}}/\tau_{\text{m}})$ as the ordinate. The red colour coding denotes the maximal anomalous diffusion coefficient, which is close to three in that top right region. For clarity, the contour line for $\alpha_{\text{max}} = 2.5$ is shown. For short immobilisations, $\tau_{\text{im}} \ll \tau_{\text{m}}$, the cubic term in the asymptote (35) dominates for $\tau_v \ll t \ll \tau_{\text{im}}$, which limits the parameter space for the cubic scaling to occur to $\frac{\tau_{\text{im}}}{\tau_{\text{m}}} \gg \text{Pe}^{-1}$. This can be seen in the map in figure J1, where the relation $\frac{3}{2}\text{Pe}^{-1} \ll \frac{\tau_{\text{im}}}{\tau_{\text{m}}}$ is shown as a dashed black line. Below this line no cubic scaling is possible, meaning that for a given Péclet number the fraction $\tau_{\text{m}}/\tau_{\text{im}}$ needs to be sufficiently small.

After the cubic scaling an advection induced subdiffusion regime may emerge. The time-domain of the subdiffusion is given by $\tau_v \ll \tau_{\text{im}} \ll t \ll \tau_{\text{m}}$. Therefore, the subdiffusive regime appears only for short immobilisations, $\tau_{\text{im}} \ll \tau_{\text{m}}$. Furthermore, the condition $\tau_v \ll \tau_{\text{im}}$ translates to $\text{Pe}^{-1} \ll \tau_{\text{im}}/\tau_{\text{m}}$, shown as the dotted line in figure J1. This restricts the parameter space for the plateau. It is bound by $\tau_{\text{im}} \ll \tau_{\text{m}}$, corresponding to the horizontal boundary in figure J1. In the map in figure J1 we show α_{min} for the total MSD as a blue colour map and observe a region with $\alpha_{\text{min}} < 1/2$ in the bottom right corner for a high Péclet number and short immobilisations. As a guide to the eye we show a contour line for $\alpha_{\text{min}} = 1/2$. A corresponding MSD is shown in figure 9(b), where a plateau occurs for $\tau_{\text{im}} \ll t \ll \tau_{\text{m}}$. This is a new behaviour that does not occur in the case without advection, as is shown by the grey line in figure J1 for a small Péclet number.



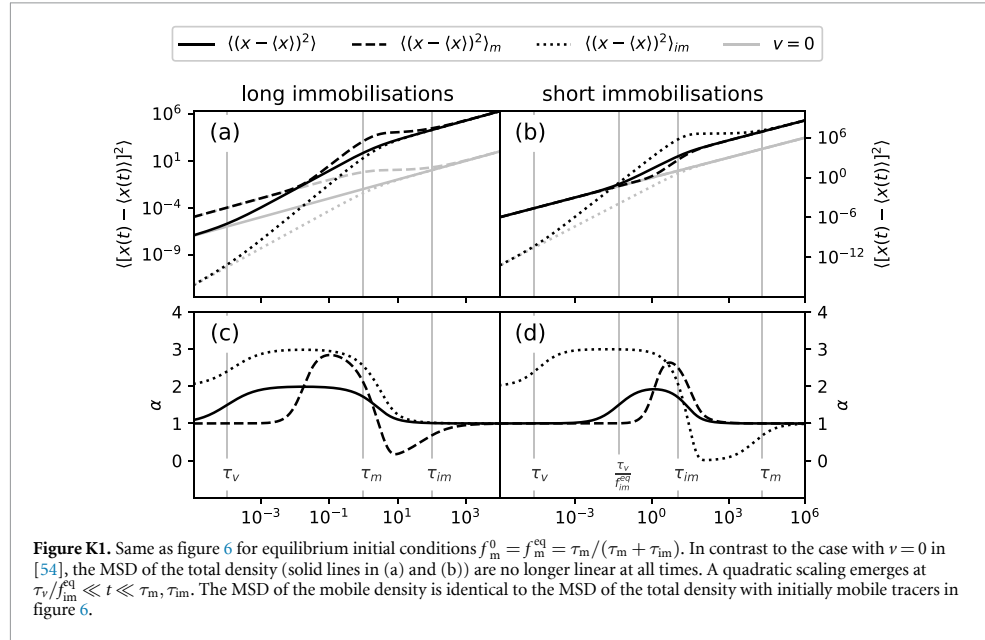
Appendix K. Equilibrium initial condition

We assume the equilibrium fractions $f_{\text{m}}^0 = f_{\text{m}}^{\text{eq}} = \tau_{\text{m}}/(\tau_{\text{m}} + \tau_{\text{im}})$ and $f_{\text{im}}^0 = f_{\text{im}}^{\text{eq}} = \tau_{\text{im}}/(\tau_{\text{m}} + \tau_{\text{im}})$ and consider the MSD of the total density. It is shown in figures K1(a) and (b) as the solid black line for long and short immobilisations, respectively. The densities are given by adding the densities for mobile and immobile initial conditions with the corresponding equilibrium fractions as factors. The MSD is not a linear function and does not follow a linear combination of the initially mobile and immobile MSDs. In contrast to the case without advection in [54], the MSD is no longer linear at all times, and we observe a quadratic scaling for $\tau_{\text{v}}(\tau_{\text{m}} + \tau_{\text{im}})/\tau_{\text{im}} \ll t \ll \tau_{\text{m}}, \tau_{\text{im}}$. A series expansion yields the asymptote for intermediate times $t \ll \tau_{\text{m}}, \tau_{\text{im}}$, where t can be shorter or longer than τ_{v} ,

$$\langle [x(t) - \langle x(t) \rangle]^2 \rangle \sim 2Df_{\text{m}}^{\text{eq}}t + v^2f_{\text{m}}^{\text{eq}}f_{\text{im}}^{\text{eq}}t^2, \text{ for } t \ll \tau_{\text{m}}, \tau_{\text{im}}. \quad (\text{K.1})$$

The quadratic term dominates over the linear term for $\frac{\tau_{\text{v}}}{f_{\text{im}}^{\text{eq}}} \ll t$. This is shown in figures K1(a) and (b). In panels (c) and (d) the instantaneous anomalous diffusion exponent is displayed, which is close to two in this domain. Note that for long immobilisations $f_{\text{im}}^{\text{eq}} \approx 1$. The quadratic scaling emerges for long immobilisations $\tau_{\text{m}} \ll \tau_{\text{im}}$ for $Pe \gg 1$ and for short immobilisations for $Pe^{-1/2} \ll \tau_{\text{im}}/\tau_{\text{m}}$.

As described in [54], the MSD of the mobile density with equilibrium initial conditions is identical to the MSD of the total density with mobile initial conditions. We discussed this case in detail in the main text. The same holds for the MSD of the immobile density. For an equilibrium fraction of initially mobile tracers the density is given by the linear combination of the results for mobile and for immobile initial conditions.



Appendix L. Comparison to CTRW

In this section we compare our results to three versions of CTRWs. For didactic purposes, we start in appendix L.1 with the classical CTRW with exponentially distributed waiting times. In appendix L.2 we compare our model to the two state CTRW [51]. Finally, in appendix L.3 we compare our model to a CTRW in which the waiting times are drawn from a waiting time distribution containing two exponential distributions [52].

L.1. Classical CTRW

We here compare the results obtained from the MIM (3) to a CTRW with advection and exponentially distributed sojourn times. The relation between MIM and CTRW has been discussed in detail, for example, in [13, 48, 70]. Let us define the sojourn time density $\psi(t) = \exp(-t/\tau)/\tau$ and the Gaussian displacement density $\lambda(x)$ with mean μ and variance σ^2 . This corresponds to the model considered in [46]. In [71] the solution of the density function $p(x, t)$ in this CTRW framework is given as

$$p(x, t) = \sum_{j=1}^{\infty} \frac{(t/\tau)^j \exp(-t/\tau)}{j!} \frac{\exp\left(-\frac{x^2}{2j\sigma^2}\right)}{\sqrt{2\pi j\sigma^2}}, \quad (\text{L.1})$$

for $\mu = 0$. We incorporate the non-zero mean μ and obtain the solution

$$p(x, t) = \sum_{j=1}^{\infty} \frac{(t/\tau)^j \exp(-t/\tau)}{j!} \frac{\exp\left(-\frac{(x-j\mu)^2}{2j\sigma^2}\right)}{\sqrt{2\pi j\sigma^2}}. \quad (\text{L.2})$$

Let us turn to the moments of $p(x, t)$ (L.2). The first moment is given by

$$\begin{aligned} \langle x(t) \rangle &= \sum_{j=1}^{\infty} \frac{(t/\tau)^j \exp(-t/\tau)}{j!} j\mu \\ &= \mu \frac{t}{\tau} \exp\left(-\frac{t}{\tau}\right) \sum_{j=0}^{\infty} \frac{(t/\tau)^j}{j!} \\ &= \mu \frac{t}{\tau}. \end{aligned} \quad (\text{L.3})$$

In the same way we obtain the second moment

$$\langle x^2(t) \rangle = \sigma^2 \frac{t}{\tau} + \mu^2 \frac{t^2}{\tau^2} + \mu^2 \frac{t}{\tau}, \quad (\text{L.4})$$

resulting in the MSD

$$\langle [x(t) - \langle x(t) \rangle]^2 \rangle = \frac{\sigma^2}{\tau} t + \frac{\mu^2}{\tau} t, \quad (\text{L.5})$$

which is linear at all times, in contrast the results obtained from our model.

L.2. Two-state CTRW

In this section we compare our model to the two-state CTRW introduced in [51] in which two transition densities

$$f_i(x, t) = \frac{1}{\sqrt{4\pi D_i t}} \exp\left(-\frac{(x - v_i t)^2}{4D_i t}\right) \psi_i(t), i = 1, 2 \quad (\text{L.6})$$

are present with average speeds v_i and diffusion constants D_i . In an alternating way jumps are drawn from $f_1(x, t)$ and $f_2(x, t)$. The long-time diffusion coefficient presented in [51] is given by

$$D_{\text{eff}} = \frac{D_1 \tau_1 + D_2 \tau_2}{\tau_1 + \tau_2} + \frac{1}{2(\tau_1 + \tau_2)} \times \left[\sigma_1^2 \left(v_1 - \frac{v_1 \tau_1 + v_2 \tau_2}{\tau_1 + \tau_2} \right) + \sigma_2^2 \left(v_2 - \frac{v_1 \tau_1 + v_2 \tau_2}{\tau_1 + \tau_2} \right) \right] \quad (\text{L.7})$$

with $\tau_i = \int_0^\infty t \psi_i(t) dt$ and $\sigma_i^2 = \int_0^\infty t^2 \psi_i(t) dt - \tau_i^2$, $i = 1, 2$. The long-time effective diffusion coefficient (L.7) matches our result (15), if we formally choose $D_1 = D$, $v_1 = v$, $D_2 = 0$, $v_2 = 0$, $\psi_1(t) = \exp(-t/\tau_m)/\tau_m$ and $\psi_2(t) = \exp(-t/\tau_{\text{im}})/\tau_{\text{im}}$.

L.3. Double exponential CTRW

In this section we compare our model to the CTRW analysed in [52], in which the waiting time distribution function is given by the weighted sum

$$\psi(t) = \frac{p}{\tau_D} \exp\left(-\frac{t}{\tau_D}\right) + \frac{(1-p)}{\tau_B} \exp\left(-\frac{t}{\tau_B}\right) \quad (\text{L.8})$$

of two exponentials, where $\tau_B \leq \tau_D$ and $p \in [0, 1]$. The jump length distribution we consider is given by the Gaussian

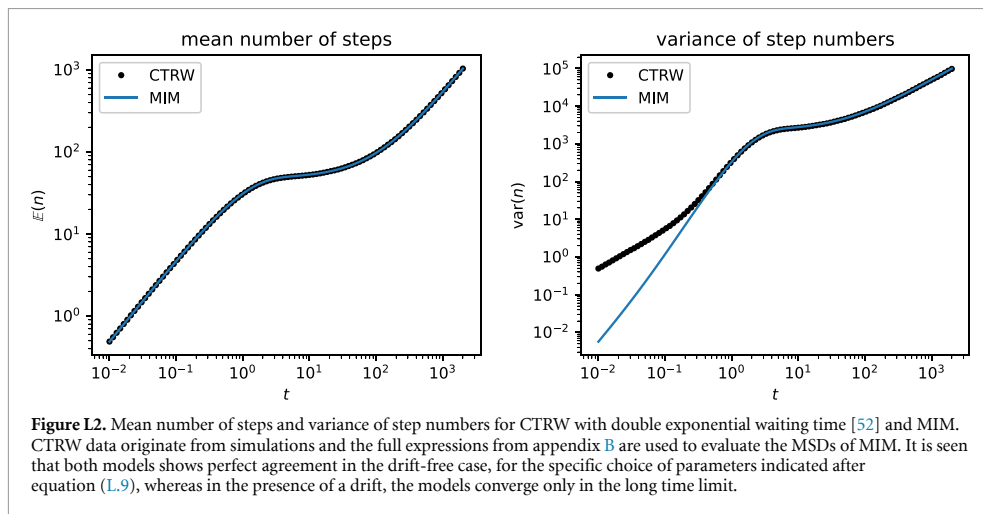
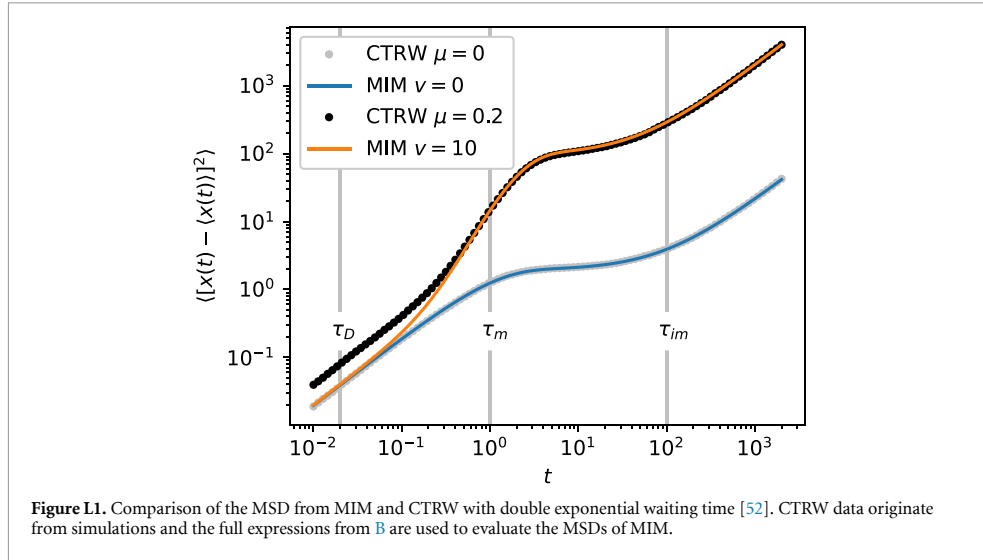
$$\lambda(x) = \frac{1}{\sqrt{2\pi\sigma^2}} \exp\left(-\frac{(x-\mu)^2}{2\sigma^2}\right), \quad (\text{L.9})$$

with mean μ and variance σ^2 . Note that in [52] $\lambda(x)$ is restricted to the case $\mu = 0$. Formally, we choose the parameters $\tau_B = \tau_{\text{im}}$, $\tau_D \ll \tau_B, \tau_{\text{im}}$, and $p = 1 - \tau_D/\tau_m$. We stress that this means that $\tau_D \neq \tau_m$ and τ_D does not have the meaning of the mean residence time in a mobile state. By choosing $\tau_D \ll \tau_m$ and $p = 1 - \tau_D/\tau_m$ close to unity there is a high probability to draw from the exponential distribution with short mean duration. This effectively models the Brownian motion of a tracer in the mobile state. After each step, the tracer immobilises with probability $1 - p$. If there was no waiting time drawn from the long exponential, on average, there are t/τ_D steps at time t . This gives an effective immobilisation rate of $1/\tau_m$, which is the same as in MIM. In figure L1 we compare the MSD of MIM for $\tau_m = 1$, $\tau_{\text{im}} = 100$, $v = 0$ or $v = 10$ and $D = 1$ with simulations of CTRW with $\tau_D = 2 \times 10^{-2}$, $\tau_B = \tau_{\text{im}}$, $\mu = v\tau_D$ and $\sigma = \sqrt{2D\tau_D}$. We find good agreement at all times for the advection-free case, while the CTRW yields higher values than MIM for $t < \tau_D$ in the case with advection.

The reason why the MSDs are identical in the advection-free case and not in the case with advection can be understood by considering the MSD in terms of step numbers n [66]

$$\text{var}(x) = \mathbb{E}(n) \text{var}(\Delta x_i) + (\mathbb{E}(\Delta x_i))^2 \text{var}(n), \quad (\text{L.10})$$


where $x = \sum_{i=1}^n \Delta x_i$, as introduced in section 2.5. We emphasise that expression (L.10) is exact. From expression (L.10) we see that in the advection-free case $\mathbb{E}(\Delta x_i) = 0$ only the mean number of steps is relevant for the MSD and not the variance of step numbers. Indeed, in figure L2 we show the mean number



of steps $\mathbb{E}(n)$ (calculated by setting $D = 0$), where the dots for CTRW and the line for MIM overlap at all times. Therefore, the MSDs in the advection-free case of CTRW and MIM in figure L1 are equivalent. In contrast, in the case of advection, the variance of step numbers $\text{var}(n)$ couples to the MSD, as can be seen in expression (L.10). The variance of step numbers differs for $t < \tau_D$. We explain this as follows. If a tracer is in the mobile state of MIM, it will have a fixed number of steps $n = t/\Delta t$ at time t . The stochasticity of step numbers arises solely from immobilisations. By setting $D = 0$ we obtain a cubic short-time growth of the variance from the short-time asymptote (27). In contrast, in the CTRW case, the number of steps is random even in the case of a simple CTRW with only one exponential waiting time distribution, as described in appendix L.1. It can be seen in the variance of CTRW (L.5) for $\sigma = 0$ and $\mu = 1$, where the variance of step numbers grows linearly. This is due to the fact that after each step a random waiting time is drawn from the exponential distribution. Therefore, the variance of step numbers is higher for small times and hence the MSDs of MIM and CTRW do not overlap for $t < \tau_D$, as shown in figure L1. We point out that the disagreement between the MSD of MIM and CTRW with advection lasts until $\approx 3 \times 10^{-1}$, which is notably larger than the chosen $\tau_D = 2 \times 10^{-2}$.

ORCID iDs

Ralf Metzler  <https://orcid.org/0000-0002-6013-7020>

Aleksei V Chechkin  <https://orcid.org/0000-0002-3803-1174>

References

- [1] Biggar J W and Nelson D R 1967 Miscible displacement and leaching phenomena *Irrigation of Agricultural Lands (Agronomy)* vol 11 (Madison, WI: American Society of Agronomy), ed R M Hagen p 254
- [2] Lapidus L and Amundson N R 1952 Mathematica of adsorption in beds. VI. the effect of longitudinal diffusion in ion exchange and chromatographic columns *J. Phys. Chem.* **56** 984
- [3] Coats K H and Smith B D 1964 Dead-end pore volume and dispersion in porous media *Soc. Pet. Eng. J.* **4** 73
- [4] Van Genuchten M T and Wierenga P J 1976 Mass transfer studies in sorbing porous media I. Analytical solutions *Soil Sci. Soc. Am. J.* **40** 473
- [5] Doerries T J, Chechkin A V, Schumer R and Metzler R 2022 Rate equations, spatial moments and concentration profiles for mobile-immobile models with power-law and mixed waiting time distributions *Phys. Rev. E* **105** 014105
- [6] Michalak A M and Kitanidis P K 2000 Macroscopic behavior and random-walk particle tracking of kinetically sorbing solutes *Water Resour. Res.* **36** 2133
- [7] Goltz M N and Tobrtyd P V 1987 Using the method of moments to analyse three-dimensional diffusion-limited solute transport from temporal and spatial perspectives *Water Resour. Res.* **23** 1575
- [8] van Genuchten M T and Wierenga P J 1976 Mass transfer studies in sorbing porous media I. Analytical solutions *Soil Sci. Soc. Am. J.* **40** 473
- [9] Deans H H 1963 A mathematical model for dispersion in the direction of flow of porous media *Soc. Pet. Eng. J.* **3** 49
- [10] Sardin M, Schweich D, Leij F J and van Genuchten M T 1991 Modeling the nonequilibrium transport of linearly interacting solutes in porous media: a review *Water Resour. Res.* **27** 2287
- [11] Haggerty R and Gorelick S M 1995 Multiple-rate mass transfer for modeling diffusion and surface reactions in media with pore-scale heterogeneity *Water Resour. Res.* **31** 2383
- [12] Schumer R, Benson D A, Meerschaert M M and Baeumer B 2003 Fractal mobile-immobile solute transport *Water Resour. Res.* **39** 1296
- [13] Dentz M and Berkowitz B 2003 Transport behavior of a passive solute in continuous time random walks and multirate mass transfer *Water Resour. Res.* **39** 1
- [14] Zhang Y, Benson D A and Baeumer B 2008 Moment analysis for spatiotemporal fractional dispersion *Water Resour. Res.* **44** W04424
- [15] Gao G, Zhan H, Feng S, Fu B, Ma Y and Huang G 2010 A new mobile-immobile model for reactive solute transport with scale-dependent dispersion *Water Resour. Res.* **46** W08533
- [16] Lu B, Zhang Y, Zheng C, Green C T, O'Neill C, Sun H-G and Qian J 2018 Comparison of time nonlocal transport models for characterizing non-Fickian transport: from mathematical interpretation to laboratory application *Water* **10** 778
- [17] Egusa N, Nakagawa K and Hirata T 2020 A retardation factor considering solute transfer between mobile and immobile water in porous media *Environ. Model. Assess.* **26** 103
- [18] Goepfert N, Goldscheider N and Berkowitz B 2020 Experimental and modeling evidence of kilometer-scale anomalous tracer transport in an alpine karst aquifer *Water Res.* **178** 115755
- [19] Weigel A V, Simon B, Tamkun M M and Krapf D 2011 Ergodic and nonergodic processes coexist in the plasma membrane as observed by single-molecule tracking *Proc. Natl Acad. Sci. USA* **108** 6438
- [20] Pulkkinen O and Metzler R 2013 Distance matters: the impact of gene proximity in bacterial gene regulation *Phys. Rev. Lett.* **110** 198101
- [21] Igaev M, Janning D, Sündermann F, Niewidok B, Brandt R and Junge W 2014 A refined reaction-diffusion model of tau-microtubule dynamics and its application in FDAP analysis *Biophys. J.* **107** 2567
- [22] Janning D, Igaev M, Sündermann F, Brühmann J, Beutel O, Heinisch J J, Bakota L, Piehler J, Junge W and Brandt R 2014 Single-molecule tracking of tau reveals fast kiss-and-hop interaction with microtubules in living neurons *Mol. Biol. Cell* **25** 3541
- [23] Yeung C, Shtrahman M and Wu X-L 2007 Stick-and-diffuse and caged diffusion: a comparison of two models of synaptic vesicle dynamics *Biophys. J.* **92** 2271
- [24] Wu M M, Covington E D and Lewis R S 2014 Single-molecule analysis of diffusion and trapping of STIM1 and Ora1 at endoplasmic reticulum-plasma membrane junctions *Mol. Biol. Cell* **25** 3672
- [25] Fernández A D, Charchar P, Cherstvy A G, Metzler R and Finnis M W 2020 The diffusion of doxorubicin drug molecules in silica nanoslits is non-Gaussian, intermittent and anticorrelated *Phys. Chem. Chem. Phys.* **22** 27955
- [26] van den Broek B, Lomholt M A, Kalisch S-M J, Metzler R and Wuite G J L 2008 How DNA coiling enhances target localization by proteins *Proc. Natl Acad. Sci.* **105** 15738
- [27] Mazza D, Abernathy A, Golob N, Morisaki T and McNally J G 2012 A benchmark for chromatin binding measurements in live cells *Nucleic Acids Res.* **40** e119
- [28] Liu Z, Legant W R, Chen B-C, Li L, Grimm J B, Lavis L D, Betzig E and Tjian R 2014 3D imaging of Sox2 enhancer clusters in embryonic stem cells *eLife* **3** e04236
- [29] Sprague B L, Pego R L, Stavreva D A and McNally J G 2004 Analysis of binding reactions by fluorescence recovery after photobleaching *Biophys. J.* **86** 3473
- [30] Chen J et al 2014 Single-molecule dynamics of enhanceosome assembly in embryonic stem cells *Cell* **156** 1274
- [31] Park S, Lee O-C, Durang X and Jeon J-H 2021 A mini-review of the diffusion dynamics of DNA-binding proteins: experiments and models *J. Korean Phys. Soc.* **78** 408
- [32] Tafvizi A, Mirny L A and van Oijen A M 2011 Dancing on DNA: kinetic aspects of search processes on DNA *ChemPhysChem* **12** 1418
- [33] Tafvizi A, Huang F, Fersht A R, Mirny L A and van Oijen A M 2011 A single-molecule characterization of p53 search on DNA *Proc. Natl Acad. Sci. USA* **108** 563
- [34] Kong M et al 2016 Single-molecule imaging reveals that Rad4 employs a dynamic DNA damage recognition process *Mol. Cell* **64** 376

- [35] Kamagata K, Mano E, Ouchi K, Kanabayashi S and Johnson R C 2018 High free-energy barrier of 1D diffusion along DNA by architectural DNA-binding proteins *J. Mol. Biol.* **430** 655
- [36] Reverey J F, Jeon J-H, Bao H, Leippe M, Metzler R and Selhuber-Unkel C 2015 Superdiffusion dominates intracellular particle motion in the supercrowded cytoplasm of pathogenoc *Acanthamoeba castellanii* *Sci. Rep.* **5** 11690
- [37] Wang L and Li P C H 2011 Microfluidic DNA microarray analysis: a review *Anal. Chim. Acta* **687** 12
- [38] Squires T M, Mesinger R J and Manalis R 2008 Making it stick: convection, reaction and diffusion in surface-based biosensors *Nat. Biotechnol.* **26** 417
- [39] Scher H and Montroll E W 1975 Anomalous transient-time dispersion in amorphous solids *Phys. Rev. B* **12** 2455
- [40] Kurilovich A A, Mantsevich V N, Mardoukhi Y, Stevenson K J, Chechkin A V and Palyulin V V 2022 Non-Markovian diffusion of excitons in layered perovskites and transition metal dichalcogenides *Phys. Chem. Chem. Phys.* **24** 13941
- [41] Kurilovich A A, Mantsevich V N, Stevenson K J, Chechkin A V and Palyulin V V 2020 Complex diffusion-based kinetics of photoluminescence in semiconductor nanoplatelets *Phys. Chem. Chem. Phys.* **22** 24686
- [42] Kurilovich A A, Mantsevich V N, Stevenson K J, Chechkin A V and Palyulin V V 2021 Trapping-influenced photoluminescence intensity decay in semiconductor nanoplatelets *J. Phys.: Conf. Ser.* **2015** 012103
- [43] Harvey C F and Gorelick S M 1995 Temporal moment-generating equations: modeling transport and mass transfer in heterogeneous aquifers *Water Resour. Res.* **31** 1895
- [44] Hughes B D 1995 *Random Walks and Random Environments: Random Walks* vol 1 (Oxford: Oxford University Press)
- [45] Montroll E W and Weiss G H 1965 Random walks on lattices. II *J. Math. Phys.* **6** 167
- [46] Burov S, Wang W and Barkai E 2022 Exponential tails and asymmetry relations for the spread of biased random walks, (arXiv:2209.03410)
- [47] Ederly Y, Guadagnini A, Scher H and Berkowitz B 2014 Origins of anomalous transport in heterogeneous media: structural and dynamic controls *Water Resour. Res.* **50** 1490
- [48] Margolin G, Dentz M and Berkowitz B 2003 Continuous time random walk and multirate mass transfer modeling of sorption *Chem. Phys.* **295** 71
- [49] Krüsemann H, Godec A and Metzler R 2014 First-passage statistics for aging diffusion in systems with annealed and quenched disorder *Phys. Rev. E* **89** 040101(R)
- [50] Berkowitz B, Klafter J, Metzler R and Scher H 2002 Physical pictures of transport in heterogeneous media: advection-dispersion, random-walk and fractional derivative formulations *Water Resour. Res.* **38** 1191
- [51] Weiss G H 1976 The two-state random walk *J. Stat. Phys.* **15** 157
- [52] Vitali S, Paradisi P and Pagnini G 2022 Anomalous diffusion originated by two Markovian hopping-trap mechanisms *J. Phys. A: Math. Theor.* **55** 224012
- [53] Hidalgo-Soria M, Barkai E and Burov S 2021 Cusp of non-Gaussian density of particles for a diffusing diffusivity model *Entropy* **23** 231
- [54] Doerries T J, Chechkin A V and Metzler R 2022 Apparent anomalous diffusion and non-Gaussian distributions in a simple mobile-immobile transport model with Poissonian switching *J. R. Soc. Interface* **19** 20220233
- [55] Gouze P, Le Borgne T, Leprovost R, Lods G, Poidras T and Pezard P 2008 Non-Fickian dispersion in porous media: 1. Multiscale measurements using single-well injection withdrawal tracer tests *Water Resour. Res.* **44** W06426
- [56] Drummond J D, Larsen L G, González-Pinzón R, Packman A I and Harvey J W 2017 Fine particle retention within stream storage areas at base flow and in response to a storm event *Water Resour. Res.* **53** 5690–705
- [57] Metzler R, Rajyaguru A and Berkowitz B 2022 Modelling anomalous diffusion in semi-infinite disordered systems and porous media *New J. Phys.* **24** 123004
- [58] Metzler R and Klafter J 2000 The random walk's guide to anomalous diffusion: a fractional dynamics approach *Phys. Rep.* **339** 1
- [59] Bochner S 1960 *Harmonic Analysis and the Theory of Probability* (Berkeley, CA: Berkeley University Press)
- [60] Chechkin A V, Seno F, Metzler R and Sokolov I M 2017 Brownian yet non-Gaussian diffusion: from superstatistics to subordination of diffusing diffusivities *Phys. Rev. X* **7** 021002
- [61] Chechkin A and Sokolov I M 2021 Relation between generalized diffusion equations and subordination schemes *Phys. Rev. E* **103** 032133
- [62] Gorenflo R and Mainardi F 2009 Some recent advances in theory and simulation of fractional diffusion processes *J. Comput. Appl. Math.* **229** 400
- [63] Fogedby H C 1994 Langevin equations for continuous time Lévy flights *Phys. Rev. E* **50** 1657
- [64] Eule S and Friedrich R 2009 Subordinated Langevin equations for anomalous diffusion in external potentials – biasing and decoupled external forces *Europhys. Lett.* **86** 30008
- [65] Gorenflo R, Mainardi F and Vivoli A 2007 Continuous-time random walk and parametric subordination in fractional diffusion *Chaos Solitons Fractals* **34** 87
- [66] Ross S M 2010 *A First Course in Probability* vol 8, ed D Lynch (London: Pearson) p 362
- [67] Muñoz-Gil G et al 2021 Objective comparison of methods to decode anomalous diffusion *Nat. Commun.* **12** 6253
- [68] Seckler H and Metzler R 2022 Bayesian deep learning for error estimation in the analysis of anomalous diffusion *Nat. Commun.* **13** 6717
- [69] Manzo C, Muñoz-Gil G, Volpe G, Garcia-March M A, Lewenstein M and Metzler R 2023 Preface: characterisation of physical processes from anomalous diffusion data *J. Phys. A* **56** 010401
- [70] Boano F, Packman A I, Cortis A, Revelli R and Ridolfi L 2007 A continuous time random walk approach to the stream transport of solutes *Water Resour. Res.* **43** 1
- [71] Barkai E and Burov S 2020 Packets of diffusing particles exhibit universal exponential tails *Phys. Rev. L* **124** 060603

T. J. Doerries, A. V. Checkin, R. Schumer, and R. Metzler, Rate equations, spatial moments, and concentration profiles for mobile-immobile models with power-law and mixed waiting time distributions, *Phys. Rev. E* **105**, 014105 (2022), <https://doi.org/10.1103/PhysRevE.105.014105> Copyright (2022) by the American Physical Society.

Rate equations, spatial moments, and concentration profiles for mobile-immobile models with power-law and mixed waiting time distributions

Timo J. Doerries¹,[✉] Aleksei V. Chechkin,^{1,2,3} Rina Schumer,⁴ and Ralf Metzler^{1,*}

¹*Institute of Physics and Astronomy, University of Potsdam, 14476 Potsdam, Germany*

²*Faculty of Pure and Applied Mathematics, Hugo Steinhaus Center, Wrocław University of Science and Technology, Wyspińskiego 27, 50-370 Wrocław, Poland*

³*Akhiezer Institute for Theoretical Physics, 61108 Kharkov, Ukraine*

⁴*Desert Research Institute, Reno, Nevada 89512, USA*



(Received 1 October 2021; accepted 17 December 2021; published 4 January 2022)

We present a framework for systems in which diffusion-advection transport of a tracer substance in a mobile zone is interrupted by trapping in an immobile zone. Our model unifies different model approaches based on distributed-order diffusion equations, exciton diffusion rate models, and random-walk models for multirate mobile-immobile mass transport. We study various forms for the trapping time dynamics and their effects on the tracer mass in the mobile zone. Moreover, we find the associated breakthrough curves, the tracer density at a fixed point in space as a function of time, and the mobile and immobile concentration profiles and the respective moments of the transport. Specifically, we derive explicit forms for the anomalous transport dynamics and an asymptotic power-law decay of the mobile mass for a Mittag-Leffler trapping time distribution. In our analysis we point out that even for exponential trapping time densities, transient anomalous transport is observed. Our results have direct applications in geophysical contexts, but also in biological, soft matter, and solid state systems.

DOI: [10.1103/PhysRevE.105.014105](https://doi.org/10.1103/PhysRevE.105.014105)

I. INTRODUCTION

In their original formulations of Brownian motion, Einstein [1], von Smoluchowski [2], Sutherland [3], and Langevin [4] assumed an isotropic homogeneous environment, and thus a constant diffusion coefficient D . In the hydrodynamic limit, these theories led to the standard diffusion equation (Fick's second law [5]) for the probability density function (PDF) $P(\mathbf{r}, t)$ to find the Brownian particle at position \mathbf{r} at time t [6,7]. In more mathematical terms this means that increments of Brownian motion, on a coarse-grained level [8], are independent and identically distributed random variables [9]. Apart from the linear time dependence $\langle \mathbf{r}^2(t) \rangle \propto Dt$ of the mean-square displacement (MSD), the quintessential consequence of these assumptions is the Gaussian PDF of a Brownian particle, $P(\mathbf{r}, t) = (4\pi Dt)^{-d/2} \exp(-\mathbf{r}^2/4Dt)$ in d spatial dimensions [7,9]. However, already in 1926 Richardson concluded from measurements of the stochastic motion of two pilot balloons in a turbulent atmosphere that the relative spreading, i.e., the diffusion coefficient for the relative coordinate of the balloons, increases with their distance l , and he fitted the data with the function $D(l) = \varepsilon l^{4/3}$ with the constant $\varepsilon \approx 0.4 \text{ cm}^2/\text{sec}$. [10]. Batchelor, in his work on homogeneous turbulence, showed that the second moment of the Richardson process can also be obtained by using the time-dependent scaling $D(t) \propto t^2$ of the diffusivity instead of the Richardson 4/3 law [11]. Today, anomalous diffusion with a power-law form $\langle \mathbf{r}^2(t) \rangle \propto t^\alpha$ is known from a wide range of systems. Based on the value of the anomalous diffusion expo-

nent, one typically distinguished subdiffusion for $0 < \alpha < 1$ and superdiffusion for $\alpha > 1$ [12–18].

The MSD and the particle displacement PDF are highly relevant quantities and they can be measured relatively straightforwardly in modern single-particle-tracking experiments [17,19]. However, they require relatively extensive experimental setups on geological scales [20]. In a typical geophysical field experiment, as schematically depicted in Fig. 1(a), a solute or a fine particle substance is injected into the site and its concentration is measured at selected points in space as a function of time [20–24]. For Brownian tracer particles advected with a drift velocity \mathbf{v} , the concentration profile has the shape $C(\mathbf{r}, t) \simeq (Dt)^{-d/2} \exp(-[\mathbf{r} - \mathbf{v}t]^2/4Dt)$. In many geophysical experiments the value of the PDF is measured at a given point \mathbf{r}_0 in space, as a function of time. This so-called breakthrough curve (BTC) at long times then shows an asymptotic exponential decay of the tracer concentration.

In contrast to this Brownian picture, power-law tails in the time dependence of BTCs have consistently been reported from the centimeter scale in the laboratory to field experiments on kilometer scales [22,25]. One example for such an experiment was reported in [22] based on the injection of fluorescent dye into sinking surface water leading to a karst aquifer under the Schwarzwasser valley, where BTCs were measured up to 7400 m away from the injection point. In such settings, the tracer motion is interrupted by immobilization periods, e.g., in dead-end pores with negligible flow, in which tracers are effectively trapped [24,26,27].

The continuous-time random walk (CTRW) is a well-established model describing power-law-tailed BTCs [22,28–32]. In a CTRW a single tracer jumps instantaneously,

*rmetzler@uni-potsdam.de

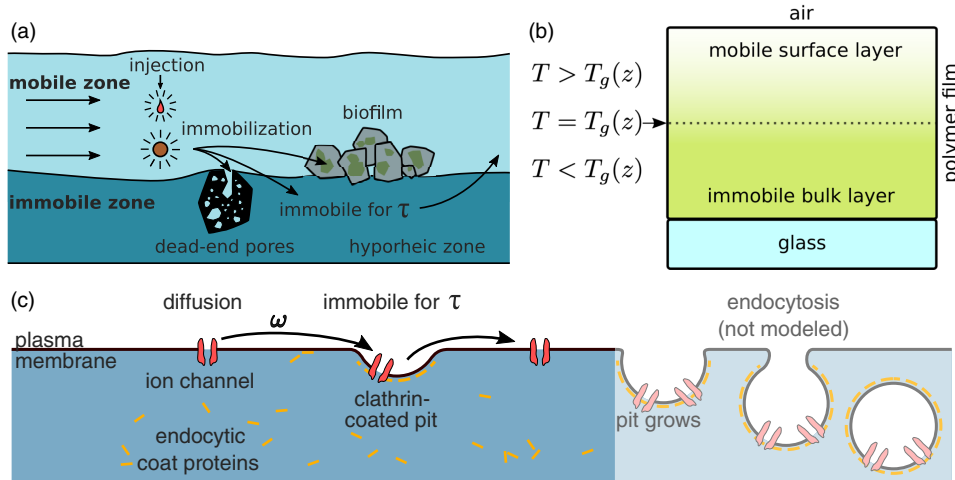


FIG. 1. Examples for systems with MIM zones. (a) Schematic of a tracer test in a typical geophysical setting. Dye or fine particles are injected into the mobile zone of a groundwater system or river. In our extended mobile-immobile model, which is based on [65,66], the tracers immobilize in dead-end pores, the hyporheic zone, or biofilms for a random time τ drawn from a probability density $\gamma(\tau)$ [see Eq. (1) for details]. After the period τ the tracers move back into the mobile zone. (b) Schematic of a thin polymer film on a glass substrate with depth-dependent glass transition temperature $T_g(z)$. Fluorescent dye is immobile in the bulk layer but mobile in the surface layer. (Figure was adapted from [59].) (c) Potassium channels diffuse in the plasma membrane of human embryonic kidney cells. Endocytic coat proteins assemble at the plasma membrane and generate clathrin-coated pits, to which the channel binds upon encounter. The majority of channels leave the pit before the clathrin-mediated endocytosis is completed. (Figure was adapted from [63].)

with variable jump lengths and waiting times drawn from respective PDFs [33,34]. A CTRW with scale-free power-law-distributed waiting times and jump lengths with a finite variance was originally introduced in the description of charge carrier motion in amorphous semiconductors [35] and is closely connected to the quenched energy landscape model [35–37]. When the waiting time PDF has a power-law tail of the form proportional to $t^{-1-\mu}$ with $0 < \mu < 1$, the associated mean waiting time diverges and anomalous non-Fickian diffusion arises [33–35]. In the quenched trap model, power-law waiting time PDFs are effected by exponential distributions of trap depths [36]. In contrast, in the model developed in [38] a particle undergoes Fickian diffusion which is interrupted by binding to spherical traps. All traps have the same binding energy. Using equilibrium statistics reveals that the densities of particles inside and outside the traps are linearly coupled with a refilling and an escape rate. This yields a linear MSD with rescaled time $t \rightarrow t/(1 + \lambda)$ with a positive parameter λ depending on the mean trapping time and trap density. For biased transport, the case of $1 < \mu < 2$ with finite mean waiting time but infinite variance still exhibits transport anomalies [39]. A power-law waiting time PDF (with exponential long-time cutoff reflecting the finiteness of the system) was indeed reconstructed from the hydraulic conductivity field in a heterogeneous porous medium [31]. Retention of chlorine tracer in catchments was also connected with power-law or Γ -distributed immobilization times [40,41]. In the CTRW picture the PDF $P(\mathbf{r}, t)$ does not distinguish between mobile and trapped particles [42].

Often, experiments in a geophysical setting yield incomplete mass recovery [20,22–24]. For instance, the setup

of the first macrodispersion experiment consisted of an array of multilevel samplers and flow meters to obtain the plume of bromide injected into a heterogeneous aquifer [20,43]. The total recovered mass monotonically decreased [20]. In addition, only (or preferably) tracers that are not immobilized may be measured, because they need to enter the detector, e.g., from a groundwater spring [22,26,44,45]. In such situations it is thus desirable to have a model that separates the mobile and immobile particle fractions. In order to distinguish between mobile and immobile particles within the CTRW a particle is defined to be mobile if it moves within a preset time interval [29]. It follows that for an exponential waiting time all particles are mobile for preset time intervals sufficiently longer than the characteristic waiting time [29].

A modeling approach that explicitly separates the two particle fractions and that is particularly popular in hydrology modeling is the mobile-immobile model (MIM) splitting the domain into mobile and immobile zones as depicted in Fig. 1(a) [26,45–49]. The description in MIM-type models typically considers one or two spatial dimensions, while transitions between the two zones occur along an eliminated dimension. In contrast to the CTRW model, where a single concentration profile describes all tracers, the MIM thus splits the concentration into a mobile and an immobile concentration [22,26,29,49]. Including a power-law distribution of transition rates between the zones yields power-law tailed BTCs. This model, called fractal MIM [45], is closely related to bifractional differential equations. Most notably in the context of this work, the MIM has been applied successfully to geophysical systems such as groundwater aquifers, rivers, and porous media [20–22,24,26,44,50,51]. Understanding the motion of introduced tracers in such systems is of high relevance

to understand the dynamics of contaminants in freshwater sources [21,22].

Figure 1(a) shows a schematic of such systems. In addition to dead-end pores, in another scenario the tracer can immobilize in streambed (benthic) biofilms [50,52–54]. Specifically, the attenuation of endocrine disruptors in a stream is attributed to sorption and biochemical reactions in biofilms [55]. Likely, adding wood to streams creates additional depositional areas for fine particles and bacteria, effectively increasing the immobile capacity [56]. Moreover, we mention the hyporheic zone, the region of near-stream aquifers [24] that is important for, *inter alia*, microplastic retention [57]. In addition, the hyporheic zone plays an important role in removing organic compounds from wastewater treatment plants that enter streams [58]. The reactivity of, e.g., metformin, a diabetes drug, is approximately 25 times higher in the hyporheic zone as compared to the in-stream reactivity [58]. The removal depends on hyporheic exchange fluxes [58]. The exchange of tracers between the mobile zone of a stream and the hyporheic zone has been studied intensively using MIM-type approaches [21,45,50].

Importantly, applications of MIM-type models go beyond geophysical settings. We mention that mobile and immobile zones can be found in polymer systems as shown in Fig. 1(b): A thin polymer film mounted on top of a glass support is kept at a temperature T slightly below the bulk glass transition temperature T_g [59]. Due to surface effects T_g is actually a decreasing function of the height z above the glass surface. Depending on z , the polymer is split into an immobile bulk layer and a shallow mobile surface layer [59–61]. Single-molecule-tracking experiments of fluorescent dyes in the polymer film corroborate this picture [59]. A second example is the transport of dye in crystalline microporous coordination polymers, showing a pronounced splitting into populations of fast, slow, and slowest fractions [62].

Another example with mobile and immobile zones stems from biophysics and is shown in Fig. 1(c). Here the potassium channel Kv2.1 diffuses in the plasma membrane of a human embryonic kidney cell. Upon encountering a clathrin-coated pit, the channels immobilize [63]. A small portion of the channels in the pit is transferred inside the cell via clathrin-mediated endocytosis [63]. The majority of channels escape the pit and continue to diffuse. The immobilization time statistic follows a power-law waiting time density with scaling exponent $\mu \approx 0.9$ [63].

In what follows we introduce and discuss in detail the extended mobile-immobile model (EMIM) describing the mobile and immobile concentrations of a given tracer substance. The dynamics is governed by a trapping time PDF of particles in the immobile zone, which in contrast to the MIM is not restricted to an exponential dynamic and is well defined in the short-time limit as compared to the case of a power-law-tailed PDF in the fractal MIM. We choose PDFs with and without characteristic waiting times. Note that while the EMIM we develop here is relevant to a broad range of systems, we will mainly use geophysical language in what follows. The reason is that this is the one of the most classical fields in which MIM-type models have been applied. However, the probabilistic formulation makes it easily accessible, and amenable for modifications, in other fields.

The paper is organized as follows. In Sec. II we present our EMIM in terms of partial integro-differential equations, we present general expressions such as the mobile mass and transport moments, and we present the BTCs. We obtain specific expressions for the observables in the EMIM and discuss possible extensions in Sec. III. In Sec. IV we derive from our EMIM bifractional models equivalent to the fractal MIM and obtain exact expressions for the moments using these models. A detailed comparison of the time evolution of the mobile mass and the BTC to experimental observations is presented in Sec. V. In Sec. VI we summarize our work and draw conclusions. In the Appendixes we introduce special functions, present details of our calculations, and show additional figures detailing the dynamics encoded in our EMIM.

II. THE EMIM

We depict the motion of tracer particles in the mobile and immobile zones in a one-dimensional two-state model, reflecting the typical situation of particles in a riverbed (or water artery), where the coordinate x measures the distance traveled along the river. Depending on its state, a tracer contributes to either the mobile concentration $C_m(x, t)$ or the immobile concentration $C_{im}(x, t)$. In our model tracers are initially placed in the mobile volume with mobile volume per unit length θ_m in which their motion combines advection and diffusion, mathematically captured by the advection-dispersion operator $L(x) = -v\partial/\partial x + D\partial^2/\partial x^2$ with the advection velocity v [64]. When entering the immobile volume θ_{im} the tracers are immobilized for a duration t drawn from the trapping time PDF $\gamma(t)$, *a priori* of arbitrary shape. We name this model the extended MIM, governed by the transport equations

$$\frac{\partial}{\partial t} C_m(x, t) = -\beta\omega C_m(x, t) + \int_0^t \gamma(t-\tau)\beta\omega C_m(x, \tau)d\tau + L(x)C_m(x, t), \quad (1a)$$

$$\frac{\partial}{\partial t} C_{im}(x, t) = \omega C_m(x, t) - \int_0^t \gamma(t-\tau)\omega C_m(x, \tau)d\tau. \quad (1b)$$

Here ω denotes the mass transfer coefficient and $\beta = \theta_{im}/\theta_m$ the capacity coefficient often used in geophysical contexts. We highlight that this EMIM is based on the two-state, non-Markovian kinetic rate equations for exciton trapping in semiconductors developed in [65] to which we added the advection-dispersion operator.

In this formulation $\gamma(t)$ indeed denotes the trapping time PDF. As can be seen from the relation (1b), particles entering the immobile zone at a previous time $t - \tau$ are released back to the mobile phase with a probability $\gamma(\tau)$. Using the masses

$$M_m(t) = \theta_m \int_{-\infty}^{\infty} dx C_m(x, t), \quad M_{im}(t) = \theta_{im} \int_{-\infty}^{\infty} dx C_{im}(x, t) \quad (2)$$

in the mobile and immobile zones, respectively, we obtain total mass conservation

$$\frac{d}{dt} [M_m(t) + M_{im}(t)] = 0. \quad (3)$$

We choose the initial condition as the sharp δ peak $C_m(x, 0) = M_0/\theta_m\delta(x)$ and $C_{im}(x, 0) = 0$, which naturally arises in typical experiments [22,50]. Using the Fourier-Laplace transform,

we obtain from (1) the solution

$$C_m(k, s) = \frac{M_0}{s + \beta\omega[1 - \gamma(s)] - ikv + k^2D} \quad (4)$$

for the mobile concentration, where $f(k, s) = \int_{-\infty}^{\infty} \int_0^{\infty} f(x, t) \exp(-st + ikx) dt dx$ denotes the Fourier-Laplace transform of $f(x, t)$, which we solely mark by replacing its arguments. We note that this equation has been previously reported, although without the corresponding equation in the time domain [66]. For the immobile concentration we find

$$C_{im}(k, s) = \omega C_m(k, s) \frac{1 - \gamma(s)}{s}. \quad (5)$$

In this two-state approach, when modeling the exchange between the mobile and immobile zones with single-rate first-order mass transfer, exponential long-time decay arises in the BTCs and hence it cannot describe power-law-tailed BTCs [45,67] (see also the discussion below). In the multi-rate mass transfer (MRMT) model, multiple rate coefficients are introduced [49], in which a continuous density of rates following a power-law distribution yields the observed BTCs with a power-law tail [45,67,68]. A distribution of rates occurs in heterogeneous mixtures of layers, cylinders, spheres, or heterogeneous porous sedimentary rock [49,69]. Often, the cumulative function of the trapping time PDF, $\Psi = \int_t^{\infty} \gamma(\tau) d\tau = 1 - \int_0^t \gamma(\tau) d\tau$ [42], is used for the characterization [24], which can, e.g., be reconstructed from a porous medium using x-ray microtomography [27]. If the jump length distribution is independent of the trapping time distribution, the total concentrations of the CTRW and MRMT approaches are indeed equivalent [29,70]. In [45] it was shown that the choice of the power-law form $\Psi(t) = t^{-\mu}/\Gamma(1 - \mu)$, with $0 < \mu < 1$, yields a bifractional diffusion-advection equation called fractal MIM [45,71]. In the long-time limit of the fractal MIM the first and second moments of the mobile concentration scale as $\langle x_m \rangle \simeq t^\mu$ and $\langle (x_m - \langle x_m \rangle)^2 \rangle \simeq t^{2\mu}$, respectively, and reveal superdiffusion for $\mu > 1/2$ and subdiffusion for $\mu < 1/2$, while the mobile particles behave like Brownian particles with drift in the short-time limit [46]. The choice $\Psi(t) = t^{-\mu}/\Gamma(1 - \mu)$, however, does not yield a finite value for $\gamma(0)$ and makes γ non-normalizable.

To circumvent this issue, we propose the EMIM (1) that consists of rate equations for both the mobile and immobile concentration. The trapping time in the immobile zone is drawn from the well-defined trapping time PDF which, in contrast to the MIM, is not restricted to an exponential. Our model unifies the following approaches. First, it is an extension of the non-Markovian rate equations used to describe excitons in semiconductors [65] to which we add an advection-dispersion operator. A similar equation exclusively for mobile tracers without advection was presented to describe fine particle deposition in benthic biofilms [52]. Second, we expand the model proposed in [72] in which a particle is mobile for a fixed duration and immobile for a random time drawn from a one-sided Lévy distribution; there, effectively the total concentration is considered and no separate equations are used for mobile and immobile particles. Third, our model corresponds to a model used for particle-tracking simulations [66]. In this work it is argued that the model incorporates waiting time

PDFs, and these PDFs are included in the Fourier-Laplace representation. Here we derive and discuss the corresponding rate equations as functions of time and space. Fourth, our model contains the fractal MIM [45] as a special case. When considering the total concentration, i.e., the sum of mobile and immobile concentrations, the fractal MIM is a special case of distributed-order diffusion with a bimodal distribution of fractional orders where the first order is unity and the second ranges between zero. Moreover, we add an advective bias term to this formulation [71].

When rewriting our rate equations in terms of the survival probability, our model matches the MRMT model in [67]. Another set of rate equations involving the immobilization time as a second temporal variable can be found in [73,74]. By choosing a Mittag-Leffler (ML) waiting time PDF our model contains the bifractional solute transport models in [45,71] in the long-time limit, including a power-law decay of the total mobile mass, while retaining a finite value of the memory function in the zero-time limit, $\gamma_{ML}(0)$. From a physical perspective, the accumulation of immobile particles is similar to particles diffusing in an energy landscape scattered with energetic traps with power-law trapping times [75–77]. We note that while many studies focus on BTCs, some work has been reported regarding the spatial tracer plumes [20,45,78,79]. We address here the question of where the contaminants are in space and how far they spread on average, given a known BTC. Spatial moments of the total concentration and their derivative, the center-of-mass velocity, were, *inter alia*, discussed in [29]. We distinguish here between mobile and immobile distributions, reflecting that in some situations, including the transport dynamics in rivers, only the mobile particles can be detected [22,78]. In [46], approximations for the first five moments are derived, *inter alia*, for the fractal MIM including moments of the mobile plume. Building on such concepts, from our ML waiting time PDF, we obtain explicit expressions for the spatial moments of the mobile, immobile, and total masses.

A. General expressions

We now present the central observables of our model that are calculated as function of a general trapping time PDF.

1. Mobile mass

We set $k = 0$ in Eq. (4) to arrive at the mobile mass in Laplace space. Moreover, we set $\theta_m = 1$ as a unit volume, without loss of generality. We then obtain

$$M_m(s) = \frac{M_0}{s + \beta\omega[1 - \gamma(s)]}. \quad (6)$$

The long-time behavior depends on the exact form of the immobilization time PDF, in particular, on whether we have a finite or infinite mean immobilization time. Let us first assume the general waiting time PDF $\gamma_f(t)$ (f denotes finite) with a finite mean $\langle \tau \rangle$. For a small Laplace variable s it can be approximated by $\gamma_f(s) \sim 1 - s\langle \tau \rangle$, which yields the corresponding long-time limit from (6) in terms of the constant value

$$\lim_{t \rightarrow \infty} M(t) = \lim_{s \rightarrow 0} sM(s) = \frac{M_0}{1 + \beta\omega\langle \tau \rangle}, \quad (7)$$

which is consistent with [26,44,66] since $\beta\omega\langle\tau\rangle$ corresponds to the ratio of the time spent in the mobile zone to that in the immobile zone.

For a general PDF $\gamma_d(\tau)$ (d denotes divergent) with diverging mean, we consider its representation for small s with $0 < \mu < 1$ and $\tau_* > 0$, of the form $\gamma_d(s) \sim 1 - (\tau_*s)^\mu$, where τ_* is a scaling factor, and plug it into the general expression (6), where we look for the long-time limit using the Tauberian theorem [80],

$$\lim_{s \rightarrow 0} M(s) \sim \frac{M_0}{\beta\omega\tau_*^\mu s^\mu} \quad \text{s.t.} \quad \lim_{t \rightarrow \infty} M(t) \sim M_0 \frac{t^{\mu-1}}{\beta\omega\tau_*^\mu \Gamma(\mu)}. \quad (8)$$

We conclude that a waiting time PDF with diverging mean will, remarkably, yield a long-time power-law decay of the mobile mass and thus leave no particles in the mobile zone in the long-time limit, in contrast to a waiting time PDF with finite mean as seen in (7).

2. Moments

From the PDF

$$\begin{aligned} \rho(k, s) &= \frac{1}{M_0} [C_m(k, s) + \beta C_{im}(k, s)] \\ &= \frac{1}{s} \frac{s + \beta\omega[1 - \gamma(s)]}{s + \beta\omega[1 - \gamma(s)] - ikv + k^2D} \end{aligned} \quad (9)$$

in Fourier-Laplace space we can calculate the n th moment in Laplace space via

$$\langle x^n(s) \rangle = (-i)^n \frac{\partial^n}{\partial k^n} \rho(k, s) \Big|_{k=0}. \quad (10)$$

We are interested in the motion of the solute in the mobile phase, as this is the typically accessible experimental quantity [20,22,26,43,52]. Since the mass in the mobile phase changes over time we consider both the unnormalized and the normalized moments, where normalization means dividing the unnormalized moment (denoted by u) (10) by the mobile mass (6) [20,81],

$$\langle x_m^n(t) \rangle = \langle x^n(t) \rangle_u M_0 / M_m(t). \quad (11)$$

We start with the first moment. In the unnormalized form, we have

$$\langle x_m(s) \rangle_u \equiv -i \frac{\partial}{\partial k} \frac{C_m(k, s)}{M_0} \Big|_{k=0} = \frac{v}{\{s + \beta\omega[1 - \gamma(s)]\}^2}. \quad (12)$$

The short-time behavior $\langle x_m(s) \rangle_u = \frac{v}{\{s + \beta\omega[1 - \gamma(s)]\}^2} \sim \frac{v}{s^2}$ of this expression can be obtained independently of the trapping time PDF by using the Tauberian theorem for $s \rightarrow \infty$ and $\gamma(s) \leq 1$, which yields $\langle x \rangle_u(t) = vt$ for small t . This is an expected result, since essentially all mass is mobile at $t = 0$, our initial condition. We obtain

$$\langle x(t) \rangle \stackrel{t \rightarrow 0}{\sim} \langle x_m(t) \rangle_u \stackrel{t \rightarrow 0}{\sim} vt. \quad (13)$$

To assess the long-time behavior we need to know the specific form of the waiting time PDF $\gamma(t)$. We will analyze the long-time behavior for different cases below.

The unnormalized second moment can be calculated analogously,

$$\begin{aligned} \langle x_m^2(s) \rangle_u &= -\frac{\partial^2}{\partial k^2} \frac{C_m(k, s)}{M_0} \Big|_{k=0} = \frac{2v^2}{\{s + \beta\omega[1 - \gamma(s)]\}^3} \\ &+ \frac{2D}{\{s + \beta\omega[1 - \gamma(s)]\}^2}. \end{aligned} \quad (14)$$

The corresponding normalized form $\langle x^2(t) \rangle$ follows in the time domain by multiplication with $M_0/M_m(t)$ [Eq. (6)]. The short-time behavior $\langle x^2(s) \rangle_u \sim \frac{2v^2}{s^3} + \frac{2D}{s^2}$ of the second moment can be obtained via the Tauberian theorem for $s \rightarrow \infty$ and the above limit form $\gamma(s) \leq 1$, which yields $\langle x^2(t) \rangle_u \sim 2Dt + v^2t^2$ at short times. Since the mobile mass is approximately M_0 , initially we obtain Brownian motion with advection,

$$\langle x^2(t) \rangle \stackrel{t \rightarrow 0}{\sim} 2Dt + v^2t^2, \quad (15)$$

a result that holds for both $\langle x^2(t) \rangle_u$ and $\langle x^2(t) \rangle$ in this $t \rightarrow 0$ limit.

From the general relation (5) between C_m and C_{im} and the n th unnormalized moment (12) we obtain

$$\begin{aligned} \langle x_{im}^n \rangle_u &= \beta (-i)^n \frac{\partial^n}{\partial k^n} \frac{C_{im}(k, s)}{M_0} \Big|_{k=0} \\ &= \beta\omega \frac{1 - \gamma(s)}{s} (-i)^n \frac{\partial^n}{\partial k^n} \frac{C_m(k, s)}{M_0} \Big|_{k=0} \\ &= \langle x_m^n \rangle_u \beta\omega \frac{1 - \gamma(s)}{s}. \end{aligned} \quad (16)$$

This quantity describes the spreading of particles in the immobile zone, as they progress by joining the mobile phase and getting absorbed into the immobile zone again. In the expression (16) we notice the factor β that appears when integrating over the immobile domain, i.e., setting $k = 0$, because the immobile domain is larger by this factor than the mobile domain. In addition, we calculate the n th moment of the full concentration using Eq. (9) for $\rho(k, s)$,

$$\langle x^n \rangle = \langle x_m^n \rangle_u + \beta \langle x_{im}^n \rangle_u. \quad (17)$$

3. Breakthrough curves

A typical tracer experiment on the field scale records the mobile concentration at a fixed location as a function of time. The obtained statistic is called the breakthrough curve [22,27,28,45,53,54]. When comparing BTCs at different sites with different volumetric fluid discharges Q , it is convenient to analyze the quantity $C \times Q / M_{\text{recov}}$, with the total recovered mass M_{recov} [22]. Inverse Fourier transformation of (4) yields the concentration in the space domain,

$$C_m(x, s) = \frac{\exp\left(\frac{vx}{2D}\right)}{\sqrt{v^2 + 4\phi(s)D}} \exp\left(-\sqrt{v^2 + 4\phi(s)D} \frac{|x|}{2D}\right), \quad (18)$$

with $\phi(s) = s + \beta\omega[1 - \gamma(s)]$. Its form in the time domain requires an explicit input for $\phi(s)$ (discussed below).

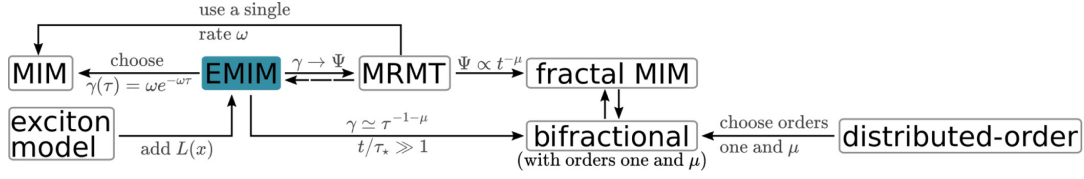


FIG. 2. Relation between different transport models. The EMIM follows from the exciton model [65] by adding the transport operator $L(x)$. The EMIM contains the MIM as a special case for $\gamma(\tau) = \omega e^{-\omega\tau}$, as shown in Sec. III A. Using the cumulative Ψ probability function of γ , the EMIM can be rewritten as an MRMT model, as presented in Sec. IV. Going the opposite direction requires $\Psi(0) = 1$. If $\Psi \propto t^{-\mu}$, the MRMT model is equivalent to the fractal MIM [45]. The full concentration follows a bifractional diffusion equation. The latter arises directly from the EMIM in the long-time limit, when the waiting time PDF asymptotically behaves like $\tau^{-1-\mu}$. The bifractional diffusion equation is a special case of distributed-order diffusion where instead of a continuous distribution the values one and μ for the diffusion exponents are chosen.

III. EMIM DYNAMICS FOR SPECIFIC TRAPPING PDFS

We now obtain explicit forms for the characteristic observables in the EMIM dynamics for exponential and ML-type trapping time density functions and discuss possible extensions of our model.

A. Exponential trapping time distribution

We start with the choice of an exponential distribution for the trapping time PDF,

$$\gamma(\tau) = \omega e^{-\omega\tau}, \quad (19)$$

with mean $\langle \tau \rangle = 1/\omega$. The variable ω is identical to the mass transfer coefficient from the rate equations (1). In the following, we demonstrate three implications of this choice. First, when choosing an exponential distribution in the EMIM the mobile concentration reflects one state of a general Markovian two-state model. Second, it follows immediately that matching ω with the mass transfer coefficient from our rate equations (1) is not a restriction when only considering mobile tracers. Hence, we make this choice in (19). Third, we show the equivalence of both EMIM rate equations with the choice (19) in the model of [26].

To this end let us consider a general Markovian two-state MIM with immobilization rate ω_1 and remobilization rate ω_2 as discussed in [65],

$$\begin{aligned} \frac{\partial}{\partial t} C_m &= -\omega_1 C_m + \omega_2 C_{im} + L(x) C_m, \\ \frac{\partial}{\partial t} C_{im} &= \omega_1 C_m - \omega_2 C_{im}, \end{aligned} \quad (20)$$

where we added the advection-diffusion operator $L(x)$ to the mobile rate equation. From (20) with the initial conditions $C_{im}(x, 0) = 0$ and $C_m(x, 0) = M_0 \delta(x)$ we obtain the formal solution [65]

$$C_{im}(x, t) = \int_0^t \omega_1 e^{-\omega_2(t-\tau)} C_m(x, \tau) d\tau. \quad (21)$$

We insert this solution into (20) to find

$$\begin{aligned} \frac{\partial}{\partial t} C_m(x, t) &= -\omega_1 C_m(x, t) + \omega_1 \int_0^t \omega_2 e^{-\omega_2(t-\tau)} C_m(x, \tau) d\tau \\ &\quad + L(x) C_m(x, t). \end{aligned} \quad (22)$$

If we now replace ω_2 with ω and ω_1 with $\beta\omega$, we recover the mobile rate equation of the EMIM (1a) with the specific choice (19). The rate equation for the immobile concentration,

$$\frac{\partial}{\partial t} C_{im}(x, t) = \beta\omega C_m(x, t) - \beta \int_0^t \gamma(t-\tau) \omega C_m(x, \tau) d\tau, \quad (23)$$

differs from our immobile rate equation (1b) only by the factor β . Note that the equivalence of the mobile concentrations suffices because C_{im} is typically not measured. We can repeat the same steps with the rate equations, which are equivalent to the model proposed in [26],

$$\frac{\partial C_m}{\partial t} + \beta \frac{\partial C_{im}}{\partial t} = L(x) C_m, \quad (24a)$$

$$\frac{\partial C_{im}}{\partial t} = \omega(C_m - C_{im}), \quad (24b)$$

for which we obtain

$$\frac{\partial}{\partial t} C_{im}(x, t) = \omega C_m(x, t) - \int_0^t \omega e^{-\omega(t-\tau)} C_m(x, \tau) d\tau. \quad (25)$$

Note specifically the equivalence with both our mobile and immobile rate equations (1), as can be seen from inserting (25) in (24a). Equations (24) are first-order rate equations. Therefore, we refer to the choice $\gamma(\tau) = \omega \exp(-\omega\tau)$ as the first-order model or simply exponential model. Figure 2 visualizes the relation of the EMIM to the MIM and other models.

In the long-time limit corresponding to $s \rightarrow 0$ in Laplace space, the mobile concentration is equal to the immobile concentration, as we show in the following calculation starting from the general relation (5) between C_{im} and C_m :

$$\begin{aligned} \lim_{s \rightarrow 0} C_{im}(k, s) &= \lim_{s \rightarrow 0} \omega C_m(k, s) \frac{1 - \frac{\omega}{s+\omega}}{s} \\ &= \lim_{s \rightarrow 0} \frac{\omega}{s + \omega} C_m(k, s) = \lim_{s \rightarrow 0} C_m(k, s). \end{aligned} \quad (26)$$

Therefore, it suffices to calculate the long-time limits of the normalized moments of the mobile concentration to obtain the long-time limits of the moments of the immobile and full concentrations. Note that, due to different mobile and immobile volumes, the respective masses differ, which, however, does not restrict generality.

1. Mobile mass

Inverse Laplace transformation of the mobile mass (6) yields

$$M_m(t) = \frac{M_0}{1+\beta} (1 + \beta e^{-\omega(1+\beta)t}), \text{ and thus}$$

$$\lim_{t \rightarrow \infty} M_m(t) = \frac{M_0}{1+\beta} \quad (27)$$

in the long-time limit, in accordance with (7) with $\langle \tau \rangle = 1/\omega$.

2. Moments

Using the general equation (12) for $\langle x_m(s) \rangle_u$, we obtain the result for the unnormalized first moment in time domain through inverse Laplace transformation,

$$\langle x_m(t) \rangle_u = \frac{vt}{(1+\beta)^2} (1 + \beta^2 e^{-\omega(1+\beta)t}) + v \frac{2\beta}{(1+\beta)^3 \omega} (1 - e^{-\omega(1+\beta)t}), \quad (28)$$

from which we find the long-time behavior

$$\langle x_m(t) \rangle_u \stackrel{t \rightarrow \infty}{\sim} \frac{vt}{(1+\beta)^2}. \quad (29)$$

We divide (28) by the mobile mass for normalization,

$$\langle x_m(t) \rangle = \frac{vt}{(1+\beta)} \frac{1 + \beta^2 e^{-\omega(1+\beta)t}}{1 + \beta e^{-\omega(1+\beta)t}} + v \frac{2\beta}{(1+\beta)^2 \omega} \frac{1 - e^{-\omega(1+\beta)t}}{1 + \beta e^{-\omega(1+\beta)t}}, \quad (30)$$

and find the corresponding long-time behavior

$$\langle x_m(t) \rangle \stackrel{t \rightarrow \infty}{\sim} \frac{vt}{1+\beta}. \quad (31)$$

The normalization thus corresponds to rescaling time as $t \rightarrow t/(1+\beta)$.

After Laplace inversion of (14) we find the unnormalized second moment valid at all times,

$$\langle x_m^2(t) \rangle_u = \frac{2v^2}{(1+\beta)^3} \left[t^2 \left(\frac{1}{2} + \frac{\beta^3}{2} e^{-(1+\beta)\omega t} \right) + t \frac{3\beta}{(1+\beta)\omega} (1 - \beta e^{-(1+\beta)\omega t}) + \frac{3(\beta^2 - \beta)}{(1+\beta)^2 \omega^2} (1 - e^{-(1+\beta)\omega t}) \right] + 2D \frac{t}{(1+\beta)^2} (1 + \beta^2 e^{-(1+\beta)\omega t}) + 2D \frac{2\beta}{(1+\beta)^3 \omega} (1 - e^{-(1+\beta)\omega t}), \quad (32)$$

and after normalizing with $M_m(t)$ [expression (27)], we obtain the normalized second mobile moment

$$\langle x_m^2(t) \rangle = \frac{2v^2}{(1+\beta)^2 (1 + \beta e^{-(1+\beta)\omega t})} \left[t^2 \left(\frac{1}{2} + \frac{\beta^3}{2} e^{-(1+\beta)\omega t} \right) + t \frac{3\beta}{(1+\beta)\omega} (1 - \beta e^{-(1+\beta)\omega t}) \right]$$

$$+ \frac{3(\beta^2 - \beta)}{(1+\beta)^2 \omega^2} (1 - e^{-(1+\beta)\omega t}) \Big] + 2D \frac{t}{(1+\beta)} \frac{1 + \beta^2 e^{-(1+\beta)\omega t}}{1 + \beta e^{-(1+\beta)\omega t}} + 2D \frac{2\beta}{(1+\beta)^2 \omega} \frac{1 - e^{-(1+\beta)\omega t}}{1 + \beta e^{-(1+\beta)\omega t}}. \quad (33)$$

In the long-time limit $t \gg 1/(1+\beta)\omega$ we find from (32) that

$$\langle x_m^2(t) \rangle_u \stackrel{t \rightarrow \infty}{\sim} \frac{v^2}{(1+\beta)^3} t^2 + 2D \frac{t}{(1+\beta)^2}. \quad (34)$$

When we account for the change of mobile mass, we obtain

$$\langle x_m^2(t) \rangle \stackrel{t \rightarrow \infty}{\sim} \frac{v^2}{(1+\beta)^2} t^2 + 2D \frac{t}{1+\beta}, \quad (35)$$

which, as for the first moment, corresponds to rescaling time $t \rightarrow t/(1+\beta)$ [see the relation (69) in [45]]. In fact, the expression (35) in terms of $t/(1+\beta)$ is exactly the expected combination of advection and diffusion of a Brownian particle in a drift flow v , $v^2 t^2 + 2Dt$.

In the long-time limit we obtain the second central moment for the classical model in the form

$$\langle (x - \langle x \rangle)^2 \rangle \stackrel{t \rightarrow \infty}{\sim} 2 \frac{D}{1+\beta} t, \quad (36)$$

which grows linearly and corresponds to free Brownian motion with rescaled time $t \rightarrow t/(1+\beta)$. These results coincide with those reported in [79].

3. Breakthrough curves

We finally calculate the long-time behavior of the mobile concentration $C_m(x, t)$, whose interpretation at a fixed point x is that of the BTC. Starting from the general expression (18) for $C_m(k, s)$, we find for a small Laplace variable s that $\phi \sim s(1+\beta)$. Fourier-Laplace inversion to the space-time domain yields the expected Gaussian form

$$C_m(x, t) \sim \frac{M_0}{1+\beta} \frac{\sqrt{1+\beta}}{\sqrt{4\pi Dt}} \exp \left(- \left[x - \frac{vt}{1+\beta} \right]^2 \frac{1+\beta}{4Dt} \right). \quad (37)$$

This result quantifies the concentration of a free Brownian particle with rescaled time $t \rightarrow t/(1+\beta)$. Note that the immobile concentration has the same long-time limit as shown in (26).

B. Mittag-Leffler trapping time distribution

We now turn to the case when the characteristic trapping time becomes infinite and, as an explicit form, choose the generalized or two-parametric ML trapping time PDF [82,83]

$$\gamma_{\text{ML}}(t) = \frac{(t/\tau_*)^\mu}{t} E_{\mu, \mu}(-[t/\tau_*]^\mu), \quad (38)$$

with $0 < \mu < 1$ and $\tau_* > 0$. This distribution has the power-law tail $\simeq t^{-1-\mu}$ that indeed produces a diverging mean. We refer to the choice (38) as the ML model in the following. The corresponding PDF in the Laplace domain reads [84]

$$\gamma_{\text{ML}}(s) = \frac{1}{1 + (\tau_* s)^\mu}. \quad (39)$$

In Sec. IV we show that the dynamics of the total tracer concentration in our model is a particular case of the bifractional diffusion equation [71], to which a transport term is added, and the fractal model [45], in the long-time limit $t \gg \tau_*$. We note that another common choice for a PDF with a power-law tail is the one-sided Lévy distribution [34,65,71]. While the latter is supported formally by the generalized central limit theorem [85], its more intricate Laplace transform $\exp[-(\tau_*s)^\mu]$ renders analytical calculations virtually impossible. As the results are expected to be very close to those of the ML model, we use the more easily tractable ML PDF as the basis for our further study.

1. Mobile mass decay

For the mobile mass $M_m(s)$ [see the expression (6)], we obtain in Appendix A that

$$M_m(t) = M_0 e^{-\beta\omega t} + M_0 \beta\omega \tau_*^\mu t \sum_{k=1}^{\infty} (-1)^{k+1} \left(\frac{t}{\tau_*}\right)^{\mu k} \times E_{1,\mu k+2}^{k+1}(-\beta\omega \tau_*^\mu t), \quad (40)$$

which yields the short-time behavior

$$M_m(t) \sim M_0(1 - \beta\omega t) + M_0 \frac{\beta\omega t}{\Gamma(\mu + 2)} \left(\frac{t}{\tau_*}\right)^\mu + O(t^\alpha). \quad (41)$$

Here the first term contains the initial mobile mass and immobilization with rate $\beta\omega$. The second term contains the lowest order of the tracer remobilization proportional to $t^{1+\mu}$. The Landau symbol $O(\cdot)$ here represents higher-order terms with $\alpha = \min(1 + 2\mu, 2)$. Note that the series (40) converges relatively slowly in numerical implementations.

We calculate the long-time limit of the mobile mass from its Laplace representation. For $t \rightarrow \infty$, corresponding to $s \rightarrow 0$, we can approximate $\gamma_{\text{ML}} \sim 1 - (\tau_*s)^\mu$. We plug this form into the general expression of $M_m(s)$ [Eq. (6)] and find $M_m(s) \sim \frac{M_0}{\beta\omega \tau_*^\mu s^\mu}$ for $s \ll 1/\tau_*$. Via the Tauberian theorem, we obtain the result in the time domain,

$$M_m \stackrel{t \rightarrow \infty}{\sim} M_0 \frac{t^{\mu-1}}{\beta\omega \tau_*^\mu \Gamma(\mu)}, \quad (42)$$

in agreement with result (8).

2. Moments

We calculate the long-time limits of the moments using the same approximation $\gamma(s)_{\text{ML}} \sim 1 - (\tau_*s)^\mu$ for $t \rightarrow \infty$ as for the mobile mass asymptotes. Using the general formula (12) for the first unnormalized moment in Laplace space, we find

$$\begin{aligned} \langle x_m \rangle_u &= i \frac{\partial}{\partial k} \frac{C_m(s)}{M_0} \Big|_{k=0} = \frac{v}{(s + \beta\omega \tau_*^\mu s^\mu)^2} \\ &= \frac{v}{s^2 + 2\beta\omega \tau_*^\mu s^{1+\mu} + \beta^2 \omega^2 s^{2\mu}} \stackrel{s \rightarrow 0}{\sim} \frac{v}{\beta^2 \omega^2 \tau_*^{2\mu} s^{2\mu}}. \end{aligned} \quad (43)$$

In the last step, we used that $0 < \mu < 1$. This corresponds to

$$\langle x_m \rangle_u \stackrel{t \rightarrow \infty}{\sim} v \frac{t^{2\mu-1}}{\beta^2 \omega^2 \tau_*^{2\mu} \Gamma(2\mu)}. \quad (44)$$

We now turn to the normalized first moment for large $t \rightarrow \infty$ and take the quotient of (44) and (42), namely,

$$\langle x_m \rangle \stackrel{t \rightarrow \infty}{\sim} \frac{v \frac{t^{2\mu-1}}{\beta^2 \omega^2 \tau_*^{2\mu} \Gamma(2\mu)}}{\frac{t^{\mu-1}}{\beta\omega \tau_*^\mu \Gamma(\mu)}} = \frac{v t^\mu}{\beta\omega \tau_*^\mu} \frac{\Gamma(\mu)}{\Gamma(2\mu)}. \quad (45)$$

The asymptote of the first moment is hence nonlinear, similar to the subdiffusive CTRW case [14].

To obtain the asymptote of the first moment from the immobile concentration, we start from the general relation (16) between $\langle x_m^n \rangle_u$ and $\langle x_{im}^n \rangle_u$ for $n = 1$, obtaining, for $s \rightarrow 0$,

$$\begin{aligned} \langle x_{im} \rangle_u &= \omega \beta v \frac{1}{\{s + \beta\omega[1 - \gamma(s)]\}^2} \frac{1 - \gamma(s)}{s} \\ &= \omega \beta v \frac{\tau_*^\mu s^{\mu-1}}{(s + \beta\omega \tau_*^\mu s^\mu)^2} \stackrel{s \rightarrow 0}{\sim} v \frac{s^{-\mu-1}}{\beta\omega \tau_*^\mu}, \end{aligned} \quad (46)$$

which in the time domain corresponds to

$$\langle x_{im} \rangle \stackrel{t \rightarrow \infty}{\sim} \frac{v t^\mu}{\beta\omega \tau_*^\mu \Gamma(1 + \mu)}. \quad (47)$$

Note that in the long-time limit all mass is immobile and hence we do not need to normalize the moment. This result differs from $\langle x_m \rangle$ only by the factor $\Gamma(2\mu)/\Gamma(\mu)\Gamma(1 + \mu)$, which is unity for $\mu = 1$ and larger than unity for $0 < \mu < 1$. Thus, the mobile particles travel further on average than the immobile particles in the long-time limit, as it should be.

In what follows, we restrict ourselves to the mobile moments. Calculations of higher immobile moments are fully analogous to the mobile moments and the first immobile moment.

Let us turn to the second unnormalized mobile moment for $s \rightarrow 0$,

$$\langle x_m^2 \rangle_u = - \frac{\partial^2}{\partial k^2} \frac{C_m(s)}{M_0} \Big|_{k=0} \stackrel{s \rightarrow 0}{\sim} \frac{2D}{\beta^2 \omega^2 \tau_*^{2\mu} s^{2\mu}} + \frac{2v^2}{\beta^3 \omega^3 \tau_*^{3\mu} s^{3\mu}}. \quad (48)$$

This corresponds, in the time domain, to

$$\langle x_m^2 \rangle_u \stackrel{t \rightarrow \infty}{\sim} 2D \frac{t^{2\mu-1}}{\beta^2 \omega^2 \tau_*^{2\mu} \Gamma(2\mu)} + 2v^2 \frac{t^{3\mu-1}}{\beta^3 \omega^3 \tau_*^{3\mu} \Gamma(3\mu)}. \quad (49)$$

Let us look at the normalized second moment for long t and take the quotient of (49) and (42), namely,

$$\begin{aligned} \langle x_m^2 \rangle &\stackrel{t \rightarrow \infty}{\sim} \frac{2D \frac{t^{2\mu-1}}{\beta^2 \omega^2 \tau_*^{2\mu} \Gamma(2\mu)} + 2v^2 \frac{t^{3\mu-1}}{\beta^3 \omega^3 \tau_*^{3\mu} \Gamma(3\mu)}}{\frac{t^{\mu-1}}{\beta\omega \tau_*^\mu \Gamma(\mu)}} \\ &= 2D \Gamma(\mu) \frac{t^\mu}{\beta\omega \tau_*^\mu \Gamma(2\mu)} + 2v^2 \Gamma(\mu) \frac{t^{2\mu}}{\beta^2 \omega^2 \tau_*^{2\mu} \Gamma(3\mu)}. \end{aligned} \quad (50)$$

If only mobile tracers can be observed and the waiting time PDF does not depend on β or ω , the parameters β and ω cannot be determined individually, because they only appear as the product $\beta\omega$ in the Fourier-Laplace solution (4) of $C_m(k, s)$ and all quantities derived therefrom. Additionally, in the long-time limits of the ML model the parameter τ_* solely appears in the product $\beta\omega \tau_*^\mu$ and hence cannot be determined separately. When only the long-time behavior of the mobile

tracers is known, it therefore makes sense to only consider the parameter $\beta'_s = \beta\omega\tau_*^\mu$. At intermediate times, the parameter τ_* can be obtained independently of $\beta\omega$, as the mobile mass (40) shows for the ML model.

Using the asymptotes (45) and (50) of the first and second moments, we obtain the second central moment

$$\begin{aligned} & \{[x_m(t) - \langle x_m(t) \rangle]^2\} \\ &= 2D\Gamma(\mu) \frac{t^\mu}{\beta\omega\tau_*^\mu\Gamma(2\mu)} \\ &+ v^2\Gamma(\mu) \frac{t^{2\mu}}{(\beta\omega\tau_*^\mu)^2} \left(\frac{2}{\Gamma(3\mu)} - \frac{\Gamma(\mu)}{\Gamma^2(2\mu)} \right). \end{aligned} \quad (51)$$

The expression in the large parentheses only vanishes for $\mu = 1$. In the long-time limit, the second central moment hence behaves as $t^{2\mu}$, i.e., subdiffusively for $0 < \mu < 1/2$ and superdiffusively for $1/2 < \mu < 1$. The occurrence of a superdiffusive behavior in a process dominated by a scale-free waiting time PDFs is known for subdiffusive CTRW processes with drift [35]. The phenomenon stems from the fact that the process has a strong memory of the initial position, its amplitude decaying only as $\simeq t^{-\mu}$. Concurrently, the mobile particles are advected, thus creating a highly asymmetric position PDF of the process. In fact, while for a Brownian particle the ratio of standard deviation to mean position decays as $\simeq t^{-1/2}$, for the subdiffusive particle the ratio is asymptotically constant, reflecting the large particle spread [35]. This behavior is also witnessed by the slope of the concentration profiles discussed below.

3. Breakthrough curves

In Appendix B we calculate the long-time limit of the mobile concentration using the special function of Wright type M_μ (Mainardi function) [84],

$$M_\mu(z) = \sum_{n=0}^{\infty} \frac{(-z)^n}{n!\Gamma[-\mu n + (1-\mu)]}. \quad (52)$$

From the general equation for $C_m(x, s)$ [Eq. (18)] we find in the limit $s \ll (v^2/4\beta\omega\tau_*^\mu D)^{1/\mu}$ for $v > 0$, using the Laplace inversion (B3),

$$\begin{aligned} C_m(x, t) &\sim \frac{\beta\omega\tau_*^\mu\mu}{v^2} \exp\left(\frac{v}{2D}(x - |x|)\right) |x|t^{-1-\mu} M_\mu \\ &\times \left(\frac{\beta\omega\tau_*^\mu}{v} |x|t^{-\mu}\right). \end{aligned} \quad (53)$$

For long times $t \gg \tau_* (\frac{\beta\omega}{v} |x|)^{1/\mu}$ the argument of M_μ in (53) goes to zero. With the limit $M_\mu(z) \sim 1$ for $z \rightarrow 0$, we thus have the asymptotic scaling $C_m \simeq t^{-1-\mu}$ for fixed x . In the long-time limit, we find the immobile concentration profile using the Laplace inversion (B4),

$$C_{im}(x, t) \sim \frac{\beta\omega\tau_*^\mu}{v} \exp\left(\frac{v}{2D}(x - |x|)\right) t^{-\mu} M_\mu\left(\frac{\beta\omega\tau_*^\mu}{v} |x|t^{-\mu}\right). \quad (54)$$

Equations (53) and (54) clearly show exponential cutoffs for $x < 0$, i.e., a strong suppression against the direction of the advection, as it should be. For $x > 0$ the exponential function

in Eq. (54) vanishes and a cusp emerges. Conversely, at short times and fixed x we find a Gaussian expression of C_m .

C. Comparison of the two EMIM cases

When choosing an exponential trapping time distribution, our model follows the dynamic equations (24) corresponding to the first-order mass transfer model (24) [26]. In the long-time limit the mobile and immobile concentrations are equal and the mass fraction $1/(1+\beta)$ remains mobile. The unnormalized and normalized moments remain unchanged except for the rescaled time $t \rightarrow t/(1+\beta)$. In the ML model, the diverging mean trapping time leads to different mobile and immobile concentrations and a power-law decay of the mobile mass. The first and second moments grow nonlinearly and nonquadratically in time, respectively. The second central moment shows anomalous diffusion, i.e., subdiffusion for $0 < \mu < 1/2$ and superdiffusion for $1/2 < \mu < 1$. All long-time limiting behaviors are summarized in Table I. In Appendix E we validate our results with particle-tracking simulations.

D. Tempered power-law and composite models

The ML model features a diverging characteristic trapping time. While in many cases such models reveal adequate descriptions (e.g., in [40,41] in which fits with a γ function reveal a cutoff at the very end of the experimental window) in other cases experiments explore time ranges in which the finiteness of the system becomes significant. A finite system size implies a finite number of locations, e.g., pores, where the tracers can immobilize. This implies that a finite waiting time exists, which has been measured, e.g., for dye dispersion in a saturated sand pack [69]. A typical approach is to introduce an exponential cutoff in the power-law waiting time PDF of the form [22,29,31,52,69]

$$\gamma_i(t) = \frac{\exp(-t/\tau_i)}{\gamma(s = 1/\tau_i)} \gamma(t), \quad (55)$$

with the characteristic crossover time $\tau_i > 0$. An interesting case is reported in [54] for which τ_i increases with biofilm growth. In Laplace space we find

$$\gamma_i(s) = \frac{\gamma(s + 1/\tau_i)}{\gamma(s = 1/\tau_i)}. \quad (56)$$

If we choose the ML model as a special example, the associated tempered PDF has the characteristic waiting time

$$\langle t \rangle = \frac{\tau_*^\mu \mu}{\tau_i^{\mu-1} [1 + (\tau_*/\tau_i)^\mu]}. \quad (57)$$

Together with the general limit (7) of $M_m(t)$ we find

$$\lim_{t \rightarrow \infty} M_m(t) = \frac{M_0}{1 + \beta\omega \frac{\tau_*^\mu \mu}{\tau_i^{\mu-1} (1 + \tau_*^\mu \tau_i^{-\mu})}}. \quad (58)$$

The assumption $\tau_i \gg \tau_*$ appears reasonable; therefore, the short-time expansion of the mobile mass coincides with the untempered ML model (41).

We now calculate an estimation of $M_m(t)$ for $\tau_* \ll t \ll \tau_i$ using γ_i (56) and the general formula for M_m (6) in Laplace

TABLE I. Main long-time behavior of the mobile-immobile moments with section and equation numbers. At short times, regardless of the trapping time PDF, we have $\langle x_m \rangle \approx vt$ and $\langle x_m^2 \rangle \approx v^2 t^2 + 2Dt$, due to $C_m(x, 0) = M_0 \delta(x)$ and $C_{im}(x, 0) = 0$.

Moment	Long-time behavior, mobile phase	Long-time behavior, immobile phase
	Exponential model (Sec. III A)	
$M_m(t)/M_0$	$\frac{1}{1+\beta}$ [Eq. (27)]	
$\langle x \rangle$		$\frac{vt}{1+\beta}$ [Eq. (31)]
$\langle x^2 \rangle$		$2D \frac{t}{1+\beta} + \frac{v^2 t^2}{(1+\beta)^2}$ [Eq. (35)]
$\langle (x - \langle x \rangle)^2 \rangle$		$2D \frac{t}{1+\beta}$ [Eq. (36)]
$C_{m,im}(x, t)$	$C_{m,im}(x, t) = \frac{M_0}{\sqrt{\frac{2Dt}{1+\beta}}} \exp[-(x - \frac{vt}{1+\beta})^2 \frac{1}{4Dt/(1+\beta)}]$ [Eq. (37)]	
	ML model (Sec. III B)	
$M_{m,im}(t)/M_0$	$\frac{t^{\mu-1}}{\beta \omega \tau_*^\mu \Gamma(\mu)}$ [Eq. (42)]	
$\langle x_{m,im} \rangle$	$v \Gamma(\mu) \frac{t^\mu}{\beta \Gamma(\mu)}$ [Eq. (45)]	$\frac{vt^\mu}{\beta \omega \tau_*^\mu \Gamma(1+\mu)}$ [Eq. (47)]
$\langle x_{m,im}^2 \rangle$	$\frac{t^\mu 2D \Gamma(\mu)}{\beta \Gamma(2\mu)} + \frac{t^{2\mu} 2v^2 \Gamma(\mu)}{\beta^2 \omega^2 \tau_*^{2\mu} \Gamma(3\mu)}$ [Eq. (50)]	
$\langle (x_{m,im} - \langle x_{m,im} \rangle)^2 \rangle$	$\frac{t^\mu 2D \Gamma(\mu)}{\beta \omega \tau_*^\mu \Gamma(2\mu)} + \frac{t^{2\mu} v^2 \Gamma(\mu)}{(\beta \omega \tau_*^\mu)^2} (\frac{2}{\Gamma(3\mu)} - \frac{\Gamma(\mu)}{\Gamma^2(2\mu)})$ [Eq. (51)]	
$C_{m,im}(x, t)$	$\frac{\beta \omega \tau_*^\mu}{v^2} e^{\frac{v}{2D}(x- x)} \frac{ x }{1+\mu} M_\mu(\frac{\beta \omega \tau_*^\mu}{v} x t^{-\mu})$ [Eq. (53)]	$\frac{\beta \omega \tau_*^\mu}{v t^\mu} e^{\frac{v}{2D}(x- x)} M_\mu(\frac{\beta \omega \tau_*^\mu}{v} x t^{-\mu})$ [Eq. (54)]

space,

$$M_m(s') = \frac{M_0}{s' - \frac{1}{\tau_i} + \beta \omega (1 - \frac{1}{1+(\tau_* s')^\mu} - \frac{\tau_*^\mu \tau_i^{-\mu}}{1+(\tau_* s')^\mu})}, \quad (59)$$

where we define $s' = s + 1/\tau_i$. This definition allows us to analyze (59) for small s' ,

$$M_m(s') \stackrel{s' \rightarrow 0}{\sim} \frac{M_0}{\beta \omega [(\tau_* s')^\mu (1 + \tau_*^\mu \tau_i^{-\mu}) - \tau_*^\mu \tau_i^{-\mu}] - \frac{1}{\tau_i}} \quad (60)$$

$$\sim \frac{M_0}{\beta \omega \tau_*^\mu (1 + \tau_*^\mu \tau_i^{-\mu})} \frac{1}{s^\mu - \frac{\tau_*^\mu \tau_i^{-\mu} + (\tau_i \beta \omega)^{-1}}{\tau_*^\mu + \tau_*^{2\mu} \tau_i^{-\mu}}} \quad (61)$$

and thus, after Laplace inversion [see [84], Eq. (4.10.1)],

$$M_m(t) \sim \frac{M_0}{\beta \omega \tau_*^\mu (1 + \tau_*^\mu \tau_i^{-\mu})} t^{\mu-1} E_{\mu, \mu}(\lambda t^\mu), \quad (62)$$

with $\lambda = [\tau_*^\mu \tau_i^{-\mu} + (\tau_i \beta \omega)^{-1}] / [\tau_*^\mu + \tau_*^{2\mu} \tau_i^{-\mu}]$. Since we have $\tau_i \gg \tau_*$, λ simplifies to $\lambda = 1/\tau_*^\mu \tau_i \beta \omega$. Using $\mathcal{L}^{-1}\{f(s + 1/\tau_i)\} = \exp(-t/\tau_i) f(t)$, we find

$$M_m(t) \sim \frac{M_0}{\beta \omega \tau_*^\mu (1 + \tau_*^\mu \tau_i^{-\mu})} t^{\mu-1} E_{\mu, \mu}(\lambda t^\mu), \quad \tau_* \ll t \ll \tau_i. \quad (63)$$

Another class of modification to the models considered above arises for the case of composite systems, in which two distinct immobile zones with different trapping time PDFs $\gamma_1(\tau)$ and $\gamma_2(\tau)$ exist. Analogously to (1), these systems are described by

$$\begin{aligned} \frac{\theta_m}{\theta_{im}} \frac{\partial}{\partial t} C_m(x, t) &= -\omega C_m(x, t) + \int_0^t [b\gamma_1(t-\tau) + (1-b) \\ &\quad \times \gamma_2(t-\tau)] \omega C_m(x, t) d\tau \\ &\quad + \frac{\theta_m}{\theta_{im}} L(x) C_m(x, t), \end{aligned} \quad (64a)$$

$$\frac{\partial}{\partial t} C_{im,1}(x, t) = b\omega C_m(x, t) - \int_0^t b\gamma_1(t-\tau) \omega C_m(x, t) d\tau, \quad (64b)$$

$$\begin{aligned} \frac{\partial}{\partial t} C_{im,2}(x, t) &= (1-b)\omega C_m(x, t) \\ &\quad - \int_0^t (1-b)\gamma_2(t-\tau) \omega C_m(x, t) d\tau. \end{aligned} \quad (64c)$$

Here the particle immobilizes into the first immobile zone with probability b and into the second zone otherwise. The combination of two remobilization processes arises, for instance, in intragranular diffusion processes, where mesopores and micropores are present and the latter lead to slow diffusion with γ -distributed diffusion rates [51]. We are mainly interested in the mobile zone; consequently, we define

$$\gamma(\tau) = b\gamma_1(\tau) + (1-b)\gamma_2(\tau) \quad (65)$$

and consider (1a) only. All observables can be obtained by plugging the corresponding (composite) trapping time PDFs into the general expressions that we presented in Sec. II A and numerically calculating the Laplace inversion (see the explicit results in Sec. V A). We note that we calculate all Laplace inversions using the implementation of the de Hoog method [86] using the PYTHON package MPMATH [87].

IV. CONNECTION TO FRACTIONAL MODELS

We now proceed to show that the EMIM formalism developed here is consistent with the bifractional diffusion equation model [71] and the fractal MIM presented in [45] in the limit $t \gg \tau_*$. The relations between these models and the EMIM are outlined in Fig. 2.

A. Connection to bifractional diffusion equation and fractal MIM

To this end, we recall our definition of the cumulative function of the waiting time PDF, $\Psi(t) = \int_t^\infty \gamma(\tau) d\tau$, i.e., the survival probability in the trapped state. Since $\int_0^\infty \gamma(\tau) d\tau = 1$, we have $1 - \Psi(t) = \int_0^t \gamma(\tau) d\tau$. From here we obtain $\gamma(\tau) = -\partial \Psi(t)/\partial t$ and $\Psi(s) = [1 - \gamma(s)]/s$. Now we aim at

rewriting the dynamic equations (1) of the EMIM in terms of this survival probability. We start with the relation (1a) and use integration by parts in the second term of the right-hand side,

$$\begin{aligned} & \int_0^t \gamma(t-\tau)C_m(x,t)d\tau \\ &= \Psi(t)C_m(0) + \Psi(0)C_m(t) - \int_0^t d\tau \Psi(t-\tau) \frac{d}{d\tau} C_m(\tau). \end{aligned} \quad (66)$$

Thus, our model (1a) is equivalent to

$$\begin{aligned} & \frac{\partial}{\partial t} C_m(t) + \beta\omega \int_0^t \Psi(t-\tau) \frac{\partial C_m(\tau)}{\partial \tau} d\tau \\ &= -\beta\omega \Psi(t)C_m(0) + L(x)C_m(x,t). \end{aligned} \quad (67)$$

Now, for our ML model $\gamma(s) = 1/[1 + (\tau_*s)^\mu]$ the survival probability in the Laplace domain reads

$$\Psi(s) = \frac{s^{\mu-1}\tau_*^\mu}{1 + (\tau_*s)^\mu}. \quad (68)$$

Thus, in our approach $\Psi(t) = E_\mu[-(t/\tau_*)^\mu] \rightarrow e^{-t/\tau_*}$ for $\mu = 1$. The ML function converges to unity when $t \rightarrow 0$ and decays as the power law $t^{-\mu}\tau_*^\mu/\Gamma(1-\mu)$ at large t . If we only retain the long-time asymptotes we arrive at the model in [45] in terms of the fractional Caputo derivative of order $0 < \mu < 1$ [88].

For the specific choice $\Psi(t) = \omega e^{-\omega t}$ the fractal model in [45] leads to the classical mass transfer model (24a). Note that this choice is equivalent to our exponential model with $\gamma(t) = \omega e^{-\omega t}$. It leads to the linear retardation factor $(1 + \beta)$ [45] and the dynamic equation

$$(1 + \beta) \frac{\partial C_{\text{tot}}}{\partial t} = L(x)C_{\text{tot}}, \quad C_{\text{tot}}(x, 0) = \theta_m C_{m,0}(x) \quad (69)$$

for the total concentration that we also found in the long-time limit of our exponential model. In this sense our approach is fully consistent with the fractal MIM developed in [45]. However, in our EMIM formulation the trapping time distribution $\gamma(t)$ is a proper PDF including the case of PDFs with diverging mean; in particular, no divergence at $\gamma(0)$ occurs.

We proceed to analyze the connection of the EMIM to the bifractional diffusion equation. In the long-time limit we can rewrite the total concentration (9) using a ML PDF and the approximation $\gamma(s) = 1 - \tau_*^\mu s^\mu$ to obtain

$$\begin{aligned} & sC_{\text{tot}}(k, s) - M_0 + \beta\omega\tau_*^\mu s^\mu C_{\text{tot}}(k, s) - M_0\beta\omega\tau_*^\mu s^{\mu-1} \\ &= (ikv - k^2D)C_{\text{tot}}(k, s). \end{aligned} \quad (70)$$

We can now identify a first-order derivative and a Caputo fractional derivative, yielding in the time-space domain

$$\frac{\partial C_{\text{tot}}}{\partial t} + \beta'_s \frac{\partial^\mu C_{\text{tot}}}{\partial t^\mu} = L(x)C_{\text{tot}}, \quad (71)$$

which is a bifractional diffusion equation, as discussed in [71,72,89] and reported in [45] for $\theta_m C_{m,0}(x) = C_{\text{tot}}(x, 0)$, with a generalized transport operator $L(x)$.

B. Analytical forms of the transport moments

For a small Laplace variable s the Laplace transform of the ML PDF behaves like $\gamma(s) \sim 1 - \tau_*^\mu s^\mu$. Plugging this limiting form into the Fourier-Laplace transform of the mobile concentration (4), we find

$$C_m(k, s) = \frac{M_0}{s + \beta\omega\tau_*^\mu s^\mu - ikv + k^2D}. \quad (72)$$

We call this asymptotic form the fractal model, which coincides with the model analyzed in [45,71,72], as discussed above. We note that even though our model includes the fractal model in the limit $t \gg \tau_*$, the bifractional models are full models valid for all t on their own. Therefore, we calculate the mobile mass and the moment for all t and not only in the limit $t \rightarrow \infty$. The advantage of the ML model is that the trapping PDF (38) is well defined in the limit $t \rightarrow 0$.

To find the mobile mass using the fractal model, we set $k = 0$ in $C_m(k, s)$ in Eq. (72) and use the properties of the ML function [see [84], Eq. (3.7.8)], yielding

$$M_m(t) = M_0 E_{1-\mu}(-\beta\omega\tau_*^\mu t^{(1-\mu)}). \quad (73)$$

For the unnormalized first moment we use the fractal model and the general formula (12) for $\langle x_m(s) \rangle_u$ to find

$$\langle x_m(s) \rangle_u = \frac{v}{[s + \beta\omega(\tau_*s)^\mu]^2} = \frac{vs^{-2\mu}}{(s^{1-\mu} + \beta\omega\tau_*^\mu)^2}, \quad (74)$$

which we transform to time domain using [see [90], Eq. (2.5)]

$$\langle x_m(t) \rangle_u = vt E_{1-\mu,2}^2(-\beta\omega\tau_*^\mu t^{(1-\mu)}). \quad (75)$$

Dividing the unnormalized first moment (75) by the mobile mass (73) normalizes the first moment,

$$\langle x_m(t) \rangle = \frac{vt E_{1-\mu,2}^2(-\beta\omega\tau_*^\mu t^{(1-\mu)})}{E_{1-\mu}(-\beta\omega\tau_*^\mu t^{(1-\mu)})}. \quad (76)$$

We plug the fractal model with $\gamma(s) \sim 1 - (\tau_*s)^\mu$ into the general relation (16) between $\langle x_m^u \rangle_u$ and $\langle x_{im}^u \rangle_u$ for $n = 1$, obtaining

$$\begin{aligned} \langle x_{im} \rangle_u &= \omega\beta v \frac{1}{[s + \beta\omega[1 - \gamma(s)]]^2} \frac{1 - \gamma(s)}{s} \\ &= \omega\beta v \frac{\tau_*^\mu s^{\mu-1}}{(s + \beta\omega\tau_*^\mu s^\mu)^2}. \end{aligned} \quad (77)$$

In the time domain we find, using (77) and Eq. (2.5) in [90], that

$$\langle x_{im} \rangle_u = \omega\beta\tau_*^\mu t^{2-\mu} E_{1-\mu,3-\mu}^2(-\beta\omega\tau_*^\mu t^{1-\mu}). \quad (78)$$

Dividing by the immobile fraction mass $M_{im}(t)/M_0 = 1 - M_m(t)/M_0$ yields the normalized first moment

$$\langle x_{im} \rangle = \frac{\omega\beta\tau_*^\mu t^{2-\mu} E_{1-\mu,3-\mu}^2(-\beta\omega\tau_*^\mu t^{1-\mu})}{1 - E_{1-\mu}(-\beta\omega\tau_*^\mu t^{(1-\mu)})}. \quad (79)$$

Consider next the unnormalized second moment obtained via the second derivative of $C_m(k, s)$ in Eq. (72),

$$\begin{aligned} \langle x_m^2(s) \rangle_u &= \frac{2D}{(s + \beta\omega\tau_*^\mu s^\mu)^2} + \frac{2v^2}{(s + \beta\omega\tau_*^\mu s^\mu)^3} \\ &= \frac{2Ds^{-2\mu}}{(s^{1-\mu} + \beta\omega\tau_*^\mu)^2} + \frac{2v^2 s^{-3\mu}}{(s^{1-\mu} + \beta\omega\tau_*^\mu)^3}, \end{aligned} \quad (80)$$

which we transform back to the time domain using Eq. (2.5) in [90],

$$\langle x_m^2(t) \rangle_u = 2Dt E_{1-\mu,2}^2(-\beta\omega\tau_*^\mu t^{1-\mu}) + 2t^2 v^2 E_{1-\mu,3}^3(-\beta\omega\tau_*^\mu t^{1-\mu}). \quad (81)$$

With the mobile mass (73) we normalize (81) to

$$\langle x_m^2(t) \rangle = 2Dt \frac{E_{1-\mu,2}^2(-\beta\omega\tau_*^\mu t^{1-\mu})}{E_{1-\mu}(-\beta\omega\tau_*^\mu t^{1-\mu})} + 2t^2 v^2 \frac{E_{1-\mu,3}^3(-\beta\omega\tau_*^\mu t^{1-\mu})}{E_{1-\mu}(-\beta\omega\tau_*^\mu t^{1-\mu})}. \quad (82)$$

We find the second central moment of the fractal model by using relations (76) and (82),

$$\begin{aligned} \langle [x_m(t) - \langle x_m(t) \rangle]^2 \rangle &= 2Dt \frac{E_{1-\mu,2}^2(-\beta\omega\tau_*^\mu t^{1-\mu})}{E_{1-\mu}(-\beta\omega\tau_*^\mu t^{1-\mu})} \\ &+ 2v^2 t^2 \frac{E_{1-\mu,3}^3(-\beta\omega\tau_*^\mu t^{1-\mu})}{E_{1-\mu}(-\beta\omega\tau_*^\mu t^{1-\mu})} \\ &- v^2 t^2 \left(\frac{E_{1-\mu,2}^2(-\beta\omega\tau_*^\mu t^{1-\mu})}{E_{1-\mu}(-\beta\omega\tau_*^\mu t^{1-\mu})} \right)^2. \end{aligned} \quad (83)$$

We note that the asymptotics of the moments presented in this section can be obtained by rewriting the three-parametric ML functions in terms of two-parametric ML functions with Eq. (2.4) in [90] and approximating them up to second order with Eq. (6.11) in [91]. These limits match our results for the EMIM ML model in Sec. III B in Eqs. (42), (45), and (50) and what has been reported previously [46].

V. COMPARISON TO EXPERIMENTS

We apply our model to two different experimental data sets that we discuss in detail. The study reported in [22] probes fluorescent dye in an alpine karst aquifer in the Hochifen-Gottesacker area (Austria). The dye was injected into actively sinking surface water and measured at two karst springs up to 7400 m away [22]. We show the resulting BTC of the data set IP Gb (2) in Fig. 5. It was measured 3500 m downstream from the injection point and was previously reported in [22,92]. Our aim is to obtain the moments of the mobile concentration from this BTC, because BTCs are commonly measured while moments provide important additional information on the transport dynamics [22,27,31,54,69].

One crucial idea of our model is the division into mobile and immobile particles. However, the tracers are not detected while moving through the karst aquifer and hence we cannot directly compare our predicted mobile mass decay to experiments that only measure BTCs. Therefore, we consider a second experiment where the tracer concentration profile is measured. This experiment is the first macrodispersion experiment (MADE-1) [20,43]. The authors of this study realized a 48-h pulse injection of bromide into a heterogeneous aquifer near Columbus, Mississippi (USA). A network of multilevel sampling wells covering around 300 m along the flow direction with approximately 6000 sampling points allowed the observation of the plume profile at eight snapshots up

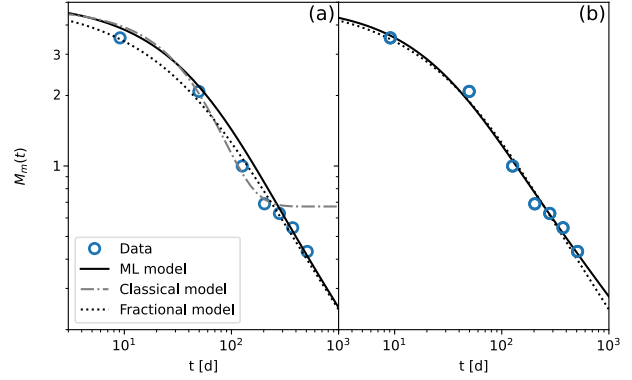


FIG. 3. Fraction of measured mass in the MADE-1. Data points are taken from [45], extracting the data from the PDF paper file. (a) The fractal MIM is fitted to the data; the parameters are $\beta_s = 0.08 \text{ d}^{-0.67}$ and $\mu = 0.33$ with an initial mobile mass of 5, as obtained in [45]. For the ML model (38) we choose $\mu = 0.33$ and $\beta\omega\tau_*^\mu = 0.08 \text{ d}^{\mu-1}$ such that both the ML and fractal models yield the same long-time asymptotic behaviors. The asymptote does not depend on the ratio $\beta\omega/\tau_*^\mu$, for which we choose 1/10, 1/5, and 10 from top to bottom. This ratio affects the short-time behavior $\simeq \exp(-\omega\beta t)$. Small values of τ_* lead to an early asymptotic behavior and hence a match with the fractal model appears sooner. (b) The exponential model, ML model, and fractal MIM are fitted individually to the data. The asymptotic power law of the ML EMIM has a different exponent of $\mu - 1 = 0.33 - 1 = -0.67$ compared to the fractal model with $\mu - 1 = 0.33 - 1 = -0.67$. The exponential model has the parameters $\beta = 6$, $M_0 = 4.7$, and $\omega = 0.003 \text{ d}^{-1}$, as obtained in [45]. The associated parameters of the remaining models are listed in Table II. Note that “d” represents “day” in SI units.

to 594 d after injection. Using linear interpolation between sampling points, the authors obtained the total measured mass by integrating over all three spatial dimensions. The total recovered mass exceeded the initial input mass, which the authors explained by a “spurious hydraulic connection among [the sampling stations]” or higher concentrations in regions with higher hydraulic conductivity and subsequent inaccurate linear interpolation [20]. Nevertheless, a power-law tail was clearly observed in the decay of recovered mass, as demonstrated in [45]. In addition to the mobile mass, the authors obtained the moments of the tracer distribution in the MADE-1 [20]. Notably, the plume consisted of a virtually stationary distribution with a slowly decaying shoulder [20].

A. Mobile mass

Figure 3 shows the measured mobile mass decay of the MADE-1 [20] as circles. In Fig. 3(a) we show the best fit of the fractal MIM from [45] (see Sec. IV) along with our ML model. For the latter we do not fit the data but choose the model parameters such that the ML model has the same asymptotic long-time behavior as the fractal model. This is achieved for the parameters $\mu = 0.33$, $\beta\omega\tau_*^\mu = 0.08 \text{ days}^{\mu-1}$, where in SI units “d” stands for “days”, and $M_0 = 5$ for the mobile mass. For the ML model we show the numerical Laplace inversion of the mobile mass in Laplace space (6) using γ_{ML} . At short times all models are dominated by the

TABLE II. Fit parameters and coefficient of determination of fits to $M_m(t)$ from Figs. 3(b) and 4. The parameters β and ω only appear as a product in the mobile concentration and hence cannot be determined separately.

Model	M_0	μ	$\beta\omega$ (d $^{-1}$)	τ_* (d)	τ_t (d)	ω_1 (d $^{-1}$)	ω_2 (d $^{-1}$)	b	R^2
ML	4.833	0.417	0.060	9.549					0.992
truncated	4.726	0.226	0.913	0.934	11530				0.994
ML+exp	4.2	0.104	0.0227	25.18		0.0052		0.56	0.998
exp+exp	3.78		0.01983			0.00182	5713	0.61	0.989

identical initial value M_0 ; hence the ML and fractal models differ only at intermediate timescales of around 50 d. Note that as long as the product $\beta\omega\tau_*^\mu$ remains constant, the same long-time limit is reached. Therefore, we can choose different ratios $\beta\omega/\tau_*^\mu$. From top to bottom we use in Fig. 3 the values 1/10, 1/5, and 10. A small ratio will decrease the initial decay $\simeq \exp(-\beta\omega t)$, while a large ratio corresponding to small τ_* leads to earlier appearance of the asymptotic behavior, and for the ratio 10, the ML model coincides with the fractal model.

In Fig. 3(b) we show a fit with our model (27) with an exponential trapping time distribution with $\beta = 6$, $M_0 = 4.7$, and $\omega = 0.003\ 108\ 11\ \text{d}^{-1}$. These parameters correspond to a fit to the data shown in [45], where a model matching (24) was used. The fit does not describe the data well, because it reaches the steady-state value (27), in contrast to the continued decay shown by the data. In addition, we show fits of both the fractal and ML models to the MADE-1 data. Both models describe the data well, as demonstrated by the coefficient of determination $R^2 = 0.992$ (we calculate all coefficients of determination using the PYTHON module SCIKIT LEARN [93]). In Table II we show the fit parameters, observing no significant difference in goodness of fit between the ML and fractal models. We note, however, that μ differs: It is 0.33 for the fractal model and 0.42 for the ML model. This observation demonstrates that the fully quantitative behavior of the seemingly very similar models is indeed notably different.

Figure 4 shows fits using our extended models from Sec. III D to the MADE-1 data [20,45]; see Table II for the fit parameters. First we consider the composite model with two exponential terms $\gamma(\tau) = b\omega_1 \exp(-\omega_1\tau) + (1-b)\omega_2 \exp(-\omega_2\tau)$ with $0 < b < 1$. The result is shown by the dotted line, which quantitatively behaves quite similarly to the exponential model. It approximates all but the last data point well with a coefficient of determination of $R^2 = 0.988$, which is notably worse than all models containing power-law waiting times (see Table II). This indicates the necessity of including long-tailed trapping time PDFs for these data. Of course, adding additional exponentials would improve the fit, however, at the cost of a larger number of fit parameters.

The second composite form that we consider reads, in Laplace space,

$$\gamma(s) = \frac{b}{1 + (\tau_*s)^\mu} + (1-b)\frac{\omega_1}{\omega_1 + s} \quad (84)$$

and corresponds to the combination of an exponential and an ML trapping time PDF. In Fig. 4 the orange dash-dotted line shows the best fit using this model, with a coefficient of determination of $R^2 = 0.998$. In fact, this is the only model considered here capable of reproducing the apparent shoulder in the data around 200 d. Concurrently, the long-time behavior

exhibits a scaling exponent μ that is significantly different from the pure ML model. We highlight that both the truncated ML model (55) with $R^2 = 0.993$ and the combination of the ML and exponential model (84) with $R^2 = 0.998$ fit the data better than the ML model alone ($R^2 = 0.992$). This indicates that the data indeed encode finite-size effects needing a tempering of the power-law tail of the trapping time PDF. However, we stress that we fit to seven data points only and the extended models have more parameters than the ML or exponential model. Therefore, the extended models might be subject to overfitting. Improved data will be needed to be more accurate in this interpretation.

B. Breakthrough curves

In Fig. 5 we show the BTC of the IP Gb (2) experiment, in which fluorescent dye travels in the underground aquifer in the Schwarzwasser valley [22]. All fit parameters are listed in Table III. A fit using the ML trapping time PDF describes the data well with $R^2 = 0.990$. The fractal model describes the data equally well with the same $R^2 = 0.990$. Its peak is slightly higher than that of the ML model. The classical model fails to describe the power-law decay at long times and hence yields the notably worse value $R^2 = 0.940$, with

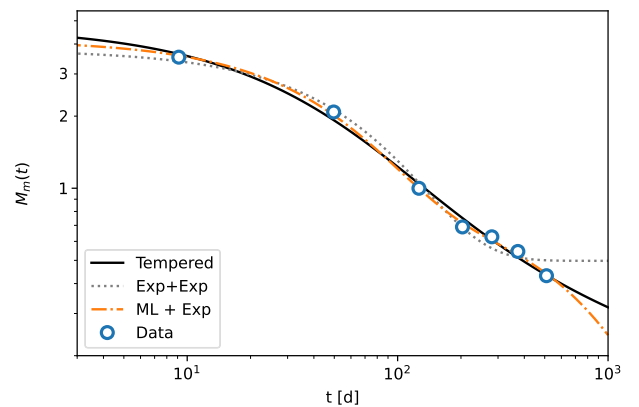


FIG. 4. Fitted extended models. The tempered ML model $\gamma_{\text{ML}}^*(s) = [1 + (\tau_*/\tau_t)^\mu]/[1 + (\tau_*s + \tau_*/\tau_t)^\mu]$ (solid line) and two combinations of γ are fitted to the experimental mobile mass decay of the MADE-1 [20]. At around 900 d, the deviation from the power-law trend is visible in the tempered model. The combination of two exponential functions (dotted line) behaves quite similarly to the pure exponential model in Fig. 3. Combining the ML and exponential models yields the orange dash-dotted line. It is the only model considered capable of describing the shoulder of the data at around 300 d. The fit parameters are given in Table II.

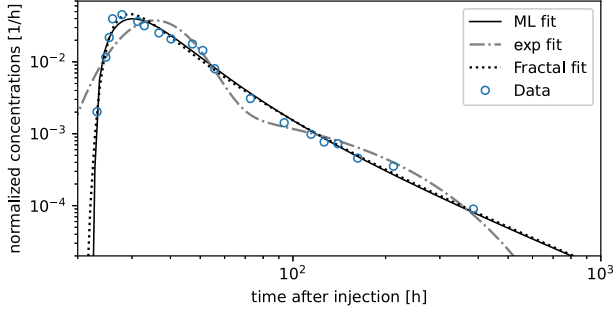


FIG. 5. Fits to the BTC for fluorescent dye measured 3500 m downstream from the injection point in the Schwarzwasser experiment [22,92]. The solid line shows a fit using the ML model with $R^2 = 0.990$ and the dashed line a fit using the fractal model with $R^2 = 0.990$. Both differ mainly in the peak height. An exponential trapping time PDF yields a significantly worse fit ($R^2 = 0.940$) with an additional shoulder and an exponential decay instead of the power-law decay at long times. [Data were taken from [22], IP Gb (2).] The fit parameters are listed in Table III.

an unlikely high fit value for the diffusion coefficient, $D_{\text{exp}} = 9527 \text{ m}^2/\text{h}$, and a considerably lower $v_{\text{exp}} = 94.9 \text{ m/h}$. In this model, the tracers diffuse very fast while the advection is slow. This way, the exponential fit compensates for the lack of the power-law decay. Note also the exponential decay in the fit of the exponential model and the fact that it completely misses the short-time behavior. We conclude that power-law tails introducing a wide range of timescales appear necessary for a proper description of the experimental data. We use the parameters from the fits to the BTC for the remainder of this work.

C. Concentration profile

Next we focus on the spatial distribution of the solute, i.e., the plume profiles. In Fig. 6 we show the concentrations corresponding to the BTC fits in Fig. 5. We logarithmically present the Laplace inversion of the mobile concentration (18) in the top row for the ML model (solid line), the fractal model (dotted line), and the exponential model (dash-dotted line). The left column shows the short-time behavior 1 min after injection. The ML and fractal models show a comparatively narrow bell-shaped behavior, while the exponential model already exhibits a considerable spread due to its high value of D . At intermediate times of 30 h (middle column) all mobile concentrations are increasingly skewed to the right and

TABLE III. Fit parameters and coefficients of determination for the BTCs shown in Fig. 5. The parameters β and ω only appear as a product in the mobile concentration of the ML and fractal model and hence cannot be determined separately.

Model	M_0	μ	$\beta\omega$ (h^{-1})	ω (h^{-1})	τ_* (h)	v (m/h)	D (m^2/h)	R^2
ML	155.7	0.737	0.406		0.922	151.4	35.2	0.990
limit	242.8	0.771	0.841		1.00	232.9	21.8	0.990
exp	96.3		0.006	0.011		94.9	9527.0	0.940

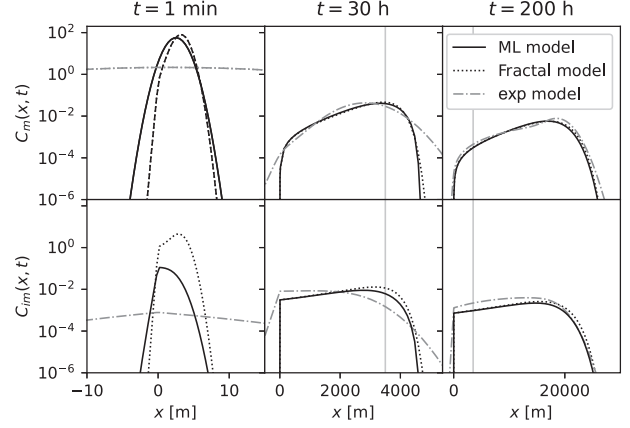


FIG. 6. Logarithmic representation of the concentration profiles of the mobile and immobile particles 1 min, 30 h, and 200 h after injection from the left to the right panels, respectively. Note the different ranges of the horizontal axes for each delay time. At short times all models yield a Gaussian mobile distribution, which is increasingly skewed at later times. The diffusion coefficient $D_{\text{exp}} = 9527 \text{ m}^2/\text{h}$ of the exponential model is exceptionally high compared to that of the ML model ($D_{\text{ML}} = 35.2 \text{ m}^2/\text{h}$) and of the fractal model ($D_{\text{limit}} = 21.8 \text{ m}^2/\text{h}$). Thus the concentration of the exponential model has spread significantly further than the other models at shorter times. The immobile particle fraction has a non-Gaussian distribution at all times and has cusps at $x = 0$, which are typical transport features for systems with diverging waiting times [14,35,71]. The parameters of all models correspond to the fit to the BTC in Fig. 5. The BTC was measured at 3500 m, as marked by the vertical line. See Table III for fit values.

are significantly non-Gaussian (note the different ranges of the horizontal axes for different t). The vertical line denotes the position at which the experimental BTC was measured (3500 m downstream from the injection point). Quick decays to zero concentration around 0 and 4000 m characterize the skewed limit and ML model concentrations. At 200 h, the difference between the three models is quite small. At the measurement position, the limit and ML model are particularly similar.

The immobile concentrations in the bottom row of Fig. 6 are pronouncedly non-Gaussian at all times. We obtain them by taking a numerical Laplace inversion of the mobile concentration (18) plugged into the general relation (5) between the mobile and immobile concentration. At $t = 1 \text{ min}$ the fractal model's immobile concentration is one order of magnitude higher than that of the ML model. In addition, the peak of the ML model is close to $x = 0 \text{ m}$, while the peak of the fractal model is around $x = 5 \text{ m}$. At 30 h the ML and fractal models are very similar, have a sharp rise from zero to approximately 10^{-3} at 0 m, and show a peak around 3000 m. In contrast, the exponential model has its peak close to 0 m and falls off monotonically in both directions. At 200 h the ML and fractal models almost coincide and have qualitatively the same shape as for 30 h, although they have spread up to 22 km. Notably, the exponential model has a similar concentration. In the next section we characterize these concentrations further in terms of their first and second moments.

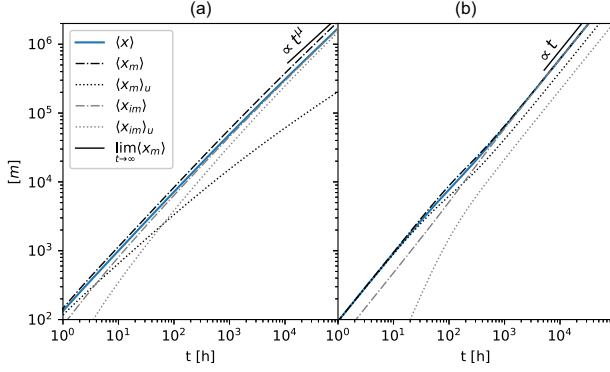


FIG. 7. Comparison of the normalized ($\langle x_{m,im} \rangle$), unnormalized ($\langle x_{m,im} \rangle_u$), and total ($\langle x \rangle$) first moments for the mobile and immobile tracers on a double-logarithmic scale using (a) the ML model and (b) the exponential model. In both panels, both $\langle x_m \rangle_u$ and $\langle x_m \rangle$ are a good approximation for $\langle x \rangle$ at short times, due to the high mobile fraction. The same holds for long times for the immobile moment. In the ML model, the first moment of the mobile particles has the same power-law behavior $\simeq t^\mu$ as the immobile tracers but with a larger coefficient. The black solid line shows the asymptote (45) of $\langle x_m \rangle$ as a guide to the eye. The parameters correspond to the fit to the BTC in Fig. 5 as listed in Table III.

D. Moments

We show the first moment $\langle x \rangle$ in Fig. 7 with parameters corresponding to the fit of our model to the BTC in Fig. 5. In addition to $\langle x \rangle$ we show the first moment of the mobile and immobile tracers $\langle x_m \rangle$ and $\langle x_{im} \rangle$, respectively. For the exponential model we use the analytic expressions (28) for $\langle x_m \rangle_u$ and (30) for $\langle x_m \rangle$. All remaining first moments are obtained through Laplace inversion of the general expressions (12) for $\langle x_m \rangle_u$ and (16) for $\langle x_{im} \rangle_u$. Subsequent normalization with the mobile mass (40) yields $\langle x_m \rangle$ and $\langle x_{im} \rangle$ for the ML model.

The first moment $\langle x \rangle$ of the total mass in Fig. 7 demonstrates a crossover from linear to power-law ($\simeq t^\mu$) scaling in time when using the ML model. At short times it matches $\langle x_m \rangle$ and $\langle x_m \rangle_u$, while coinciding with $\langle x_{im} \rangle$ and $\langle x_{im} \rangle_u$ at long times, as expected by the immobilization of all tracers in the long-time limit. The moments $\langle x_m \rangle$ and $\langle x_{im} \rangle$ have the same long-time power-law behavior, albeit with different coefficients. The black solid line in Fig. 7(a) shows the long-time limit of $\langle x_m \rangle$ using the ML model as given by the expression (45). In contrast, the center of mass of the mobile plume of the ML model is ahead at all times after injection. In Fig. 11 the described behavior is easier to discern with a significantly lower $\mu = 0.33$. We use the parameters of the fit to the mobile mass in [45] of Fig. 3 along with $v = 0.8$ m/d and $D = 4\text{m}^2/\text{d}$. The advection speed v was measured in the experiment and D is our estimate. In the time interval in which the BTC data were collected, the first mobile moments almost coincide and grow nonlinearly $\simeq t^\mu$, including the exponential model, as shown in Fig. 8.

In Fig. 9 we show the second moments corresponding to the BTC fits from Fig. 5. We obtain the moments through Laplace inversion of the general expressions (14) for $\langle x_m^2(s) \rangle_u$ and (16) for $\langle x_{im}^2(s) \rangle_u$ after normalization with $M_m(t)$

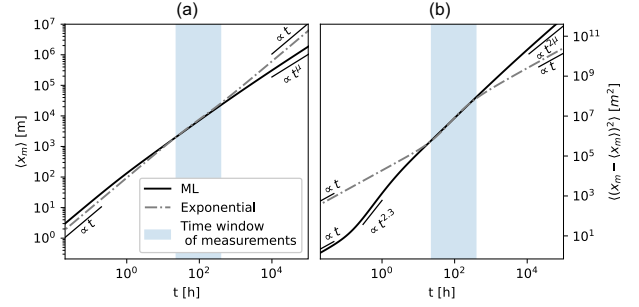


FIG. 8. First ($\langle x_m \rangle$) and second [$[(x_m - \langle x_m \rangle)^2]$] central moments. In (a) we show the first mobile moment using the exponential and ML model (see Fig. 7 for details). In (b) the second central moment of the ML and exponential models scales like $2Dt$ at short times. The exponential model is linear in the long-time limit as well. The ML model grows $\simeq t^{2\mu}$ for $t > 10$ h. The parameters of both models in both panels are taken from the fit to the BTC in Fig. 5 and are listed in Table III. In the shaded regions corresponding to the time window in which the data of the fitted BTCs were taken, the exponential model displays apparent anomalous diffusion and almost coincides with the power-law from the ML model.

or $M_{im} = M_0 - M_m$ [obtained from the general expression (6) for $M_m(s)$]. The second moment of the total concentration obtained from the general expression (17) for $\langle x^2 \rangle$ agrees with $\langle x_m^2 \rangle$ for both the ML and exponential order models at short times as almost all tracers are mobile at this time. In contrast to the ML model, the first-order model shows a crossover from linear to quadratic behavior. Around 1000 h, $\langle x^2 \rangle$ and $\langle x_{im}^2 \rangle$ coincide and grow proportionally to $t^{2\mu}$. The second mobile moment has the same power-law growth, albeit with a higher prefactor, as demonstrated by the long-time limit (50) of $\langle x_m^2 \rangle$

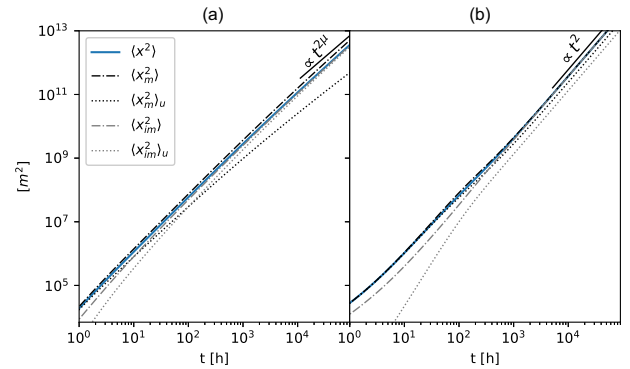


FIG. 9. Comparison of the normalized ($\langle x_{m,im}^2 \rangle$), unnormalized ($\langle x_{m,im}^2 \rangle_u$), and total ($\langle x^2 \rangle$) second moments for the mobile and immobile tracers on a double-logarithmic scale. All models yield $\langle x^2(t) \rangle = \langle x^2(t) \rangle_u \approx 2Dt$ at short times. (a) At long times the ML model show anomalous diffusion $\langle x^2 \rangle \simeq t^{2\mu}$, i.e., superdiffusion for $1/2 < \mu < 1$. (b) The exponential trapping time PDF leads to the long-time growth $v^2 t^2 / (1 + \beta)^3$ and $v^2 t^2 / (1 + \beta)^2$ of $\langle x_m^2 \rangle_u$ and $\langle x_{im}^2 \rangle_u$, respectively. The black solid line shows the asymptote (50) of $\langle x_m^2 \rangle$ as a guide to the eye. The parameters are the same as in Fig. 3(a).

shown as a black solid line. In the exponential model, all normalized second moments grow quadratically and overlap around 1000 d, as expected by the equivalence of C_m and C_{im} [Eq. (26)] at long times. Figure 8 shows the first and second central moments of the mobile concentration, the latter of which is obtained via $\langle (x_m - \langle x_m \rangle)^2 \rangle = \langle x_m^2 \rangle - \langle x_m \rangle^2$. Note that only the analysis of normalized second central moments is meaningful; therefore, we do not explicitly study the second central moment of the unnormalized moments. At short times, both the ML (solid line) and exponential (dash-dotted line) models grow linearly. The prefactor D of the latter is two orders of magnitude larger and the linear regime lasts until around 10 h. The ML model yields linear growth up to 6 min and transitions to the power law $t^{2\mu}$ after a transient growth proportional to $t^{2.3}$ around 30 min. In the range from 20 to 300 h we fitted our models to the BTCs as shown in Fig. 5. In this range, which we highlight by the shaded areas in Fig. 8 (and only in this range), the first and second central moments of the two models almost coincide. Hence, the exponential model can show transient anomalous diffusion. This is a remarkable result. Outside this time window at longer times the moments demonstrate distinct differences. The exponential model shows normal diffusion with $\langle (x_m - \langle x_m \rangle)^2 \rangle \simeq t$, while the mobile particles in the ML model spread faster with $\langle (x_m - \langle x_m \rangle)^2 \rangle \simeq t^{2\mu}$.

Here we analyzed anomalous diffusion using the first and second moments, while higher moments can reveal non-Gaussianity properties of the concentration profile. In Appendix D we calculate the skewness and kurtosis. These clearly show that after short times both the mobile and immobile concentrations are non-Gaussian when using the ML model. For $t \rightarrow \infty$, we find that the skewness and kurtosis only depend on μ . Notably, both appear to be discontinuous at $\mu = 1$ and jump to their respective Gaussian values.

VI. CONCLUSION

We introduced and discussed the extended mobile-immobile model for tracer motion in which the residence time in the immobile domain is drawn from a general trapping time PDF $\gamma(t)$. The mobile times were chosen to always follow an exponential distribution. A system with an exponential trapping time PDF could then be rewritten in terms of a classical first-order mass transfer model [26]. We considered the initial condition when all particles are mobile after a pulse injection. This leads to a Gaussian mobile plume at short times for any $\gamma(t)$. At intermediate times particles in the mobile phase are trapped in the immobile zone following an exponential trapping time PDF which renders the mobile concentration non-Gaussian and the moments grow nonlinearly. The second central moment exhibits an apparent anomalous diffusion in this time regime. In the long-time limit the mobile and immobile concentrations coincide and we recover normal diffusion with a rescaled time $t/(1 + \beta\langle\tau\rangle\omega)$, where β denotes the ratio of immobile to mobile volume, $\langle\tau\rangle$ represents the average immobilization time, and ω in time stands for the mass transfer coefficient.

When using a scale-free trapping time PDF with power-law tail $\simeq t^{-\mu-1}$ with $0 < \mu < 1$ and diverging mean waiting time,

such as the ML PDF considered here, all tracers immobilize eventually with a long-time power-law decay $\simeq t^{\mu-1}$ of the mobile mass. Our model with a ML PDF contains the fractal MIM from [45] and the bifractional diffusion model from [71,72,89] for specific choices of the scaling exponents as special cases. We found analytical results up to the second moment in this special case that hold for all times. Our ML model showed good fit results to the mobile mass decay of the MADE-1 [20]. In addition, we considered two extensions of the immobilization time PDF $\gamma(\tau)$. First we introduced an exponential tempering to analyze truncation effects. Second we considered a weighted sum of an ML PDF and an exponential PDF. Both modifications yielded even better fit results than the ML model alone. While these extended forms involve additional model parameters, their better fit indicates that cutoffs in the power-law trapping time density reflect better the physical situation, i.e., the system appears to show finite-size effects, similar to those obtained in trapping time PDFs in the conductivity study [31].

The ML model yielded a good fit to the BTC ($R^2 = 0.990$) of tracers in karst aquifers from [22]. This allowed us to obtain model parameters including the advection velocity and dispersion coefficient in the mobile zone. Subsequently, we calculated the moments of the mobile distribution and accounted for time-dependent normalizations. We found temporally nonlinear mass transport $\langle x \rangle \simeq t^\mu$ and anomalous diffusion $\langle (x - \langle x \rangle)^2 \rangle \simeq t^{2\mu}$ in the long-time limit. Concurrently, the concentration crossed over to a non-Gaussian immobile concentration. Mobile tracers led the immobile tracers in this long-time limit. We characterized the non-Gaussianity using the skewness and kurtosis, of which the long-time limit only depends on μ , as shown in Appendix D.

Notably, a fit to the BTC with an exponential model matched the data quite reasonably ($R^2 = 0.940$) but yielded an unlikely high diffusion constant. Nevertheless, the mobile concentration profiles appeared reasonably similar for $t = 30$ h and almost matched for $t = 200$ h. The exponential model showed transient anomalous diffusion in this time window, and the second central moment almost coincided with the ML model. It is remarkable that the exponential and ML models have a fundamentally different long-time behavior but yield very similar first, second, and second central moments in the intermediate time window, where the BTC measurements were taken. In fact, our analysis demonstrated that from experimental data it is rather tricky to distinguish even fundamentally different models based on transport moments. The mobile mass, BTC, and concentration profile are much better suited for this purpose. However, once fitted to the data, the moments demonstrate the massively different transport efficiency at long times. Such knowledge is of high relevance, e.g., to study the environmental impact of chemicals released into rivers or aquifers. The existence of long retention times may be underestimated by fits to exponential models and thus neglect potentially dangerous leakage of chemicals at much longer times.

The situation is quite different in other systems in which more extensive data are available, such as from simulations or single-particle-trapping experiments in live biological cells

or complex liquids. In such systems the moments can be efficiently extracted and compared to different models. There, particles can undergo diffusion with intermittent immobilization as well. An example could be proteins diffusing in the bulk cytoplasm of a live cell with intermittent binding to membrane receptors. In fact, three-dimensional trajectories of mRNA particles in yeast cells have been observed to switch between diffusive, directed, and confined motion as well as becoming stationary [94], similar to amoeboid motion on surfaces [95]. Single-molecule tracking of signaling proteins reveals intermittent dynamics during which proteins effectively immobilize on activation [96]. Membrane proteins and proteins in the cell nucleus have been observed to split into mobile and immobile populations [63,97,98]. We mention molecular dynamics simulations of drug molecules in a water layer confined in a silica slit unveiling intermittent immobilization due to surface adsorption with power-law-distributed trapping times [99]. Similar waiting time distributions are observed in the short-time motion of lipid granules in live yeast cells [100]. In fact, for systems with power-law-distributed immobilization times or diffusion with strongly position-dependent diffusivity populations, splitting is a salient feature [75,76,101].

The MIM can also be thought of as a special case of switching diffusion, when a particle intermittently undergoes different modes of transport within a single trajectory [102–104]. When adding an advection-diffusion operator to the immobile concentration of the EMIM a switching diffusion process could be obtained. In [102,103] a single particle switches between states with different diffusivities with fixed rates. If the observation time is small compared to the mean residence time, transport anomalies arise. Examples for switching diffusion include quantum dot tracers in the cytoplasm of mammalian cells which switch between different mobilities [105]. Molecular dynamics simulations show that conformational changes of proteins induce fluctuations of the protein diffusivity [106]. A simple model of particles that can aggregate and separate shows similar behavior [107]. Polymers change diffusivity during (de)polymerization due to varying chain lengths leading to transient non-Gaussian displacement PDFs [104]. Switching behavior is also seen in potassium channels and nonintegrin receptors in living cell membranes [108,109] as well as for lipid motion in molecular dynamics simulations of protein-crowded bilayer membranes [110]. Similar population splitting is observed in the passive motion of tracers in mucin gels [111,112] or acetylcholine receptors in live cell membrane [113]. Population splitting into fractions with different diffusivities was also observed for individually labeled lipids in the phospholipid membrane and of H-Ras proteins at the plasma membrane [114,115]. Moreover, G proteins have been observed to switch between states with different diffusivities due to conformational changes and increased immobilization after interaction [116]. These cases of molecular transport can represent scenarios in which our EMIM or its extensions can provide relevant insight into population splitting between mobile and immobile particle fractions and their respective transport dynamics. Moreover, the breakthrough curves discussed here can be used to deduce the first-passage dynamics to some reaction center.

Our model is a starting point to describe molecular reactions of anomalously diffusing tracers, such as reactions occurring in mobile and immobile zones in rivers or reactions of molecules or tracers in biological cells. Recently, reaction-subdiffusion systems have been analyzed using the Fokker-Planck-Kolmogorov equation [117]. With our model it is possible to model reactions that only occur when the particles immobilize and to find explicit equations for the reaction products. We believe that the EMIM presented here provides a flexible and unified description for mobile-immobile transport.

ACKNOWLEDGMENTS

We acknowledge funding from the German Science Foundation (Grant No. DFG ME 1535/12-1). R.M. acknowledges the Foundation for Polish Science (Fundacja na rzecz Nauki Polskiej) for funding within an Alexander von Humboldt Polish Honorary Research Scholarship. A.V.C. acknowledges support from the Polish National Agency for Academic Exchange (NAWA).

APPENDIX A: MOBILE MASS USING THE ML TRAPPING TIME PDF

We calculate the mobile mass (6) for the concrete ML form of the trapping time PDF. In Laplace space we find

$$M_m(s) = \frac{M_0}{s + \omega\beta\left[1 - \frac{1}{1 + \tau_*^\mu s^\mu}\right]} \quad (\text{A1})$$

$$= \frac{M_0(1 + \tau_*^\mu s^\mu)}{s(1 + \tau_*^\mu s^\mu) + \omega\beta\tau_*^\mu s^\mu} \quad (\text{A2})$$

$$= \frac{M_0(1 + \tau_*^\mu s^\mu + \beta\omega\tau_*^\mu s^{\mu-1}) - M_0\beta\omega\tau_*^\mu s^{\mu-1}}{s(1 + \tau_*^\mu s^\mu + \beta\omega\tau_*^\mu s^{\mu-1})} \quad (\text{A3})$$

$$= \frac{M_0}{s} - M_0\beta\omega\tau_*^\mu \frac{s^{\mu-2}}{\tau_*^\mu s^\mu + \beta\omega\tau_*^\mu s^{\mu-1} + 1}. \quad (\text{A4})$$

Now we use the geometric series for $s^{1-\mu} < \tau_*^\mu s + \beta\omega\tau_*^\mu$,

$$\frac{1}{\tau_*^\mu s^\mu + \beta\omega\tau_*^\mu s^{\mu-1} + 1} = \frac{s^{1-\mu}}{\tau_*^\mu s + \beta\omega\tau_*^\mu} \frac{1}{1 + \frac{s^{1-\mu}}{\tau_*^\mu s + \beta\omega\tau_*^\mu}} \quad (\text{A5})$$

$$= \frac{s^{1-\mu}}{\tau_*^\mu s + \beta\omega\tau_*^\mu} \sum_{k=0}^{\infty} (-1)^k \frac{s^{k(1-\mu)}}{(\tau_*^\mu s + \beta\omega\tau_*^\mu)^k} \quad (\text{A6})$$

$$= \sum_{k=0}^{\infty} \frac{(-1)^k s^{k(1-\mu)+(1-\mu)}}{\tau_*^{\mu(1+k)} (s + \beta\omega)^{k+1}} \quad (\text{A7})$$

$$= \frac{1}{s\tau_*^\mu (s + \beta\omega)} + \sum_{k=1}^{\infty} (-1)^k \frac{(-1)^k s^{k(1-\mu)+(1-\mu)}}{\tau_*^{\mu(1+k)} (s + \beta\omega)^{k+1}}. \quad (\text{A8})$$

We use the Laplace inversion [Eq. (2.5) in [90]] and (A8) to transform (A4) to the time domain

$$\begin{aligned} M_m(t) &= M_0 - M_0 \beta \omega \tau_*^\mu \left[\frac{1}{\beta \omega \tau_*^\mu} (1 - e^{-\beta \omega t}) \right. \\ &\quad \left. + M_0 e^{-\beta \omega t} \sum_{k=1}^{\infty} (-1)^{k+1} \frac{t^{\mu k+1}}{\tau^{\mu(k+1)}} E_{1, \mu k+2}^{k+1}(-\beta \omega t) \right] \\ &= M_0 e^{-\beta \omega t} + N_0 \beta \omega t \sum_{k=1}^{\infty} (-1)^{k+1} \left(\frac{t}{\tau} \right)^{\mu k} \\ &\quad \times E_{1, \mu k+2}^{k+1}(-\beta \omega t). \end{aligned} \quad (\text{A9})$$

According to Gorenflo *et al.* [see [84], Eq. (5.1.54)], $E_{1, \beta}^\delta(z) = \frac{1}{\Gamma(\beta)} F_1(\delta, \beta, z)$ and thus from (A9),

$$\begin{aligned} M_m(t) &= M_0 e^{-\beta \omega t} + M_0 \beta \omega t \sum_{k=1}^{\infty} \frac{(-1)^{k+1}}{\Gamma(\mu k + 2)} \left(\frac{t}{\tau} \right)^{\mu k} \\ &\quad \times M(k+1, \mu k + 2, -\beta \omega t), \end{aligned} \quad (\text{A10})$$

where ${}_1F_1(a, b, z) \equiv M(a, b, z)$ is the Kummer function [84].

APPENDIX B: LONG-TIME CONCENTRATION PROFILE

Consider the fractal model. We approximate $C_m(x, s)$ [Eq. (18)] using $\sqrt{1+z} \sim 1+z/2$ in the exponential and

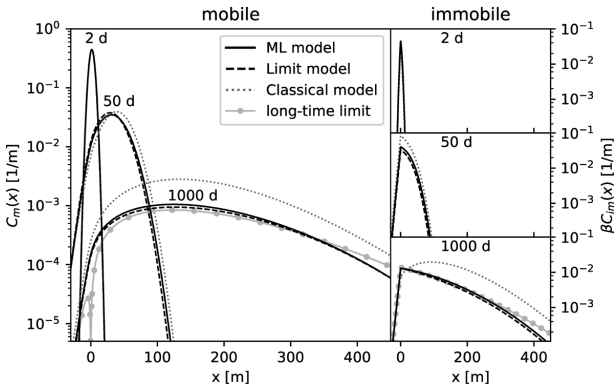


FIG. 10. Concentrations of mobile and immobile particles 2, 50, and 1000 d after injection in the main and right panels, respectively. The parameters of all models correspond to the fit to the mobile mass decay shown in Fig. 3. At short times all models yield a Gaussian mobile distribution, which is increasingly skewed for later times. Immobile particles have a non-Gaussian distribution at all times. Cusps are clearly visible at $x = 0$ and are a typical transport feature for systems with diverging trapping times [14,35]. The long-time behaviors (B6) and (B7) are shown by the gray lines with markers. The root at $x = 0$ for the mobile concentration is an artifact of our approximation (see the text). We use 0.8 m/d and 4 m²/d for v and D , respectively. The parameters of the ML model can be found in Table II. The parameters for the classical and fractional model correspond to a fit in [45] to the mobile mass decay of the MADE-1, as can be seen in Fig. 3 together with the parameters [45].

$\sqrt{1+z} \sim 1$ in the first fraction for $z = 4\phi(s)D/v^2 \ll 1$,

$$C_m(x, s) \stackrel{s \rightarrow 0}{\sim} \frac{e^{vx/2D}}{v} e^{-(v/2D)[1+2\phi(s)D/v^2]|x|} \quad (\text{B1})$$

$$\stackrel{s \rightarrow 0}{\sim} \frac{1}{v} e^{(v/2D)(x-|x|)} e^{-\beta \omega \tau_*^\mu s^\mu (|x|/v)}, \quad (\text{B2})$$

by using $\phi(s) = s + \beta \omega \tau_*^\mu s^\mu \approx \beta \omega \tau_*^\mu s^\mu$ for small s . In [84], Sec. 7.5, we find the Laplace transform pairs

$$\mathcal{L}^{-1}\{e^{-cs^\mu}\} = \frac{c^\mu}{\Gamma(\mu+1)} M_\mu(ct^{-\mu}), \quad (\text{B3})$$

$$\mathcal{L}^{-1}\{s^{\mu-1} e^{-cs^\mu}\} = \frac{1}{\Gamma(\mu)} M_\mu(ct^{-\mu}) \quad (\text{B4})$$

for $c > 0$, with the auxiliary function of Wright type

$$M_\mu(z) = \sum_{n=0}^{\infty} \frac{(-z)^n}{n! \Gamma[-\mu n + (1 - \mu)]}. \quad (\text{B5})$$

This yields the long-time limit of the mobile concentration

$$C_m(x, t) \approx \frac{\beta \omega \tau_*^\mu}{v^2} e^{(v/2D)(x-|x|)} |x| t^{-1-\mu} M_\mu\left(\frac{\beta \omega \tau_*^\mu}{v} |x| t^{-\mu}\right) \quad (\text{B6})$$

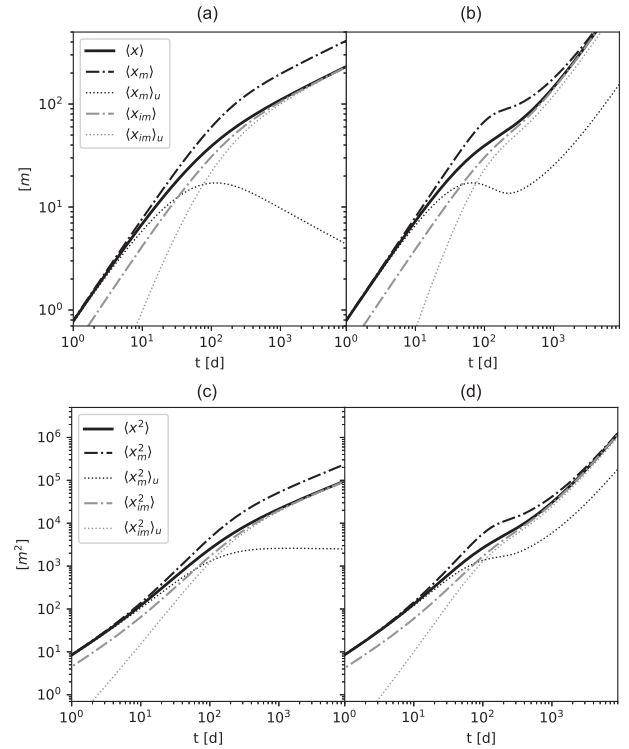


FIG. 11. Comparison of the normalized ($\langle x_{m,im}^n \rangle$), unnormalized ($\langle x_{m,im} \rangle_u$) and total n th-order ($\langle x^n \rangle$) moments, for (a) and (b) $n = 1$ and (c) and (d) $n = 2$ with double-logarithmic scales, using (a) and (c) the ML model and (b) and (d) the exponential model. For both models, both $\langle x_m \rangle_u$ and $\langle x_m \rangle$ are a good approximation for $\langle x \rangle$ for short times, due to the high mobile fraction. The same holds for long times for the immobile moment. In the ML model, the first moment of the mobile particles has the same power-law behavior (proportional to t^μ) as the immobile tracers but with a larger coefficient. The parameters are the same as in Fig. 3(a) and are given in Table II.

and the long-time limit of the immobile concentration using $C_{im}(x, s) = \omega \frac{1-\gamma(s)}{s} C_m(x, s)$ with $\gamma(s) \approx 1 - \tau_*^\mu s^\mu$,

$$C_{im}(x, t) \approx \frac{\beta \omega \tau_*^\mu}{v} e^{(v/2D)(x-|x|)t^{-\mu}} M_\mu \left(\frac{\beta \omega \tau_*^\mu}{v} |x| t^{-\mu} \right). \quad (\text{B7})$$

In Fig. 10 we show these approximations. Notice that at $t = 1000$ d, these approximations, shown as a gray line with markers, indeed estimate quite well the results obtained from the inverse Laplace inversion. Note also how the factor $|x|$ and finite value of $M_\mu(0) = 1/\Gamma(1-\mu)$ lead to a dip to zero at $x = 0$ for this approximation. This is an artifact of our approximation of $C_m(x, s)$ [Eq. (B2)], as it does not depend on s for $x = 0$.

APPENDIX C: ADDITIONAL PLOTS OF MOMENTS

We show additional plots of the first and second moments in Fig. 11. Figures 11(a) and 11(c) show our model using an ML trapping time PDF and Figs. 11(b) and 11(d) using an exponential trapping time PDF. The former demonstrates a transition from normal Brownian to anomalous behavior.

APPENDIX D: SKEWNESS AND KURTOSIS

Similarly to (14), we calculate the third and fourth unnormalized moments

$$\begin{aligned} \langle x_m^3(s) \rangle_u &= -i \frac{\partial^3}{\partial k^3} \frac{C_m(k, s)}{M_0} \Big|_{k=0} = \frac{12Dv}{\{s + \beta\omega[1 - \gamma(s)]\}^3} \\ &\quad + \frac{6v^3}{\{s + \beta\omega[1 - \gamma(s)]\}^4}, \\ \langle x_m^4(s) \rangle_u &= \frac{\partial^4}{\partial k^4} \frac{C_m(k, s)}{M_0} \Big|_{k=0} = \frac{24D^2}{\{s + \beta\omega[1 - \gamma(s)]\}^3} \\ &\quad + \frac{72Dv^2}{\{s + \beta\omega[1 - \gamma(s)]\}^4} \\ &\quad + \frac{24v^4}{\{s + \beta\omega[1 - \gamma(s)]\}^5}. \end{aligned} \quad (\text{D1})$$

When dividing by the fraction of mobile mass, we can calculate the skewness

$$\tilde{\mu}_{3,m} = \left\langle \left(\frac{x_m - \langle x_m \rangle}{\sqrt{\langle (x_m - \langle x_m \rangle)^2 \rangle}} \right)^3 \right\rangle \quad (\text{D2})$$

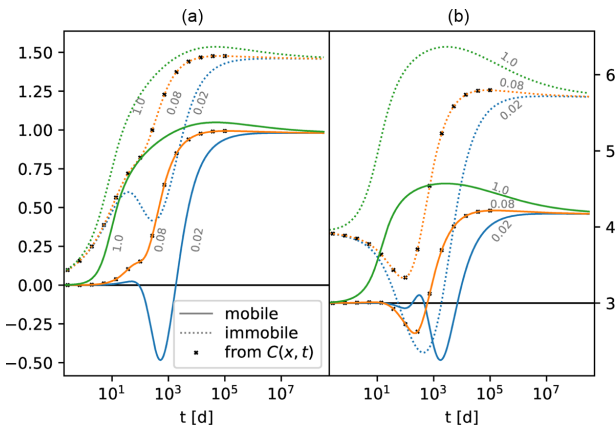


FIG. 12. (a) Skewness and (b) kurtosis for the ML model. Limits are calculated with the derivatives (D1) in Fourier space. Small numbers next to the lines indicate the values of β . Crosses mark the corresponding values for $\beta = 0.08$ obtained from the plume profile (18) after numerical Laplace inversion. The remaining parameters are the same as in Fig. 3(a), i.e., we have $\mu = 0.33$, $\omega = 1 \text{ d}^{-1}$, and $\tau_* = 1 \text{ d}$.

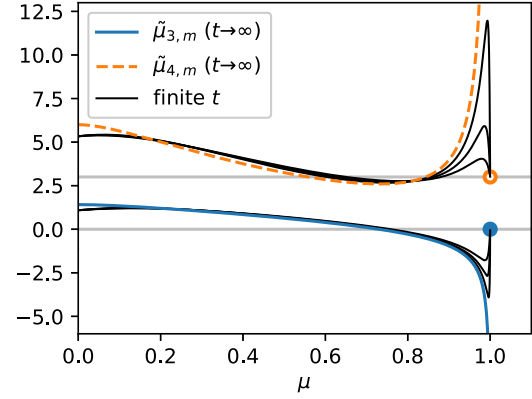


FIG. 13. Long-time limits of the skewness (D2) and kurtosis (D3) that only depend on μ and the sign of v (chosen positive here) for the ML and fractal models. The expressions for $\mu < 1$ diverge for $\mu \rightarrow 1$. For $\mu = 1$, we have $\tilde{\mu}_{3,m} = 0$ and $\tilde{\mu}_{4,m} = 1$. Gray lines indicate these values. Black solid lines indicate the kurtosis for finite $t = 500, 200, 100$ from top to bottom. They all reach the Gaussian value of 3 at $\mu = 1$ and are continuous. The skewness for finite $t = 500, 1000, 2000$ shows black solid lines ending at zero for $\mu = 1$. They are continuous as well. Black lines were obtained from the asymptotic expressions of the moments for $\beta = v = D = 1$.

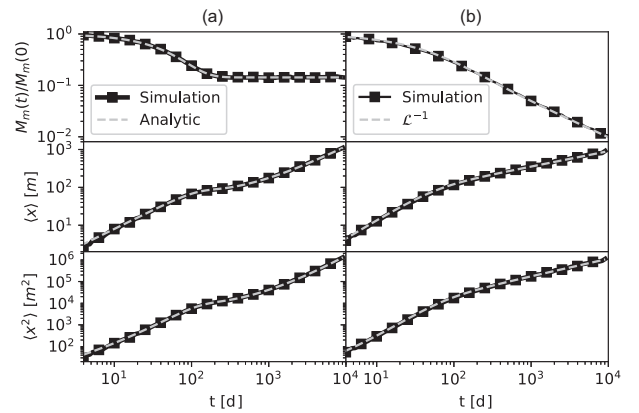


FIG. 14. Validation of our results with particle-tracking simulations. Square symbols denote values obtained from simulations using the method proposed in [66]. (a) For the exponential model we use our analytical results and (b) for the ML model we compare the simulations results to Laplace inversions of (12) and (14). The parameters are the same as in Fig. 3(a).

and kurtosis

$$\tilde{\mu}_{4,m} = \left\langle \left(\frac{x_m - \langle x_m \rangle}{\sqrt{\langle (x_m - \langle x_m \rangle)^2 \rangle}} \right)^4 \right\rangle \quad (\text{D3})$$

of the mobile solutes. Using (5), we obtain the skewness and kurtosis for the immobile plume.

A normal distribution in one dimension has skewness 0 and kurtosis 3. Deviations from these values characterize non-Gaussianity. Figure 12 shows the skewness and kurtosis using the ML model for different values of β for $\omega\tau_* = 1$. The mobile plume shows no initial skewness, as expected by the short-term Gaussian distribution. Small values of β yield negative skewness for intermediate timescales, i.e., a leading edge of the mobile plume profile. In [45] negative skewness is found for small β as well. We find that the long-time limit of the skewness is independent of β and positive for $\mu \gtrsim 0.73$. In addition, we numerically find positive skewness for intermediate times when decreasing v and leaving all remaining parameters constant for $\mu = 0.33$ and $\beta = 0.01$.

The long-time limit is independent of β and positive for the chosen $\mu = 0.33$. This corresponds to a leading tail of the mobile plume profile. The immobile distribution has positive skewness at all timescales and is nonmonotonic for $\beta = 0.02$.

To verify our results, we additionally calculate the skewness and kurtosis from the plume profile (18) for $\beta = 0.08$. The resulting crosses in Fig. 12 show good agreement.

The kurtosis measures how much of a distribution is concentrated in the tails. As Fig. 12 shows, the mobile distribution starts at 3 and has minima at intermediate times below this value for $\beta = 0.02$ and 0.08 .

We calculate the long-time limits

$$\langle x_m^3 \rangle \approx \frac{12Dvt^{3\mu-1}}{\beta^3\Gamma(3\mu)} + \frac{6v^3t^{4\mu-1}}{\beta^4\Gamma(4\mu)} \quad (\text{D4})$$

and

$$\langle x_m^4 \rangle \approx \frac{24D^2t^{3\mu-1}}{\beta^3\Gamma(3\mu)} + \frac{72Dv^2t^{4\mu-1}}{\beta^4\Gamma(4\mu)} + \frac{24v^4t^{5\mu-1}}{\beta^5\Gamma(5\mu)} \quad (\text{D5})$$

by using the Tauberian theorem. These results match earlier results found in [46]. We plug these into (D2) and (D3). For $\mu = 1$ we find $\tilde{\mu}_3 = 0$ and $\tilde{\mu}_4 = 3$, which match the normal distribution for $\mu = 1$ found in [45]. The long-time limits of the skewness only depend on μ and the sign of v , which we assume to be positive, here

$$\begin{aligned} \lim_{t \rightarrow \infty} \tilde{\mu}_3 = & - \frac{2\sqrt{\frac{\Gamma(3\mu)}{\Gamma(\mu)}} [12\sqrt{\pi}\Gamma(\mu)\Gamma(2\mu)^3\Gamma(4\mu) - 12\sqrt{\pi}\Gamma(2\mu)^4\Gamma(3\mu)]}{[2\Gamma(2\mu)^2 - \Gamma(\mu)\Gamma(3\mu)]^{3/2} [4\sqrt{\pi}\Gamma(2\mu)\Gamma(4\mu) - 16\mu\Gamma(\mu)\Gamma(3\mu)\Gamma(2\mu + \frac{1}{2})]} \\ & - \frac{2\sqrt{\frac{\Gamma(3\mu)}{\Gamma(\mu)}} [16\mu\Gamma(\mu)^3\Gamma(3\mu)^2\Gamma(2\mu + \frac{1}{2}) - 4\sqrt{\pi}\Gamma(\mu)^2\Gamma(2\mu)\Gamma(3\mu)\Gamma(4\mu)]}{[2\Gamma(2\mu)^2 - \Gamma(\mu)\Gamma(3\mu)]^{3/2} [4\sqrt{\pi}\Gamma(2\mu)\Gamma(4\mu) - 16\mu\Gamma(\mu)\Gamma(3\mu)\Gamma(2\mu + \frac{1}{2})]} \\ & - \frac{2\sqrt{\frac{\Gamma(3\mu)}{\Gamma(\mu)}} \{-3\Gamma(\mu)\Gamma(2\mu)^2\Gamma(3\mu)[16\mu\Gamma(\mu)\Gamma(2\mu + \frac{1}{2}) - 2\sqrt{\pi}\Gamma(3\mu)]\}}{[2\Gamma(2\mu)^2 - \Gamma(\mu)\Gamma(3\mu)]^{3/2} [4\sqrt{\pi}\Gamma(2\mu)\Gamma(4\mu) - 16\mu\Gamma(\mu)\Gamma(3\mu)\Gamma(2\mu + \frac{1}{2})]}, \end{aligned} \quad (\text{D6})$$

while the long-time limit of the kurtosis only depends on μ ,

$$\begin{aligned} \lim_{t \rightarrow \infty} \tilde{\mu}_4 = & - \frac{3\Gamma(3\mu)[8\Gamma(\mu)\Gamma(2\mu)^3\Gamma(3\mu)\Gamma(5\mu) - 8\Gamma(2\mu)^4\Gamma(3\mu)\Gamma(4\mu)]}{\Gamma(\mu)[\Gamma(\mu)\Gamma(3\mu) - 2\Gamma(2\mu)^2]\Gamma(4\mu)\Gamma(5\mu)} \\ & - \frac{3\Gamma(3\mu)[\Gamma(3\mu)\Gamma(4\mu)\Gamma(5\mu)\Gamma(\mu)^3 + 4\Gamma(2\mu)^2\Gamma(4\mu)\Gamma(5\mu)\Gamma(\mu)^2]}{\Gamma(\mu)[\Gamma(\mu)\Gamma(3\mu) - 2\Gamma(2\mu)^2]\Gamma(4\mu)\Gamma(5\mu)}. \end{aligned} \quad (\text{D7})$$

Figure 13 shows the limiting values. The skewness takes positive values for $\mu < 0.73$, i.e., the mobile plume has a leading tail, and negative values otherwise. The kurtosis is always higher than 3 except for $0.56 < \mu < 0.84$, meaning that for $0.56 < \mu < 0.84$ more mobile particles are within the standard deviation than for a normal distribution and thus effect a pronouncedly non-Gaussian distribution.

We note the apparent discontinuity of the long-time limits of the skewness (D6) and kurtosis (D7), as shown in Fig. 13. Note that we get finite values of the kurtosis for finite t , as evidenced by Fig. 13. A more detailed analysis of this property is beyond the scope of the present work.

APPENDIX E: SIMULATION

We implement a particle-tracking simulation using the space-domain method [66], in which the particle makes a jump Δx drawn from the jump length PDF $\lambda(x)$ in the fixed time Δt [66]. After each jump the particle immobilizes for a duration drawn from $\psi(t)$ with probability $1 - \exp(-\omega\beta\Delta t)$. For a waiting time PDF with the tail $\psi(t) \propto 1/t^{1+\mu}$ we use the method proposed by Kleinhans and Friedrich [118]. Results for the mobile mass and the first and second moments are shown in Fig. 14.



- [1] A. Einstein, Über die von der molekularkinetischen Theorie der Wärme geforderte Bewegung von in ruhenden Flüssigkeiten suspendierten Teilchen, *Ann. Phys. (Leipzig)* **322**, 549 (1905).
- [2] M. von Smoluchowski, Zur kinetischen theorie der Brownschen molekularbewegung und der suspensionen, *Ann. Phys. (Leipzig)* **326**, 756 (1906).
- [3] W. Sutherland, A dynamical theory of diffusion for non-electrolytes and the molecular mass of albumin, *Philos. Mag.* **9**, 781 (1905).
- [4] P. Langevin, Sur la théorie du mouvement brownien, *C. R. Acad. Sci.* **146**, 530 (1908).
- [5] A. Fick, Über Diffusion, *Ann. Phys. (Leipzig)* **170**, 59 (1855).
- [6] L. D. Landau and E. M. Lifshitz, *Physical Kinetics* (Butterworth Heinemann, Oxford, 1999).
- [7] N. G. van Kampen, *Stochastic Processes in Physics and Chemistry* (North-Holland, Amsterdam, 1981).
- [8] P. Lévy, *Processus stochastiques et mouvement brownien* (Stochastic processes and Brownian motion) (Gauthiers-Villars, Paris, 1948).
- [9] B. D. Hughes, *Random Walks and Random Environments* (Oxford University Press, Oxford, 1995), Vol. 1.
- [10] L. F. Richardson, Atmospheric diffusion shown on a distance-neighbour graph, *Proc. R. Soc. London Ser. A* **110**, 709 (1926).
- [11] G. K. Batchelor, Diffusion in a field of homogeneous turbulence. II. Relative motion of particles, *Math. Proc. Cambridge* **48**, 345 (1952).
- [12] J. Klafter, M. F. Shlesinger, and G. Zumofen, Beyond Brownian motion, *Phys. Today* **49**(2), 33 (1996).
- [13] J.-P. Bouchaud and A. Georges, Anomalous diffusion in disordered media: Statistical mechanisms, models and physical applications, *Phys. Rep.* **195**, 127 (1990).
- [14] R. Metzler and J. Klafter, The random walk's guide to anomalous diffusion: A fractional dynamics approach, *Phys. Rep.* **339**, 1 (2000).
- [15] I. M. Sokolov, Models of anomalous diffusion in crowded environments, *Soft Matter* **8**, 9043 (2012).
- [16] E. Barkai, Y. Garini, and R. Metzler, Strange kinetics of single molecules in living cells, *Phys. Today* **65**(8), 29 (2012).
- [17] F. Höfling and T. Franosch, Anomalous transport in the crowded world of biological cells, *Rep. Prog. Phys.* **76**, 046602 (2013).
- [18] D. Krapf and R. Metzler, Strange interfacial molecular dynamics, *Phys. Today* **72**(9), 48 (2019).
- [19] K. Nørregaard, R. Metzler, C. Ritter, K. Berg-Sørensen, and L. Oddershede, Manipulation and motion of organelles and single molecules in living cells, *Chem. Rev.* **117**, 4342 (2017).
- [20] E. E. Adams and L. W. Gelhar, Field study of dispersion in a heterogeneous aquifer: 2. Spatial moments analysis, *Water Resour. Res.* **28**, 3293 (1992).
- [21] J. Drummond, N. Schmadel, C. Kelleher, A. Packman, and A. Ward, Improving predictions of fine particle immobilization in streams, *Geophys. Res. Lett.* **46**, 13853 (2019).
- [22] N. Goeppert, N. Goldscheider, and B. Berkowitz, Experimental and modeling evidence of kilometer-scale anomalous tracer transport in an alpine karst aquifer, *Water Res.* **178**, 115755 (2020).
- [23] K. Singha and S. M. Gorelick, Saline tracer visualized with three-dimensional electrical resistivity tomography: Field-scale spatial moment analysis, *Water Resour. Res.* **41**, W05023 (2005).
- [24] R. Haggerty, S. M. Wondzell, and M. A. Johnson, Power-law residence time distribution in the hyporheic zone of a 2nd-order mountain stream, *Geophys. Res. Lett.* **29**, 18 (2002).
- [25] A. F. Aubeneau, B. Hanrahan, D. Bolster, and J. L. Tank, Substrate size and heterogeneity control anomalous transport in small streams, *Geophys. Res. Lett.* **41**, 8335 (2014).
- [26] K. H. Coats and B. D. Smith, Dead-end pore volume and dispersion in porous media, *Soc. Petrol. Eng. J.* **4**, 73 (1964).
- [27] P. Gouze, Y. Melean, T. Le Borgne, M. Dentz, and J. Carrera, Non-Fickian dispersion in porous media explained by heterogeneous microscale matrix diffusion, *Water Resour. Res.* **44**, W11416 (2008).
- [28] G. Margolin, M. Dentz, and B. Berkowitz, Continuous time random walk and multirate mass transfer modeling of sorption, *Chem. Phys.* **295**, 71 (2003).
- [29] M. Dentz and B. Berkowitz, Transport behavior of a passive solute in continuous time random walks and multirate mass transfer, *Water Resour. Res.* **39**, 1111 (2003).
- [30] B. Berkowitz, J. Klafter, R. Metzler, and H. Scher, Physical pictures of transport in heterogeneous media: Advection-dispersion, random-walk, and fractional derivative formulations, *Water Resour. Res.* **38**, 1191 (2002).
- [31] Y. Edery, A. Guadagnini, H. Scher, and B. Berkowitz, Origins of anomalous transport in heterogeneous media: Structural and dynamic controls, *Water Resour. Res.* **50**, 1490 (2014).
- [32] H. Krüsemann, A. Godec, and R. Metzler, First-passage statistics for aging diffusion in systems with annealed and quenched disorder, *Phys. Rev. E* **89**, 040101(R) (2014).
- [33] J. Klafter and I. M. Sokolov, *First Steps in Random Walks* (Cambridge University Press, Cambridge, 2011).
- [34] R. Metzler, J.-H. Jeon, A. G. Cherstvy, and E. Barkai, Anomalous diffusion models and their properties: Non-stationarity, non-ergodicity, and ageing at the centenary of single particle tracking, *Phys. Chem. Chem. Phys.* **16**, 24128 (2014).
- [35] H. Scher and E. W. Montroll, Anomalous transit-time dispersion in amorphous solids, *Phys. Rev. B* **12**, 2455 (1975).
- [36] C. Monthus and J.-P. Bouchaud, Models of traps and glass phenomenology, *J. Phys. A: Math. Gen.* **29**, 3847 (1996).
- [37] E. Barkai and S. Burov, Packets of Diffusing Particles Exhibit Universal Exponential Tails, *Phys. Rev. Lett.* **124**, 060603 (2020).
- [38] S. Mora and Y. Pomeau, Brownian diffusion in a dilute field of traps is Fickian but non-Gaussian, *Phys. Rev. E* **98**, 040101(R) (2018).
- [39] W. Wang and E. Barkai, Fractional Advection-Diffusion-Asymmetry Equation, *Phys. Rev. Lett.* **125**, 240606 (2020).
- [40] J. W. Kirchner, X. Feng, and C. Neal, Fractal stream chemistry and its implications for contaminant transport in catchments, *Nature (London)* **403**, 524 (2000).
- [41] H. Scher, G. Margolin, R. Metzler, J. Klafter, and B. Berkowitz, The dynamical foundation of fractal stream chemistry: The origin of extremely long retention times, *Geophys. Res. Lett.* **29**, 1061 (2002).
- [42] J. Klafter, A. Blumen, and M. F. Shlesinger, Stochastic pathway to anomalous diffusion, *Phys. Rev. A* **35**, 3081 (1987).
- [43] J. M. Boggs, S. C. Young, L. M. Beard, L. W. Gelhar, K. R. Rehfeldt, and E. E. Adams, Field study of dispersion

- in a heterogeneous aquifer: 1. Overview and site description, *Water Resour. Res.* **28**, 3281 (1992).
- [44] C. Harvey and S. M. Gorelick, Rate-limited mass transfer or macrodispersion: Which dominates plume evolution at the Macrodispersion Experiment (MADE) site? *Water Resour. Res.* **36**, 637 (2000).
- [45] R. Schumer, D. A. Benson, M. M. Meerschaert, and B. Baeumer, Fractal mobile-immobile solute transport, *Water Resour. Res.* **39**, 1296 (2003).
- [46] Y. Zhang, D. A. Benson, and B. Baeumer, Moment analysis for spatiotemporal fractional dispersion, *Water Resour. Res.* **44**, W04424 (2008).
- [47] G. Gao, H. Zhan, S. Feng, B. Fu, Y. Ma, and G. Huang, A new mobile-immobile model for reactive solute transport with scale-dependent dispersion, *Water Resour. Res.* **46**, W08533 (2010).
- [48] M. T. van Genuchten and P. J. Wierenga, Mass transfer studies in sorbing porous media I. Analytical solutions, *Soil Sci. Soc. Am. J.* **40**, 473 (1976).
- [49] R. Haggerty and S. M. Gorelick, Multiple-rate mass transfer for modeling diffusion and surface reactions in media with pore-scale heterogeneity, *Water Resour. Res.* **31**, 2383 (1995).
- [50] J. D. Drummond, L. G. Larsen, R. González-Pinzón, A. I. Packman, and J. W. Harvey, Fine particle retention within stream storage areas at base flow and in response to a storm event, *Water Resour. Res.* **53**, 5690 (2017).
- [51] J. A. Cunningham, C. J. Werth, M. Reinhard, and P. V. Roberts, Effects of grain-scale mass transfer on the transport of volatile organics through sediments: 1. Model development, *Water Resour. Res.* **33**, 2713 (1997).
- [52] K. R. Roche, J. D. Drummond, F. Boano, A. I. Packman, T. J. Battin, and W. R. Hunter, Benthic biofilm controls on fine particle dynamics in streams, *Water Resour. Res.* **53**, 222 (2017).
- [53] K. R. Roche, A. J. Shogren, A. Aubeneau, J. L. Tank, and D. Bolster, Modeling benthic versus hyporheic nutrient uptake in unshaded streams with varying substrates, *J. Geophys. Res.: Biogeosci.* **124**, 367 (2019).
- [54] A. F. Aubeneau, B. Hanrahan, D. Bolster, and J. Tank, Biofilm growth in gravel bed streams controls solute residence time distributions, *J. Geophys. Res.: Biogeosci.* **121**, 1840 (2016).
- [55] J. H. Writer, J. N. Ryan, S. H. Keefe, and L. B. Barber, Fate of 4-nonylphenol and 17 β -estradiol in the Redwood River of Minnesota, *Environ. Sci. Technol.* **46**, 860 (2012).
- [56] J. Drummond, A. Wright-Stow, P. Franklin, J. Quinn, and A. Packman, Fine particle transport dynamics in response to wood additions in a small agricultural stream, *Hydrol. Process.* **34**, 4128 (2020).
- [57] J. D. Drummond, H. A. Nel, A. I. Packman, and S. Krause, Significance of hyporheic exchange for predicting microplastic fate in rivers, *Environ. Sci. Technol. Lett.* **7**, 727 (2020).
- [58] J. L. Schaper, M. Posselt, J. L. McCallum, E. W. Banks, A. Hoehne, K. Meinikmann, M. A. Shanafield, O. Batelaan, and J. Lewandowski, Hyporheic exchange controls fate of trace organic compounds in an urban stream, *Environ. Sci. Technol.* **52**, 12285 (2018).
- [59] B. M. Flier, M. C. Baier, J. Huber, K. Müllen, S. Mecking, A. Zumbusch, and D. Wöll, Heterogeneous diffusion in thin polymer films as observed by high-temperature single-molecule fluorescence microscopy, *J. Am. Chem. Soc.* **134**, 480 (2012).
- [60] J. L. Keddie, R. A. Jones, and R. A. Cory, Size-dependent depression of the glass transition temperature in polymer films, *Europhys. Lett.* **27**, 59 (1994).
- [61] Z. Yang, Y. Fujii, F. K. Lee, C. H. Lam, and O. K. Tsui, Glass transition dynamics and surface layer mobility in unentangled polystyrene films, *Science* **328**, 1676 (2010).
- [62] Y. Liao, S. K. Yang, K. Koh, A. J. Matzger, and J. S. Biteen, Heterogeneous single-molecule diffusion in one-, two-, and three-dimensional microporous coordination polymers: Directional, trapped, and immobile guests, *Nano Lett.* **12**, 3080 (2012).
- [63] A. V. Weigel, M. M. Tamkun, and D. Krapf, Quantifying the dynamic interactions between a clathrin-coated pit and cargo molecules, *Proc. Natl. Acad. Sci. USA* **110**, E4591 (2013).
- [64] I. M. Sokolov, M. G. W. Schmidt, and F. Sagués, Reaction-subdiffusion equations, *Phys. Rev. E* **73**, 031102 (2006).
- [65] A. A. Kurilovich, V. N. Mantsevich, K. J. Stevenson, A. V. Chechkin, and V. V. Palyulin, Complex diffusion-based kinetics of photoluminescence in semiconductor nanoplatelets, *Phys. Chem. Chem. Phys.* **22**, 24686 (2020).
- [66] D. A. Benson and M. M. Meerschaert, A simple and efficient random walk solution of multi-rate mobile-immobile mass transport equations, *Adv. Water Resour.* **32**, 532 (2009).
- [67] R. Haggerty, S. A. McKenna, and L. C. Meigs, On the late-time behavior of tracer test breakthrough curves, *Water Resour. Res.* **36**, 3467 (2000).
- [68] R. Haggerty and S. M. Gorelick, Modeling mass transfer processes in soil columns with pore-scale heterogeneity, *Soil Sci. Soc. Am. J.* **62**, 62 (1998).
- [69] B. Berkowitz, A. Cortis, M. Dentz, and H. Scher, Modeling non-Fickian transport in geological formations as a continuous time random walk, *Rev. Geophys.* **44**, RG2003 (2006).
- [70] F. W. Schmidlin, Theory of trap-controlled transient photoconduction, *Phys. Rev. B* **16**, 2362 (1977).
- [71] T. Sandev, A. V. Chechkin, N. Korabel, H. Kantz, I. M. Sokolov, and R. Metzler, Distributed-order diffusion equations and multifractality: Models and solutions, *Phys. Rev. E* **92**, 042117 (2015).
- [72] B. Maryshev, M. Joelson, D. Lyubimov, T. Lyubimova, and M. C. Néel, Non Fickian flux for advection-dispersion with immobile periods, *J. Phys. A: Math. Theor.* **42**, 115001 (2009).
- [73] T. R. Ginn, L. G. Schreyer, and K. Zamani, Phase exposure-dependent exchange, *Water Resour. Res.* **53**, 619 (2017).
- [74] T. R. Ginn, Generalization of the multirate basis for time convolution to unequal forward and reverse rates and connection to reactions with memory, *Water Resour. Res.* **45**, W12419 (2009).
- [75] J. H. Schulz, E. Barkai, and R. Metzler, Aging Effects and Population Splitting in Single-Particle Trajectory Averages, *Phys. Rev. Lett.* **110**, 020602 (2013).
- [76] J. H. P. Schulz, E. Barkai, and R. Metzler, Aging Renewal Theory and Application to Random Walks, *Phys. Rev. X* **4**, 011028 (2014).
- [77] H. Krüsemann, A. Godec, and R. Metzler, Ageing first passage time density in continuous time random walks and quenched energy landscapes, *J. Phys. A: Math. Theor.* **48**, 285001 (2015).
- [78] D. N. Bradley, G. E. Tucker, and D. A. Benson, Fractional dispersion in a sand bed river, *J. Geophys. Res. Earth Surf.* **115**, F00A09 (2010).

- [79] A. M. Michalak and P. K. Kitanidis, Macroscopic behavior and random-walk particle tracking of kinetically sorbing solutes, *Water Resour. Res.* **36**, 2133 (2000).
- [80] W. Feller, *An Introduction to Probability Theory and its Applications* (Wiley, New York, 1971), Vol. 2.
- [81] A. V. Chechkin, I. M. Zaid, M. A. Lomholt, I. M. Sokolov, and R. Metzler, Bulk-mediated surface diffusion along a cylinder: Propagators and crossovers, *Phys. Rev. E* **79**, 040105(R) (2009).
- [82] R. Hilfer and L. Anton, Fractional master equations and fractal time random walks, *Phys. Rev. E* **51**, 848(R) (1995).
- [83] T. Sandev, R. Metzler, and A. Chechkin, From continuous time random walks to the generalized diffusion equation, *Frac. Calc. Appl. Anal.* **21**, 10 (2018).
- [84] R. Gorenflo, A. A. Kilbas, F. Mainardi, and S. V. Rogosin, *Mittag-Leffler Functions, Related Topics and Applications* (Springer, Berlin, 2014), Vol. 2.
- [85] B. V. Gnedenko and A. N. Kolmogorov, *Limit Distributions for Sums of Random Variables* (Addison-Wesley, Reading, 1954).
- [86] F. R. de Hoog, J. H. Knight, and A. N. Stokes, An improved method for numerical inversion of Laplace transforms, *SIAM. J. Sci. Stat. Comput.* **3**, 357 (1982).
- [87] F. Johansson *et al.*, mpmath: A Python library for arbitrary-precision floating-point arithmetic, version 1.1.0 (2013), <http://mpmath.org/>
- [88] I. Podlubny, *Fractional Differential Equations* (Academic Press, New York, 1998).
- [89] A. V. Chechkin, R. Gorenflo, and I. M. Sokolov, Retarding subdiffusion and accelerating superdiffusion governed by distributed-order fractional diffusion equations, *Phys. Rev. E* **66**, 046129 (2002).
- [90] T. R. Prabhakar, A singular integral equation with a generalized Mittag-Leffler function in the kernel. *Yokohama Math. J.* **19**, 7 (1971).
- [91] H. J. Haubold, A. M. Mathai, and R. K. Saxena, Mittag-Leffler functions and their applications, *J. Appl. Math.* **2011**, 298629 (2011).
- [92] N. Goldscheider, Fold structure and underground drainage pattern in the alpine karst system Hochifen-Gottesacker, *Eclogae Geol. Helv.* **98**, 1 (2005).
- [93] O. Grisel *et al.*, scikit-learn/scikit-learn: scikit-learn 0.24.2, version 0.24.2, <http://doi.org/10.5281/zenodo.4725836>
- [94] M. A. Thompson, J. M. Casolari, M. Badieirostami, P. O. Brown, and W. E. Moerner, Three-dimensional tracking of single mRNA particles in *Saccharomyces cerevisiae* using a double-helix point spread function, *Proc. Natl. Acad. Sci. USA* **107**, 17864 (2010).
- [95] A. G. Cherstvy, O. Günther, C. Beta, and R. Metzler, Non-Gaussianity, population heterogeneity, and transient superdiffusion in the spreading dynamics of amoeboid cells, *Phys. Chem. Chem. Phys.* **20**, 23034 (2018).
- [96] H. Murakoshi, R. Iino, T. Kobayashi, T. Fujiwara, C. Ohshima, A. Yoshimura, and A. Kusumi, Single-molecule imaging analysis of Ras activation in living cells, *Proc. Natl. Acad. Sci. USA* **101**, 7317 (2004).
- [97] S. Manley, J. M. Gillette, G. H. Patterson, H. Shroff, H. F. Hess, E. Betzig, and J. Lippincott-Schwartz, High-density mapping of single-molecule trajectories with photoactivated localization microscopy, *Nat. Methods* **5**, 155 (2008).
- [98] T. Kues, R. Peters, and U. Kubitschek, Visualization and tracking of single protein molecules in the cell nucleus, *Biophys. J.* **80**, 2954 (2001).
- [99] A. D. Fernández, P. Charchar, A. G. Cherstvy, R. Metzler, and M. W. Finnis, The diffusion of doxorubicin drug molecules in silica nanoslits is non-Gaussian, intermittent and anticorrelated, *Phys. Chem. Chem. Phys.* **22**, 27955 (2020).
- [100] J.-H. Jeon, V. Tejedor, S. Burov, E. Barkai, C. Selhuber-Unkel, K. Berg-Sørensen, L. Oddershede, and R. Metzler, *In Vivo* Anomalous Diffusion and Weak Ergodicity Breaking of Lipid Granules, *Phys. Rev. Lett.* **106**, 048103 (2011).
- [101] A. G. Cherstvy and R. Metzler, Population splitting, trapping, and non-ergodicity in heterogeneous diffusion processes, *Phys. Chem. Chem. Phys.* **15**, 20220 (2013).
- [102] D. S. Grebenkov, Time-averaged mean square displacement for switching diffusion, *Phys. Rev. E* **99**, 032133 (2019).
- [103] N. Tyagi and B. J. Cherayil, Non-Gaussian Brownian diffusion in dynamically disordered thermal environments, *J. Phys. Chem. B* **121**, 7204 (2017).
- [104] F. Baldovin, E. Orlandini, and F. Seno, Polymerization induces non-Gaussian diffusion, *Front. Phys.* **7**, 124 (2019).
- [105] A. Sabri, X. Xu, D. Krapf, and M. Weiss, Elucidating the Origin of Heterogeneous Anomalous Diffusion in the Cytoplasm of Mammalian Cells, *Phys. Rev. Lett.* **125**, 058101 (2020).
- [106] E. Yamamoto, T. Akimoto, A. Mitsutake, and R. Metzler, Universal Relation between Instantaneous Diffusivity and Radius of Gyration of Proteins in Aqueous Solution, *Phys. Rev. Lett.* **126**, 128101 (2021).
- [107] M. Hidalgo-Soria and E. Barkai, Hitchhiker model for Laplace diffusion processes, *Phys. Rev. E* **102**, 012109 (2020).
- [108] A. V. Weigel, B. Simon, M. M. Tamkun, and D. Krapf, Ergodic and nonergodic processes coexist in the plasma membrane as observed by single-molecule tracking, *Proc. Natl. Acad. Sci. USA* **108**, 6438 (2011).
- [109] C. Manzo, J. A. Torreno-Pina, P. Massignan, G. J. Lapeyre, Jr., M. Lewenstein, and M. F. Garcia Parajo, Weak Ergodicity Breaking of Receptor Motion in Living Cells Stemming from Random Diffusivity, *Phys. Rev. X* **5**, 011021 (2015).
- [110] J.-H. Jeon, M. Javanainen, H. Martinez-Seara, R. Metzler, and I. Vattulainen, Protein Crowding in Lipid Bilayers Gives Rise to Non-Gaussian Anomalous Lateral Diffusion of Phospholipids and Proteins, *Phys. Rev. X* **6**, 021006 (2016).
- [111] C. E. Wagner, B. S. Turner, M. Rubinstein, G. H. McKinley, and K. Ribbeck, A rheological study of the association and dynamics of MUC5AC gels, *Biomacromol.* **18**, 3654 (2017).
- [112] A. G. Cherstvy, S. Thapa, C. E. Wagner, and R. Metzler, Non-Gaussian, non-ergodic, and non-Fickian diffusion of tracers in mucin hydrogels, *Soft Matter* **15**, 2526 (2019).
- [113] W. He, H. Song, Y. Su, L. Geng, B. J. Ackerson, H. B. Peng, and P. Tong, Dynamic heterogeneity and non-Gaussian statistics for acetylcholine receptors on live cell membrane, *Nat. Commun.* **7**, 11701 (2016).
- [114] G. J. Schütz, H. Schindler, and T. Schmidt, Single-molecule microscopy on model membranes reveals anomalous diffusion, *Biophys. J.* **73**, 10730 (1997).
- [115] P. H. Lommerse, B. E. Snaar-Jagalska, H. P. Spaink, and T. Schmidt, Single-molecule diffusion measurements of H-Ras at the plasma membrane of live cells reveal

- microdomain localization upon activation, *J. Cell Sci.* **118**, 1799 (2005).
- [116] T. Sungkaworn, M. L. Jobin, K. Burnecki, A. Weron, M. J. Lohse, and D. Calebiro, Single-molecule imaging reveals receptor-G protein interactions at cell surface hot spots, *Nature (London)* **550**, 543 (2017).
- [117] A. M. Alexander and S. D. Lawley, Reaction-subdiffusion equations with species-dependent movement, *SIAM J. Appl. Math.* **81**, 2457 (2021).
- [118] D. Kleinhans and R. Friedrich, Continuous-time random walks: Simulation of continuous trajectories, *Phys. Rev. E* **76**, 061102 (2007).

T. J. Doerries, A. V. Chechkin, R. Schumer, and R. Metzler, Erratum: Rate equations, spatial moments, and concentration profiles for mobile-immobile models with power-law and mixed waiting time distributions, *Phys. Rev. E* **105**, 014105 (2022), <https://doi.org/10.1103/PhysRevE.105.029901> Copyright (2022) by the American Physical Society.

Erratum: Rate equations, spatial moments, and concentration profiles for mobile-immobile models with power-law and mixed waiting time distributions [Phys. Rev. E **105, 014105 (2022)]**Timo J. Doerries, Aleksei V. Chechkin, Rina Schumer, and Ralf Metzler  (Received 2 February 2022; published 14 February 2022)DOI: [10.1103/PhysRevE.105.029901](https://doi.org/10.1103/PhysRevE.105.029901)

We found that Eqs. (34)–(37) of this paper describing the long-time behavior of our model with an exponential waiting time distribution require the inequality $v^2 \frac{\beta}{(1+\beta)^2 \omega} \ll D$ to hold. When this inequality is not satisfied, we obtain that the second central moment has the limiting form

$$\langle (x - \langle x \rangle)^2 \rangle \sim 2 \left(\frac{D}{1+\beta} + \frac{v^2 \beta}{(1+\beta)^3 \omega} \right) t \quad \text{for } t(1+\beta)\omega \gg 1, \quad (1)$$

with the effective diffusivity $D_{\text{eff}} = \frac{D}{1+\beta} + v^2 \frac{\beta}{(1+\beta)^3 \omega}$. Note that Eq. (36) of the paper should be replaced by Eq. (1). We calculated the asymptotic values of the skewness and kurtosis of the concentration profile $C_m(x, s)$ of the mobile phase via the third and fourth moments and obtain the values zero and three, respectively. This implies that $C_m(x, t)$ can be approximated with a Gaussian concentration profile,

$$C_m(x, t) \sim \frac{1}{1+\beta} \frac{1}{\sqrt{4\pi D_{\text{eff}} t}} \exp \left(-\frac{\left[x - \frac{vt}{1+\beta} \right]^2}{4D_{\text{eff}} t} \right) \quad \text{for } t(1+\beta)\omega \gg 1, \quad (2)$$

at long times. In Fig. 1 the Laplace inversion of the exact expression for $C_m(x, s)$ is shown along expression (2) at long times. Both show good agreement, in contrast to a Gaussian in which the velocity contribution is missing in the effective diffusivity. The conclusion for the long-time behavior in the paper, thus, changes because the concentration profile does not correspond to that of a free Brownian particle with rescaled time. In the general case, due to the combination of immobilization events and transient advection, the particles asymptotically spread faster. We emphasize that this effect only occurs for appreciable values of v .

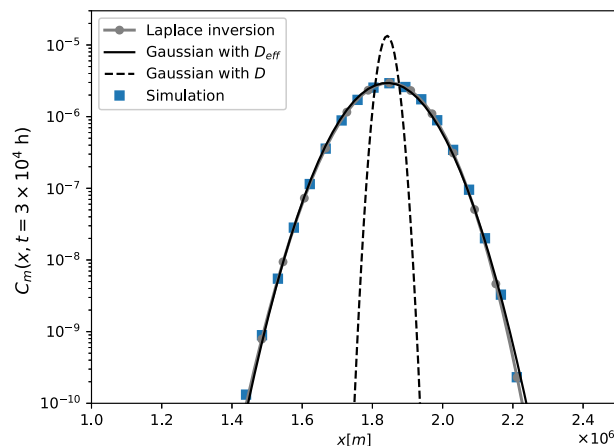


FIG. 1. Long-time behavior of the mobile concentration $C_m(x, s)$. The gray line with circle symbols is obtained from Laplace inversion of Eq. (18) of the paper using the exact expression for $\gamma(s)$. The solid black line shows Eq. (2). It matches the exact Laplace inversion result over two orders of magnitude. Both functions agree well with simulations results shown as squares. The dashed line shows the long-time behavior (37) of our paper for $v^2 \frac{\beta}{(1+\beta)^2 \omega} \ll D$. We here used the parameters from Table III. For these parameters the inequality does not hold.

Bibliography

- [D1] T.J. Doerries, A.V. Chechkin, and R. Metzler, Apparent anomalous diffusion and non-Gaussian distributions in a simple mobile-immobile transport model with Poissonian switching, *J. R. Soc. Interface* **19**, 20220233 (2022).
- [D2] T. J. Doerries, R. Metzler, and A. V. Chechkin, Emergent anomalous transport and non-Gaussianity in a simple mobile-immobile model: the role of advection, *New J. Phys.* **25**, 063009 (2023).
- [D3] T. J. Doerries, A. V. Chechkin, R. Schumer, and R. Metzler, Rate equations, spatial moments, and concentration profiles for mobile-immobile models with power-law and mixed waiting time distributions, *Phys. Rev. E* **105**, 014105 (2022).
- [1] J. Ingen-Housz, Über den Gebrauch des Vergrößerungsglases (On the use of the magnifying glass), *Vermischte Schriften physisch-medicenschen Inhalts* **2**, 123 (1784).
- [2] R. Brown, A brief account of microscopical observations made in the months of June, July and August 1827, on the particles contained in the pollen of plants; and on the general existence of active molecules in organic and inorganic bodies, *Philos. Mag. and Ann. Philos.* (**21**), 161 (1828).
- [3] A. Fick, Über Diffusion (On diffusion), *Ann. Phys. (Leipzig)* **170**, 59 (1855).

- [4] A. Einstein, Über die von der molekularkinetischen Theorie der Wärme geforderte Bewegung von in ruhenden Flüssigkeiten suspendierten Teilchen (On the movement of particles suspended in stationary liquids as required by the molecular-kinetic theory of heat), *Ann. Phys. (Leipzig)* **322**, 549 (1905).
- [5] W. Sutherland, A dynamical theory of diffusion for non-electrolytes and the molecular mass of albumin, *Phil. Mag.* **9**, 781 (1905).
- [6] M. v. Smoluchowski, Zur kinetischen Theorie der Brownschen Molekularbewegung und der Suspensionen (On the kinetic theory of Brownian molecular movement), *Ann. Phys. (Leipzig)* **326**, 756 (1906).
- [7] J. Perrin, L'agitation moléculaire et le mouvement brownien, *Acad. Sci., Paris, C. R.* **146**, 967 (1908).
- [8] P. Langevin, Sur la théorie du mouvement brownien (On the theory of Brownian motion), *C. R. Acad. Sci. (Paris)* **146**, 530 (1908).
- [9] J. Perrin, Moivement brownien et réalité moléculaire, *Ann. Chim. Phys.* **18**, 5 (1909).
- [10] I. Nordlund, A new determination of Avogadro's number from Brownian motion of small mercury spherules, *Z. Phys. Chem.* **87**, 40 (1914).
- [11] E. Kappler, Versuche zur Messung der Avogadro-Loschmidtschen Zahl aus der Brownschen Bewegung einer Drehwaage, *Ann. Phys. (Leipzig)* **11**, 233 (1931).
- [12] E. Yamamoto, T. Akimoto, A. Mitsutake, and R. Metzler, Universal relation between instantaneous diffusivity and radius of gyration of proteins in aqueous solution, *Phys. Rev. Lett.* **126**, 128101 (2021).
- [13] R. Metzler, J.-H. Jeon, A. G. Cherstvy, and E. Barkai, Anomalous diffusion models and their properties: non-stationarity, non-ergodicity, and ageing at the centenary of single particle tracking, *Phys. Chem. Chem. Phys.* **16**, 24128 (2014).

- [14] H. Risken, *The Fokker-Planck Equation*, (Springer-Verlag Berlin Heidelberg, 1996).
- [15] N. G. van Kampen, *Stochastic Processes in Physics and Chemistry* (North-Holland, Amsterdam, 1981).
- [16] H. H. Deans, A mathematical model for dispersion in the direction of flow of porous media, *Soc. Pet. Eng. J.* **3**, 49 (1963).
- [17] K. H. Coats and B. D. Smith, Dead-end pore volume and dispersion in porous media. *Soc. Petrol. Eng. J.* **4**, 73 (1964).
- [18] M. T. van Genuchten and P. J. Wierenga, Mass transfer studies in sorbing porous media I. Analytical solutions. *Soil Science Soc. Am. J.* **40**, 473 (1976).
- [19] N. Goepfert, N. Goldscheider, and B. Berkowitz, Experimental and modeling evidence of kilo-scale anomalous tracer transport in an alpine karst aquifer, *Water Res.* **178**, 115755 (2020).
- [20] C. Harvey and S. M. Gorelick, Rate-limited mass transfer or macrodispersion: Which dominates plume evolution at the Macrodispersion Experiment (MADE) site?, *Water Res. Res.* **36**, 637 (2000).
- [21] R. Schumer, D. A. Benson, M. M. Meerschaert, and B. Baeumer, Fractal mobile-immobile solute transport, *Water Res. Res.* **39**, 1296 (2003).
- [22] R. Haggerty and S. M. Gorelick, Multiple-rate mass transfer for modeling diffusion and surface reactions in media with pore-scale heterogeneity, *Water Res. Res.* **31**, 2383 (1995).
- [23] M. Dentz and B. Berkowitz, Transport behavior of a passive solute in continuous time random walks and multirate mass transfer. *Water Res. Res.* **39**, 1111 (2003).
- [24] M. Sardin, D. Schweich, F. J. Leij, and M. T. van Genuchten, Modeling the nonequilibrium transport of linearly interacting solutes in porous media: A review, *Water Res. Res.* **27**, 2287 (1991).

- [25] R. Haggerty, S. A. McKenna, and L. C. Meigs, L. C. (2000). On the late-time behavior of tracer test breakthrough curves, *Water Res. Res.* **36**, 3467 (2000).
- [26] A. F. Aubeneau, B. Hanrahan, D. Bolster, and J. L. Tank, Substrate size and heterogeneity control anomalous transport in small streams, *Geophys. Res. Lett.* **41**, 8335 (2014).
- [27] R. Haggerty, S. M. Wondzell, and M. A. Johnson, Power-law residence time distribution in the hyporheic zone of a 2nd-order mountain stream. *Geophys. Res. Lett.* **29**, 18 (2002).
- [28] F. W. Schmidlin, Theory of trap-controlled transient photoconduction, *Phys. Rev. B* **16**, 2362 (1977).
- [29] D. Mazza, A. Abernathy, N. Golob, T. Morisaki, and J.G. McNally, A benchmark for chromatin binding measurements in live cells, *Nucleic Acids Res.* **40**, e119 (2012).
- [30] C. Yeung, M. Shtrahman, and X. L. Wu, Stick-and-diffuse and caged diffusion: a comparison of two models of synaptic vesicle dynamics, *Biophys. J.* **92**, 2271 (2007).
- [31] A. G. Cherstvy, A. V. Chechkin, and R. Metzler, Particle invasion, survival, and non-ergodicity in 2D diffusion processes with space-dependent diffusivity, *Soft Matter* **10**, 1591 (2014).
- [32] Y. Golan and E. Sherman, Resolving mixed mechanisms of protein subdiffusion at the T cell plasma membrane, *Nat. Commun.* **8**, 25851 (2017).
- [33] Z. R. Fox, E. Barkai, and D. Krapf, Aging power spectrum of membrane protein transport and other subordinated random walks, *Nat. Commun.* **12**, 6162 (2012).
- [34] J. Janczura, M. Balcerek, K. Burnecki, A. Sabri, M. Weiss, and D. Krapf, Identifying heterogeneous diffusion states in the cytoplasm by a hidden Markov model, *New J. Phys.* **23**, 053018 (2021).

- [35] M. N. Goltz and P. V. Tobrtyd, Using the Method of Moments to analyse Three-Dimensional Diffusion-Limited Solute Transport From Temporal and Spatial Perspectives, *Water Res. Res.* **23**, 1575 (1987).
- [36] A. M. Michalak and P. K. Kitanidis, Macroscopic behavior and random-walk particle tracking of kinetically sorbing solutes, *Water Res. Res.* **36**, 2133 (2000).
- [37] M. Kolarova, F. García-Sierra, A. Bartos, J. Ricny, and D. Ripova, Structure and pathology of tau protein in Alzheimer disease, *J. Alzheimer's Dis.* **2012**, 731526 (2012).
- [38] M. Igaev, D. Janning, F. Sündermann, B. Niewidok, R. Brandt, and W. Junge, A Refined Reaction-Diffusion Model of Tau-Microtubule Dynamics and its Application in FDAP Analysis, *Biophys. J.* **107**, 2567 (2014).
- [39] A. V. Weigel, B. Simon, M. M. Tamkun, and Diego Krapf, Ergodic and nonergodic processes coexist in the plasma membrane as observed by single-molecule tracking, *Proc. Natl. Acad. Sci. U.S.A.* **108**, 6438 (2011).
- [40] S. M. A. Tabei, S. Burov, H. Y. Kim, A. Kuznetsov, T. Huynh, J. Jureller, L. H. Philipson, A. R. Dinner, and N. F. Scherer, Intracellular transport of insulin granules is a subordinated random walk, *Proc. Natl. Acad. Sci. U.S.A.* **110**, 4911 (2013).
- [41] J.-H. Jeon, V. Tejedor, S. Burov, E. Barkai, C. Selhuber-Unkel, K. Berg-Sørensen, L. Oddershede, and Ralf Metzler, In Vivo Anomalous Diffusion and Weak Ergodicity Breaking of Lipid Granules, *Phys. Rev. Lett.* **106**, 048103 (2011).
- [42] W. He, H. Song, Y. Su, L. Geng, B. J. Ackerson, H. B. Peng, and P. Tong, Dynamic heterogeneity and non-Gaussian statistics for acetylcholine receptors on live cell membrane, *Nat. Comm.* **7**, 11701 (2016).

- [43] A. D. Fernández, P. Charchar, A. G. Cherstvy, R. Metzler, and M. W. Finnis, The diffusion of doxorubicin drug molecules in silica nanoslits is non-Gaussian, intermittent and anticorrelated, *Phys. Chem. Chem. Phys.* **22**, 27955 (2020).
- [44] M. J. Skaug, J. Mabry, and D. K. Schwartz, Intermittent Molecular Hopping at the Solid-Liquid Interface, *Phys. Rev. Lett.* **110**, 256101 (2013).
- [45] T. O. E. Skinner, S. K. Schnyder, D. G. A. L. Aarts, J. Horbach, and R. P. A. Dullens, Localization dynamics of fluids in random confinement, *Phys. Rev. Lett.* **111**, 128301 (2013).
- [46] D. Wang, H. Wu, L. Liu, J. Chen, and D. K. Schwartz, Diffusive escape of a nanoparticle from a porous cavity, *Phys. Rev. Lett.* **123**, 118002 (2019).
- [47] J. Ślęzak and S. Burov, From diffusion in compartmentalized media to non-Gaussian random walks, *Sci. Rep.* **11**, 1 (2021).
- [48] J. M. Miotto, S. Pigolotti, A. V. Chechkin, and S. Roldán-Vargas, Length scales in Brownian yet non-Gaussian dynamics, *Phys. Rev. X* **11**, 031002 (2021).
- [49] K. Kamagata, E. Mano, K. Ouchi, S. Kanabayashi, and R. C. Johnson, High Free-Energy Barrier of 1D Diffusion Along DNA by Architectural DNA-Binding Proteins, *J. Mol. Biol.* **430**, 655 (2018)
- [50] S. P. Hancock, D. Cascio, and R. C. Johnson, DNA Sequence Determinants Controlling Affinity, Stability and Shape of DNA Complexes Bound by the Nucleoid Protein Fis, *PLoS ONE* **11**, e0150189 (2016).
- [51] S. P. Hancock, D. Cascio, and R. C. Johnson, Crystal structure of Fis bound to 27bp DNA F1-8A (AAATTAGTTTGAATTTTGAGC-TAATTT), Worldwide Protein Data Bank, <https://doi.org/10.2210/pdb5ds9/pdb> (2016).

- [52] B. Wang, S. M. Anthony, S. C. Bae, and S. Granick, Anomalous yet brownian, *Proc. Natl. Acad. Sci. USA* **106**, 15160 (2009).
- [53] I. Chakraborty, and Y. Roichman, Disorder-induced Fickian, yet non-Gaussian diffusion in heterogeneous media. *Phys. Rev. Res.* **2**, 022020 (2020).
- [54] A. V. Chechkin, F. Seno, R. Metzler, and I. M. Sokolov, Brownian yet Non-Gaussian Diffusion: From Superstatistics to Subordination of Diffusing Diffusivities, *Phys. Rev. X* **7**, 021002 (2017)
- [55] V. Sposini, A. V. Chechkin, F. Seno, G. Pagnini, and R. Metzler, Random diffusivity from stochastic equations: comparison of two models for Brownian yet non-Gaussian diffusion, *New. J. Phys.* **20**, 043044 (2018).
- [56] T. Miyaguchi, T. Akimoto, and E. Yamamoto, Langevin equation with fluctuating diffusivity: A two-state model, *Phys. Rev. E* **94**, 012109 (2016).
- [57] M. Hidalgo-Soria, E. Barkai, and S. Burov, Cusp of Non-Gaussian Density of Particles for a Diffusing Diffusivity Model, *Entropy* **23**, 231 (2020).
- [58] H. Scher and M. Lax, Stochastic Transport in Disordererd Solid. I. Theory, *Phys. Rev. B* **7**, 7 (1973).
- [59] H. Scher and E. W. Montroll, Anomalous transient-time dispersion in amorphous solids, *Phys. Rev. B.* **12**, 2455 (1975).
- [60] C. Monthus and J. P. Bouchaud, Models of traps and glass phenomenology, *J. Phys. A:Math. Gen* **29**, 3847 (1996).
- [61] I. Y. Wong, M. L. Gardel, D. R. Reichmann, E. R. Weeks, M. T. Valentine, A. R. Bausch, and D. A. Weitz, Anomalous diffusion probes microstructure dynamics of entangled F-actin networks, *Phys. Rev. Lett.* **92**, 178101 (2004).

- [62] E. Yamamoto, T. Akimoto, M. Yausi, and K. Yasuoka, Origin of subdiffusion of water molecules on cell membrane surfaces, *Sci. Rep.* **4**, 4720 (2014).
- [63] R. Metzler and J. Klafter, The random walk's guide to anomalous diffusion: a fractional dynamics approach, *Phys. Rep.* **339**, 1 (2000).
- [64] H. C. Fogedby, Langevin equations for continuous time Lévy flights, *Phys. Rev. E* **50**, 1657 (1994).
- [65] R. Gorenflo and F. Mainardi, Some recent advances in theory and simulation of fractional diffusion processes, *J. Comp. Appl. Math.* **229**, 400 (2009).
- [66] R. Hilfer and L. Anton, Fractional master equations and fractal time random walks, *Phys. Rev. E* **51**, R848(R) (1995).
- [67] T. Sandev, A. Chechkin, H. Kantz, and R. Metzler, Diffusion and Fokker-Planck-Smoluchowski equations with generalized memory kernel, *Frac. Calc. Appl. Anal.* **18**, 1006 (2015).
- [68] M. Caputo, Linear Models of Dissipation whose Q is almost Frequency Independent - II, *Geophys. J. R. astr. Soc.* **13**, 529 (1967).
- [69] T. Sandev, A. V. Chechkin, N. Korabel, H. Kantz, I. M. Sokolov, and R. Metzler, Distributed-order diffusion equations and multifractality: Models and solutions, *Phys. Rev. E* **92**, 042117 (2015).
- [70] S. Vitaly, P. Paradisi, and G. Pagnini, Anomalous diffusion originated by two Markovian hopping-trap mechanisms, *J. Phys. A: Math. Theor.* **55**, 224012 (2022).
- [71] E. Barkai and S. Burov, Packets of Diffusing Particles Exhibit Universal Exponential Tails, *Phys. Rev. Lett.* **124**, 060603 (2020).
- [72] B. Berkowitz, J. Klafter, R. Metzler, and H. Scher, Physical pictures of transport in heterogeneous media: Advection-dispersion, random-walk, and fractional derivative formulations, *Water Res. Res.* **38**, 1191 (2002).

- [73] G. Margolin, M. Dentz, and B. Berkowitz, Continuous time random walk and multirate mass transfer modeling of sorption, *Chem. Phys.* **295**, 71 (2003).
- [74] A. F. Aubeneau, B. Hanrahan, D. Bolster, and J. Tank, J. Biofilm growth in gravel bed streams controls solute residence time distributions, *J. Geophys. Res.: Biogeosc.* **121**, 1840 (2016).
- [75] H. B. Fischer, Longitudinal dispersion and turbulent mixing in open-channel flow, *Annu. Rev. Fluid Mech.* **5**, 59 (1973).
- [76] F. Boano, J. W. Harvey, A. Marion, A. I. Packman, R. Revelli, L. Ridolfi, and A. Wörman, Hyporheic flow and transport processes: Mechanisms, models, and biogeochemical implications, *Rev. Geophys.* (**52**), 603 (2014).
- [77] M. W. Becker and A. M. Shapiro, Tracer transport in fractured crystalline rock: Evidence of nondiffusive breakthrough tailing, *Water Res. Res.* **36**, 1677 (2000).
- [78] B. Berkowitz, H. Scher, and S. E. Silliman, Anomalous transport in laboratory-scale, heterogeneous porous media, *Water Resour. Res.* **36**, 149 (2000).
- [79] G. Margolin, M. Dentz, and B. Berkowitz, Continuous time random walk and multirate mass transfer modeling of sorption, *Chem. Phys.* **295**, 71 (2003).
- [80] B. Berkowitz, A. Cortis, M. Dentz, and H. Scher, Modeling non-Fickian transport in geological formations as a continuous time random walk, *Rev. Geophys.* **44**, RG2003 (2006).
- [81] F. Boano, A. I. Packman, A. Cortis, R. Revelli, and L. Ridolfi, A continuous time random walk approach to the stream transport of solutes, *Water Res. Res.* **43**, 1 (2007)

- [82] M. Dentz, A. Cortis, H. Scher, and B. Berkowitz, Time behavior of solute transport in heterogeneous media: transition from anomalous to normal transport, *Adv. Water. Resour.* **27**, 155 (2004).
- [83] F. Boano, J. W. Harvey, A. Marion, A. I. Packman, R. Revelli, L. Ridolfi, and A. Wörman, Hyporheic flow and transport processes: Mechanisms, 10.1002/2012RG000417 models, and biogeochemical implications, *Rev. Geophys.* **52**, 603 (2014)
- [84] T. Orghidan, Ein neuer Lebensraum des unterirdischen Wassers: Der hyporheische Boptop, *Arch. Hydrobiol.* **55**, 392 (1959).
- [85] K. R. Roche, A. J. Shogren, A. Aubeneau, J. L. Tank, and D. Bolster, Modeling benthic versus hyporheic nutrient uptake in unshaded streams with varying substrates, *J. Geophys. Res.: Biogeosc.* **124**, 367 (2019).
- [86] Y. Edery, A. Guadagnini, H. Scher, and B. Berkowitz, Origins of anomalous transport in heterogeneous media: Structural and dynamic controls. *Water Res. Res.* **50**, 1490 (2014).
- [87] E. E. Adams and L. W. Gelhar, Field study of dispersion in a heterogeneous aquifer: 2. Spatial moments analysis. *Water Res. Res.* **28**, 3293 (1992).
- [88] J. M. Boggs, S. C. Young, L. M. Beard, L. W. Gelhar, K. R. Rehfeldt, and E. E. Adams, Field study of dispersion in a heterogeneous aquifer: 1. Overview and site description, *Water Res. Res.* **28**, 3281 (1992).
- [89] R. Haggerty and S. M. Gorelick, Multiple-rate mass transfer for modeling diffusion and surface reactions in media with pore-scale heterogeneity, *Water Res. Res.* **31**, 2383 (1995).
- [90] A. A. Kurilovich, V. N. Mantsevich, Y. Mardoukhi, K. J. Stevenson, A. V. Chechkin, and V. V. Palyulin, Non-Markovian diffusion of excitons in layered perovskites and transition metal dichalcogenides, *Phys. Chem. Chem. Phys.* **24**, 13941 (2022).

- [91] P. J. Pedler, Occupation times for two state Markov chains, *J. Appl. Prob.* **8**, 381 (1971).
- [92] B. L. Sprague, R. L. Pego, D. A. Stavreva, and J. G. McNally, Analysis of binding reactions by fluorescence recovery after photobleaching, *Biophys. J.* **86**, 3473 (2004).
- [93] R. Zwanzig, *Nonequilibrium Statistical Mechanics*, (Oxford university Press, Oxford 2001).
- [94] A. A. Kurilovich, V. N. Mantsevich, K. J. Stevenson, A. V. Chechkin, and V. V. Palyulin, Complex diffusion-based kinetics of photoluminescence in semiconductor nanoplatelets, *Phys. Chem. Chem. Phys.* **22**, 24686 (2020).
- [95] J. Chen, Z. Zhang, L. Li, B. C. Chen, A. Revyakin, B. Hajj, W. Legant, M. Dahan, T. Lionnet, E. Betzig, R. Tjian, and Z. Liu, Single-molecule dynamics of enhanceosome assembly in embryonic stem cells, *Cell* **156**, 1274 (2014).
- [96] D. Mazza, A. Abernathy, N. Golob, T. Morisaki, and J.G. McNally, A benchmark for chromatin binding measurements in live cells, *Nucleic Acids Res.* **40**, e119 (2012).
- [97] M. Hidalgo-Soria and E. Barkai, Hitchhiker model for Laplace diffusion processes, *Phys. Rev. E* **102**, 012109 (2020).
- [98] R. Haggerty, and S. M. Gorelick, S. M. (1998). Modeling mass transfer processes in soil columns with pore-scale heterogeneity, *Soil Sc. Soc. Am. J.* **62**, 62 (1998).
- [99] S. Bochner, *Harmonic Analysis and the Theory of Probability*, Berkeley University Press, Berkeley, CA (1960)
- [100] B. D. Hughes, *Random walks and random environments*, vol 1: random walks (Oxford University Press, Oxford, UK, 1995.)

- [101] A. Chechkin, and I. M. Sokolov, Relation between generalized diffusion equations and subordination schemes, *Phys. Rev. E* **103**, 032133 (2021).
- [102] C. E. Brown, Coefficient of Variation. In: *Applied Multivariate Statistics in Geohydrology and Related Sciences*. Springer, Berlin, Heidelberg (1998).
- [103] S. Park, O. C. Lee, X. Durang, and J.- H. Jeon, A mini-review of the diffusion dynamics of DNA-binding proteins: experiments and models, *J. Korean Phys. Soc.* **78**, 408 (2021).
- [104] A. Tafvizi, L. A. Mirny, and A. M. van Oijen, Dancing on DNA: Kinetic aspects of search processes on DNA, *ChemPhysChem* **12**, 1418 (2011).
- [105] A. Tafvizi, F. Huang, A. R. Fersht, L. A. Mirny, and A. M. van Oijen, A single-molecule characterization of p53 search on DNA, *Proc. Natl. Acad. Sci. USA* **108**, 563 (2011).
- [106] M. Kong *et al.*, Single-Molecule Imaging Reveals that Rad4 Employs a Dynamic DNA Damage Recognition Process, *Mol. Cell* **64**, 376 (2016).
- [107] T. Guo, W. Noble, and D. P. Hanger, Roles of tau protein in health and disease, *Acta Neuropathol.* **133**, 665 (2017).
- [108] W. Feller, *An Introduction to Probability Theory and its Applications*, Vol. 2 (Wiley, New York, NY, 1971).
- [109] R. Metzler and A. V. Chechkin, Non-Gaussianity in stochastic transport: phenomenology and modelling, E-print arXiv: 2204.01048.
- [110] D. Wang, H. Wu, L. Liu, J. Chen, and D. K. Schwartz, Diffusive Escape of a Nanoparticle from a Porous Cavity, *Phys. Rev. Lett.* **123**, 118002 (2019).
- [111] S. Mora and Y. Pomeau, Brownian diffusion in a dilute field of traps is Fickian but non-Gaussian, *Phys. Rev. E*, **98**, 040101 (2018).
- [112] D. S. Grebenkov, Time-averaged mean square displacement for switching diffusion, *Phys. Rev. E* **99**, 032133 (2019).

- [113] K. Roth and W. A. Jury, Linear transport models for adsorbing solutes, *Water Res. Res.* **29**, 1195 (1993).
- [114] J. Villiermaux, A flexible method for representing complex phenomena from simple concepts, *J. Chromatogr.* **406**, 11 (1987).
- [115] R. Metzler and J. Klafter, The random walk's guide to anomalous diffusion: a fractional dynamics approach, *Phys. Rep.* **339**, 1 (2000).
- [116] B. E. Rapp, *Microfluidics: Modeling, Mechanics and Mathematics*, (Elsevier, Amsterdam 2017).
- [117] S. M. Ross, *A first course in probability*, edited by D. Lynch (Pearson, New Jersey, 2010), Vol. 8, p. 362.
- [118] S. Burov, W. Wang, and E. Barkai, Exponential Tails and Asymmetry Relations for the Spread of Biased Random Walks, *ArXiv* 2209.03410 (2022).
- [119] B. R. Rinn, P. Maass, and J-P. Bouchaud, Hopping in the glass configuration space: Subaging and generalized scaling laws, *Phys. Rev. B* **64**, 104417 (2001).
- [120] G. H. Weiss, The Two-State Random Walk, *J. Stat. Phys.* (**15**), 157 (1976).
- [121] C. E. Wagner, B. S. Turner, M. Rubinstein, G. H. McKinley, and K. Ribbeck, *Biomacromol.* **18**, 3654 (2017).
- [122] A. G. Cherstvy, S. Thapa, C. E. Wagner, and R. Metzler, Non-Gaussian, non-ergodic, and non-Fickian diffusion of tracers in mucin hydrogels, *Soft Matt.* **15**, 2526 (2019).
- [123] J. Carrera, X. Sánchez-Vila, I. Benet, A. Medina, G. Galarza, and J. Guimerà, On matrix diffusion: formulations, solution methods and qualitative effects, *Hydrogeo. J.* **6**, 178 (1998).

- [124] B. Maryshev, M. Joelson, D. Lyubimov, T. Lyubimova, and M. C. N'eel, Non Fickian flux for advection-dispersion with immobile periods, *J. Phys.* **42**, 115001 (2009).
- [125] K. R. Roche, J. D. Drummond, F. Boano, A. I. Packman, T. J. Battin, and W. R. Hunter, Benthic biofilm controls on fine particle dynamics in streams, *Water Res. Res.* **53**, 222 (2017).
- [126] R. Gorenflo, A. A. Kilbas, F. Mainardi, and S. V. Rogosin, Mittag-Leffler functions, related topics and applications, Vol. 2 (Springer, Berlin, 2014).
- [127] R. Metzler and A. Compte, Generalized Diffusion-Advection Schemes and Dispersive Sedimentation: A Fractional Approach, *J. Phys. Chem. B* **104**, 3858 (2000).
- [128] H. Scher and E. W. Montroll, Anomalous transit-time dispersion in amorphous solids, *Phys. Rev. B* **12**, 2455 (1975).
- [129] R. Metzler and J. Klafter, The random walk's guide to anomalous diffusion: A fractional dynamics approach, *Phys. Rep.* **339**, 1 (2000).
- [130] Y. Zhang, D. A. Benson, and B. Baeumer, Moment analysis for spatiotemporal fractional dispersion, *Water Res. Res.* **44**, W04424 (2008).
- [131] T. R. Prabhakar, A singular integral equation with a generalized Mittag Leffler function in the kernel. *Yokohama Math. J.* **19**, 7 (1971).
- [132] H. J. Haubold, A. M. Mathai, and R. K. Saxena, Mittag-Leffler functions and their applications, *J. Appl. Math.* **2011**, 298629 (2011).
- [133] A. Bodrova, A. V. Checkkin, A. G. Cherstvy, and R. Metzler, Quantifying non-ergodic dynamics of force-free granular gases, *Phys. Chem. Chem. Phys.* **17**, 21791 (2015).
- [134] J.-H. Jeon, A. V. Checkkin, and R. Metzler, Scaled Brownian motion: a paradoxical process with a time dependent diffusivity for the description of anomalous diffusion, *Phys. Chem. Chem. Phys.* **16**, 15811 (2014).

- [135] A. Fulinski, Communication: How to generate and measure anomalous diffusion in simple systems, *J. Chem. Phys.* **138**, 021101 (2013).
- [136] J. Klafter, A. Blumen, and M. F. Shlesinger, Stochastic pathway to anomalous diffusion, *Phys. Rev. A* **7**, 3081 (1987).
- [137] D. Janning, M. Igaev, F. Sündermann, J. Brühmann, O. Beutel, J. J. Heinisch, L. Bakota, J. Piehler, W. Junge, and R. Brandt, Single-molecule tracking of tau reveals fast kiss-and-hop interaction with microtubules in living neurons, *Mol. Biol. Cell.* **25**, 3541 (2014).
- [138] M. Haro, V. Singh, S. Steinhauer, and E. Toulkeridou, Nanoscale Heterogeneity of Multilayered Si Anodes with Embedded Nanoparticle Scaffolds for Li-Ion Batteries, *Adv. Sci.* **4**, 1700180 (2017).
- [139] P. Gouze, Y. Melean, T. Le Borgne, M. Dentz, and J. Carrera, Non-Fickian dispersion in porous media explained by heterogeneous microscale matrix diffusion. *Water Res. Res.* **44**, W11416 (2008).
- [140] M. Schwarzl, A. Godec, and R. Metzler, Quantifying non-ergodicity of anomalous diffusion with higher order moments, *Sci. Rep.* **7**, 3878 (2017).